

A Comparison of Jet Properties  
Between p+p, d+Au, and Au+Au Collisions  
at RHIC Using  $\gamma$ -Hadron  
Angular Correlation Measurements

Mickey G. Chiu

Submitted in partial fulfillment of the  
requirements for the degree  
of Doctor of Philosophy  
in the Graduate School of Arts and Sciences

COLUMBIA UNIVERSITY  
2004

© 2004

Mickey G. Chiu

All Rights Reserved

## ABSTRACT

### A Comparison of Jet Properties

Between p+p, d+Au, and Au+Au Collisions

at RHIC Using  $\gamma$ -Hadron

Angular Correlation Measurements

Mickey G. Chiu

With the advent of the Relativistic Heavy Ion Collider (RHIC), collisions of heavy ions at collider energies make jet physics accessible as a probe of the properties of a quark-gluon plasma (QGP). This was borne out by the observation of a factor of five suppression in the yield of high- $p_T$  particles in central Au+Au collisions, when compared to the expectation from binary scaling of nucleon-nucleon collisions. To move beyond the simple information presented by inclusive distributions, we look at the angular correlations between associated charged hadrons and leading high- $p_T$  photons ( $p_T > 2.25$  GeV/c). Photons at high- $p_T$  are primarily from the decays of fragmentation products of a jet, and thus the photon serves as a good proxy for the underlying jet axis. The width and yield of the jet associated hadrons, after subtracting the background from the underlying event, then tell us about the properties of jets in different systems. Using  $p+p$  data as a baseline, we find no strong changes in the jet widths in both  $d$ +Au and Au+Au, pointing towards a scenario where outgoing partons leave the nuclear medium and then fragment in vacuum. In  $d$ +Au, we observe a 20% decrease with centrality in the yields of moderate  $p_T$  (2.0-4.0 GeV/c) jet associated particles, pointing towards a cold nuclear effect on jets in  $d$ +Au collisions. In the Au+Au case, a strong quenching of the away side jet is observed, consistent with scenarios where jets lose large amounts of energy in the dense medium created in the aftermath of an heavy-ion collision.

# Contents

<b>1</b>	<b>Introduction</b>	<b>1</b>
1.1	Exploring QCD with Heavy-Ion Collisions	1
1.2	Reaching the Critical Limit in QCD	2
1.3	Confinement and a Path to Deconfinement	3
1.4	Hard Scattering in p+p Collisions	9
1.4.1	Collinear Factorization	10
1.5	Translating pQCD calculations to Nuclei	11
1.5.1	Multiple Scattering, Intrinsic $k_T$ , and the Cronin Effect	14
1.5.2	Shadowing	16
1.6	Parton Energy Loss	17
1.6.1	Coherent Quantum Chromodynamic Effects at High Energies	18
1.6.2	Gyulassy-Wang Model	19
1.6.3	BDMPS	20
1.7	Angular Correlations from the Fragmentation Products of Jets	20
1.8	Correlations with the Reaction Plane: Elliptic Flow and Jet Energy Loss	21
<b>2</b>	<b>Experimental Apparatus</b>	<b>24</b>
2.1	RHIC	24
2.2	PHENIX Overview	26
2.2.1	Trigger and Event Characterization Detectors	30
2.2.2	Magnetic Field	34

2.2.3	Charged Particle Tracking . . . . .	41
2.2.4	Particle Identification . . . . .	54
2.2.5	Electro-Magnetic Calorimeter (EMC) . . . . .	55
2.3	Data Acquisition System (DAQ) . . . . .	65
2.4	Level-1 Triggers . . . . .	70
2.4.1	BBC Local-Level1 (BBC-LL1) Trigger . . . . .	70
2.4.2	ZDC Coincidence (ZDCNS) Trigger . . . . .	71
2.4.3	EmCal (ERT) Trigger . . . . .	71
<b>3</b>	<b>Data Analysis</b>	<b>73</b>
3.1	Measuring Angular Correlations To Deduce Jet Properties . . . . .	73
3.2	Run Selection . . . . .	75
3.3	Event Selection . . . . .	76
3.4	Centrality Determination . . . . .	77
3.5	Trigger Particle Selection (Photon Identification) . . . . .	80
3.5.1	PC3 Charged Particle Veto . . . . .	82
3.5.2	Time of Flight Cut . . . . .	85
3.5.3	Shape Cut using Shower Dispersion . . . . .	85
3.5.4	Neutron/Anti-Neutron Contamination . . . . .	90
3.5.5	Warm/Hot Towers . . . . .	90
3.6	Associated Particles Selection (Charged Hadrons Selection) . . . . .	92
3.7	Estimating the Acceptance Function . . . . .	93
3.8	Charged Track Efficiency Calculations . . . . .	95
3.8.1	Efficiency Losses in High Multiplicity Events . . . . .	96
3.9	Corrections for Particles that Fall out of Eta Acceptance . . . . .	100
3.9.1	Threshold Bias of the ERT Trigger . . . . .	102
3.10	Verification of Method using Monte Carlo . . . . .	104
3.11	Measuring Elliptic Flow . . . . .	105
3.12	Systematic Errors . . . . .	106

<b>4 Results</b>	<b>108</b>
4.1 Per-Trigger Differential Yields in $\Delta\phi$	108
4.1.1 Behavior of the Underlying Event (Pedestal)	109
4.1.2 Dependence of Underlying Event on Trigger	111
4.1.3 Jet Widths	112
4.1.4 Jet Yields in $p+p$ and $d+\text{Au}$	113
4.2 Jet Yields in $\text{Au}+\text{Au}$	118
4.2.1 Preliminaries, Assumptions	119
4.3 Yield Analysis	122
4.4 Au+Au Results	124
4.4.1 Au+Au Background	125
<b>5 Discussion</b>	<b>133</b>
5.1 Sources of Trigger Photons	133
5.2 Cold Nuclear Effects in $d+\text{Au}$	136
5.3 Jets in $\text{Au}+\text{Au}$	140
<b>A Associated Yields</b>	<b>149</b>
A.1 Associated Yields in $p+p$	150
A.2 Associated Yields in $d+\text{Au}$	155
A.3 Associated Yields in $\text{Au}+\text{Au}$	175
<b>B Phenix Collaboration, Run02 and Run03</b>	<b>180</b>

# List of Figures

1.1	Energy Density from Lattice Calculations . . . . .	3
1.2	QCD phase diagram in the temperature-density plane . . . . .	4
1.3	QED Vacuum Polarization . . . . .	5
1.4	QCD Vacuum Polarization . . . . .	7
1.5	Heavy Quark Potential in a High-Temperature QGP . . . . .	9
1.6	Collinear Factorization . . . . .	11
1.7	Comparison of $p+p$ $\pi^0$ spectra to NLO calculation . . . . .	12
1.8	Head-On View of Two Nuclei Colliding . . . . .	13
1.9	$\pi^0 R_{AA}$ . . . . .	15
1.10	Ca and Au Structure Functions . . . . .	17
1.11	LPM Coherence Length . . . . .	18
1.12	Elliptic Flow of Identified Particles . . . . .	23
2.1	Au Acceleration in RHIC . . . . .	25
2.2	PHENIX Detector Layout . . . . .	28
2.3	PHENIX Central Arm Layout, Beam View . . . . .	29
2.4	PHENIX BBC . . . . .	30
2.5	PHENIX BBC Location . . . . .	31
2.6	PHENIX BBC Rings . . . . .	31
2.7	PHENIX BBC Timing Resolution . . . . .	32
2.8	PHENIX BBC Slew Correction . . . . .	33
2.9	ZDC Location . . . . .	35
2.10	ZDC Module . . . . .	36

2.11	PHENIX Magnets . . . . .	37
2.12	PHENIX Magnet Coils . . . . .	38
2.13	PHENIX Magnetic Field . . . . .	39
2.14	PHENIX Magnetic Field Values . . . . .	40
2.15	PHENIX Tracking . . . . .	42
2.16	PHENIX Drift Chamber . . . . .	44
2.17	PHENIX Drift Chamber . . . . .	45
2.18	Drift Chamber Hough Transform . . . . .	46
2.19	PHENIX Pad Chamber Mechanical Components . . . . .	50
2.20	PHENIX PC Pixels and Pads . . . . .	51
2.21	PHENIX PC Resolution . . . . .	51
2.22	PHENIX PC Online Monitor . . . . .	52
2.23	PHENIX RICH . . . . .	55
2.24	Electron Identification in the RICH . . . . .	56
2.25	PHENIX EMCal . . . . .	57
2.26	PHENIX PbSc Energy Resolution . . . . .	59
2.27	Pb-scintillator timing resolution for different particles. Top: line-shape for 1 GeV/c electrons, pions and protons. Bottom: resolution in the momentum range 0.3-1.0 GeV/c . . . . .	60
2.28	PHENIX PbGl Module . . . . .	61
2.29	PbGl energy resolution versus incident energy. . . . .	62
2.30	PHENIX PbGl . . . . .	63
2.31	PHENIX DAQ Rates . . . . .	66
2.32	PHENIX DAQ Schematic . . . . .	67
2.33	PHENIX EventBuilder . . . . .	69
2.34	PHENIX EmCal Trigger . . . . .	72
3.1	DC $\phi$ vs. run, Run03 p+p . . . . .	76
3.2	DC $\phi$ vs. run, Run03 d+Au . . . . .	77
3.3	DC $\phi$ vs. run, Run02 Au+Au . . . . .	78

3.4	Z-Vertex Distributions	79
3.5	Centrality in $d$ +Au	80
3.6	Centrality in Au+Au	81
3.7	pc3d from the same event (black) and from mixed events (red) for PbSc (top) and PbGl (bottom)	83
3.8	fractional charged contamination vs. pc3d cut for PbSc (top) and PbGl (bottom)	84
3.9	Dispersion in $y$ as a function of $\eta$ for PbSc (left) and PbGl (right)	86
3.10	Dispersion in $z$ as a function of $\eta$ for PbSc (left) and PbGl (right). The top plots are uncorrected while the bottom has the $\eta$ dependence corrected out	87
3.11	Maximum dispersion for photons as a function of pc3d for the PbSc (top) and PbGl (bottom)	88
3.12	Fraction of charged contamination vs. pc3d cut for $2.0 < p_T < 2.5$ GeV/c (circles) and $p_T > 2.5$ GeV/c (squares) photons. The filled symbols are for PbSc, and the open circles are for the PbGl	89
3.13	Central Tower Positions of Trigger Photons, Au+Au Run02	91
3.14	Central Tower Positions of Trigger Photons, Run03 p+p. Left, PbSc, Right, PbGl	91
3.15	Central Tower Positions of Trigger Photons, Run03 d+Au, Left, PbSc, Right, PbGl	92
3.16	Left: The acceptance function for various $p_T$ bins, from 0.3-0.4 (black), 0.4-0.5 (red), and so on. Right: The acceptance function for three $\Delta\phi$ bins vs $p_T$ } for Run03 p+p (left) and d+Au (right). Red is for the bin centered at $90^\circ$ and is 3 times the actual acceptance value, green is the bin centered at $180^\circ$ , and black is for the bin centered at $0^\circ$	94
3.17	The acceptance in phi vs. $1/p_T$	94

3.18	The efficiency correction function $1/\epsilon$ , for a detector with full $2\pi$ coverage and $ \eta  < 0.3$ . . . . .	96
3.19	Run by Run Efficiency, Au+Au . . . . .	97
3.20	Estimating Efficiency from Matching Areas of High Efficiency. . . . .	98
3.21	The DC $\phi$ distribution for accepted tracks, for the West (left) and East (right) Arms. Once a region of high efficiency in $\phi$ is matched, the ratio of the integral of the above distributions gives a measure of the relative efficiency between the two runs. Note that the vertical scale is in arbitrary units. . . . .	98
3.22	The multiplicity dependent efficiency as a function of $p_T$ for different centralities in Au+Au. There is about a 70% efficiency loss in the most central Au+Au events. . . . .	99
3.23	The PHENIX acceptance in $\eta$ for a jet with a gaussian profile. . . . .	101
3.24	The p+p and d+Au near and far jet widths as a function of centrality	101
3.25	The ratio of the trigger photon spectrum in ERT over MinBias triggers (left). The ratio of the photon spectrum for different centralities in ERT events (right). . . . .	102
3.26	A comparison of conditional yields in d+Au for ERT vs. MinBias events. On the left is the conditional yield for trigger $p_T > 2.0$ GeV/c, where a clear trigger bias can be seen, while on the right the bias disappears for trigger $p_T > 3.5$ GeV/c. . . . .	103
3.27	The effect of the trigger bias on the p+p yields. On the left is the comparison between the yield in ERT events compared to min-bias, while on the right is the ratio between the trigger photon spectrum and the min-bias photon spectrum. . . . .	103
3.28	Comparison between reconstructed correlations in PHENIX simulation (red) and original PYTHIA input (black), for trigger photons with $p_T > 2.5$ GeV/c, and associated charged hadrons with $1.0 < p_T < 2.0$ (left) and $2.0 < p_T < 4.0$ (right). . . . .	104

4.1	Run02, Run03 Correlations	109
4.2	The level of the background under the jet peaks, for $p+p$ ( $N_{part} = 2$ ) and $d+Au$ . The solid circles are determined via a fit and the open circles are determined absolutely by weighting minimum bias multiplicities (see text).	110
4.3	The yield of particles in the underlying event for $p+p$ , as a function of the trigger $p_T$ , for associated particles with $1 < p_T < 2$ (blue) and $2 < p_T < 4$ (magenta)	111
4.4	The $p+p$ and $d+Au$ near jet widths as a function of centrality	113
4.5	The $p+p$ and $d+Au$ far jet widths as a function of centrality	114
4.6	$p+p$ , $3.5 < p_T^{trig} < 20.0 GeV/c$ , $\Delta\eta$ distribution	114
4.7	$d+Au$ , $3.5 < p_T^{trig} < 20.0 GeV/c$ , $\Delta\eta$ distribution, 0-20% Central	115
4.8	$d+Au$ , $3.5 < p_T^{trig} < 20.0 GeV/c$ , $\Delta\eta$ distribution, 20-40% Central	115
4.9	$d+Au$ , $3.5 < p_T^{trig} < 20.0 GeV/c$ , $\Delta\eta$ distribution, 40-60% Central	115
4.10	$d+Au$ , $3.5 < p_T^{trig} < 20.0 GeV/c$ , $\Delta\eta$ distribution, 60-88% Central	116
4.11	The $p+p$ and $d+Au$ near jet associated yields after pedestal subtraction. The color codes represent the $p_T$ bin of the associated particles, with black = 0.3-0.6 GeV, red = 0.6-1.0 GeV, green = 1.0-2.0 GeV, and blue = 2.0-4.0 GeV	116
4.12	The $p+p$ and $d+Au$ away jet associated yields after pedestal subtraction. The color codes represent the $p_T$ bin of the associated particles, with black = 0.3-0.6 GeV, red = 0.6-1.0 GeV, green = 1.0-2.0 GeV, and blue = 2.0-4.0 GeV	117
4.13	The $p+p$ integrated near and far side jet yields, after pedestal subtraction, as a function of the trigger $p_T$	118
4.14	The $p+p$ integrated near and far side jet yields, after pedestal subtraction, as a function of the trigger $p_T$	119
4.15	$Au+Au$ , $2.25 < p_T^{trig} < 20.0 GeV/c$ , $1.0 < p_T^{assoc} < 2.0 GeV/c$	126
4.16	$Au+Au$ , $2.25 < p_T^{trig} < 20.0 GeV/c$ , $2.0 < p_T^{assoc} < 4.0 GeV/c$	127

4.17 Run02 Au+Au, $2.25GeV/c < p_T^{trig}$ , Background subtracted $\frac{1}{N_{trig}} \frac{dN^{ch}}{d\phi}$ distributions, for associated bins of $1.0 < p_T^{assoc} < 2.0$ (left) and $2.0 < p_T^{assoc} < 4.0$ (right). From top to bottom are centralities 0-10,10-20,20-40,40-60,60-90%.	128
4.18 Run02 Au+Au, $2.25GeV/c < p_T^{trig}$ , jet widths	129
4.19 Run02 Au+Au, $2.25GeV/c < p_T^{trig}$ , $1.0 < p_T^{assoc} < 2.0$ , Associated Jet Yields	130
4.20 Run02 Au+Au, $2.25GeV/c < p_T^{trig}$ , $2.0 < p_T^{assoc} < 4.0$ , Associated Jet Yields	131
4.21 Run02 Au+Au, $2.25GeV/c < p_T^{trig}$ , Background subtracted $\frac{1}{N_{trig}} \frac{dN^{ch}}{d\phi}$ distributions, for associated bins of $2.0 < p_T^{assoc} < 4.0$ , centralities 0-10 and 60-90%.	132
5.1 Meson Decays to Photons	135
5.2 Jet Propagation in $d+Au$	137
5.3 Brahms $R_{CP}(\eta)$	139
5.4 PHENIX $R_{CP}(\eta)$	140
5.5 Jet Survival Positions	142
A.1 $p+p$ , $2.25 < p_T^{trig} < 20.0GeV/c$	150
A.2 $p+p$ , $2.25 < p_T^{trig} < 2.75GeV/c$	151
A.3 $p+p$ , $2.75 < p_T^{trig} < 3.5GeV/c$	152
A.4 $p+p$ , $3.5 < p_T^{trig} < 4.5GeV/c$	153
A.5 $p+p$ , $4.5 < p_T^{trig} < 20.0GeV/c$	154
A.6 $d+Au$ , $2.25 < p_T^{trig} < 20.0GeV/c$ , 0-20% central	155
A.7 $d+Au$ , $2.25 < p_T^{trig} < 20.0GeV/c$ , 20-40% central	156
A.8 $d+Au$ , $2.25 < p_T^{trig} < 20.0GeV/c$ , 40-60% central	157
A.9 $d+Au$ , $2.25 < p_T^{trig} < 20.0GeV/c$ , 60-88% central	158
A.10 $d+Au$ , $2.25 < p_T^{trig} < 2.75GeV/c$ , 0-20% central	159
A.11 $d+Au$ , $2.25 < p_T^{trig} < 2.75GeV/c$ , 20-40% central	160

A.12 $d+Au$ , $2.25 < p_T^{trig} < 2.75 GeV/c$ , 40-60% central . . . . .	161
A.13 $d+Au$ , $2.25 < p_T^{trig} < 2.75 GeV/c$ , 60-88% central . . . . .	162
A.14 $d+Au$ , $2.75 < p_T^{trig} < 3.5 GeV/c$ , 0-20% central . . . . .	163
A.15 $d+Au$ , $2.75 < p_T^{trig} < 3.5 GeV/c$ , 20-40% central . . . . .	164
A.16 $d+Au$ , $2.75 < p_T^{trig} < 3.5 GeV/c$ , 40-60% central . . . . .	165
A.17 $d+Au$ , $2.75 < p_T^{trig} < 3.5 GeV/c$ , 60-88% central . . . . .	166
A.18 $d+Au$ , $3.5 < p_T^{trig} < 4.5 GeV/c$ , 0-20% central . . . . .	167
A.19 $d+Au$ , $3.5 < p_T^{trig} < 4.5 GeV/c$ , 20-40% central . . . . .	168
A.20 $d+Au$ , $3.5 < p_T^{trig} < 4.5 GeV/c$ , 40-60% central . . . . .	169
A.21 $d+Au$ , $3.5 < p_T^{trig} < 4.5 GeV/c$ , 60-88% central . . . . .	170
A.22 $d+Au$ , $4.5 < p_T^{trig} < 20.0 GeV/c$ , 0-20% central . . . . .	171
A.23 $d+Au$ , $4.5 < p_T^{trig} < 20.0 GeV/c$ , 20-40% central . . . . .	172
A.24 $d+Au$ , $4.5 < p_T^{trig} < 20.0 GeV/c$ , 40-60% central . . . . .	173
A.25 $d+Au$ , $4.5 < p_T^{trig} < 20.0 GeV/c$ , 60-88% central . . . . .	174
A.26 $Au+Au$ , $2.25 < p_T^{trig} < 20.0 GeV/c$ , $0.3 < p_T^{assoc} < 0.6 GeV/c$ . . . . .	176
A.27 $Au+Au$ , $2.25 < p_T^{trig} < 20.0 GeV/c$ , $0.6 < p_T^{assoc} < 1.0 GeV/c$ . . . . .	177
A.28 $Au+Au$ , $2.25 < p_T^{trig} < 20.0 GeV/c$ , $1.0 < p_T^{assoc} < 2.0 GeV/c$ . . . . .	178
A.29 $Au+Au$ , $2.25 < p_T^{trig} < 20.0 GeV/c$ , $2.0 < p_T^{assoc} < 4.0 GeV/c$ . . . . .	179

# List of Tables

2.1	Design Performance Parameters for RHIC	26
2.2	Summary of the PHENIX Detector Subsystems. [5]	47
2.3	PHENIX Central Magnet Parameters	48
2.4	Pad Chamber Parameters	51
2.5	Individual Pb-Scintillator Calorimeter Tower Parameters	58
2.6	Lead-Glass Physical Parameters	64
2.7	Collider Parameters	65
3.1	Correction parameters to the dispersion in the z direction.	86
3.2	Maximum Estimated Neutron/Anti-Neutron Contamination to Photon Triggers	90
4.1	$v_2$ values	125
5.1	Parameters for Hadron Decays to Gamma	134

## Acknowledgements

This all started in the beginning of the summer of 1998, after I had just finished my required classes. Unlike most of my peers at Columbia, I had not decided which research group to join. So I sent an email to Bill Zajc asking if he needed any students for the summer. Fortunately for me, there was an opening for a student to help on the DCM's with Cheng-yi Chi and Jamie Nagle. As is well known by now, I decided to stay on and it has been truly a wonderful experience ever since. I would especially like to express my gratitude towards Bill for just about everything, to Brian Cole for many stimulating discussions about jet physics, and to Jamie and Chi for not just their electronics expertise, but also for endowing me with the right attitude towards life.

To Justin Frantz, Chun Zhang, Cristine Aidala, Sean Kelly, Sotiria Batsouli, David d'Enterria, Peter Steinberg, and David Winter, aka the greatest bunch of students and post-docs alive, thanks for keeping things fun through those long cold nights in the counting house. In the inimitable words of Chun, "I love you guys, man! You guys are like a family to me." To the newer members of the Columbia Heavy-Ion group, Jiamin, Yueshi, and Jiangyong, I wish you the best of luck. I'm sure with such talent you won't need it.

I would like to personally thank the entire PHENIX collaboration (all 450+ of them). There are too many to name, but in particular I would like to thank Takashi, Tomoaki, Tatsuya, Susumu, Sebastian, and Alexei for all their help with their respective hardware. I would especially like to acknowledge my fondness for the multiply talented DAQ group at BNL: John Haggerty, Martin Purschke, Chris Pinkenburg, Ed Desmond, Sergei Belikov, and Stephen Adler. I don't even want to imagine how much longer this thesis might take without the data to analyze it. I would also like to thank my new friends in the Illinois group, Matthias Grosse-Perdekamp, Jen-Chieh Peng, and Hiro Hiejima, for many useful discussions and their utmost patience in waiting for me to finish.

As with all Nevis students, Ann Therrien was always there when I needed her,

and I am deeply indebted to her for her tireless devotion to us all. May she always be the shepherd for the new particles at Nevis.

I've had the wonderful fortune to have met and worked with some of the best people in the entire field of heavy-ion physics. To that end, I consider myself quite a lucky guy.

To Yi-Ju

# Chapter 1

## Introduction

### 1.1 Exploring QCD with Heavy-Ion Collisions

Our current understanding of the physical laws of the Universe, with the exception of gravity, is encapsulated in the Standard Model (SM), which is a gauge theory based on the symmetry  $SU(3) \times SU(2) \times U(1)_Y$ .  $SU(2) \times U(1)_Y$  is the underlying symmetry group for the electro-weak interactions, and at lower energies is spontaneously broken down to  $U(1)_Q$ , the symmetry group for electric charge  $e$ , and forms the basis for Quantum Electrodynamics (QED).  $SU(3)$  is the symmetry of color in Quantum Chromodynamics (QCD), which governs the interactions between quarks and gluons, and is by far the least understood sector in the standard model, due largely to the failure of perturbative calculations and the non-abelian nature of the  $SU(3)$  group.

At present, QCD has found spectacular success in describing interactions at high- $Q^2$ , where the coupling  $\alpha_s$  is weak and allows for perturbative expansion techniques, or where the mass is high so that non-relativistic QCD may be applied, such as in charmonium states. However, these can be understood using quarks and gluons as the fundamental degrees of freedom, while in general one can only observe hadrons as color singlets in the world around us. The effect of QCD dynamics can be seen in the masses of the hadrons. Even though the light quarks have current masses of  $u = 1.5\text{-}4.5 \text{ MeV}$ ,  $d = 5.0\text{-}8.5 \text{ MeV}$ , protons have masses of 938 MeV. Thus, 98% of

the proton mass comes from QCD dynamics.

However, even though the structure of the theory is well known, most of the phenomena that QCD governs, such as the mass spectrum of the hadrons, cannot be easily computed from perturbative expansions. This is due to the property of confinement, and also because the coupling constant becomes large at low  $p_T$ , so that perturbative methods are unreliable. It is hoped that by colliding nuclei one may have enough reinteractions that the matter may be described as a bulk system in local thermal equilibrium. From this, one may learn, through its behavior, how QCD behaves when in bulk, much as QED describes a regular plasma.

## 1.2 Reaching the Critical Limit in QCD

Unlike the simple case of an individual hadron, which is dominated by its dynamical behavior, one can consider a system of many hadrons. By doing this one can use statistical methods to study the system thermodynamically. Besides being an alternate way to study QCD, there are some distinct advantages to this approach. While one can try to reduce the physical laws to a few simple rules, the universe is not made of individual collisions but is instead full of complex phenomena from many-body interactions.

Also, we have seen that due to the property of confinement, one cannot see the quarks and gluons since they are confined to a length on the order of  $\Lambda_{QCD}$ . The density of ordinary nuclear matter is  $\rho_0 = 0.135 \text{ GeV/fm}^3$ , and the typical nucleon spacing is  $d = (V/A)^{\frac{1}{3}} = 1.95 \text{ fm}$ . Thus, if one imagines “squeezing” a nucleus down so that the typical separation between nucleons were of the same order as the nucleon size,  $d \sim \langle r^2 \rangle^{\frac{1}{2}} \sim 0.84 \text{ fm}$  [27], at a critical density of  $\rho \sim 13\rho_0$ , the nucleons themselves must lose their individual identity.

This very simple consideration of hadronic and nuclear length scales can be more quantitatively pursued in Lattice Gauge QCD, which discretizes spacetime to non-perturbatively calculate QCD. In figure 1.1, Karsch and collaborators calculate the energy density as a function of the temperature for a thermal QCD system. One can

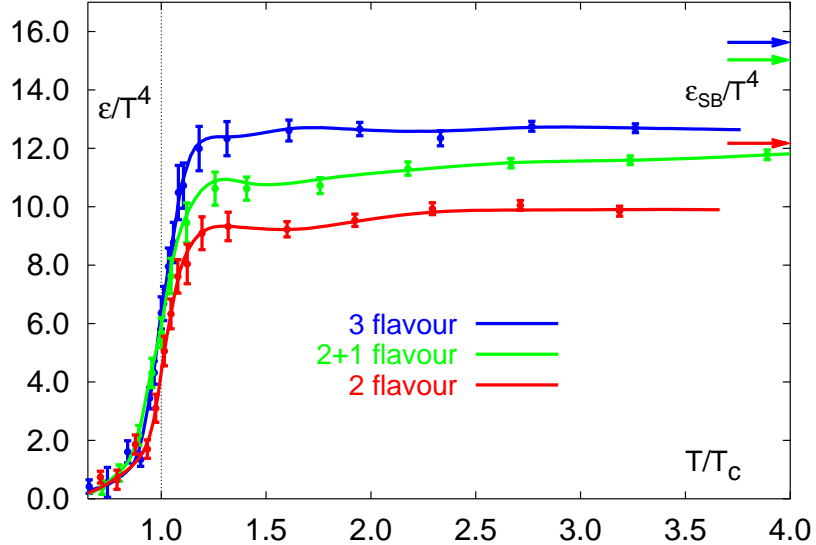


Figure 1.1: Energy Density as a function of the temperature  $T$ , as calculated in Lattice Gauge QCD.  $T_C$  is the critical temperature. The limiting Boltzmann behavior is indicated by the arrows on the right. [44]

see the large increase in the energy density as new degrees of freedom are excited at the critical temperature  $T_C$ . This is the transition to the Quark-Gluon Plasma.

Experimentally, to achieve this transition requires high energy densities over regions larger than the typical hadronic scale of 1 fm. The size of the region automatically makes nuclei leading candidates as an ingredient for stimulating QGP formation in the laboratory. Since the pressures needed to compress a nucleus are far beyond what is currently available, the more accessible experimental technique is to collide heavy nuclei at high energies.

### 1.3 Confinement and a Path to Deconfinement

The major difference between QED and QCD is that QCD is a non-Abelian theory. The major consequence of this is confinement. To illustrate this, we first begin with the case in QED, where standard renormalization theory tells us that the coupling

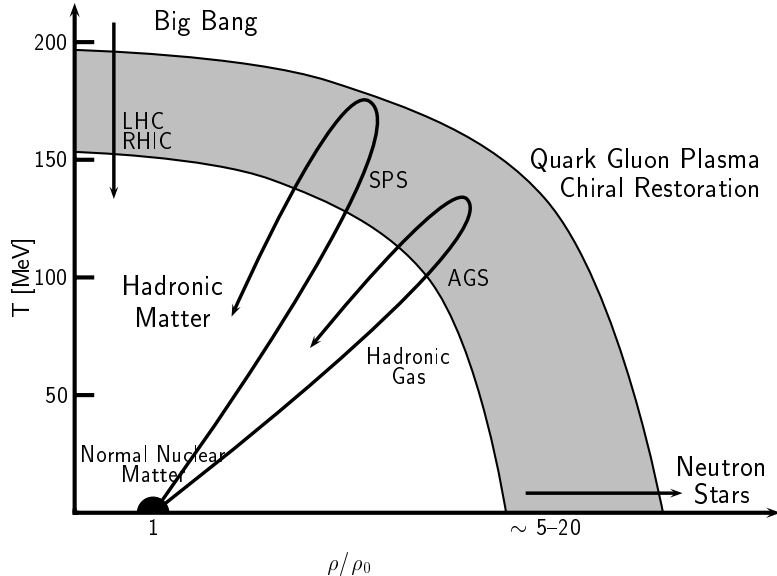


Figure 1.2: QCD phase diagram in the temperature-density plane, showing the predicted transitions between various phases.

$\alpha_{em}$  runs with the momentum scale of the probe  $Q^2$  as

$$\alpha_{em}(Q^2) = \frac{\alpha_{em}(Q_0^2)}{1 - \frac{\alpha_{em}(Q_0^2)}{3\pi} \log(\frac{Q^2}{Q_0^2})} \quad (1.1)$$

This running of the coupling has a simple physical interpretation. Imagine a net source of charge  $e$  sitting in space. At long distances, the potential of this point charge will be screened by the production of virtual particle/anti-particle pairs that are aligned opposite to the electric field, creating a dielectric effect in the vacuum. This effect is called vacuum polarization, and due to this effect one sees a screening of the charge at large distances, while the larger true potential of a bare charge shows up at shorter distances:

$$V(r) \sim -\frac{\alpha_{em}}{r}(1 + \alpha_{em}f(r)) \quad (1.2)$$

Since the length scale probed is inversely proportional to the momentum of the probe,  $l \sim 1/Q$ , higher momentum probes penetrate closer to bare charge and are therefore screened less, leading to an increase of the coupling. Thus, perturbative calculations in QED break down at short distances.

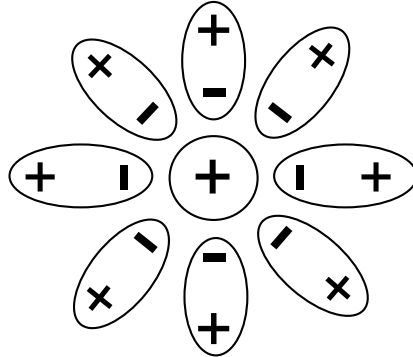


Figure 1.3: A single QED charge, and the associated dielectric vacuum polarization

One can quantify the running of the coupling constant in the framework of perturbative field theory by calculating the  $\beta$  function, which is given by the renormalization group equation in the QCD case by

$$Q^2 \frac{d\alpha_s(Q^2)}{dQ^2} = \beta(\alpha_s(Q^2)) \quad (1.3)$$

The running of the coupling, to first order, is then given by

$$\alpha_s(Q^2) = \frac{\alpha_s(Q_0^2)}{1 + \beta_0 \alpha_s(Q_0^2) \ln Q^2/Q_0^2} \quad (1.4)$$

where

$$\beta_0 = \frac{11N_C - 2n_f}{12\pi} \quad (1.5)$$

Here  $N_C$  is the number of colors and  $n_f$  are the number of flavors. This can be compared to the QED  $\beta$  function,  $\beta = -1/3\pi$ . The very remarkable aspect of QCD (and of any non-Abelian theory) is that depending on the quantitative values of  $N_C$  and  $n_f$ , the sign of the beta function may be positive, which produces theories that are asymptotically free.  $N_C = 3$  and  $n_f = 6$  for the case experimentalists are interested in, making QCD an asymptotically free theory, and confined at large distance scales.

Here we offer an heuristic description of how this confinement comes about in non-Abelian theories. In QED we have seen that there is a screening effect due to vacuum polarization. There is also that screening in QCD, as evidenced by the fermion term  $2n_f/12\pi$  in the QCD  $\beta$  function. However, the gauge boson term is opposite in sign.

Interpretations of these effects depend on the gauge one chooses. Following Peskin and Schroeder <sup>1</sup> we choose the simplest to describe, the Coulomb gauge,  $\partial_i A^{ai} = 0$ , in the gauge group  $SU(2)$ , where  $i$  runs over spacetime indices and  $a$  runs over the 3 gauge boson types. Assuming a point source of charge type  $a = 1$  and magnitude +1, the form of Gauss's Law in this gauge is

$$\partial_i E^{ai} = g\delta^{(3)}(\mathbf{x})\delta^{\mathbf{a1}} + g\epsilon^{\mathbf{abc}}\mathbf{A}^{\mathbf{bi}}\mathbf{E}^{\mathbf{ci}} \quad (1.6)$$

where  $E^{ai} = F^{a0i}$  is the “electric” field and  $A^{ai}$  is the vector potential for  $a$ . The first term in equation 1.6 is the familiar point source term. The second term shows that regions containing vector potentials and electric fields are also sources of electric fields (a consequence of the non-Abelian aspect of the theory).

A pictorial representation of this is shown in figure 1.4. The top figure shows a point source of charge +1 at  $\mathbf{x} = \mathbf{0}$  (where +1 indicates a sign of +, and *type* 1, with all magnitudes in this discussion are assumed to be unity). It emanates lines of field  $E^1$ , which somewhere crosses a vector potential  $A^{2i}$  generated as a fluctuation out of the vacuum and pointing in some direction diagonal to the field  $E^1$ . Then, the second term of eq. 1.6 is non-zero and negative; thus, there is a sink of charge -3 at the location of the  $A^2$  fluctuation, producing fields  $E^{3i}$ . The newly generated  $E^3$  fields are parallel to  $A^2$  for the  $E^3$  fields that are closer to the original +1 source, and anti-parallel for those  $E^3$  that are further away. Again from the second term in eq. 1.6, we see that the  $E^3$  and  $A^2$  fields are a source of type 1 charge, but have opposite signs. In parallel, they produce a +1 charge, and anti-parallel, they produce -1 charge. This effectively creates a dipole that is oriented so that it *adds* to the net +1 charge within a given volume. Thus, the effect of the original charge gets stronger at larger distances.

In QCD the potential is parametrized by

$$V = -\frac{4}{3}\frac{\alpha_s}{r} + \sigma r \quad (1.7)$$

---

<sup>1</sup>We follow the discussion on p. 541 of Peskin and Shroeder [52]. See the text for quantitative derivations of the  $\beta$  function.

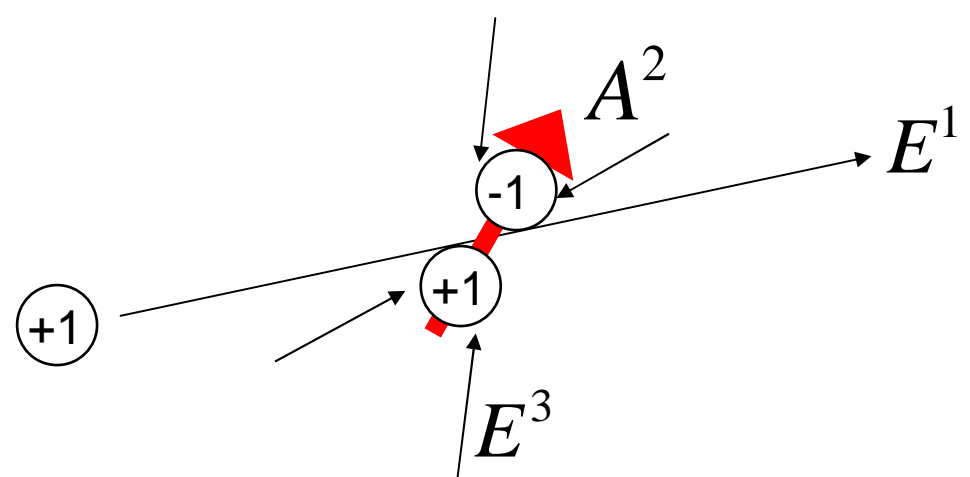
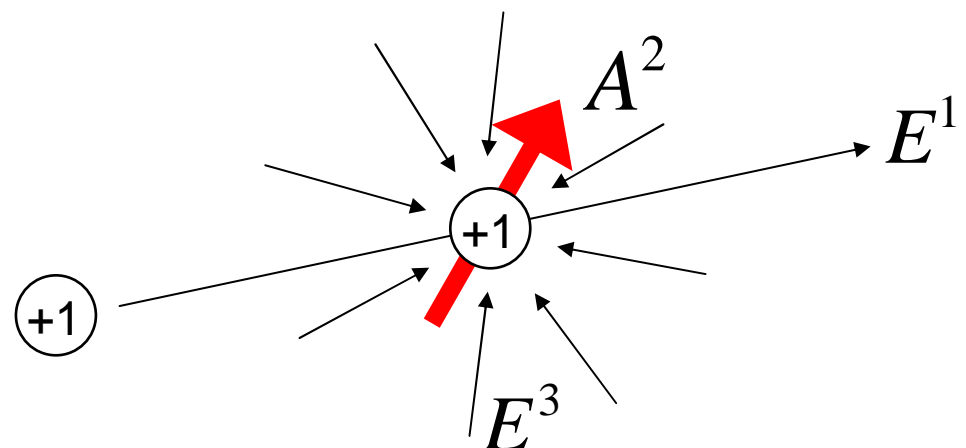
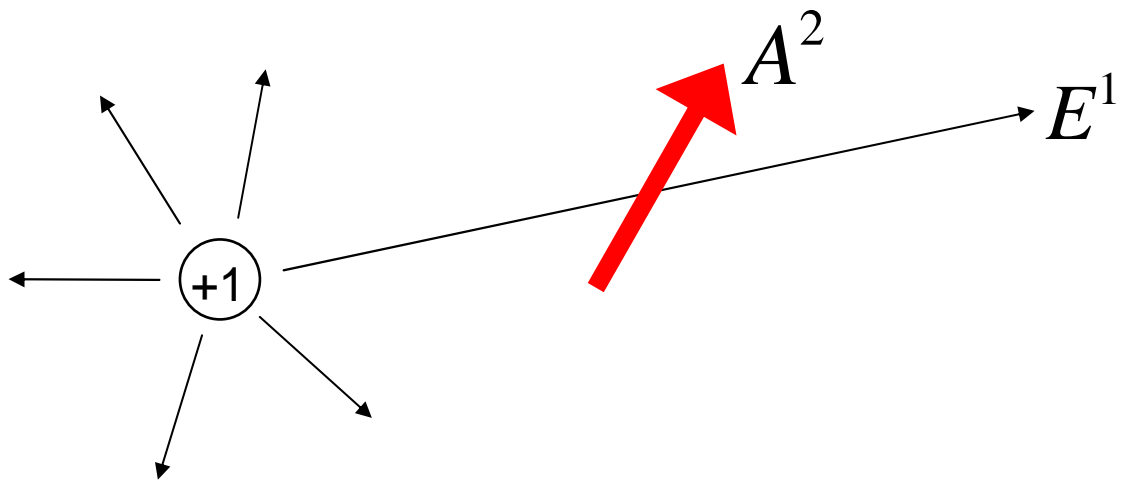


Figure 1.4: A single SU(2) charge of +1, and the associated vacuum polarization (from [52]).

where  $\sigma$  is the string tension and has a value  $\sigma \sim 1\text{GeV}/\text{fm}$ . It is this second term that describes the behavior of this anti-screening. So thinking about the behavior of the QGP in perturbative terms, it is hoped that the density of color charges is high enough that colored objects quickly reconfigure themselves to deter these long range forces, analogous to Debye screening in a plasma. Referring to figure 1.4, instead of the single charge +1 there are many charges scattered all over, averaging to zero over large distances, and interfering with the anti-screening effects.

This is not to say that the partons in a QGP will be weakly-interacting; rather, it is thought that the long range, confining term in the potential is reduced or removed, allowing the partons of the QGP to roam and interact with only the Coulombic term in the potential (or a Debye modified potential  $\sim e^{-\mu r}/r$ ). However, since the strength of the interactions run with  $Q^2$ , except for the very highest temperatures the strong force is strong (in the sense of strength). It can be compared with the electromagnetic coupling, which is about an order of magnitude lower.

The effects of this “deconfinement” of strongly colored objects has been quantitatively calculated in Lattice Thermal QCD. In figure 1.5, the free energy of a single isolated heavy quark is plotted for various temperatures. The solid line is the confining potential given by eqn. 1.7. As the temperature is increased, the long range term in the potential is reduced relative to the Coulombic part, ultimately leaving only a Debye screened Coulombia potential.

Though we have given a simple perturbative picture of how deconfinement might come about from a single isolated charge sitting in empty vacuum, there is evidence that the effects of raising the temperature has dramatic effects on the vacuum. Besides the extraordinarily rapid rise in the energy density with temperature (figure 1.1), Lattice QCD studies have also found that Chiral Symmetry is restored at the same temperatures as the deconfinement transition. This points towards modifications of the condensates living in the vacuum, since their vacuum expectation values are being changed from the ground state values found at low energies. One goal of heavy ion studies is to understand the nature of this transition, and whether

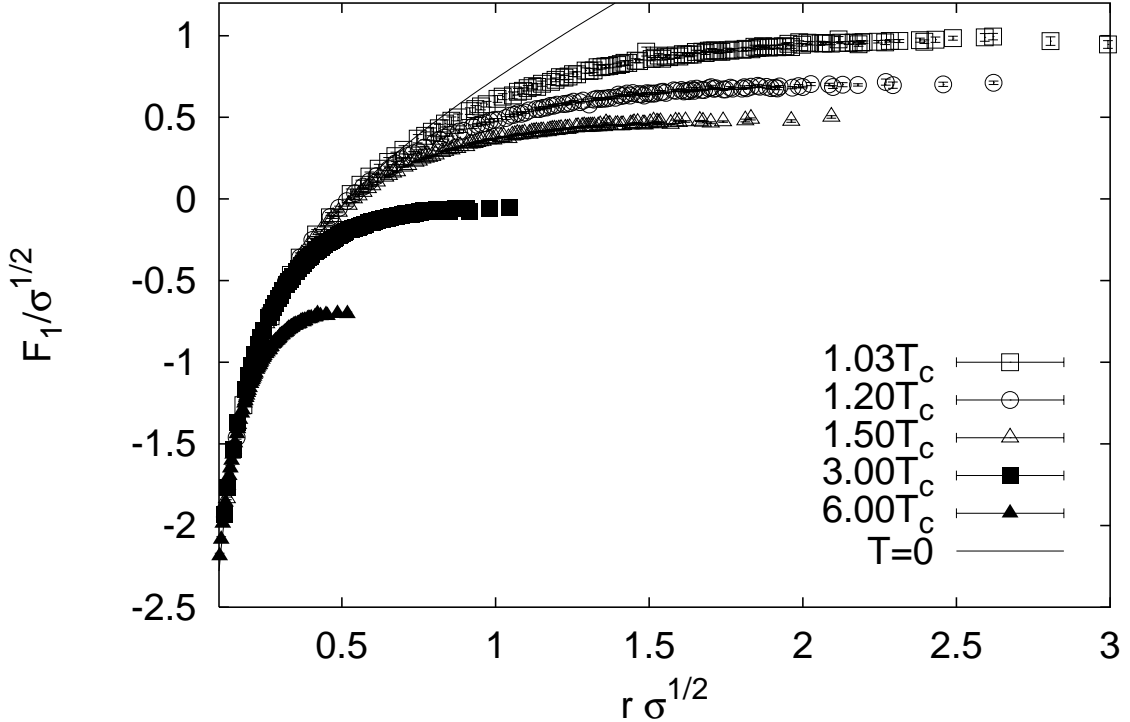


Figure 1.5: The color singlet heavy quark free energy ( $F_1$ ) in units of the string tension  $\sigma$ , versus  $r/\sqrt{\sigma}$ , for various temperatures near the critical temperature. The confining vacuum potential is indicated by the line. [43]

the vacuum is modified in the process.

## 1.4 Hard Scattering in p+p Collisions

With the advent of RHIC a new era has begun in Heavy Ion Collisions, when some of the precision theoretical understanding of pQCD can be brought to use to calculate from first principles what is going on in the underlying complicated heavy-ion collision. In this chapter we attempt a review of the physics needed to understand what jets are, and how they are useful as probes of the collision debris. We will begin by reviewing collinear factorization in the elementary proton-proton collision, which lets one calculate inclusive cross-sections of parton scatterings. We also emphasize areas where the assumptions made in the simpler  $p+p$  system break down

in collisions of nuclei, and what that can teach us about QCD.

### 1.4.1 Collinear Factorization

One of the few areas where QCD has been successfully applied is in the description of the hard elastic scattering between the constituents of hadrons. These constituents are quarks, anti-quarks, and gluons. Collectively they are called partons. The success of QCD in this area comes from the applicability of factorization in the calculation of hadron-hadron collisions. Simply put, factorization is the splitting of an hadron-hadron collision into perturbative and non-perturbative pieces, allowing one to separate the calculable parts from the soft physics that can not be calculated but which can be measured experimentally. Figure 1.6 shows a schematic view of the factorized components in a collision. The calculable part consists of the perturbatively calculable cross-section  $d\sigma$ , which can in principle be computed to all orders in perturbation theory. The non-perturbative pieces are the parton distribution function ( $f$ ), which gives the probability for finding a momentum fraction  $x$  of a parton in a hadron, and the fragmentation function  $D(z)$ , which gives the probability for an outgoing parton with momentum  $P$  to produce a hadron with momentum fraction  $z = p_h/P$ .

The cross-section to produce final-state hadrons  $h$  from a collision between hadrons  $h_1$  and  $h_2$  is given by a convolution between these factorized elements of the collision:

$$d\sigma(h_1 h_2 \rightarrow h) = \sum_{a,b} \int dx_1 dx_2 dz f_{a/h_1}(x_1, Q^2, \mu_F^2) f_{b/h_2}(x_2, Q^2, \mu_F^2) d\sigma^{(ab \rightarrow cd)}(Q^2, \mu_F^2) D_{h/c}(z_c, Q^2) \quad (1.8)$$

Here  $f_{a/h_1}$  and  $f_{b/h_2}$  are the same parton distributions functions (pdf) as one measures in DIS, using electron, muon, or neutrino beams to probe the partonic structure of a hadron,  $\mu_F$  is called the factorization scale and sets the scale that separates which processes are considered part of the hard scattering and which belong to the parton distribution functions. These distribution functions are measured over a range of  $x$  for a given  $Q^2$ , and then evolved according to the DGLAP equations.

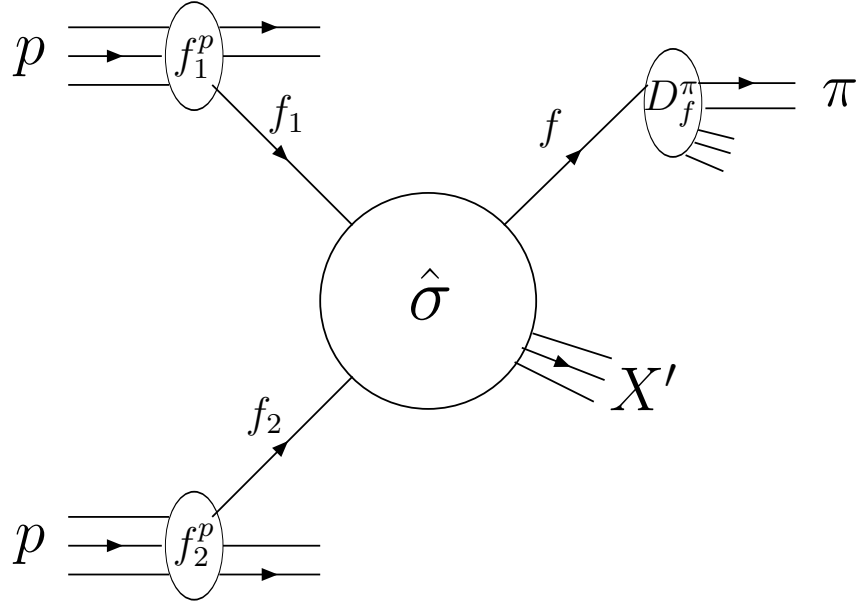


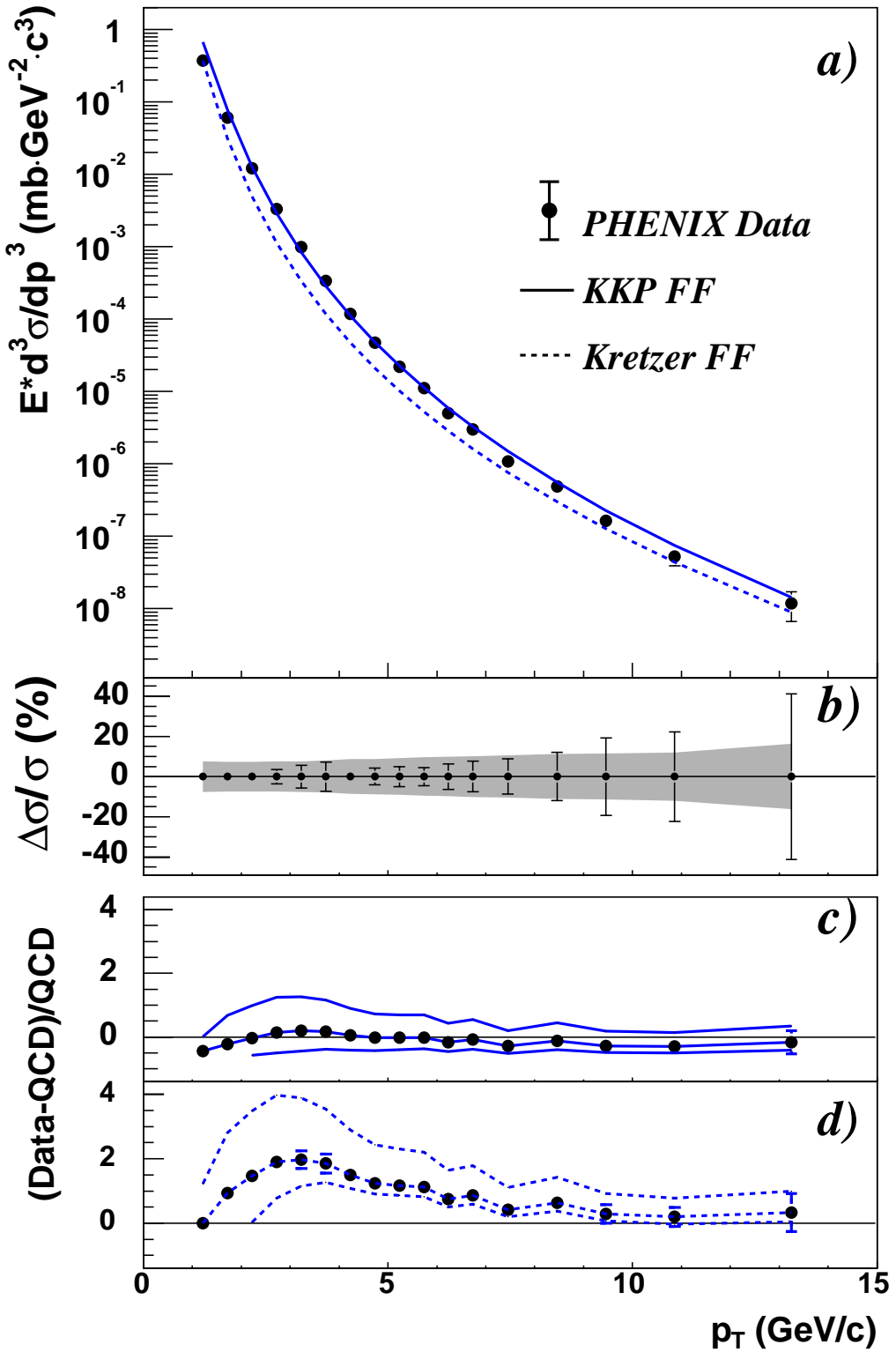
Figure 1.6: Factorization of a hadron-hadron collision separates the perturbative piece ( $d\sigma$ ) from the non-perturbative, but experimentally accessible, pieces ( $f$  and  $D$ )

This applicability of measurements made in DIS to hadron-hadron collisions is called universality, and is justified since the hard scattering timescale  $\sim 1/Q$  is much longer than the timescale of the partons in the hadron, allowing for a separation between the hadron wavefunction and the hard-scattering process.

The success of this framework can be seen in the extraordinary agreement over seven decades between next-to-leading order (NLO) calculations of the cross-section and the experimental data for  $p+p \rightarrow \pi^0 + X$  (figure 1.7).

## 1.5 Translating pQCD calculations to Nuclei

As mentioned previously, the typical separation between nucleons in a nucleus is  $\sim 1.9\text{ fm}$ . Given that the nucleons are coherent over the size of  $\sim 1\text{ fm}$ , we can largely consider a nucleus as a bag of loosely coupled nucleons, when considering the dynamics of A+B collisions. This is the basis behind the Glauber Model of collisions in nuclei, where one considers a target nucleus as a bag of free nucleons,

Figure 1.7: The invariant cross-section of  $\pi^0$ , compared to NLO calculations. [9]

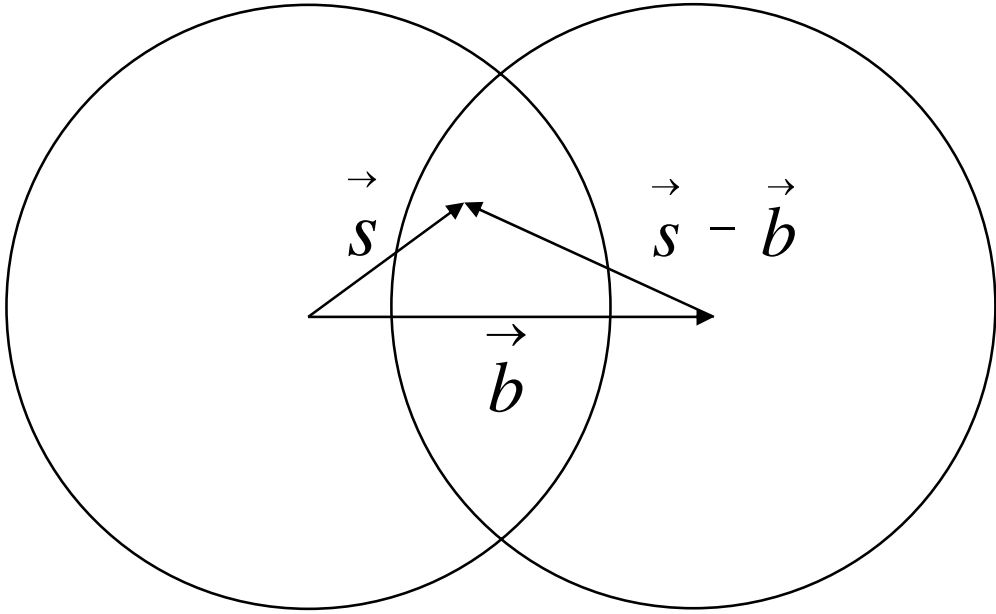


Figure 1.8: Head-On View of Two Colliding Nuclei. The impact parameter is  $b$ . and a projectile takes a straight line trajectory as it crosses the nucleus. One can understand most of the geometry of these collisions (though there are details like what happens to excited nucleons as they cross the target nucleus that are harder to quantify). The density of a nucleus is typically parameterized by a Woods-Saxon distribution:

$$\rho(r) = \frac{\rho_0(1 + wr^2/R_0^2)}{1 + e^{\frac{r-R_0}{a}}} \quad (1.9)$$

where  $R_0 = r_0 A^{1/3}$  is the nucleus radius, with  $r_0 = 1.2\text{ fm}$ , and the fall-off thickness of the nucleus skin is parametrized by  $a = 0.67\text{ fm}$ .

As a projectile goes through the nucleus along the direction  $z$ , it will see an integrated thickness  $T_A(s) = \int dz \rho_A(z, s)$ , where  $T_A(s)$  is called the thickness function and represents the number of nucleons per unit area at a distance  $s$  from the center of the nucleus. For a nucleus-nucleus collision at an impact parameter  $b$ , the number of collisions is proportional to the convolution of the thickness functions for each nucleus:

$$T_{AB}(b) = \int d^2s T_A(s) T_B(b - s) \quad (1.10)$$

If each nucleon-nucleon interaction has a cross-section  $\sigma_{NN}$ , then the probability

for an interaction at an impact parameter  $b$  is  $1 - e^{-\sigma_{NN}T_{AB}(b)}$ , and the total cross-section for a collision between nucleus A and nucleus B is the integral over all impact parameters:

$$\sigma^{AB} = \int (1 - e^{-\sigma_{NN}T_{AB}(b)})d^2b \quad (1.11)$$

For small cross-sections  $\sigma_{NN}$ , one gets

$$\sigma^{AB} \approx \int (\sigma_{NN}T_{AB}(b)d^2b) \approx \sigma_{NN}AB \quad (1.12)$$

so that small cross-section processes, such as a pQCD hard collision, scales like the binary flux of nucleons. Thus, we can define a ratio  $R_{AB}$  which compares the yield of  $\pi^0$ 's in d+Au or Au+Au collisions to the binary scaled yield in p+p collisions:

$$R_{AB}(p_T) = \frac{1/N_{evt}d^2N_{AB}/p_Tdp_Tdy}{\langle T_{AB} \rangle d^2\sigma_{pp}/p_Tdp_Tdy} \quad (1.13)$$

The results on  $R_{AB}$  for  $\pi^0$  spectra at RHIC are shown for both d+Au and Au+Au in figure 1.9. In the figure, one can see that the Au+Au yields are suppressed by a factor of 5 compared to the binary scaled expectation, which caused great excitement since they were seen as verification of a prediction that creation of Quark-Gluon Plasma would cause “jet quenching” due to induced gluon bremmstrahlung. This “jet quenching” is clearly not seen in  $R_{dA}$ , where instead there is an enhancement at moderate  $p_T$ , which was already discovered at lower energies and is known as the Cronin effect [28]. The difference between d+Au and Au+Au indicates that energy loss of the jets is caused by a final-state effect in the created matter left behind by an heavy-ion collision. Before we go on to discuss jet-quenching, we first discuss some collective effects in cold nuclei, which are necessary to understand before we can quantitatively extract properties of the medium from jet quenching in heavy-ion collisions.

### 1.5.1 Multiple Scattering, Intrinsic $k_T$ , and the Cronin Effect

As a parton projectile traverses a nucleus, it may pick up a transverse momentum component  $k_T$  from multiple scattering, and in addition it may have initially some

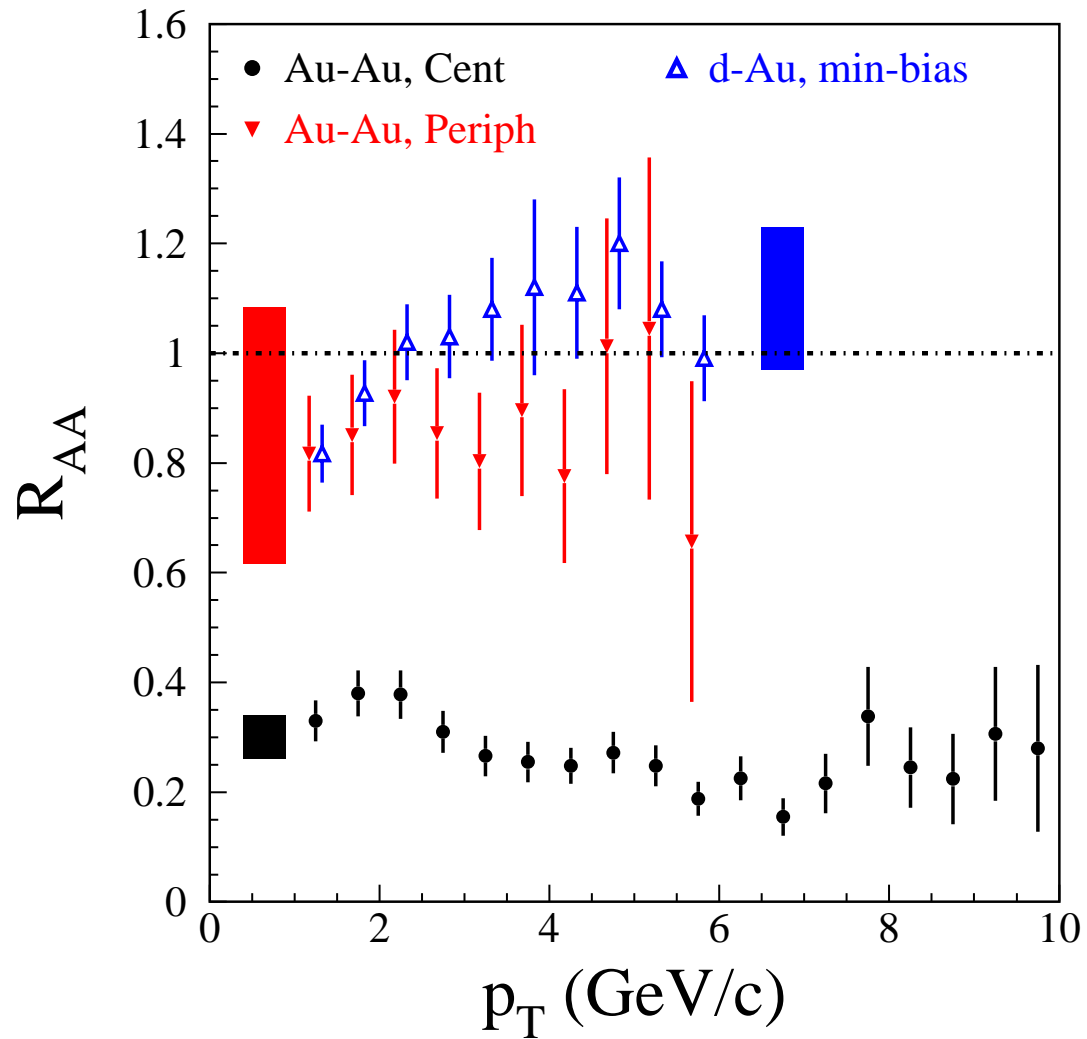


Figure 1.9:  $\pi^0 R_{AA}$  in p+p, d+Au, and Au+Au collisions at  $\sqrt{s}/NN = 200 GeV/c$  collisions. [7], [11]

$k_T$  due to, for example, Fermi motion of nucleons in the nucleus. The PDFs given in equation 1.8 can be extended to account for a transverse momentum component in the partons:

$$f_{a/p}(x, Q^2, \mu_F^2) = \int^{Q^2} \frac{dk_T^2}{k_T^2} f_{a/p}(x, k_T, Q^2) \quad (1.14)$$

A simple factorization of the intrinsic  $k_T$  that is widely used is

$$f_{a/p}(x, k_T, Q^2) = g(k_T) f_{a/p}(x, Q^2) \quad (1.15)$$

The above discussion is a simplified, phenomenological procedure to account for intrinsic  $k_T$  and initial-state multiple scattering. There are many more detailed treatments that have been published, which attempt to calculate at the diagrammatic level the effects of each partonic scatter, and some are reviewed in [1]. It was widely believed that initial-state multiple scattering was the correct explanation of the Cronin effect, and calculations of  $R_{dAu}$  in a multiple scattering framework agree quite well with the data. However, recent studies of the  $\eta$ -dependence of  $R_{dAu}$  [20], as well as the small increase in intrinsic  $k_T$  measured using jet correlations, have cast some doubt on these explanations. We will return to this later in the discussion on our results.

### 1.5.2 Shadowing

The typical energies of a nucleus are of the order of several MeV (e.g., binding energies), and the typical momenta are  $\sim 250\text{MeV}/c$  (e.g., Fermi momentum). Since these scales are much lower than the typical scale of a hard scattering,  $Q^2 \sim 2\text{GeV}^2$ , one might think that the nucleus could be thought of as a bag of completely incoherent nucleons, and there should be no modifications to the parton distribution functions. In this case, the structure functions should scale as  $F_2^A = A F_2^p$  for a nucleus A (ignoring isospin effects), where

$$F_2^p = \sum_i e_i^2 x f_i(x) \quad (1.16)$$

is the structure function measure in deep inelastic scattering experiments, and  $i$  runs over the parton types  $g$ ,  $q$ , and  $\bar{q}$ . In figure 1.10, the results of DIS studies

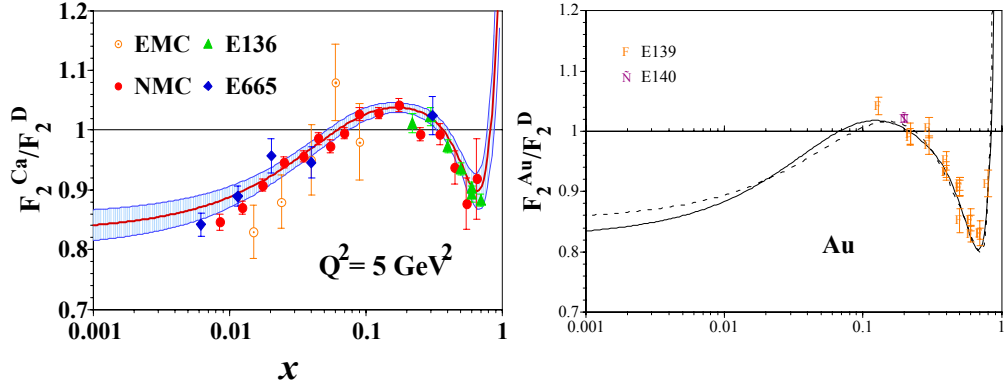


Figure 1.10: The ratio of  $F_2$  for Ca and Au, relative to that of deuterium. The structure functions for nuclei are modified relative to free nucleons. [40], [41]

of electrons, muons, and neutrinos on nuclei are shown, clearly giving evidence that pdf's are modified in a nucleus. This effect is called shadowing, and has been extensively studied by the EMC and NMC collaborations, among others. This subject has been extensively reviewed in [35] and [18]. The shadowing is observed to depend strongly on the momentum fraction  $x$ , with a Fermi region at  $x \gtrsim 0.8$ , the EMC shadowing region at  $0.4 \lesssim x \lesssim 0.8$ , an anti-shadowing region at  $0.06 \lesssim x \lesssim 0.4$ , and a shadowed region for low  $x$ ,  $x \lesssim 0.06$ . At present the causes of shadowing are not well understood, though the most commonly used parametrizations are given by [40] [41] [31] [32].

## 1.6 Parton Energy Loss

We hereby attempt to give a brief history of the theoretical calculations of the energy loss of a high energy parton traversing a dense colored medium, such as a dense nucleus or the hot dense matter formed in the aftermath of an heavy-ion collision. The first attempt was given by J.D. Bjorken, whom calculated the elastic energy loss of an energetic parton traversing a cold nucleus and found only a small effect [26].

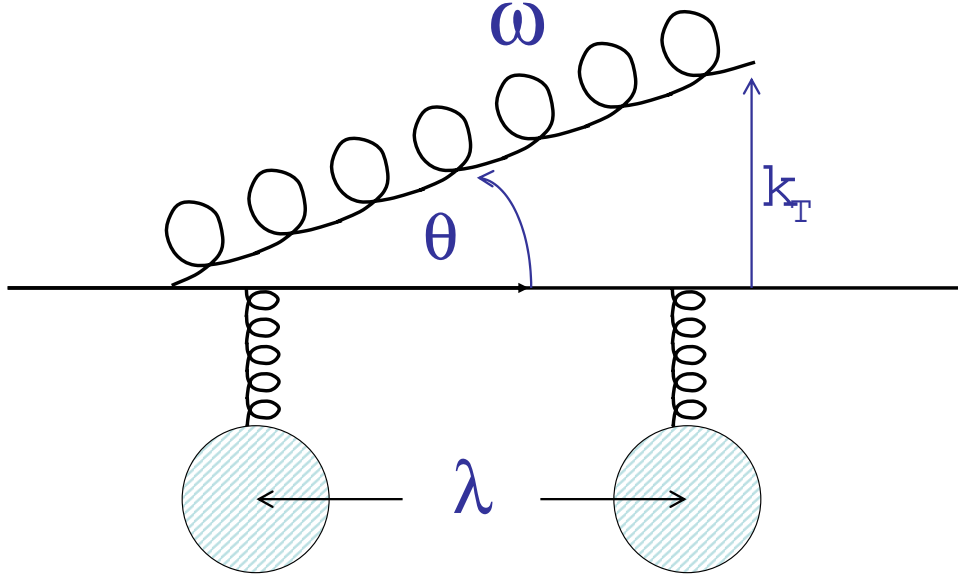


Figure 1.11: An energetic parton with energy  $E_0$  crossing two scattering centers. The scattering is coherent if  $\lambda < \omega/k_T^2$

### 1.6.1 Coherent Quantum Chromodynamic Effects at High Energies

In the 1950's Landau and Pomeranchuk considered the coherence effects on radiated photons in a highly dense medium, which led to the discovery of the Landau-Pomeranchuk-Migdal effect in QED [47] [48] [46] [49]. Here, we derive the condition when coherence effects begin to play an important role, which will be an important consideration given the high color densities expected in a QGP. Consider a highly energy quark with energy  $E_0$  crossing two fixed scattering centers separated by a distance  $\lambda$ , as in figure 1.11. A relatively soft gluon ( $\omega \ll E_0$ ) is emitted as it crosses the first scattering center, at an angle  $\theta \ll 1$  and transverse momentum  $k_T = \omega \sin(\theta)$ . This is actually the favored region for gluon emission. To be explicit, the 4-momenta of the quark and the gluon are  $p_q = (E_0, 0, E_0)$  and  $p_g = (\omega, k_T, \omega \cos(\theta))$ . Since the gluon is soft, the quark energy afterwards is assumed to be  $E \sim E_0$ . The time to build up the gluon wavefunction so that it is distinct from the emitting quark is

given by the virtuality of the emitter,  $\Delta t \sim 1/\sqrt{Q^2}$ . The virtuality is given by

$$Q^2 = 2E_0\omega(1 - \cos(\theta)) \approx E_0\omega\theta^2 = \frac{E_0}{\omega}k_T^2 \quad (1.17)$$

$\Delta t$  is the time required to build up the transverse wavefunction in the rest frame of the emitter. Taking care of the time-dilation factor  $\gamma$ , to get the formation time, we get:

$$t_{form} = (\gamma)(\Delta t) = \left(\frac{E + \omega}{\sqrt{q^2}}\right)\left(\frac{1}{q}\right) \approx \frac{E + \omega}{\omega} \frac{\omega}{k_T^2} = \frac{\omega}{k_T^2} \quad (1.18)$$

So the condition for coherence effects in the radiated gluons is seen to occur when the formation time is comparable to the distance between scatters, ie, when  $\omega/k_T^2 \sim \lambda$ . In a Quark-Gluon Plasma, this mean separation is determined by the Debye mass,  $\lambda \sim 1/\mu$ , which sets the screening scale between two colored objects.

### 1.6.2 Gyulassy-Wang Model

To take these simple considerations and calculate the radiative loss, including the expected coherence effects for a series of scatterings of an energetic parton traversing a QCD medium of length  $L$ , Gyulassy and Wang developed an Eikonal model (GW model) [37], [59], which consists of an energetic parton multiple scattering from static and uncorrelated scattering centers. Each scattering center has a local color-screened Yukawa potential

$$V(q_n) \equiv \frac{4\pi \alpha_s}{q_n^2 + \mu^2} \quad (1.19)$$

which is motivated by the expected finite range of the potential,  $\sim 1/\mu$ , due to Debye screening. The authors neglect the final state interactions of the gluons, and find an energy loss

$$-\frac{dE}{dz} \approx \frac{C_2 \alpha_s}{\pi} \langle \mathbf{q}^2 \rangle \ln \left( \frac{C_A E}{C_R \mu^2 \lambda} \right) \quad (1.20)$$

for the limit of coherent scattering  $\mu\lambda \gg 1$ , and

$$-\frac{dE}{dz} \approx \frac{C_2 \alpha_s}{2\pi\lambda} \frac{\langle \mathbf{q}^2 \rangle}{\mu^2} E \ln \left( \frac{4C_R \mu^2 \lambda}{C_A E} \right) \quad (1.21)$$

for the limit of incoherent scatterings.

### 1.6.3 BDMPS

However, in a series of works by Baier, Dokshitzer, Mueller, Peigne, and Schiff, (BDMPS) [22] [21] [23], using the GW model as above, it was discovered that the gluon final state interactions, which are there due to the non-Abelian nature of QCD, modify strongly the pattern of QCD radiation. The increased multiple scattering from these final state interactions increase the mean transverse momentum of the radiated gluons. Since the formation length is  $l_{form} = t_{form} \sim \omega/k_T^2$ , shortening the formation time reduces destructive interference effects and enhances the radiative energy loss relative to that found by GW. Heuristically, one expects that

$$-\frac{dE}{dz} \propto \frac{\omega}{l_f} \propto \langle k_T^2 \rangle \propto \frac{L\mu^2}{\lambda} \quad (1.22)$$

The last equality assumes a random walk of the gluon multiple scattering. Thus, BDMPS find a quadratic dependence on the energy loss with distance  $L$  through a dense QCD medium.

These considerations are extremely exciting, in that there might be quite remarkable behavior of jets in the heavy-ion environment, and that they might provide a theoretically well-calibrated tool that can be used to understand the medium through which the jets traverse. Currently, there is much effort to quantitatively model these effects in the collisions at RHIC and those soon to come at the Large Hadron Collider (LHC). Therefore, it is imperative to measure the properties of jets in order to constrain the theoretical models, and potentially to guide theory.

## 1.7 Angular Correlations from the Fragmentation Products of Jets

The first measurements of angular correlations between the fragmentation products of jet were made at the ISR [29] [30]. In it they show back-to-back angular correlations between di-hadrons, which we now know are due to the fragmentation of back-to-back jets. So already at the ISR people were looking for angular correlations to distinguish between the many scenarios used to explain the data. With the

dramatic display of the highly collimated cones of energy coming from  $\bar{p}$ - $p$  events at the SPS, first shown at Snowmass in 1981, the high-energy physics community quickly accepted the hypothesis that the production of high- $p_T$  particles is caused by elastic collisions between the constituents of the proton, with the outgoing partons creating a spray of particles because of the confining nature of the strong force.

For this thesis, we take measurements of jets in  $p$ + $p$ , which are fairly well understood, and use that as a baseline to look for indications of new physics when a parton traverses the nuclear medium, whether that medium is hot or cold. By doing so, we can then get a more detailed understanding of the fragmentation process, since we have added a new scale to the problem,  $r \approx A^{\frac{1}{3}}$ , that is, by placing some material in the way of an outgoing parton we can access length scales out to the size of that material, extending the knowledge of fragmentation studies from the 1 fm scale of a proton out to the  $\approx 10\text{ fm}$  scale of a nucleus.

Since the background of a heavy-ion collision is high, it is impossible to reconstruct jets using cone or  $k_T$  algorithms, as is typically done by the high energy physics community, without large systematic errors from including background particles into the jet. Therefore, one is required to go to higher  $p_T$ , where the background from soft physics is far lower. However, after having identified a high  $p_T$  particle, it is possible to then look at the angular correlations of particles in that same event to look for the expected associated nearby fragments. In a heavy-ion collision, there are other sources of angular correlations besides just from the fragmentation of a jet, which will have to be quantitatively accounted for.

## 1.8 Correlations with the Reaction Plane: Elliptic Flow and Jet Energy Loss

Due to the high densities generated in heavy-ion collisions, and due to the elliptical geometry of the overlap region, large asymmetric pressures are built up that generate strong outward flow. The largest pressure gradients occur in the direction of the impact parameter, while the smallest gradients are normal to the impact parame-

ter. This outward pressure causes the particles along the direction of the impact parameter to have greater momenta, so that the distribution in  $phi \equiv (\phi - \phi_R)$  can be described with a fourier expansion

$$\frac{d^2N}{dp_T d\phi} = N_0(1 + v_1(p_T)\cos(\phi) + 2v_2(p_T)\cos(2\phi) + \dots) \quad (1.23)$$

This has been observed at RHIC (figure 1.12). At mid-rapidity, the  $v_1$  parameter was found to be approximately zero, but a large and has generated much interest since it points toward collective, and possibly partonic, behavior.

Due to the length dependence of the jet energy loss, jets also can produce a second harmonic correlation with the reaction plane. This comes about because the average length of material traversed by jets is shorter for jets moving parallel to the reaction plane than for those jets moving perpendicular to the reaction plane.

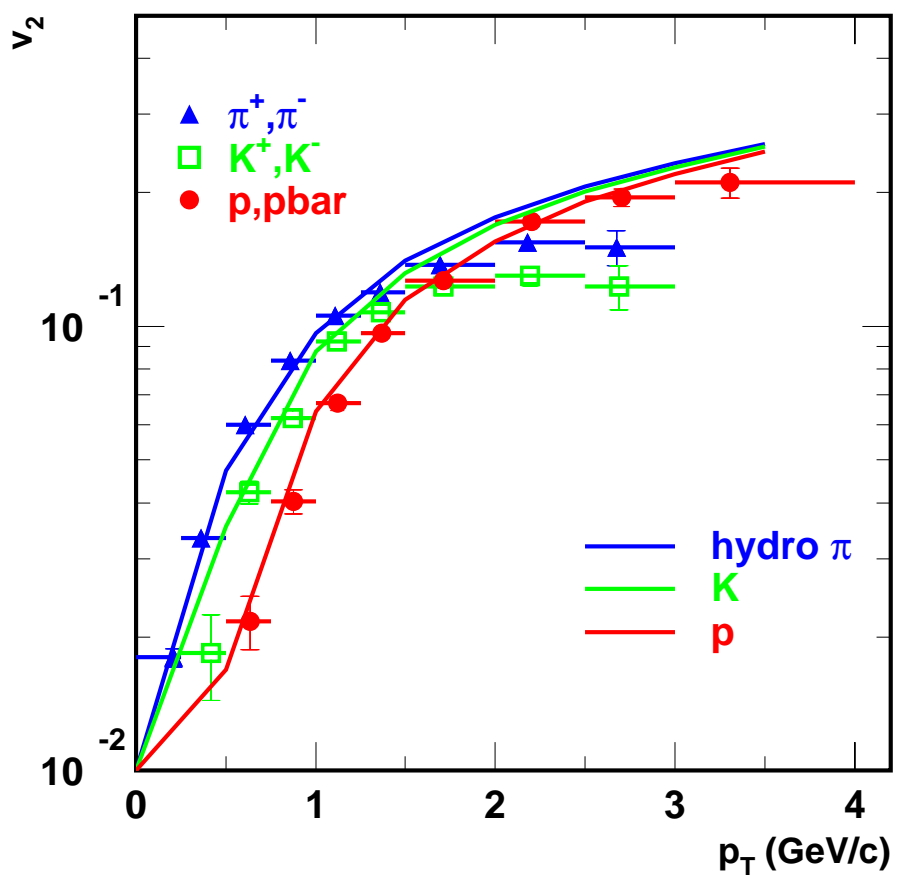


Figure 1.12: Minimum Bias elliptic flow for identified pions, kaons, and protons in the PHENIX detector. [8]

# Chapter 2

## Experimental Apparatus

### 2.1 RHIC

The Relativistic Heavy Ion Collider (RHIC) [38] [39] is located at Brookhaven National Laboratory (BNL), and is the highest energy nuclear collider in the world. For anyone interested in the decision-making and critical thinking that goes into devoting US \$1 billion to building a collider and its associated detectors, a truly fascinating account of the beginnings of the RHIC program can be found in a history written by Gordon Baym [24].

RHIC is capable of providing collisions of Au ions on Au ions at a  $\sqrt{s_{NN}} = 200$  GeV. This is vitally important because for the first time, nuclear physics has a laboratory tool that unambiguously reaches energies where a perturbative description of QCD is valid. Previous heavy-ion experiments were conducted at the SPS, which reached a maximum energy for Pb+Pb collisions of  $\sqrt{s_{NN}} = 17.2$  GeV, and the AGS, which reached  $\sqrt{s_{NN}} \approx 5$  GeV.

Besides being the highest energy nuclear collider in the world, RHIC has the distinction of being by far the most versatile, with the capability to collide virtually any species on any species, from protons to heavy nuclei such as gold. As of summer 2004, RHIC has collided Au+Au at  $\sqrt{s_{NN}} = 19.6, 56, 62.4, 130, 200$  GeV/c,  $d+Au$  at  $\sqrt{s_{NN}} = 200$  GeV/c, and polarized  $p+p$  at  $\sqrt{s} = 200$  GeV/c, with plans for an upcoming lighter ion run (such as Cu+Cu or Si+Si). This is especially essential for

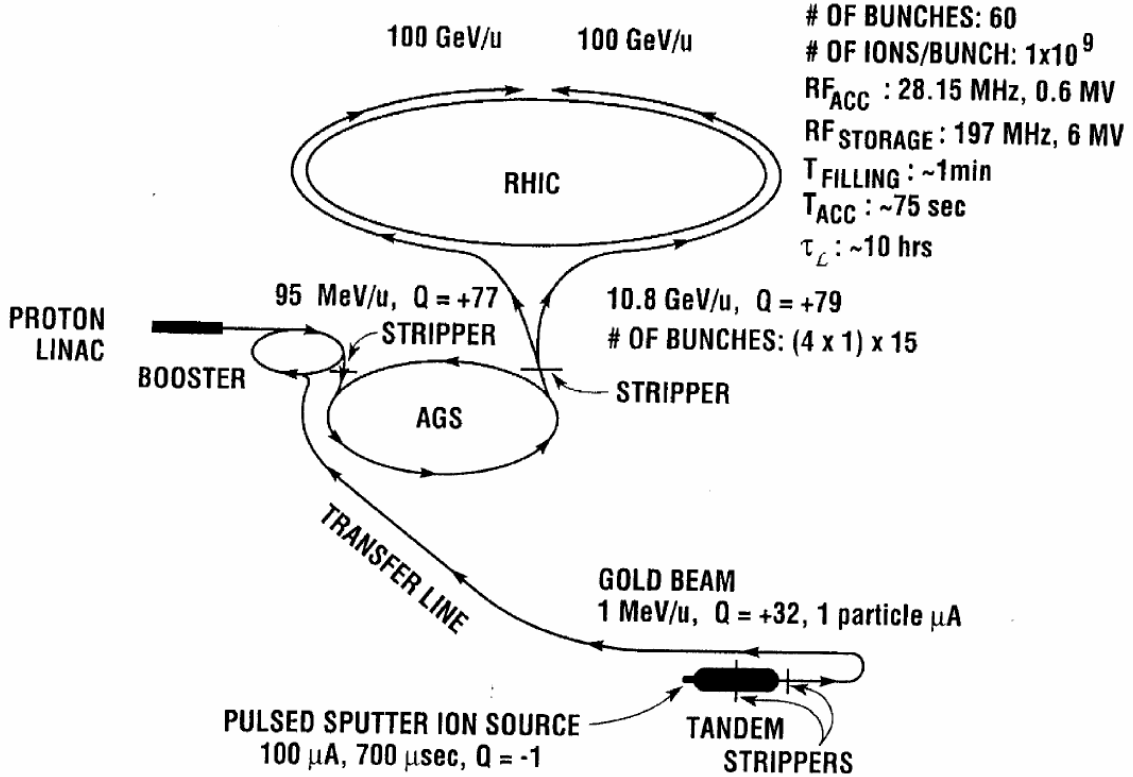


Figure 2.1: The Steps in the Acceleration of Au Ions in RHIC.[39]

experimental studies of the quark-gluon plasma (QGP). By colliding an extensive array of species combinations, one can systematically check myriad different aspects of nuclear collisions, since varying energies and species allows one to vary the deposited energy and collision geometry, and thus change in a controlled way such things that might impact QGP formation, such as the pressure and energy densities reached, and also things that affect signatures of the QGP, such as the length of produced matter that particles must traverse before reaching vacuum. This was one of the important lessons from past experiments at the SPS and the AGS; observables of the QGP have often been misinterpreted since there are myriad hadronic effects which can also mimic the signatures of the QGP, and so extensive systematic checks are necessary.

In addition to the heavy ion program, RHIC is capable of colliding polarized

Table 2.1: Design Performance Parameters for RHIC

	Au+Au	p+p
Beam Energy	$30 \rightarrow 100 \text{ GeV/u}$	$30 \rightarrow 250 \text{ GeV/u}$
Luminosity	$2 \times 10^{26} \text{ cm}^{-2} \text{ s}^{-1}$	$1.4 \times 10^{31} \text{ cm}^{-2} \text{ s}^{-1}$
Number of bunches/ring	$\approx 60 (\rightarrow 120)$	$\approx 60 (\rightarrow 120)$
$\beta^*$ at collision points	$10m \rightarrow 1m$	$10m \rightarrow 1m$

protons at energies of up to  $\sqrt{s} = 500$  GeV, making it also the premier facility for studies of the spin content of the proton. RHIC will make possible direct measurements of the gluon contribution to the proton’s spin. and thus will be the machine that should eventually resolve the “spin crisis” of the proton.

In table 2.1, we collect some of the design parameters for RHIC. RHIC consists of two 3.8 km rings, a clockwise “blue” ring and a counter-clockwise “yellow” ring. The separate rings allows for the collision of asymmetric species, since each ring can then run with its own magnetic field and tuned optics. There are 6 crossing points around the ring where the particle bunches can be steered towards each other for a collision. PHENIX sits at the “8-o'clock” interaction region.

## 2.2 PHENIX Overview

One of the large detectors at RHIC (there were one additional large and two smaller detectors), the PHENIX detector [5] consists mainly of four spectrometers of about 1 steradian each and covering the interaction point. There are two Central-Arm Spectrometers which cover  $|\eta| < 0.35$  ( $70^\circ < \theta < 110^\circ$ ), with each arm subtending  $90^\circ$  in  $\phi$  and offset from each other by  $67.5^\circ$ . The other two spectrometers where muon spectrometers covering  $1.1 < |\eta| < 2.4$  (South) or  $1.2 < |\eta| < 2.4$  (North) and the full  $2\pi$  in  $\phi$ . More details on the Muon Spectrometers can be found in various places, such as in the special edition of NIM on the RHIC detectors [14], but they were not used in this analysis. The photons and charged hadrons measured in this thesis were done using only the two Central-Arm Spectrometers. There are in addition an array of global detectors used as minimum bias triggers and to provide centrality and vertex information.

PHENIX was originally designed to meet the challenges of measurements under the demanding conditions of Heavy-Ion collisions. We now know that the most central Au+Au collisions at RHIC's maximum energy produces  $dN^{ch}/d\eta \sim 700$ , but before the first collisions of course this number was not known. When designing PHENIX, achieving good efficiency required that each detector element was designed to have an occupancy of at most 10% in the most central heavy ion collisions. A conservative estimate of the maximum expected particle density, based on simulations, extrapolations, and educated theoretical guesses, was  $dN^{ch}/d\eta \sim 2000$ . Quite prudently, this is the number that was used when designing PHENIX, and the segmentation of the detector is based on simulations with the above conservative estimate of  $dN^{ch}/d\eta$ .

In figure 2.2 we show the PHENIX Detector layout. The particles collide in the center of the picture, inside the Multiplicity and Vertex Detector (MVD). At either end of the Experimental Hall, down the beam-pipes, one can see the two DX magnets. Right in front of these magnets are the panels of the Muon Identifier (MuID). Before the MuID there are two Muon Trackers (MuTr), contained inside the lampshade of the Muon Magnets. Filling up the space at mid-rapidity are the Central Arm Spectrometers.

A beam view of the Central Arm is show in figure 2.3. The first detector in the Central Arms is the Drift Chamber (DC), which gives high resolution tracking of particles in  $r$  and  $\phi$  outside the magnetic field. Connected to the back of the DCs are two Pad Chambers (PC1). The PC1's are followed by the Ring Imaging Cerenkov detector (RICH), which provide electron identification up to  $p \sim 4.5$  GeV/c. In the West Arm the RICH is followed by two sets of Pad Chambers (PC2 and PC3). In the East Arm there is a Time-Expansion Chamber (TEC) followed by PC3. The Pad Chambers provide 3-dimensional space point measurements of particle tracks, which are crucial to pattern recognition and to provide measurements of the polar angle  $\theta$  for particle tracks. The TEC is an additional tracker which helps with momentum resolution at high  $p_T$ , and provides electron identification below 2.5 GeV through a

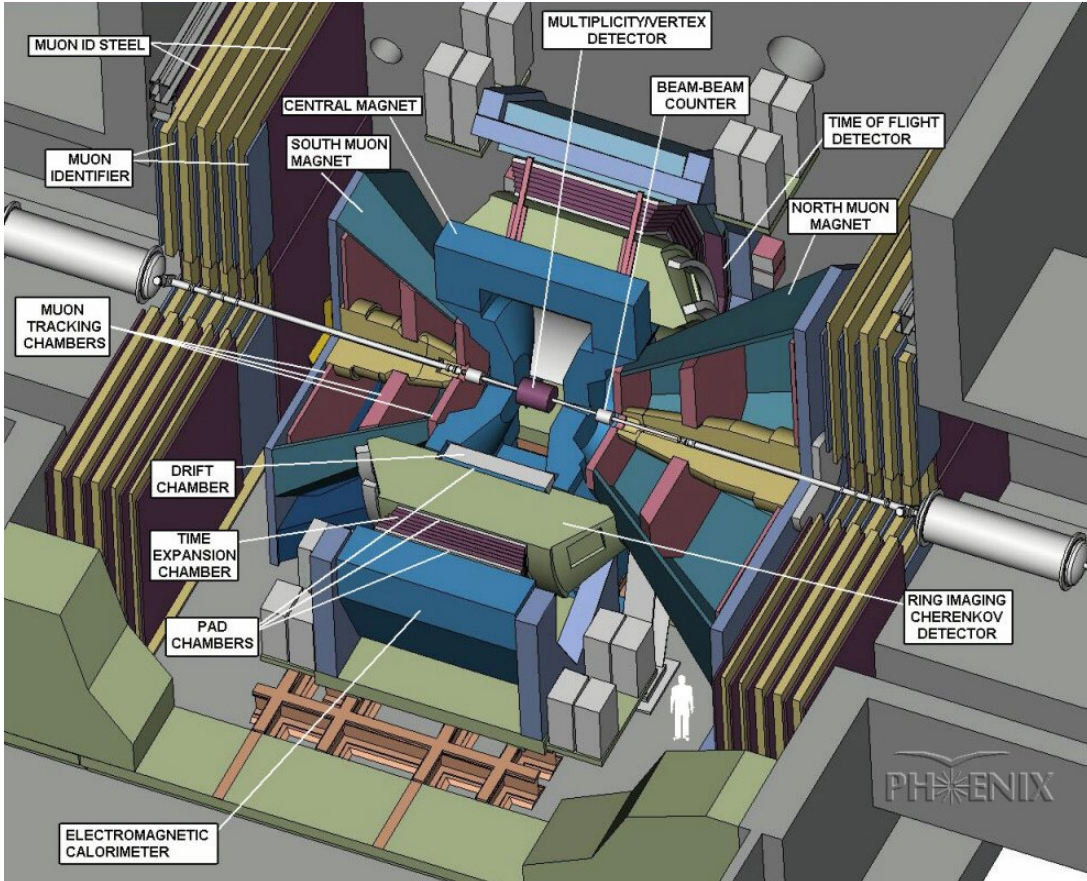


Figure 2.2: The PHENIX Detector Layout

measurement of  $dE/dx$ . Behind the TEC and covering  $\frac{1}{2}$  of the lower two sectors is the Time-of-Flight (TOF), which provides particle identification. The final layer in the Central Arms is the Electro-Magnetic Calorimeter (EMC), which makes energy measurements of photons and electrons. There are two types of calorimeters used in PHENIX: the lead-scintillator (PbSc) and the lead-glass (PbGl).

Underlying this high granularity, strong particle identification capable detector is a Data-Acquisition System (DAQ) capable of sampling data at the highest rates

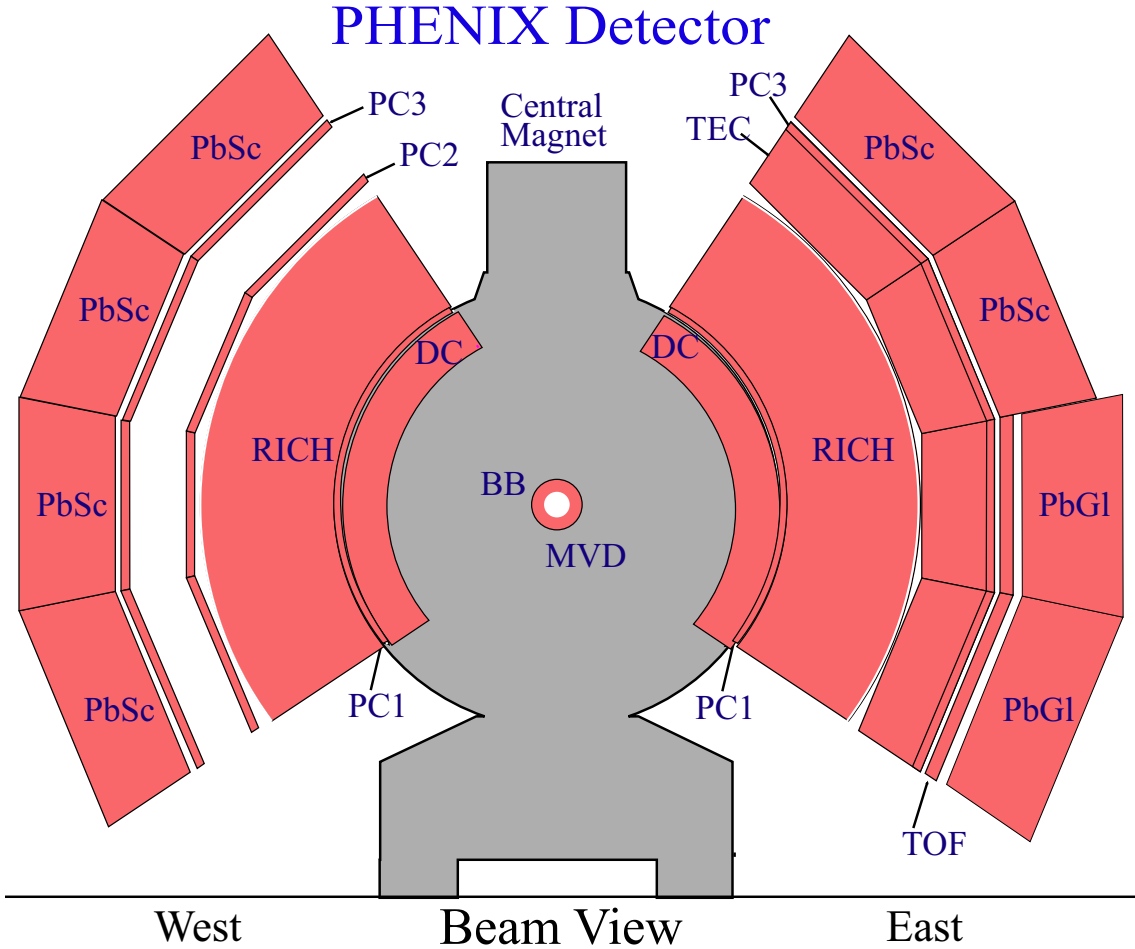


Figure 2.3: A Beam View of the PHENIX Central Arm Detectors.

delivered by RHIC. The philosophy behind PHENIX is to allow for characterization of the QGP by measuring simultaneously as many observables as possible, allowing for correlations between many different signatures. Additionally, PHENIX aspires to measure signals at all timescales of the collision. These measurements range from the hadrons produced in the late stages of the collision fireball, to high- $p_T$  particles which are thought to be produced very early in the collision, to leptons ( $e^\pm, \mu^\pm$ ) and photons, which are produced at all times in the collision.



Figure 2.4: Left: An individual BBC module, showing the Quartz radiator attached to the PMT. Right: The housing for the modules. There are two housings and each housing contains 64 modules.

## 2.2.1 Trigger and Event Characterization Detectors

### 2.2.1.1 Beam-Beam Counters (BBC)

The BBC's [42] [15] are designed to provide a minimum-bias trigger for heavy-ion collisions, to provide a start time for time-of-flight measurements, and to measure the  $z$ -vertex of the interaction. They are located 144.34 cm from each side of the interaction point, and cover  $3.0 < |\eta| < 3.9$ . They each consist of 64 modules, where each module is a 3 cm Quartz Cerenkov radiator attached to a Hamamatsu R6178 PMT. A picture of an individual BBC module is shown in figure 2.4. The right picture shows the housing for the modules. The housing has an outer diameter of 30 cm and the inner diameter is 10 cm, clearing the beam pipe by 1 cm. Since the BBC's are placed right behind the magnets (fig. 2.5), the PMTs chosen are a mesh-dynode type, which remains functional even in the 3 kG field at the location of the BBC. Even still, there are noticeable effects in the PMT gain with changes in the field. These are calibrated out using measurements of the MIP peak.

The configuration of the individual modules on the face of the BBC is shown in figure 2.6. It shows the approximate hexagonal symmetry of the detector. The modules in the inner ring see the greatest number of particles. In the most central Au+Au collisions, there can be up to 30 particles in an individual module, requiring

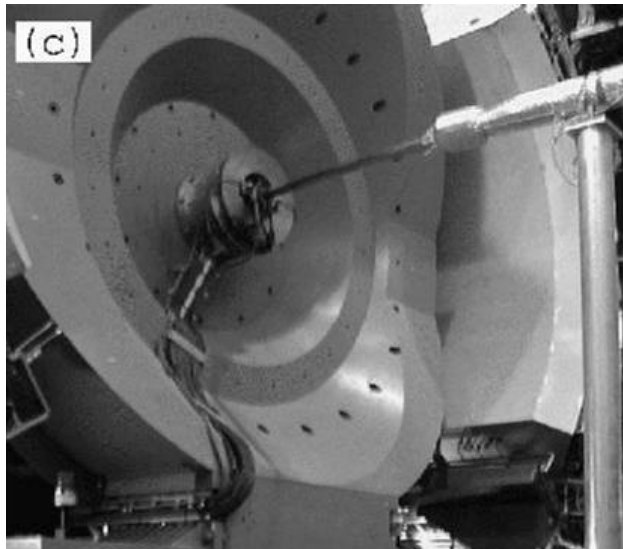


Figure 2.5: A picture of the BBC module installed in its data-taking location, in the back of the PHENIX magnet and separated from the beam pipe by 1 cm.

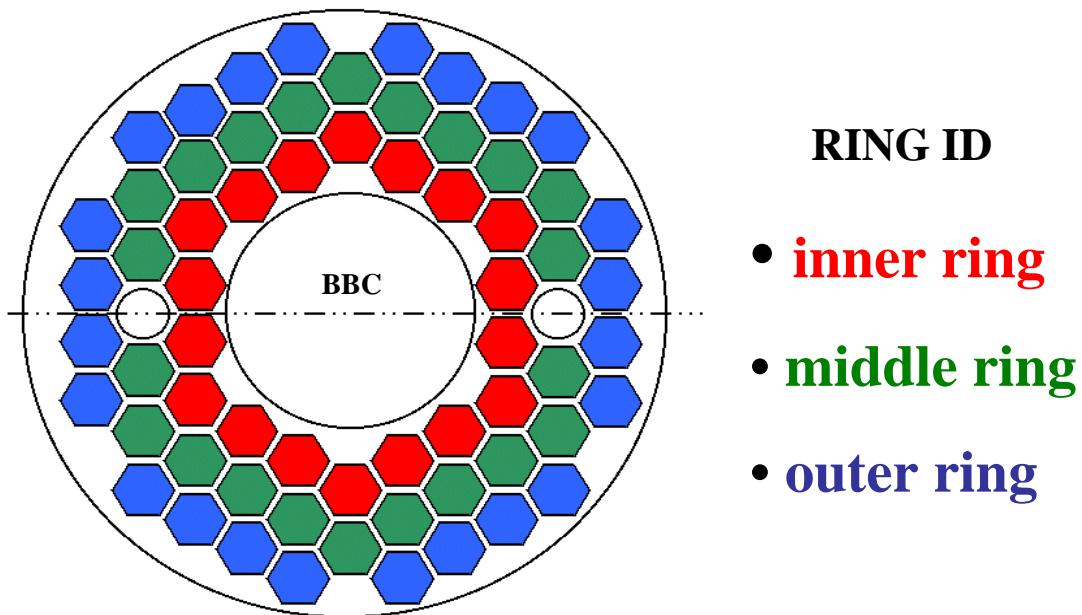


Figure 2.6: A frontal drawing of the BBC. The 64 PMTs are arranged with approximately hexagonal symmetry. Each BBC covers  $3.0 < |\eta| < 3.9$

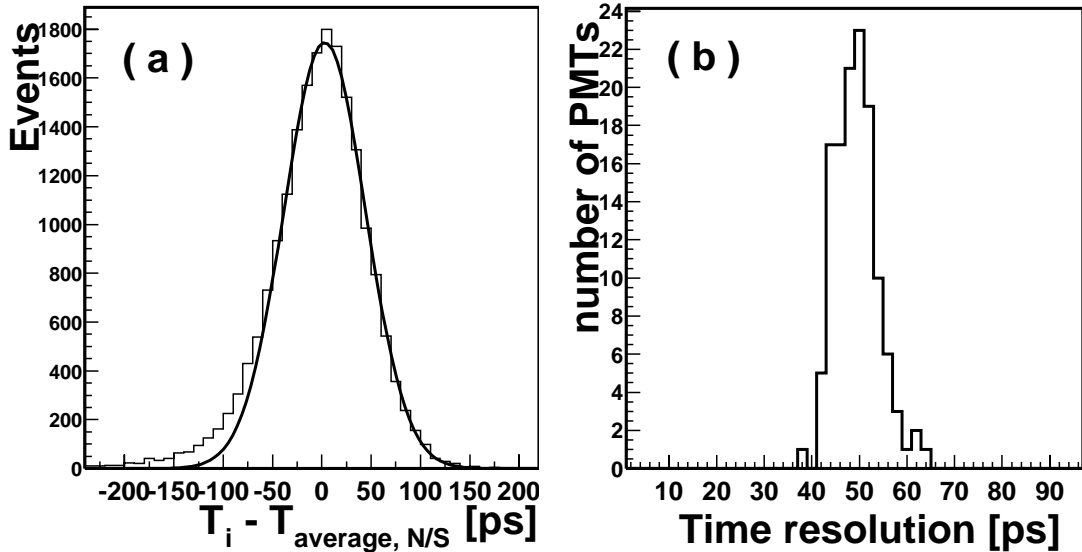


Figure 2.7: BBC Timing Resolution

quite high dynamic range.

By making two measurements of the time, where  $t_S$  ( $t_N$ ) is the average time into the south (north) BBC, one can measure the z-vertex ( $Z$ ) and start time ( $t_0$ ) of the collision:

$$Z = c(t_S - t_N)/2t_0 = (t_S + t_N)/2 - L/c \quad (2.1)$$

$L$  is the distance to the BBC and equals 144.34 cm. The resolution of the vertex and start-time measurements is determined by the timing resolution of the BBC:

$$\sigma_Z = \frac{c}{2} \sqrt{\sigma_T^2 + \sigma_T^2} \quad (2.2)$$

and is about 50 ps per PMT (fig 2.7), or a vertex resolution  $\sigma_Z = 1$  cm in the most peripheral collisions to  $\sigma_Z \lesssim 0.3$  cm in the most central collisions.

The BBC reads out the time using a Leading-Edge discriminator, which requires a slewing correction due to the change in the discriminator time with pulse-height. In figure 2.8 we show the BBC time before and after the slew correction. The fit to the slew curve is given by  $f(x) = a + b/ADC + c \cdot \log ADC$ .

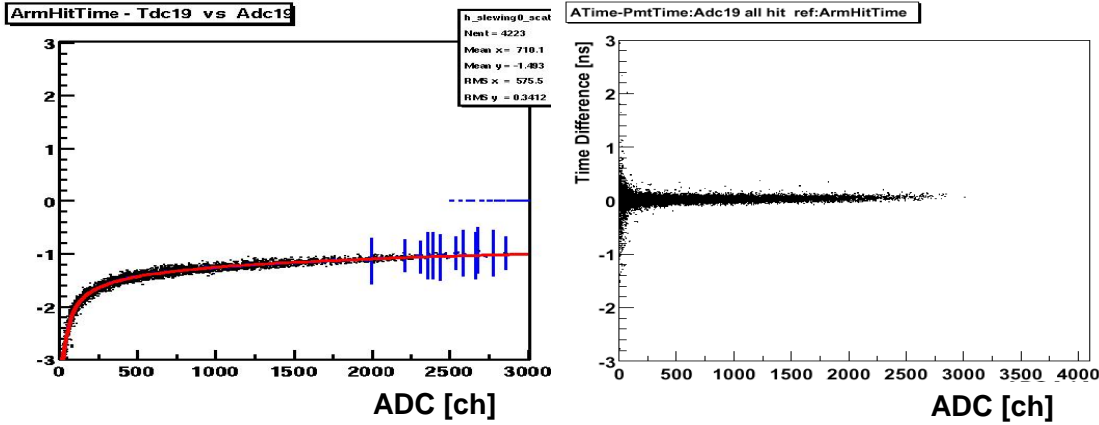


Figure 2.8: BBC Slewing correction. On the left is a plot of the BBC time (relative to some reference time), as a function of the ADC value. The fit is described in the text. On the right, after correction for the slewing effect.

### 2.2.1.2 Zero-Degree Calorimeters (ZDC)

The Zero-Degree Calorimeters [6] are unique in that they are common to all four RHIC experiments. The ZDC's were originally conceived as a common luminosity monitor for all the RHIC experiments, but they have since evolved a multitude of uses, among which are:

1. Provide a common luminosity measurement for all RHIC experiments.
2. Provide a common centrality determination for all experiments.
3. Provide a minimum bias trigger free of beam-gas backgrounds.

The original motivation for the luminosity measurements comes from the desire to exploit the large cross-section ( $\sim 11$  barns) from Mutual Coulomb Dissociation (MCD) events. When colliding two nuclei with charge  $Z$ , the strong electric charge creates a large flux of photons, and there is a high probability for photon exchange from one nucleus to the other. The photon is absorbed by the other nucleus and excites it, causing it to sometimes emit a neutron. These events are called Coulomb dissociation events. Sometimes, the two crossing nuclei each exchange a photon, causing neutrons to go in the forward region of each nucleus. This signature is easy

to tag with a coincidence of the forward and backward ZDC's, and provides a large reduction in beam-related backgrounds since there is only a very low probability for double beam-gas events to fire both ZDC's.

Since the  $p_T$  of the emitted neutrons in MCD events is very small, the ZDCs are located right down the beam-pipe and behind the DX magnets to see them. Figure 2.9 shows an overhead drawing of the PHENIX interaction region. The ZDCs are located on either side of the interaction region, 1800 cm away, and behind the DX magnet. Because of the DX magnet, any charged particles are swept away before hitting the ZDC. Figure 2.9 shows the locations of neutrons, gold, and protons after going through the DX magnet. One can see that the higher the charge to mass ratio  $Z/A$ , the more the particle is swept away.

Since the ZDC has so little space, the main design constraint is to have good containment in order to have good energy resolution. Therefore, a design based on a tungsten-PMMA fiber sandwich was used since it was found to have good energy resolution, even with only 10 cm of width. A picture of the ZDC's components are shown in figure 2.10. Besides good energy resolution, the ZDC should have good timing resolution in order to be able to trigger on coincidences. Because of the wide spatial separation of the two ZDCs, the timing resolution does not have to be very good. Even still, in Au+Au collisions the energy deposition in the ZDC is very high, giving a timing resolution of 120 ps. This resolution translates to a vertex resolution of 2.5 cm.

### 2.2.2 Magnetic Field

In figure 2.11 we show a picture of the PHENIX magnet [19], with cutaway views so that one can see the interior structures of the steel used to shape the magnet fields. The coils used to create the field are shown in figure 2.12. For the data taken in this thesis the inner coil was not energized. There is a small effect from residual fields due to the North and South Muon Magnets spilling into the Central Arm region, but this is factored in during the tracking reconstruction.

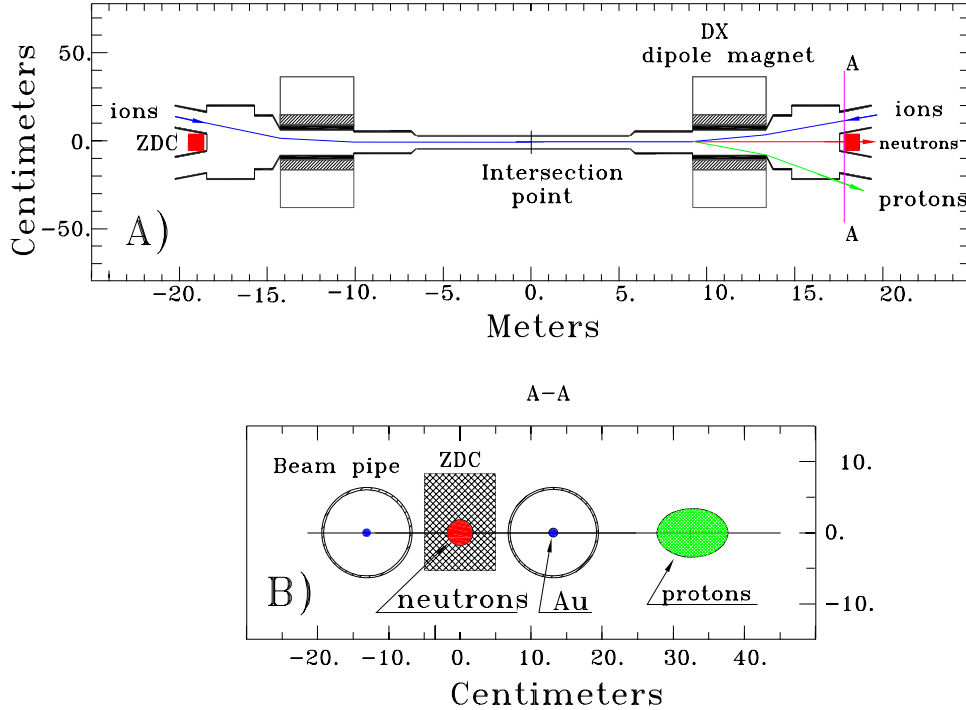


Figure 2.9: A) An overhead view of the interaction region showing the location of the ZDCs at either end, just after the DX magnets and in the crotch where the two rings merge. B) A frontal view of the ZDC and beam-pipe with the locations of neutrons, gold, and proton after they are swept by the DX magnet.

There are numerous physics requirements that shaped the design of the PHENIX magnet. These requirements are:

1. No mass in the apertures of the central spectrometer arms to minimize interactions and multiple scattering of particles produced in the primary collision and to minimize albedo from the magnet poles.
2. Dense material near the collision point in the apertures of the north and south muon spectrometers to serve as hadron absorbers. The CM pole tips serve as the hadron absorbers for the muon spectrometers. They comprise 60 cm of low-carbon steel and 20 cm of brass (about 4.9 nuclear interaction lengths).

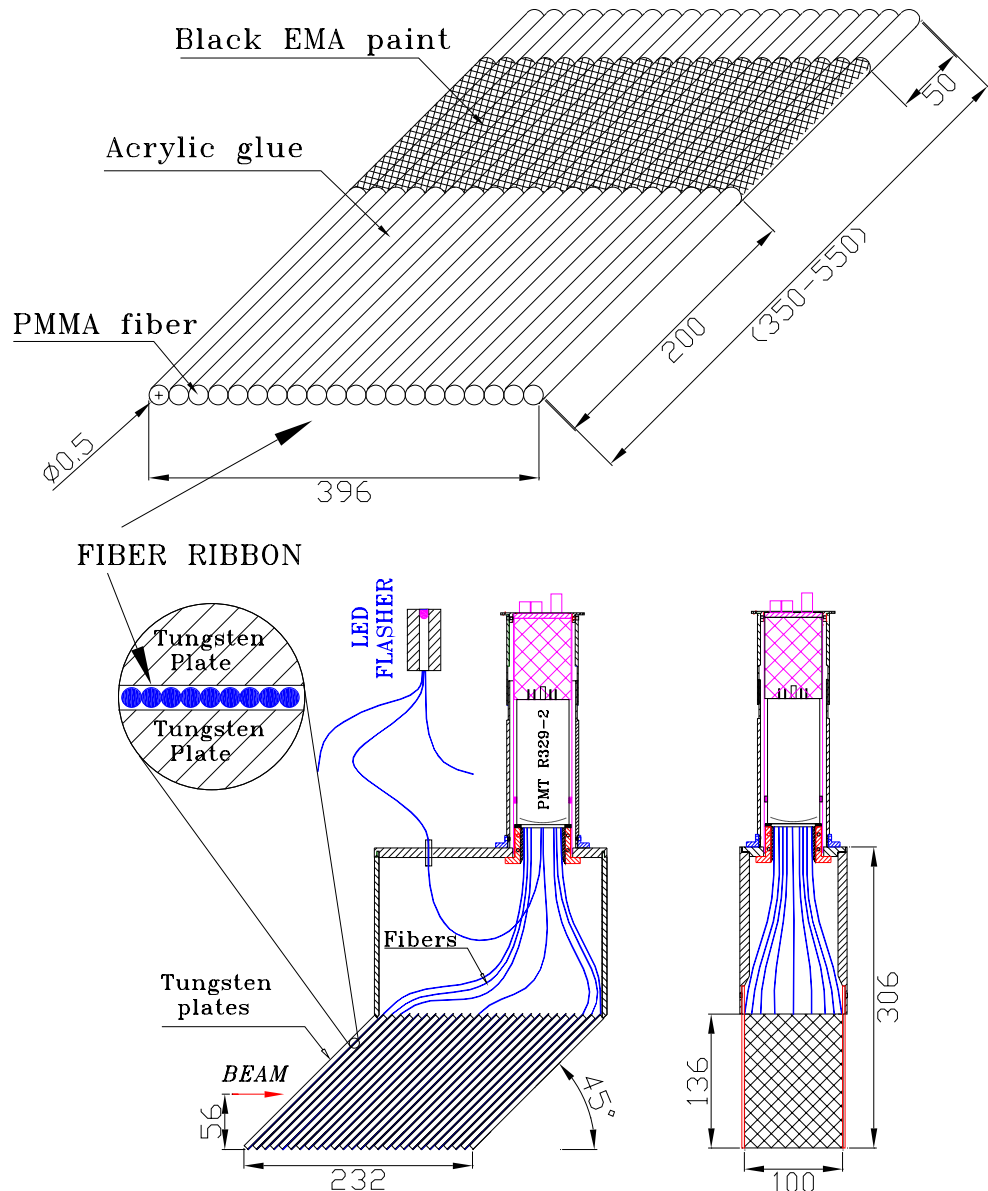


Figure 2.10: A drawing of the components of the ZDC. The values given are in mm. The top shows the PMMA fibers which are sandwiched between tungsten plates. These fibers generate and guide cerenkov light to the Hamamatsu PMT. The LED is used for gain monitoring and calibration. The red arrow on the bottom left shows the impact position of the beam. On the right is shown a head-on view of the ZDC, which is only 10 cm wide.

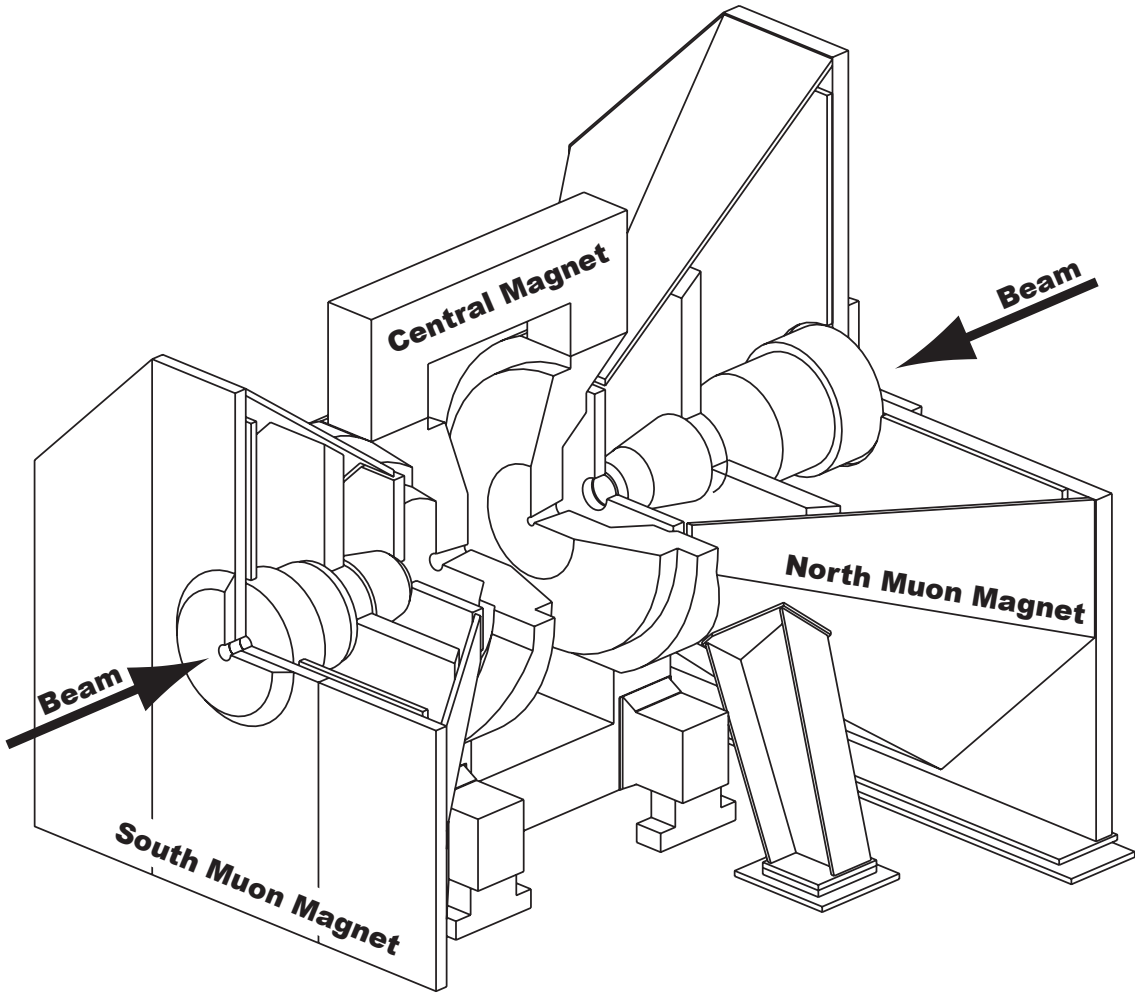


Figure 2.11: Perspective Drawing of the PHENIX Magnets.

3. Reasonably uniform field that could be mapped to a precision in the field integral of about 2 parts in  $10^3$ .
4. Control over the radial field distribution to allow creation of a "zero-field" region near  $R = 0$ .
5. Minimal field integral for the region  $R > 200 \text{ cm}$ , the radius of the Drift Chamber (DC). In particular the field integral in the Ring Imaging Cherenkov Counter (RICH) ( $2.4 \text{ m} < R < 4.0 \text{ m}$ ) was required to be less than 100 Gauss-m. This is to minimize the smearing of the rings associated with low momen-

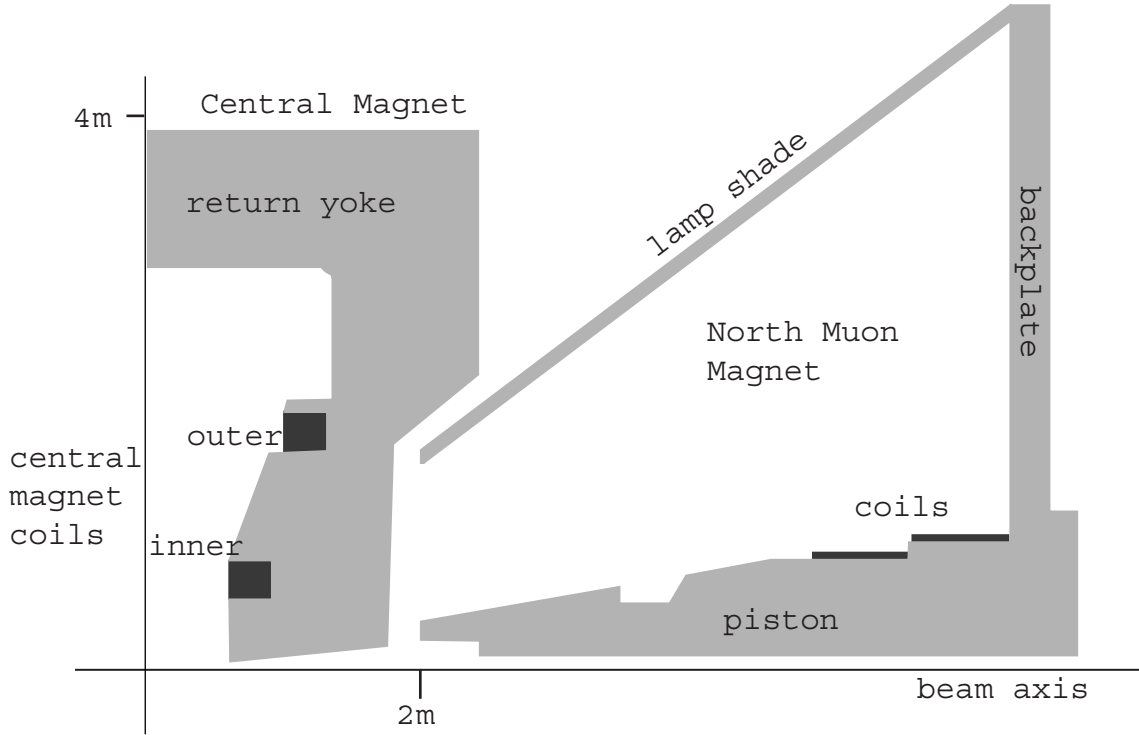


Figure 2.12: PHENIX Magnet Coils.

tum electrons. Field in the region of the photomultiplier tubes of the RICH and the Electromagnetic Calorimeter (EMCal) was also required to be low.

6. The magnet must be easily moveable to allow access to detector components for commissioning, maintenance and replacement.

The above physics requirements entailed many compromises in the final design, so that all requirements could be satisfied to some degree. For instance, the requirement of no mass in the central arm aperture has to be balanced with the requirement that there should be an hadron absorber to reduce muon decay backgrounds into the Muon spectrometer. Hence, the magnet nose-cones are placed very near the interaction region and hence limit the range of allowed vertices before background from particles hitting the nosecones becomes too severe.

The two separate coils (inner and outer) designed to satisfy the fourth requirement. The field values as a function of the radial distance  $X$  at  $\theta = 90^\circ(\eta = 0)$ ,

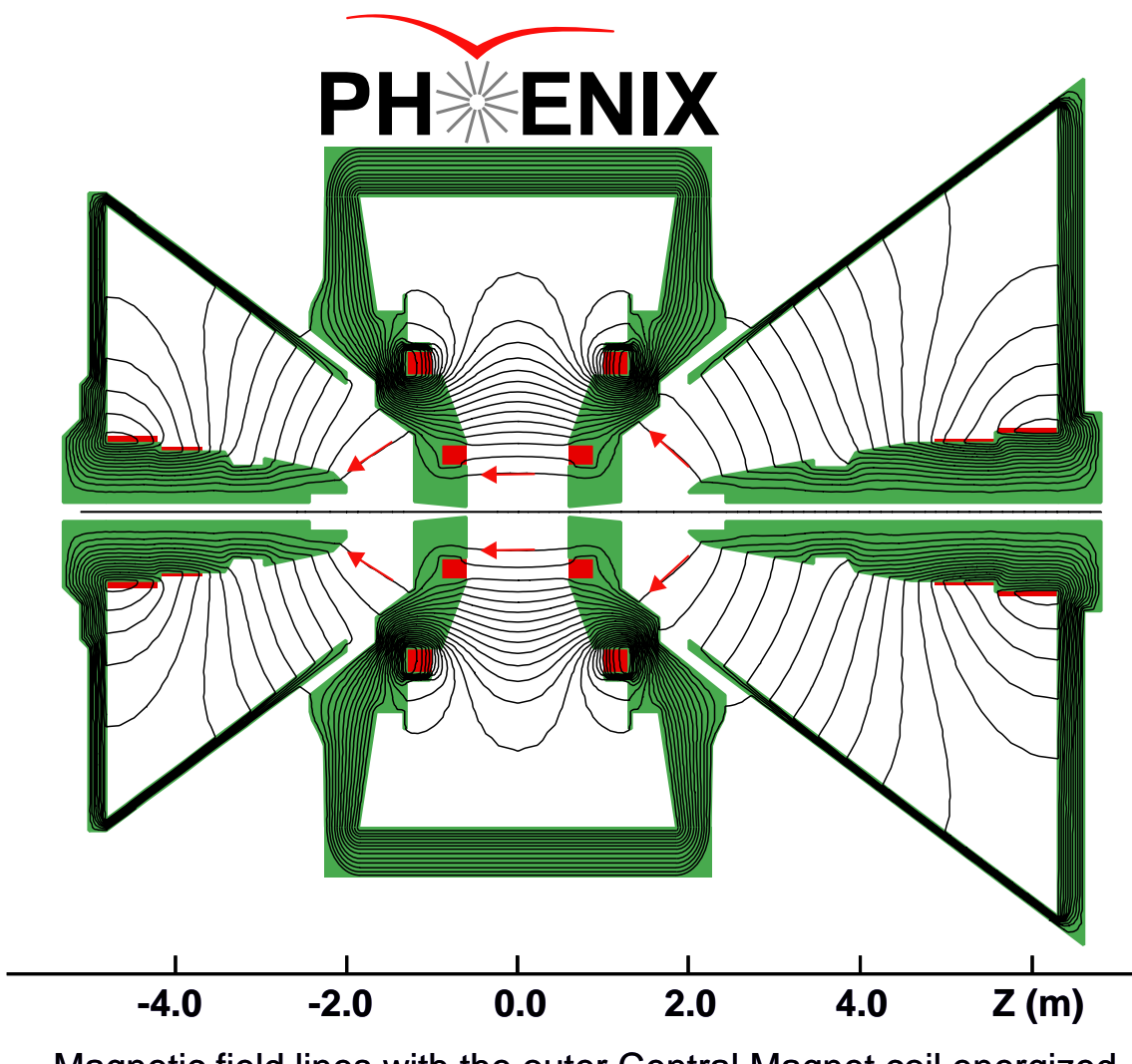


Figure 2.13: PHENIX Magnetic Field

are given in figure 2.14 for different field configurations. The “Outer - Inner” configuration, where the two coil currents go in opposite directions, and thus cancel, allows for a field region that is approximately zero in the range  $0 < X < 50$  cm. This zero-field region is important for future detectors that must be efficient for low momentum electrons, for light vector meson studies. The data in this thesis consisted solely of the “Outer” configuration, which provides an  $\int B dl = 0.78 T \cdot m$  for tracks in the Central Arm. The field lines for the “Outer” configuration are shown

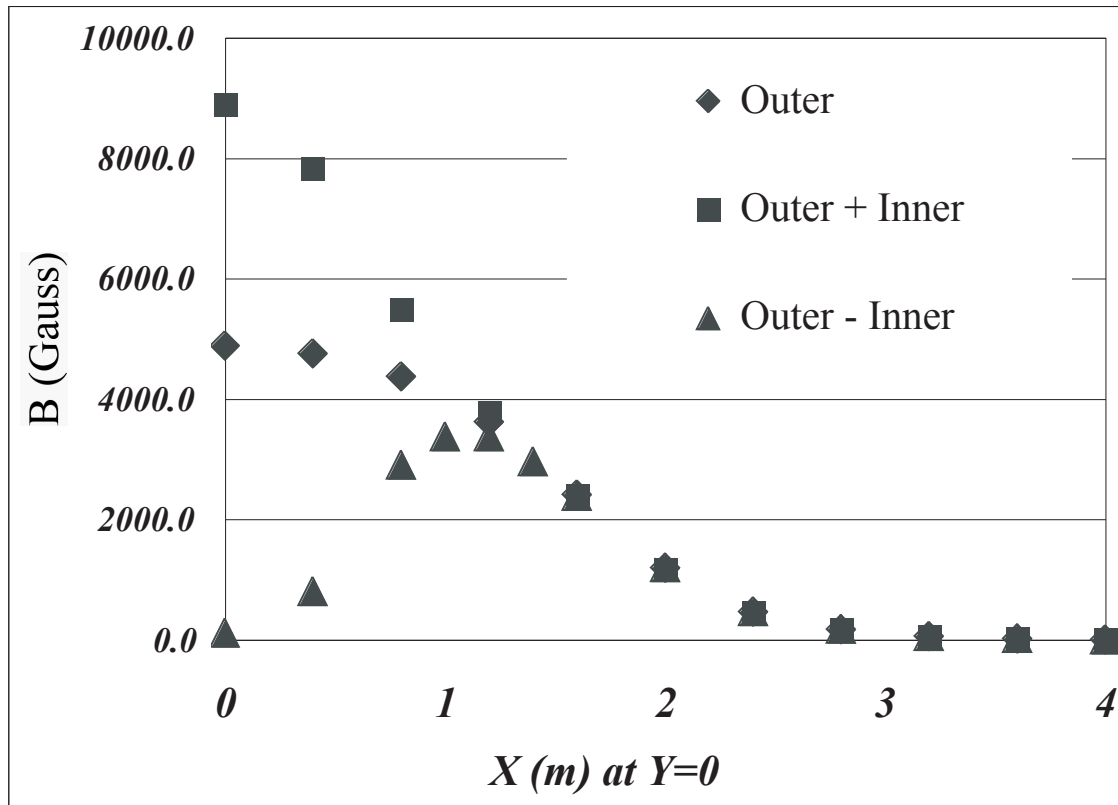


Figure 2.14: PHENIX Magnetic Field Values. During Run02 and Run03 only the Outer Coil was energized.

in figure 2.13. The field is to a very good approximation phi-symmetric, and axial, so that most of the bending occurs in phi, and not in theta. The parameters for the Central Arm magnet are show in table 2.3.

### 2.2.2.1 Magnet Field Mapping

A number of different techniques for field mapping were considered, and finally a method using maps computed using Laplace's Equation along with measurements of a single field component at points on a closed surface containing the useful field volume proved to be accurate to one part in  $10^3$ . This accuracy was checked with both direct 3-dimensional measurements of the field, and with maps calculated using a 3-dimensional field simulation program (TOSCA). In addition, there are permanent Hall probes mounted in the magnets and read out during the magnetic field mapping

done before the start of the Runs. This allows for future field normalization.

### 2.2.3 Charged Particle Tracking

There are three primary charged particle tracking sub-detectors in PHENIX, the Drift Chambers (DC), Pad Chambers (PC), and the Time Expansion Chamber (TEC) [4]. Their location on the PHENIX central arm is shown in figure 2.3. The Drift Chambers, along with PC1, form the inner tracking system, while PC2, PC3, and the TEC form an outer tracker. The Drift Chambers measure projectively in  $r - \phi$  space, and provide the main measurement of momentum. The Pad Chambers provide 3 dimensional space points to the track, and determine  $p_z/p_T$ . We will not discuss the TEC here since it was not used in the analysis for this thesis. As can be seen in the figure 2.14, the magnetic field drops down to below 1 kG after 2 meters in the radial direction. Therefore, all tracking detectors are largely out of the bend region of the magnets.

In figure 2.15, we schematically show how a single charged track is reconstructed in PHENIX [50]. A charged track is emitted from the origin at an angle  $\phi_0$ , and is bent in the magnetic field before the Drift Chamber. At the Drift Chamber and beyond, the field is relatively small and gets increasingly smaller with  $R$ , so that the tracks go largely in a straight line except for multiple scattering effects. The residual bend for tracks after  $R \sim 2$  meters is a maximum of 5% of the original deflection, that is, at most  $1^\circ$ . Also, since the magnetic field is axial, most tracks do not bend in the  $\theta$  direction, except for very low momentum particles and particles near the magnet pole tips, where the fringe field focusing effects are larger.

The reference circle is chosen at the radius of the center of the Drift Chamber, and the angle of the intersection between the tracklet through the Drift Chamber and the reference circle is  $\phi$ . The angle  $\alpha$  is then the angular deviation from the path an infinite momentum particle would take. Actually,  $\alpha$  measures the  $p_T$  deviation due to the integrated field, and thus measures the momentum.

Since the Drift Chamber measures in projective space, the Pad Chambers are

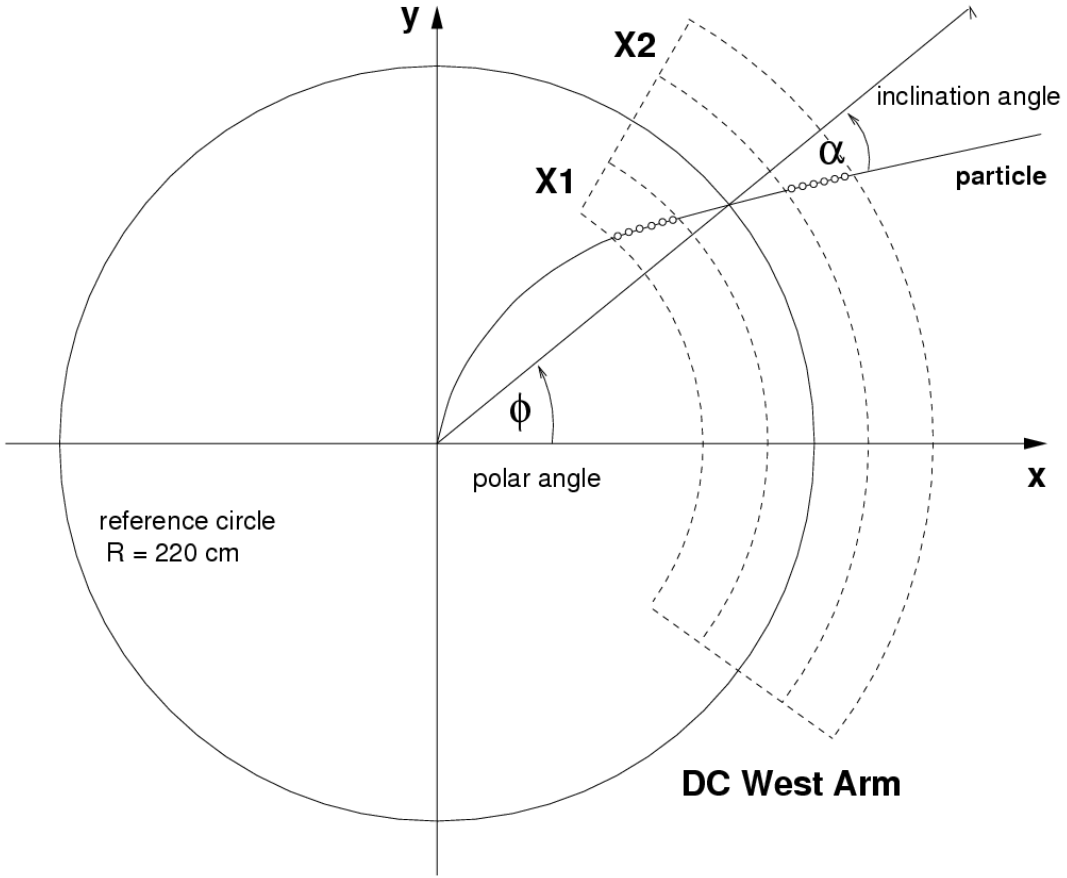


Figure 2.15: Phenix Tracking Variables

essential for determining the  $\theta$  angle of the track. Using information from projections of the track in the bend plane to PC1, and also if possible using information given by the stereo wires in the Drift Chamber, a match is made to a PC1 cluster. The tracklet from the DC/PC1 match is then projected to the outer detectors. Associations to the outer detectors, whether PC2, PC3, TEC, TOF, or EMC, can be used as necessary to reduce ghost tracks.

### 2.2.3.1 Drift Chamber

The Drift Chamber [54] sits at a radial distance of  $2.02 < R < 2.48$  m, There is one chamber on each arm, and they are mirror copies of each other, with each subtending  $90^\circ$  in azimuth, and 2 m along the z direction. The Drift Chamber is a projective tracker capable of highly precise charged track measurements in the  $r-\phi$  plane. By

measuring the track bend in phi (see figure 2.15), it is the main provider of the high momentum resolution track measurement for PHENIX. In addition, there are some stereo planes which give a z-coordinate that allows for matching of tracks to PC1, to remove the ambiguity coming from two or more tracks at the same  $\phi$ .

The main design requirements for the Drift Chamber were the following:

1. Single wire resolution better than  $150 \mu\text{m}$  in  $r\phi$  .
2. Single wire two track separation better than 1.5 mm.
3. Single wire efficiency better than 99%.
4. Spatial resolution in the z direction better than 2 mm.

This is driven by the desire to measure  $\phi \rightarrow e^+e^-$  with a mass resolution better than its natural width of 4.4 MeV, and also by the desire to have good tracking efficiency at the highest multiplicities that were anticipated at RHIC,  $dN^{ch}/d\eta \sim 2000$ .

In figure 2.16, we show a picture of the Drift Chamber frame. Each chamber volume is defined by a cylindrically concentric titanium frame. Five-mil Al-mylar windows cover the front and back of the detector, and are chosen to be nearly leak-proof while still minimizing the conversion material within the PHENIX active volume. Each chamber is filled with 20 modules, and each module contains 6 different types of wire modules: X1, U1, V1, X2, U2, and V2. The locations of these wires in a module is given in figure 2.17. The drift cells are about 2 to 2.5 cm, and drift is in the phi direction. The sense wires (anode wires) are also electrically isolated in the middle, effectively doubling the number of readout channels. This was necessary to reduce the ambiguities from double hits on a single wire.

The X1 and X2 wires run parallel to the beam, allowing them to make precise  $r\phi$  measurements. Each X wire cell is followed by U and V stereo wires. The stereo wires are angled at about  $\pm 6^\circ$  relative to the X wires (see figure 2.17. The magnitude of the stereo angle was chosen so that the z-resolution would be comparable to that of the Pad Chambers.

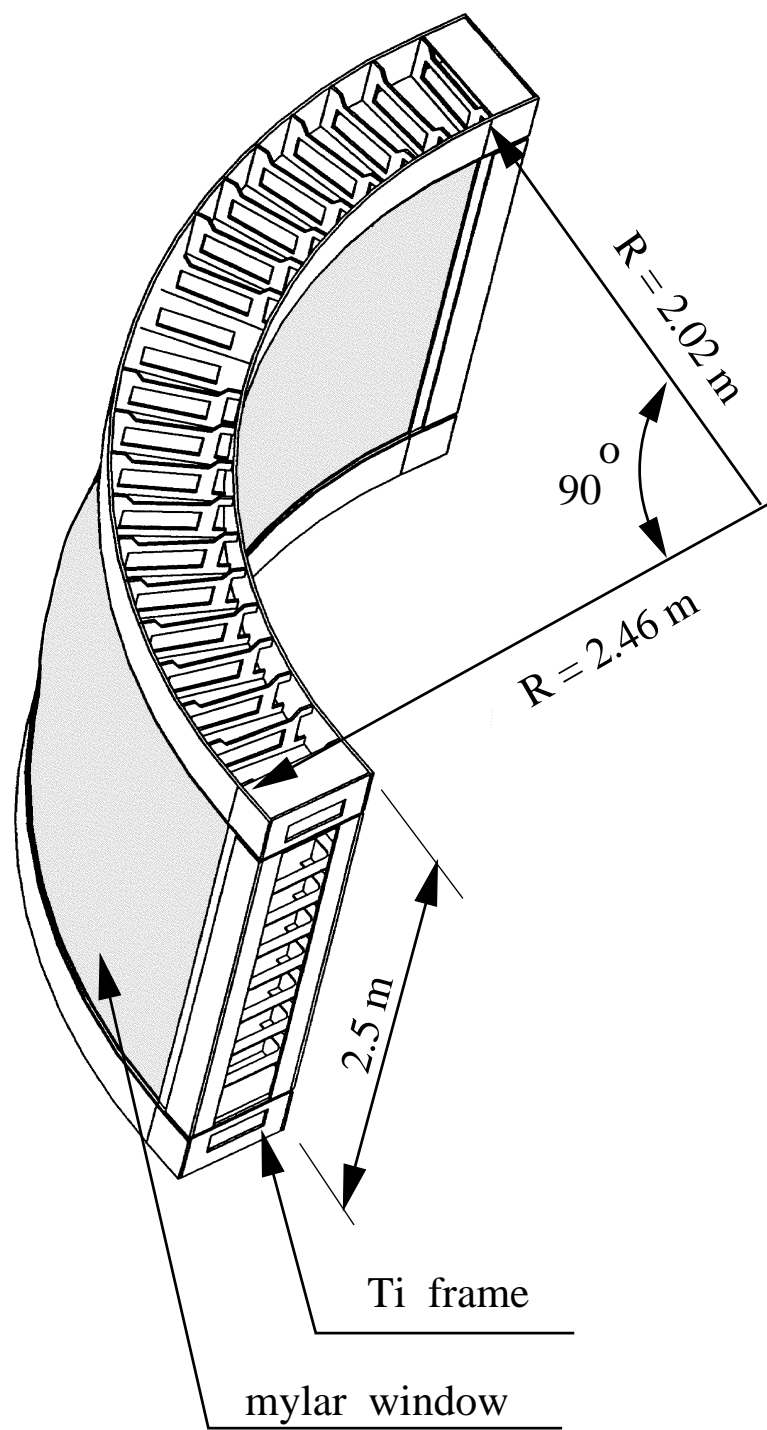


Figure 2.16: Drawing of the Phenix Drift Chamber

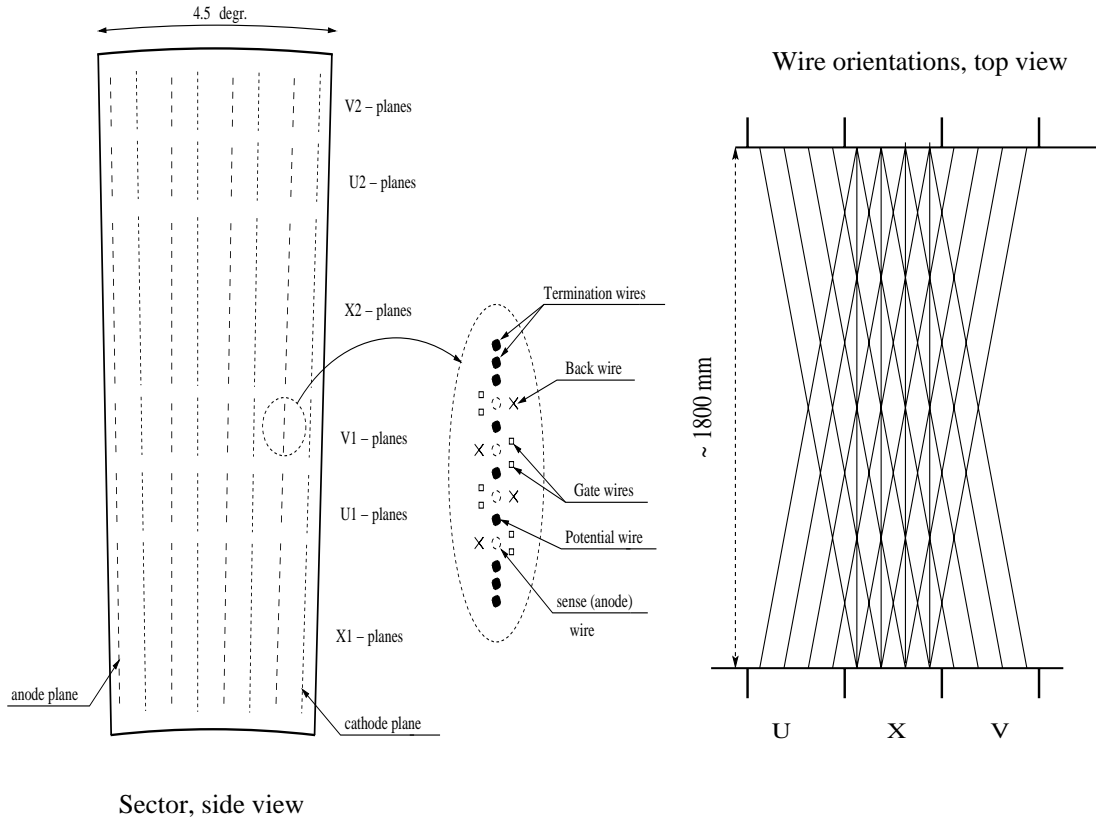


Figure 2.17: Wire Nets in the Phenix Drift Chamber

The gas mixture chosen for operation is about 49% Ar, 50%  $C_2H_6$ , and about 1% ethanol. The Ar- $C_2H_6$  mixture was shown to give good uniform drift velocity at an electric field of  $E \sim 1$  kV/cm, has high gas gain, and a low diffusion coefficient. The ethanol was added starting in Run02 to improve the ability of the wires to hold high voltage.

### 2.2.3.2 Track Reconstruction in the DC

The tracking in the Drift Chamber is done primarily through a Combinatorial Hough Transform (CHT). In this algorithm, the spatial points  $(x, y)$  are mapped onto the  $(\alpha, \phi)$  variables (see figure 2.18). For real hits, the charged hits on the X1, X2 wires, shown on the left of figure 2.18, will map onto clusters of height  $N(N - 1)/2$  in the right of figure 2.18.  $N$  is the number of hits from the track. The low-lying

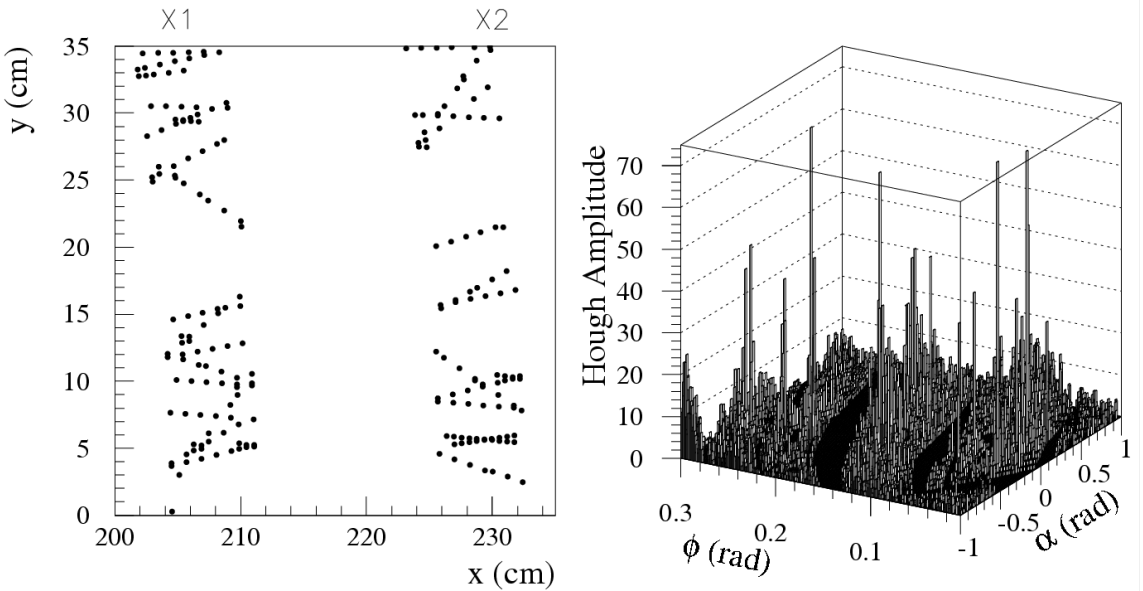


Figure 2.18: Drift Chamber Hough Transform Algorithm

“grass” comes from hits that aren’t associated together with a track. After this transformation, the finding of tracks becomes reduced to finding peaks in the  $(\alpha, \phi)$  space. All those tracks that are part of Hough  $(\alpha, \phi)$  cluster are then grouped together and associated to a single track. At this point, since we have only used information from the X wires, one only knows the track projection onto the bend plane. To get the 3-dimensional track information, the U and V stereo wires are used to get the z-coordinate of the track, and confirmed with a matching PC1 hit.

Through fine adjustment of the electrostatic field, the single wire efficiency was adjusted to a single wire efficiency of 95-96%. This allowed us to keep the mean pulse width to near 35 ns, and therefore maintain double track resolution to better than 2 mm. The single wire resolution was found to be  $165 \mu m$ , very close to the design specifications. The track finding efficiency was better than 99%. However, due to problems with broken wires, and problems holding high voltage on other wires, the overall acceptance of the Drift Chamber was a significantly lower than the design, and changed frequently over time.

Table 2.2: Summary of the PHENIX Detector Subsystems. [5]

Element	$\Delta\eta$	$\Delta\phi$	Purpose and Special Features
Magnet: central (CM) muon (MMS) muon (MMN)	$\pm 0.35$ -1.1 to -2.2 1.1 to 2.4	$360^\circ$ $360^\circ$ $360^\circ$	Up to 1.15 T·m. 0.72 T·m for $\eta = 2$ 0.72 T·m for $\eta = 2$
Silicon (MVD)	$\pm 2.6$	$360^\circ$	$d^2N/d\eta d\phi$ , precise vertex, measure reaction plane.
Beam-beam (BBC) NTC	$\pm(3.1 \text{ to } 3.9)$ $\pm(1 \text{ to } 2)$	$360^\circ$ $320^\circ$	Start timing, fast vertex. Extends coverage of BBC for p+p and p+A.
ZDC	$\pm 2 \text{ mrad}$	$360^\circ$	Minimum bias trigger.
Drift chambers (DC)	$\pm 0.35$	$90^\circ \times 2$	Good momentum and mass resolution, $\Delta m/m = 0.4\%$ at $m = 1\text{GeV}$ .
Pad chambers (PC)	$\pm 0.35$	$90^\circ \times 2$	Pattern recognition, tracking for nonbend direction.
TEC	$\pm 0.35$	$90^\circ$	Pattern recognition, $dE/dx$ .
RICH ToF T0	$\pm 0.35$ $\pm 0.35$ $\pm 0.35$	$90^\circ \times 2$ $45^\circ$ $45^\circ$	Electron identification. Good hadron identification, $\sigma < 100 \text{ ps}$ . Improve ToF timing for p+p and p+A.
PbSc EMCAL PbGl EMCAL	$\pm 0.35$ $\pm 0.35$	$90^\circ + 45^\circ$ $45^\circ$	For both calorimeters, photon and electron detection. Good $e^\pm/\pi^\pm$ separation at $p > 1 \text{ GeV}/c$ by EM shower and $p < 0.35 \text{ GeV}/c$ by ToF. $K^\pm/\pi^\pm$ separation up to 1 $\text{GeV}/c$ by ToF.
$\mu$ tracker: ( $\mu$ TS) ( $\mu$ TN)	-1.15 to -2.25 1.15 to 2.44	$360^\circ$ $360^\circ$	Tracking for muons. Muon tracker north installed for year-3
$\mu$ identifier: ( $\mu$ IDS) ( $\mu$ IDN)	-1.15 to -2.25 1.15 to 2.44	$360^\circ$ $360^\circ$	Steel absorbers and Iarocci tubes for muon/hadron separation.

Table 2.3: PHENIX Central Magnet Parameters

Parameter	CM	CM
CM coils	Inner and Outer	Outer only
Field configuration	Axial	Axial
Field integral (T-m)	0.43 to 1.15 ( $\Theta=90^\circ$ )	0.78 ( $\Theta=90^\circ$ )
Wt. (metric tons)	421	421
Pseudorapidity coverage	$-0.35 < \eta < 0.35$	$-0.35 < \eta < 0.35$
Polar angle coverage ( $^\circ$ )	$70 < \Theta < 110$	$70 < \Theta < 110$
Amp-turns	541,000	248,000
Power (kW)	928	600
Average coil temp. ( $^\circ\text{C}$ )	23.8 (I)/32.1(O)	32.1

### 2.2.3.3 Pad Chambers (PC)

The Pad Chambers [3] are multi-wire proportional chambers, with each detector containing a single plane of wires inside a gas volume bounded by two cathode planes (see figure 2.19). One of the cathode planes is finely segmented into an array of pixels. This allows the PCs to determine a 3-dimensional space point. The PCs are the only non-projective detectors in the Central Arm Tracking, and hence are a vital part of the pattern recognition and also vital for determining the  $\theta$  angle of a track. Since the PCs are located at radial distances  $R > 2.4m$ , they are well outside the field region and will track straight line trajectories beyond the Drift Chamber.

The size of the pixels is driven by the need for a low occupancy even in the highest charged multiplicities, as well as good enough position resolution in the z-direction. The design goal was 4 mm, so an anode spacing of 8.4 mm was chosen. The 0.4 extra spacing was motivated by geometrical reasons. The cell shape was chosen to be square, and so the cell size was  $8.4 \times 8.4 mm^2$ .

A picture of the PC pixel geometry is shown in figure 2.20. To reduce the amount of electronic and other noise, a special pad design was invented, where each cell contains three pixels and an avalanche must be sensed by all three pixels to form a valid hit. However, this design is costly in terms of electronics readout channels. Thus, the interleaved pixels were ganged together, nine to a group, so that the three pixels in a cell are always connected to different but neighboring channels, and each cell is connected to a unique channel triplet. This solution saves a factor of nine in readout channels.

The resolution could be determined experimentally using cosmic ray data. The chambers were laid flat on a table and triggered with a coincidence of scintillator paddles. The paddles were also used to track the cosmic rays, and the resolution determined from the difference between the scintillator tracking resolution and the pad chamber resolution. The resolution is shown in figure 2.21. A table of PC parameters is given in table 2.4.

In figure 2.22, we show a picture of the Pad Chamber Online Monitor, which

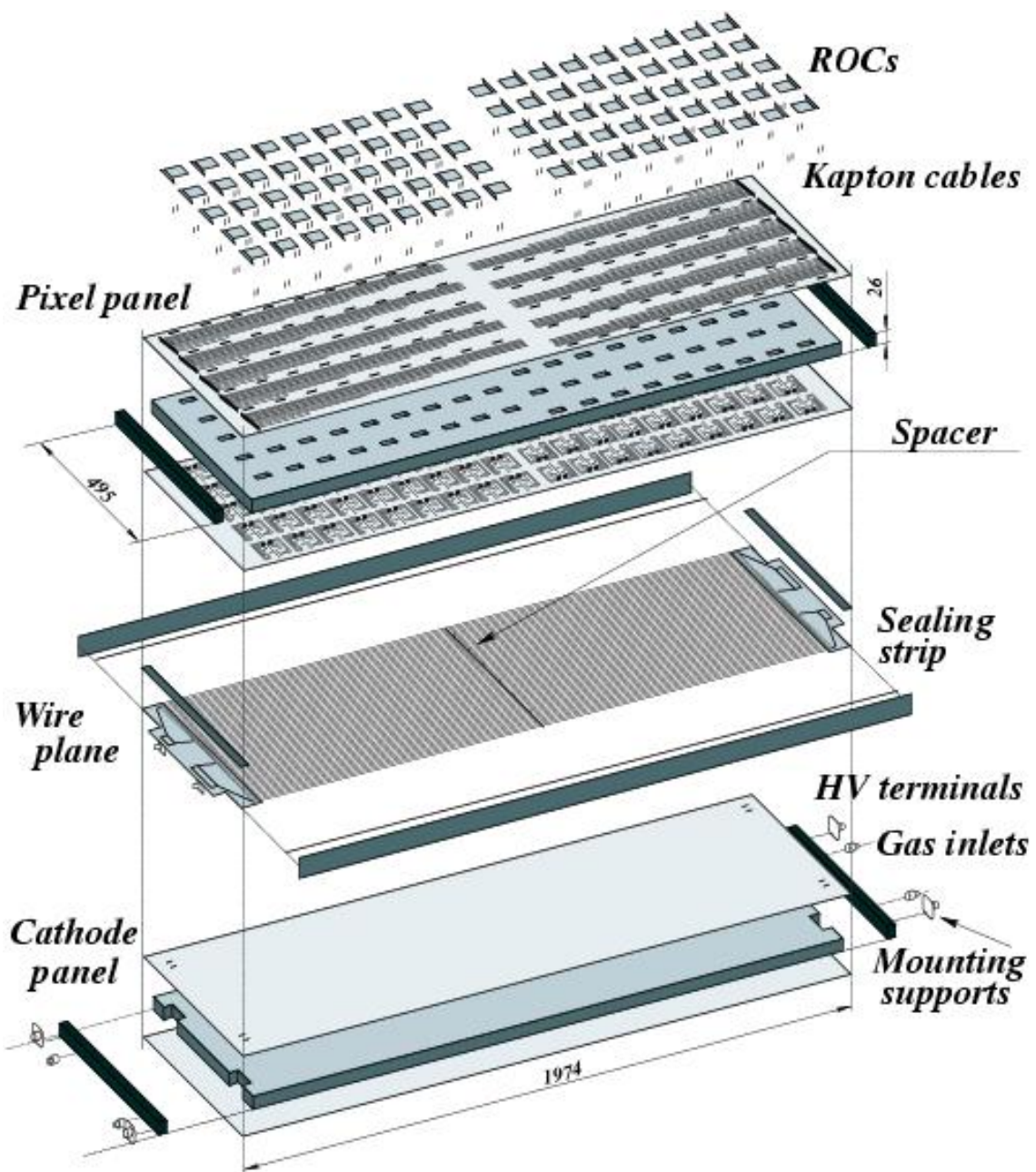


Figure 2.19: Pad Chamber Mechanical Components

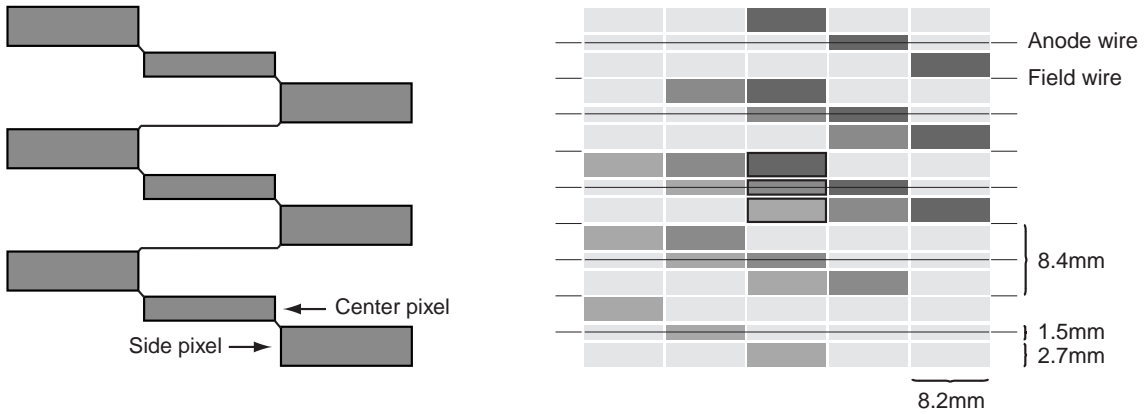


Figure 2.20: Phenix PC Pixels and Pads. The grouping of pixels into one readout is

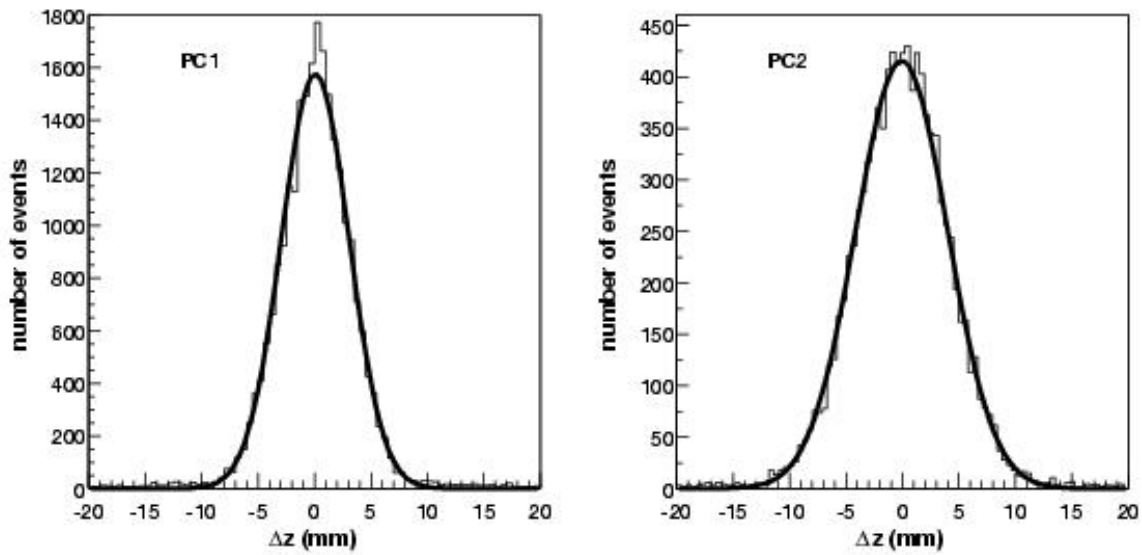


Figure 2.21: The spatial resolution of the Pad Chambers, as measured from cosmic ray data.

Chamber	Wire dist (mm)	Z Res. (mm)	Perp Res. (mm)	Rad Thicness
PC1	8.4	1.7	2.5	1.2%
PC2	13.6	3.1	3.9	2.4%
PC3	16.0	3.6	4.6	2.4%

Table 2.4: Pad Chamber Parameters

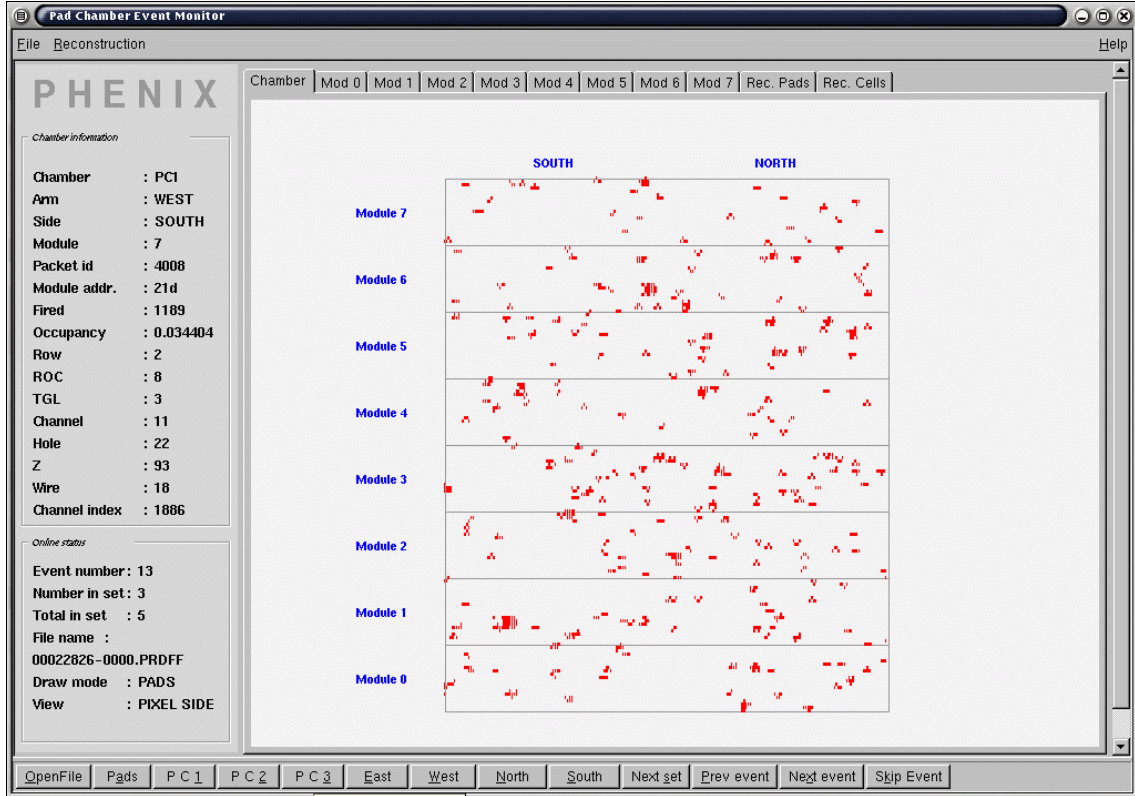


Figure 2.22: The PC Online Monitor, showing the hit occupancy in the most central Au+Au events

shows the hit distribution of cells in PC3. It shows the PC working with good efficiency, and with clearly enough segmentation to handle the large multiplicities.

#### 2.2.3.4 Detector Alignment

The process of alignment is finding the true location and orientation of each detector element. Since the resolution of the tracking detectors are generally much better than the alignment one can get through surveying, the detectors need to be aligned using data. The track alignment is done on runs with the field off, where all tracks go straight except for multiple scattering and decay effects. The general alignment in the drift chamber is done by translations and rotations of the entire detector volume until the distribution in  $(\alpha, \phi)$  is peaked along the line  $\alpha = 0$ . There is also a more involved analysis required to align each individual wire, since the survey

information on where each individual wire is placed also has uncertainties.

After the alignment is done in the drift chamber, the tracks are then projected in a straight line to the outer detectors. The mean of the residuals of this projection and the closest matching hit in the outer detector is then shifted to 0 using translations and rotations. These alignment (zero-field) runs are usually done a few times during the run, since the Central Arms can and were moved often to allow access for repairs.

### 2.2.3.5 Momentum Reconstruction

While the deflection  $\alpha$  is not a bad measure of the momentum, the assumption that the field is zero at the DC is not a perfect one. Thus, an accurate measure of the momentum must use a full tracking model to get a good momentum resolution. Analytic solutions to the tracking are not possible due to the complicated shape of the focusing magnetic field. Therefore, a field lookup table is generated,  $f(p, r, \theta_0, z)$ , which gives the field integral  $f$  as a function of  $p$ , the total track momentum,  $r$ , the radius from the beam pipe,  $\theta_0$ , the theta angle of the track, and  $z$ , the z-vertex of the collision. This field lookup table is generated by swimming particles through the field and integrating directly for each grid point, where the magnetic field was determined as described previously.

The field integral  $f(p, r, \theta_0, z)$  varies linearly with the  $\phi$  angle at a given radius  $r$ , since this is just the  $p_T$  kick given by a  $\int B dl$ . That is,

$$\phi = \phi_0 + q \frac{f(p, r, \theta_0, z)}{p} \quad (2.3)$$

Thus, we can set up an iterative procedure to find the true momentum, starting with an initial estimate of the momentum made from the reconstructed angle  $\alpha$ , and the measured polar angle  $\theta$  from the PC1/DC match. Then, for each reconstructed hit associated to the track, a four-dimensional polynomial interpolation of the field-integral grid is performed to extract a value of  $f(p, r, \theta_0, z)$  for each hit. Then, a fit in  $\phi$  and  $f$  is performed to extract the quantities  $\phi_0$  and  $q/p$  for each track. The extracted values are then fed back into eq. 2.3.

The initial polar angle,  $\theta_0$ , is also determined using an iterative procedure with the equation

$$\theta = \theta_0 + \delta(p, r = R, \theta_0, z) - g(p, r = R, \theta_0, z)/p \quad (2.4)$$

where  $\delta$  is the r-z analog of  $\alpha$  in the  $r - \phi$  plane. That is,  $\delta$  is the bend angle of a particle relative to that of an infinite momentum particle, but this time in the r-z plane.

Note that all tracks are assumed to come from the origin of the collision. One advantage of this procedure is that it also determines the track path through the detector, and this information can be used to calculate the projections of the track through the detector. The final charged track momentum resolution, as determined from reconstruction of the proton mass using time-of-flight, is

$$\left(\frac{\delta p}{p}\right)^2 = (1.5_{-0.2}^{+0.1} p \otimes (1.4_{-0.1}^{+0.1})) \quad (2.5)$$

## 2.2.4 Particle Identification

PHENIX is designed with very capable particle identification methods, using time of flight methods in the EMCAL and the TOF, and threshold Cerenkov techniques in the RICH [12].

### 2.2.4.1 Ring Imaging Cerenkov Counter (RICH)

The RICH [13] [55] is a Cerenkov detector and is used for distinguishing electrons from the far more copiously produced charged pions in heavy-ion collisions, up to the pion Cerenkov threshold, which was 4.65 GeV during Run02 and Run03. The RICH consists of two identical vessels, each containing 48 composite mirror panels forming two intersecting spherical surfaces. The spherical mirrors focus the Cerenkov light onto two arrays of 1280 Hamamatsu H3171S UV PMTs. The PMTs are fitted with 2" diameter Winston cones and have magnetic shields that let them operate in fields up to 100 gauss. A cutaway view of the RICH is displayed in figure 2.23.

The  $e/\pi$  discrimination in the RICH depends on three factors: the value of the pion Cerenkov threshold, the statistical fluctuations in the number of photo-electrons

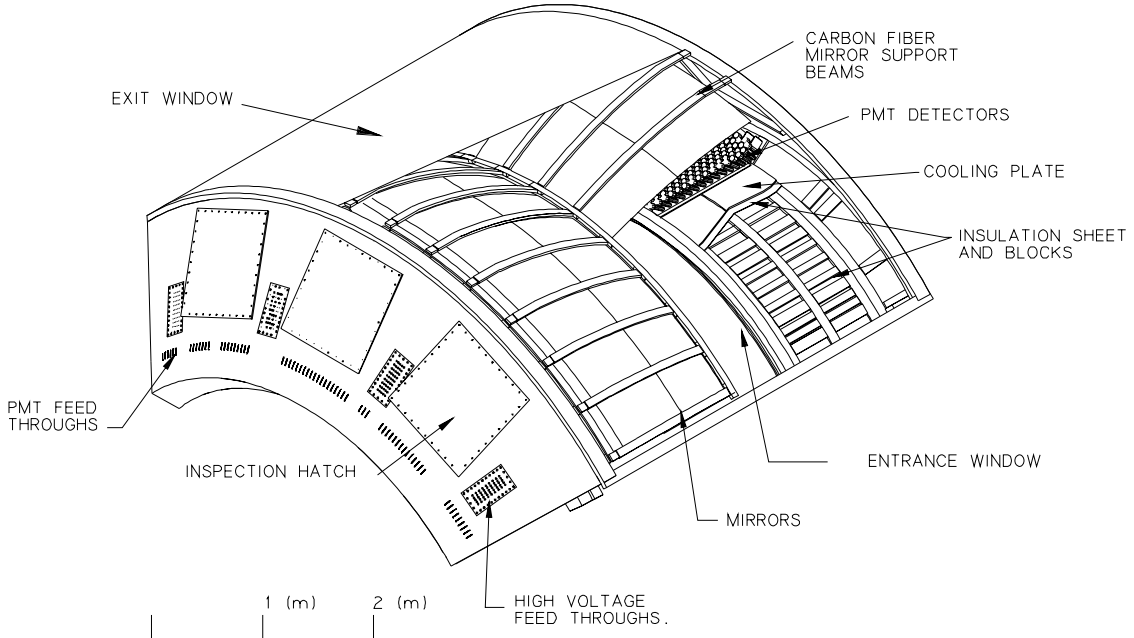


Figure 2.23: A cutaway view of the RICH, showing the spherical mirrors and the PMTs arrayed along the side of the detector, out of the PHENIX acceptance.

produced by an electron in the RICH, and the background rates. Since dark current noise produces only about 0.5 hits per RICH per event, the background is dominated by spurious electrons produced by photon conversions in the PHENIX detector. The gas used during Run02 and Run03 was  $CO_2$ , which has a pion Cerenkov threshold of 4.65 GeV/c.

Figure 2.24 shows the performance of the RICH in selecting electrons. For electrons, the ratio  $E/p$  for energy E in the calorimeter and p from the DC should equal 1. The peak in the background at  $E/p \sim 0.3$  comes from background hadrons that are accidentally associated with a RICH hit. The hadrons typically leave a MIP of  $\sim 0.3$ .

## 2.2.5 Electro-Magnetic Calorimeter (EMC)

The PHENIX EMC [17] actually consists of two subsystems utilizing different technology. The first is a sampling calorimeter of a shashlik design [33], consisting of 15552 lead-scintillator (PbSc) towers covering 3/4th of the Central Arm. The

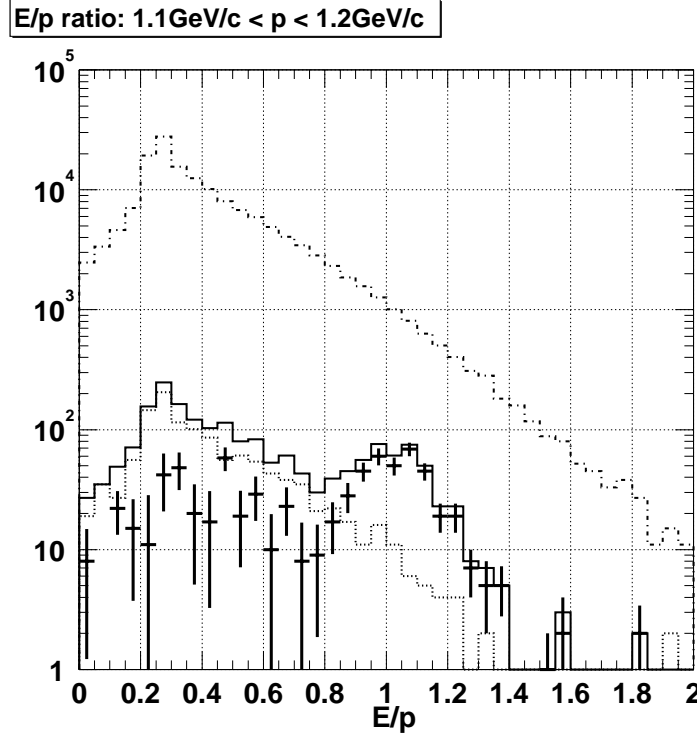


Figure 2.24: Ratio of Energy over Momentum for: All Drift Chamber tracks (dashed-dotted line), Tracks associated with a RICH ring (solid line), Estimated background for tracks with a RICH hit (dotted line), and Tracks associated with RICH hits after background subtraction (solid markers). These are for tracks with  $1.1 < p_T < 1.2$

other quarter is covered by a homogenous detector of 4608 lead-glass (PbGl) towers. Having two calorimeters with very different systematics is helpful for increasing confidence in the final result. We will briefly discuss common features between them and then discuss each in detail.

The EMC's are designed to measure the spatial position and energy of electrons and photons. They both have excellent resolutions in energy, timing, and location, though the PbSc has better timing and the PbGl has better spatial and energy resolution. In addition, even though the PbSc was designed as an electromagnetic calorimeter, it is 0.85 nuclear interaction lengths in depth, so that it has some sensitivity to hadrons, which is a useful feature for measuring  $E_T$ , for triggering, and for measurements of hadrons at high- $p_T$ . The PbGl also is  $\sim 1$  interaction length long, but since the light collection is from Cerenkov radiation in the glass, it has

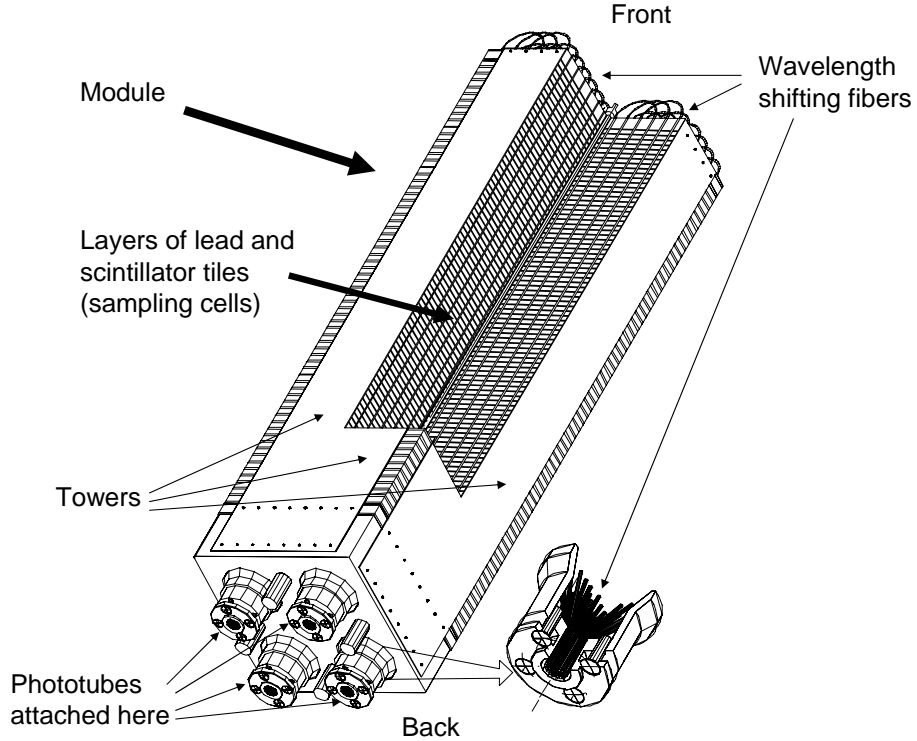


Figure 2.25: Phenix PbSc Module

much less sensitivity to hadrons. This is useful for measurements of photons, where there one is interested in reducing the hadronic background as much as possible. The very fine segmentation in tower sizes and the distance from the interaction region allows for  $\gamma - \pi^0$  separation up to 24 GeV, and keeps the occupancy low enough even in central heavy-ion collisions that the efficiency for proper reconstruction of a photon's energy remains good.

### 2.2.5.1 Lead-Scintillator (PbSc)

The parameters of the PbSc are given in table 2.5. In figure 2.25 a cutaway picture is shown of a “module”, which consists of 4 towers grouped together. It shows the sampling layers and the orientation of the wavelength shifting fibers which carry the light yield to the phototubes attached at the back. 36 of these modules are

grouped into an array of  $12 \times 12$  towers called a supermodule (SM). Then 18 of these supermodules (in a  $3 \times 6$  grid) are joined together to form a sector. There are 6 PbSc sectors. The total coverage of the PbSc is about  $48m^2$ , and sits  $\sim 5m$  from the beam pipe.

Table 2.5: Individual Pb-Scintillator Calorimeter Tower Parameters

Parameter	Value
Lateral Segmentation	$5.535 \times 5.535 \text{ cm}^2$
Active Sampling Cells	66
Scintillator	Polystyrene (1.5% PT / 0.01% POPOP), 0.4 cm
Absorber	Pb, 0.15 cm
Cell Thickness	0.56 cm (0.277 $X_0$ )
Active Depth	37.5 cm
Radiation Length	18
Nuclear Interaction Length	0.85
WLS Fiber	BCF-99-29a, 0.1 cm
WLS Fibers per Tower	36
PMT Type	FEU115M, MELS, Russia, 3.0 cm
Photocathode	Sb-K-Na-Cs
Luminous Sensitivity	$\geq 80 \mu\text{a/lm}$
Rise Time (20%–80%)	$\leq 5 \text{ ns}$

The nominal energy resolution of the PbSc is

$$\frac{\sigma_E}{E} = 8.1\%/\sqrt{E} \otimes 2.1\% \quad (2.6)$$

This resolution was determined from electron test beams at BNL and CERN (see figure 2.26) under ideal conditions. During Run02 and Run03, the actual energy resolution achieved was

$$\frac{\sigma_E}{E} = 8.1\%/\sqrt{E} \otimes 6.3\% \quad (2.7)$$

This resolution was achieved by calibrations using the measured  $\pi^0$  invariant mass, identified electrons, and data from laser injected into the PMTs. The energy resolution has been improving over time as the calibrations are fine-tuned. The ToF resolution is given in figure 2.27.

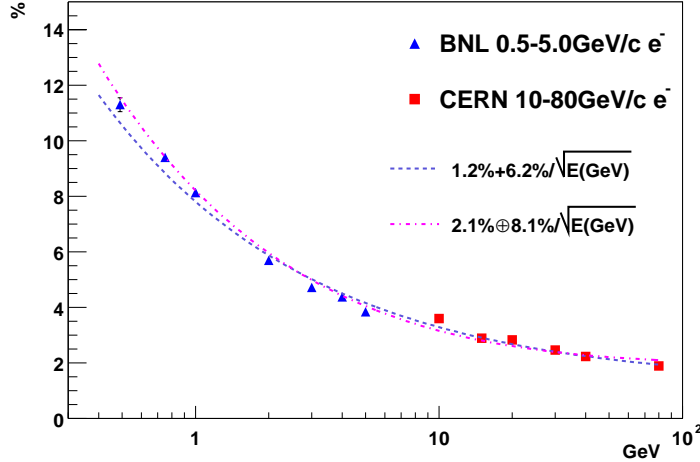


Figure 2.26: PbSc Energy Resolution, obtained from test beams at CERN and BNL.

### 2.2.5.2 Lead-Glass (PbGl)

The PbGl EMC subsystem consists of an array of thick optical glass towers embedded with 51% Pb-Oxide. Each tower is each  $4 \times 4 \times 40\text{cm}^3$  and grouped into  $6 \times 4$  modules (fig. 2.28), which are then grouped into 144 tower ( $12 \times 12$ ) supermodules (SM). There are two sectors of PbGl, and each sector contains a grid of  $4 \times 8$  supermodules. Figure 2.28 shows the contents of one PbGl module. Each PbGl tower is individually wrapped with aluminized mylar and shrink tube, then glued together with carbon fiber and epoxy resin to form a  $6 \times 4$  module. The phototubes and bases are housed in 0.5 mm steel sheets. The aluminized mirror foil covering the front face of the towers has contains holes to allow LED light to penetrate. The LED is used for gain monitoring. The LED board is covered by a polystyrene reflective dome, and a photodiode is included as an additional check on the LED calibration.

The physical parameters of the PbGl are given in table 2.6. The measured energy resolution of  $e^+$  showers from test beam versus the incident energy is shown in Fig. 2.29 for various angles of incidence on the calorimeter surface, as determined from electron showers, for various angles of incidence. A fit parametrization of

$$\frac{\sigma(E)}{E} = \frac{[5.9 \pm 0.1]\%}{\sqrt{E/\text{GeV}}} \oplus [0.8 \pm 0.1]\%. \quad (2.8)$$

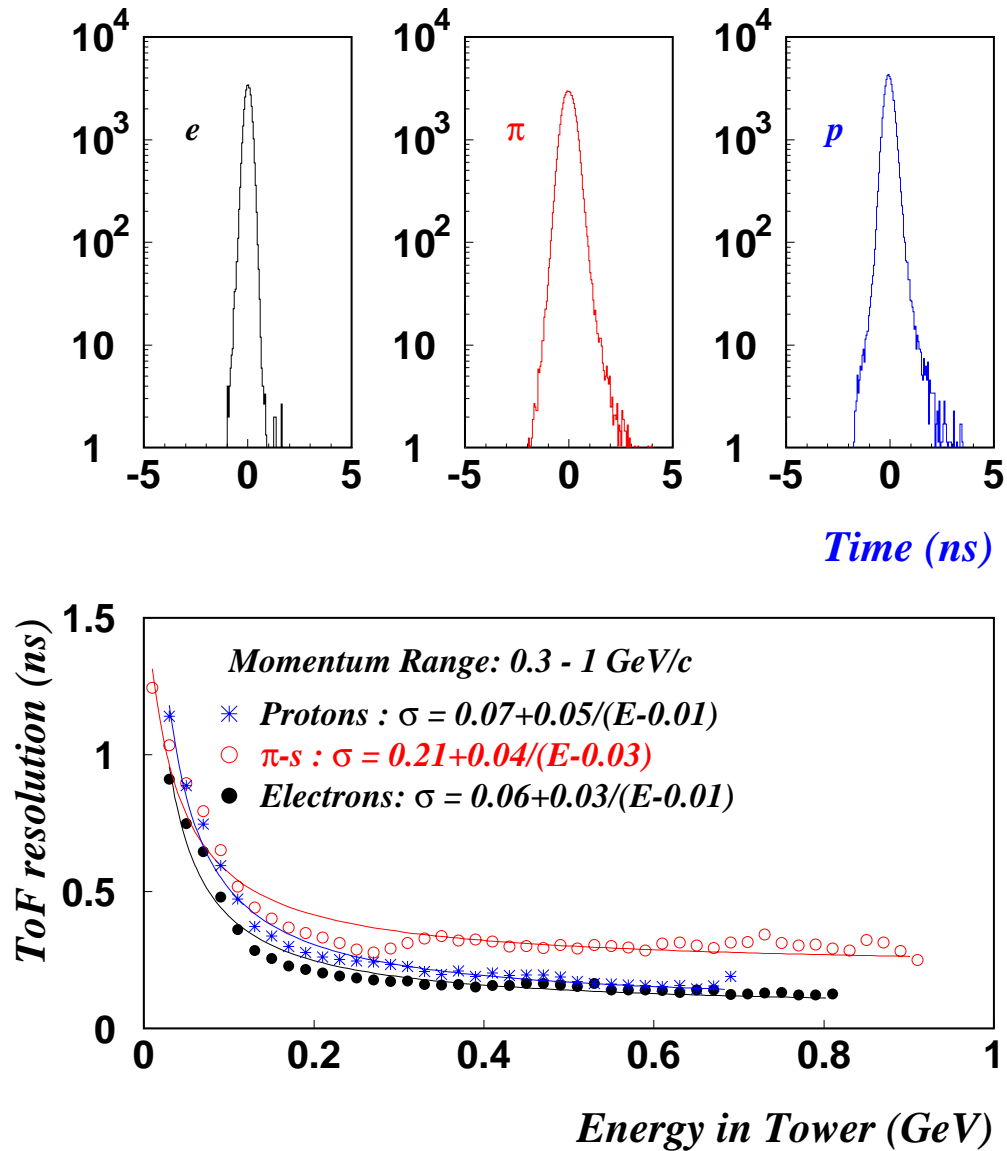


Figure 2.27: Pb-scintillator timing resolution for different particles. Top: lineshape for 1 GeV/c electrons, pions and protons. Bottom: resolution in the momentum range 0.3-1.0 GeV/c

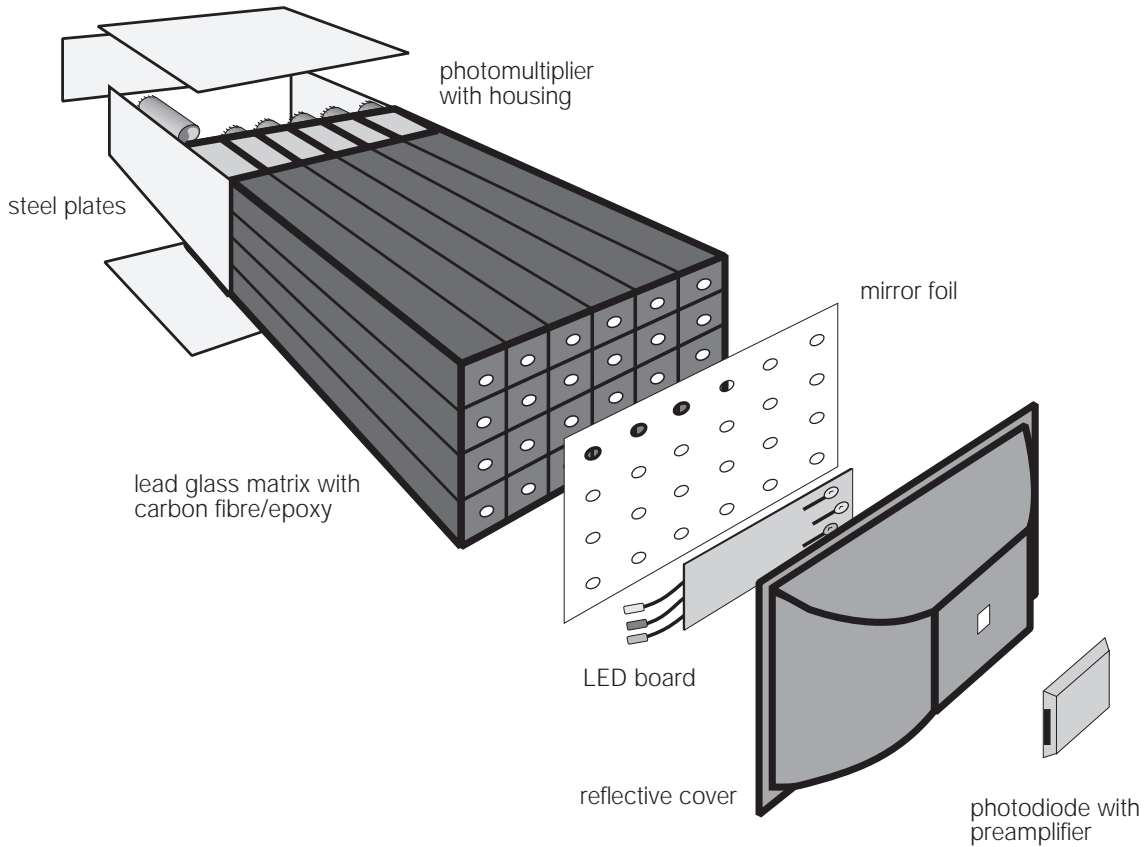


Figure 2.28: An exploded view of a PbGl module, containing 24 towers in a  $6 \times 4$  grid. See text for a detailed description.

is used to fit the data in fig. 2.29. The measured position resolution can be fit with the parameterization

$$\sigma_x(E) = \frac{[8.4 \pm 0.3]\text{mm}}{\sqrt{E/\text{GeV}}} \oplus [0.2 \pm 0.1]\text{mm}. \quad (2.9)$$

using the same data as in figure 2.29. The time-of-flight resolution can be parametrized by the equation Figure 2.30 shows the fit for positrons and pions

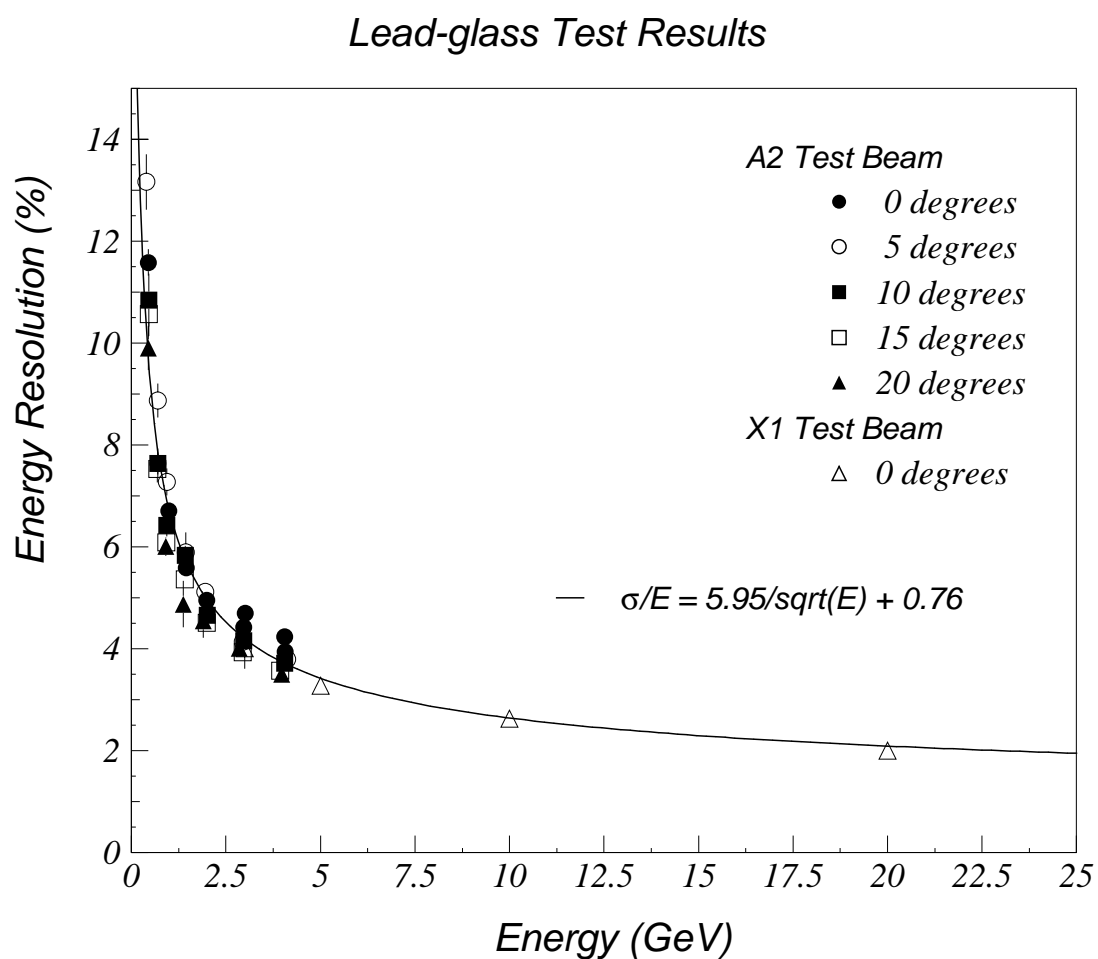


Figure 2.29: PbGl energy resolution versus incident energy.

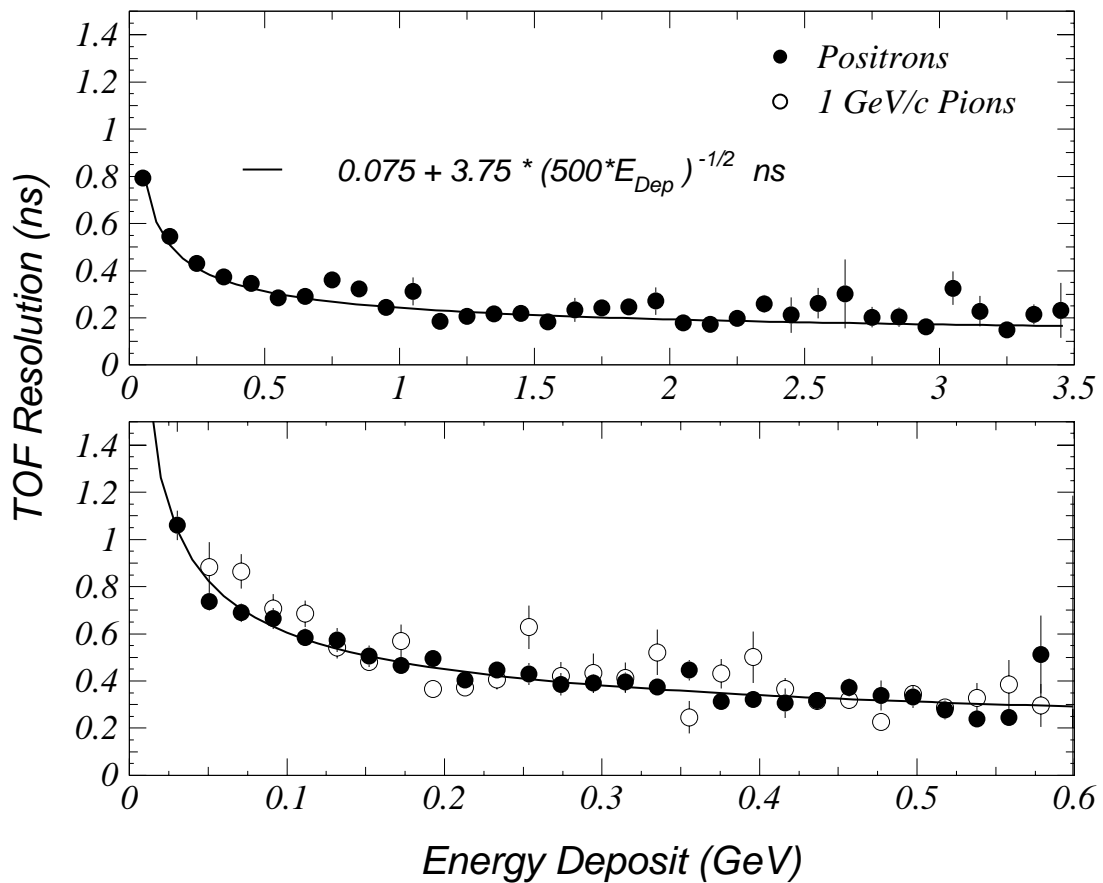


Figure 2.30: PbGl TOF Resolution versus energy deposit for positrons of various incident momenta and for 1.0 GeV/c pions

Table 2.6: Lead-Glass Physical Parameters

Quantity	Value
<b>Geometry:</b>	
Number of SM per Sector	384 Super Modules
Number of Modules per SM	192 (16 wide by 12 high)
Total Number of Modules	24 (6 wide by 4 high)
Module Front Surface	9216
Module Length	4cm x 4cm
Mylar Foil Thickness	40 cm ( $14.4 X_0$ )
Shrink Tube Thickness	12 micron
Super Module Front Surface	150 micron
	$24.6 \pm 0.02\text{cm} \times 16.4 \pm 0.02\text{cm}$
<b>Pb-glass:</b> Type	TF1
Pb-Oxide Content	51%
Density	$3.85 \text{ g/cm}^2$
Weight per Module	2.46 kg
Index of Refraction	1.648
Total Internal Reflection Angle	36 degrees
Radiation Length	2.8 cm
Moliere Radius	3.68 cm
Interaction Length	38.0 cm
Critical Energy	16 MeV

Table 2.7: Collider Parameters

		Particles	Beam Energy [GeV]	Luminosity [ $cm^{-2}s^{-1}$ ]	Crossing [ $\mu s$ ]
Tevatron	FermiLab	pp	1000	$2.5 \times 10^{31}$	3.5
Hera	DESY	$e^-p$	27.5e+920p	$2 \times 10^{31}$	0.096
RHIC	BNL	variable	250 (pp)	$2 \times 10^{32}$	0.1065
LHC	CERN	pp	7000	$10^{34}$	0.025

## 2.3 Data Acquisition System (DAQ)

As mentioned previously, what makes PHENIX most unique among the RHIC experiments is the advanced design and implementation of its Data Acquisition System (DAQ) [10]. The system is designed to be capable of taking data at a maximum rate of 25 kHz, with a total throughput of over 2 Gigabytes/sec. For monetary reasons the current practical upper limit is 12.5 kHz, and the 25 kHz limit can only be attained by installing twice as many Data Collection Modules (DCMs).

To achieve these high rates, PHENIX is designed to have a parallel, pipelined, and buffered readout. That is, each component of the DAQ is required to be able to take in data, process it, and send it out, with each process occurring in parallel. Thus, the PHENIX DAQ is designed to be nearly deadtime-less, unless the input rate is higher than the maximum data-rate.

The fundamental clock is determined by the RHIC clock, which is determined by the bunch spacings, which are 106.5 ns (9.390 MHz). In table 2.7 we give a comparison of the parameters of other colliders, which are important in determining the DAQ requirements.

Because of the variety of species that are expected to be collided at RHIC, the PHENIX DAQ has to be designed to handle two very different data-taking scenarios, from the low interaction rate but high data volume of heavy-ion collisions all the way to the very high interaction rates but low data volume of p+p collisions. These trends are shown in figure 2.31, where the interaction rate is seen to decrease with heavy nuclei, while the multiplicity increases. Coincidentally, these two trends compensate each other so that the data rate (in MB/s) remains roughly constant for all collision species.

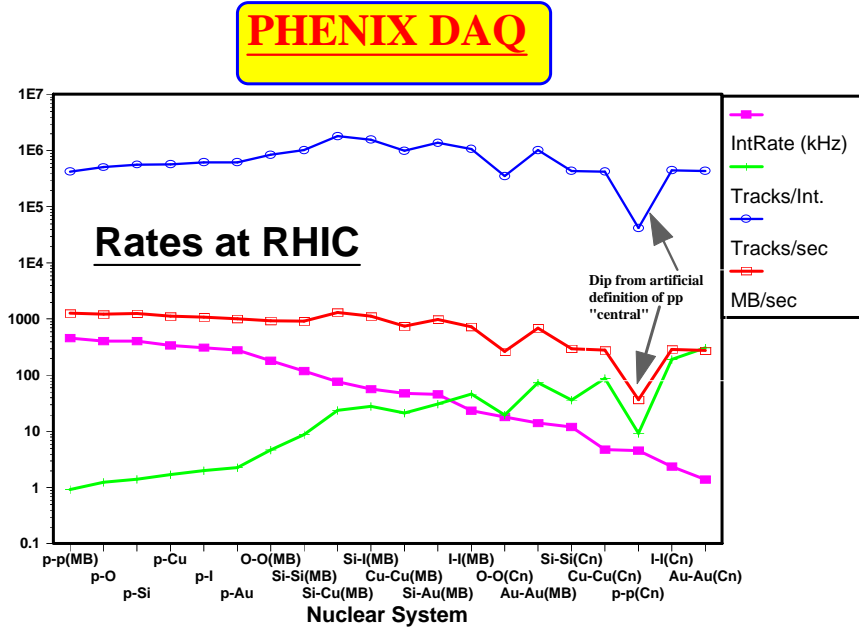


Figure 2.31: DAQ Rates

The data flow for the PHENIX DAQ is shown in figure 2.32. We'll start with some physics event, shown with the red “star” on the left. and progress through all the aspects of the DAQ. The event will generate signals in some detector, which we will take to be the BBC as an example. The PMT signals from the BBC are then digitized within 106.5 ns in the BBC-FEM, and sent to the BBC Local Level-1 board (BBC-LL1). The BBC-LL1 runs the BBC trigger algorithm on this digitized data, and sends its decision to the Global Level-1 (GL1) boards, which makes the final decision to accept the event. The GL1 takes decisions from many LL1s, and that decision is based on some logical combination of LL1s, and also whether the defined trigger defined is pre-scaled, and whether there are any busies in the system.

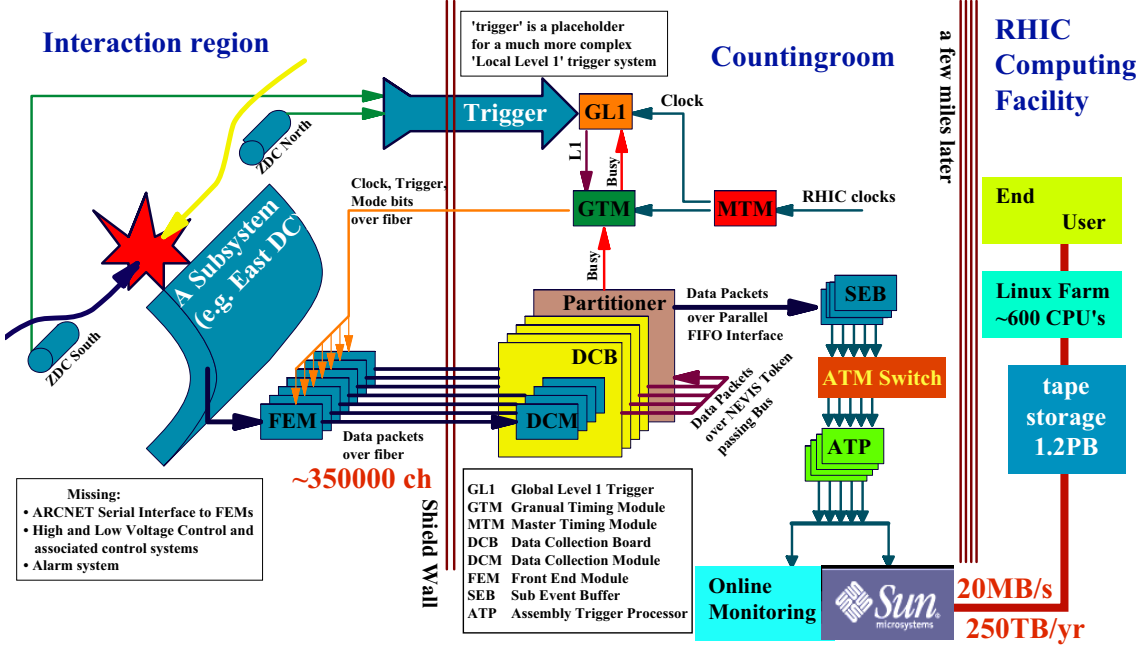


Figure 2.32: A Schematic of the PHENIX DAQ. See text for details.

The time allowed to make this trigger decision is  $4 \mu s$ , and is determined by the number of events buffered in the Front End Modules (FEM), since trigger decisions have to be made before the buffer is overrun.

Here we assume that the GL1 decides to accept the BBC-LL1 triggered event. The decision is sent to the Granule Timing Modules (GTM), which then send the decision to the FEMs. The FEMs then go back into their onboard buffer to send the data corresponding to the event that fired the BBCs. The data is sent to the Data Collection Modules (DCM) [57] over fiber-optic cable.

The DCM's are responsible for providing a uniform interface to the Front-End Electronics (FEE) for reception of data from the Interaction Region to the Counting House. In addition, they have a variety of other purposes:

1. Doing zero-suppression of empty channels to reduce data volume with no loss of information.
2. Formatting data so that the various data fragments can be assembled together

into one event.

3. First stage of event-building, where up to 8 packets of data can be assembled into one group (called a frame).
4. Generating trigger primitives for later level-2 calculations.
5. Generate busies to slow down data-taking rates when they begin to overwhelm the DAQ.

The first item allows a single place to run all zero-suppression algorithms, reducing research and design costs and offloading functionality from the FEMs. This offloading is desired since the FEMs are often located in confined spaces near the detector and thus simplifying their design reduces their heat load as well as reducing the chances of failure. The problem with failed FEMs is that they are hard to replace since they are located at the detector, which cannot be accessed except during moments when the beams are not colliding.

The DCMs then send their data over to the EventBuilder (EVB), which consists of Sub-Event Buffers (SEB) and Assembly and Trigger Processors (ATP). The SEBs and ATPs are computers running the Windows®Operating System, and are networked together over Asynchronous Transfer Mode (ATM).<sup>1</sup> The advantage of using PCs is the lower cost of off-the-shelf components, as well as the greater ease of development. The SEBs are responsible for receiving and buffering the data from the DCMs, and then sending them out to the ATPs. The ATPs assemble the event fragments from the SEBs, making sure to keep together only data that is associated to the same event, and then make Level-2 trigger decisions on the assembled event, before sending them out to the Event Pool.

The Event Pool consists of an in-memory buffer that reads events from the ATPs. One benefit of the Event Pool is that it can simultaneously provide events to various online monitoring software. Events are read from the Event Pool by a data logger,

---

<sup>1</sup>The EVB has since evolved into a Linux over Gigabit Ethernet configuration

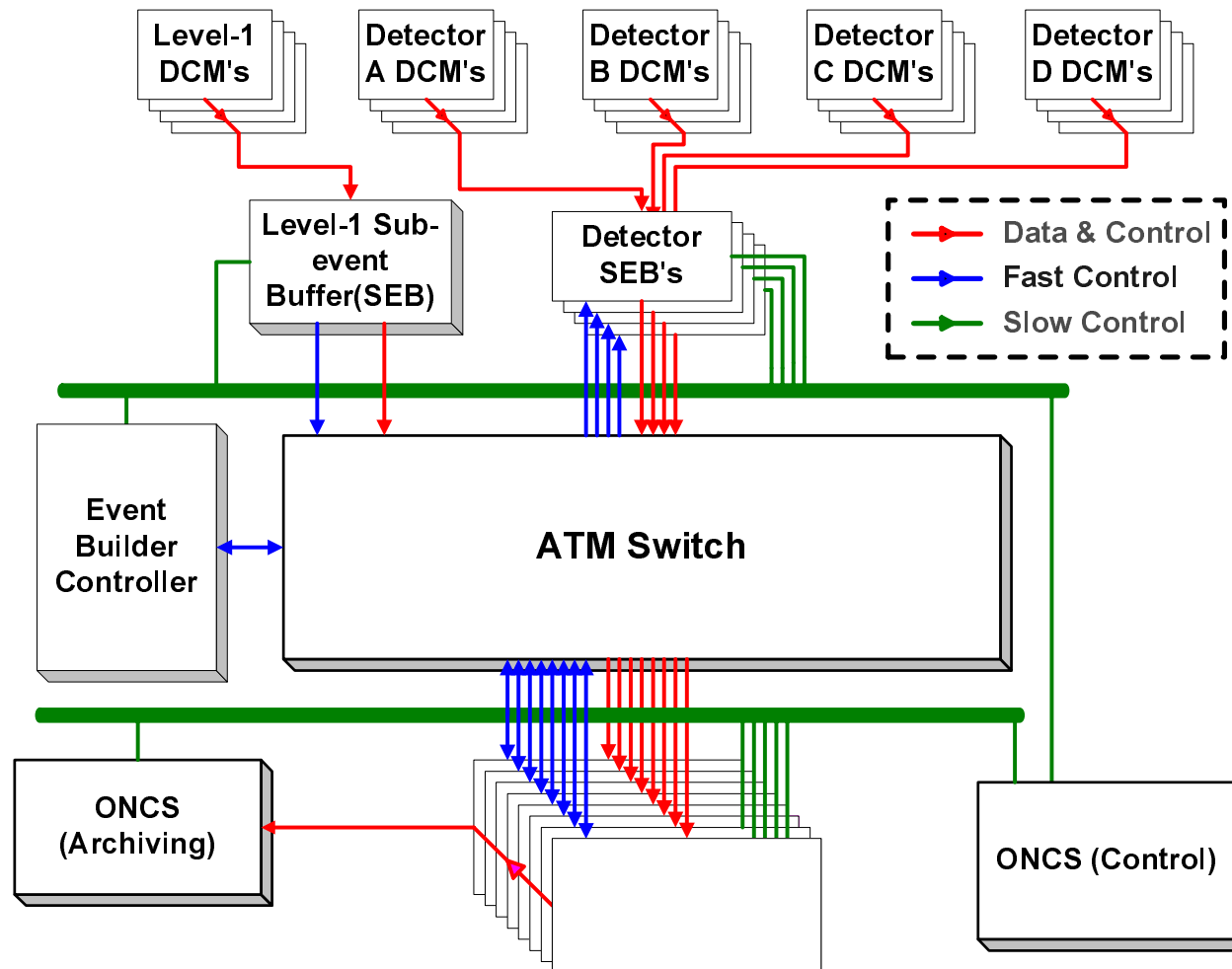


Figure 2.33: EventBuilder Architecture During Run02 and Run03

which writes them to the Buffer Boxes, which are servers with a striped RAID of size  $\sim 1TB$  each.

The data files, which are in PHENIX Raw Data Format (PRDF), are then sent over Gigabit Ethernet links to RCF HPSS, where they are written to tape.

## 2.4 Level-1 Triggers

The Level-1 Triggers [25] used during this analysis from Run02 Au+Au were the BBC-LL1 z-vertex valid, and the ZDC North-South coincidence blue-logic trigger. The minimum-bias definition for Run02 Au+Au is a coincidence between the ZDC and the BBC. For Run03  $d+Au$  and  $p+p$ , the main trigger used was the ERT Gamma Trigger. The data taken with the min-bias BBC-LL1 trigger was also used, allowing us to check trigger biases. No Level-2 triggers were used.

### 2.4.1 BBC Local-Level1 (BBC-LL1) Trigger

The BBC Level-1 takes 128 channels of data each clock cycle from the BBC FEMs. The 128 channels consist of 64 channels of TDC information from the North BBC and 64 channels from the South BBC. The BBC-LL1 algorithm consists of:

1. Check that the TDC value lies within the validity window.
2. For those channels that pass the validity window, count the total number of TDC hits, and calculate the sum of all those channels, for each side (N and S) separately.
3. For each side, if the number of hits is greater than 0, take the sum from the previous step and divide by the number of valid TDC hits. This then gives the mean time for each BBC.
4. Take the difference between the South and the North mean time to get a number proportional to the z-vertex.

Two reduced-bits are sent to GL1 from the BBC-LL1, allowing for three different signals (if both bits are 0 then nothing happened). The two main conditions on the trigger were whether greater than one or two tubes fire in each arm, and whether the collision was between some valid z-vertex range.

### 2.4.2 ZDC Coincidence (ZDCNS) Trigger

The ZDC coincidence trigger consisted of a coincidence between the north and south ZDC. Given the gate width of 15 ns and the separation time of the ZDCs of 120 ns, the trigger has zero chance of accidental overlap from single beam gas or single beam scrape, which is one reason the ZDC was a very clean trigger. Additionally, the gate width implies a coincidence window of  $\sim 30\text{ns}$ , which is wide enough to contain essentially all collisions at PHENIX, with a z-vertex range between  $\pm 450\text{cm}$ .

### 2.4.3 EmCal (ERT) Trigger

The ERT photon trigger<sup>2</sup> consists of tower sums of either 2x2 disjoint or 4x4 overlapping arrays of towers. The geometry of the disjoint and overlapping towers are shown in figure 2.34. The overlapping tower sums are designed to prevent situations where the photon or electron strikes an edge in between some group of summed towers, by doing the sums in the group of towers around that edge. In those situations the energy is shared between the disjoint sum of tower energies, and hence there is an inefficiency in the trigger. The trigger turn-on became fully efficient at  $\sim 3.5$  GeV/c during Run03  $d+\text{Au}$  and at  $\sim 2.0$  GeV/c during Run03  $p+p$ .

---

<sup>2</sup>The ERT also has a RICH coincidence capability for triggering on electrons, a feature that wasn't used here.

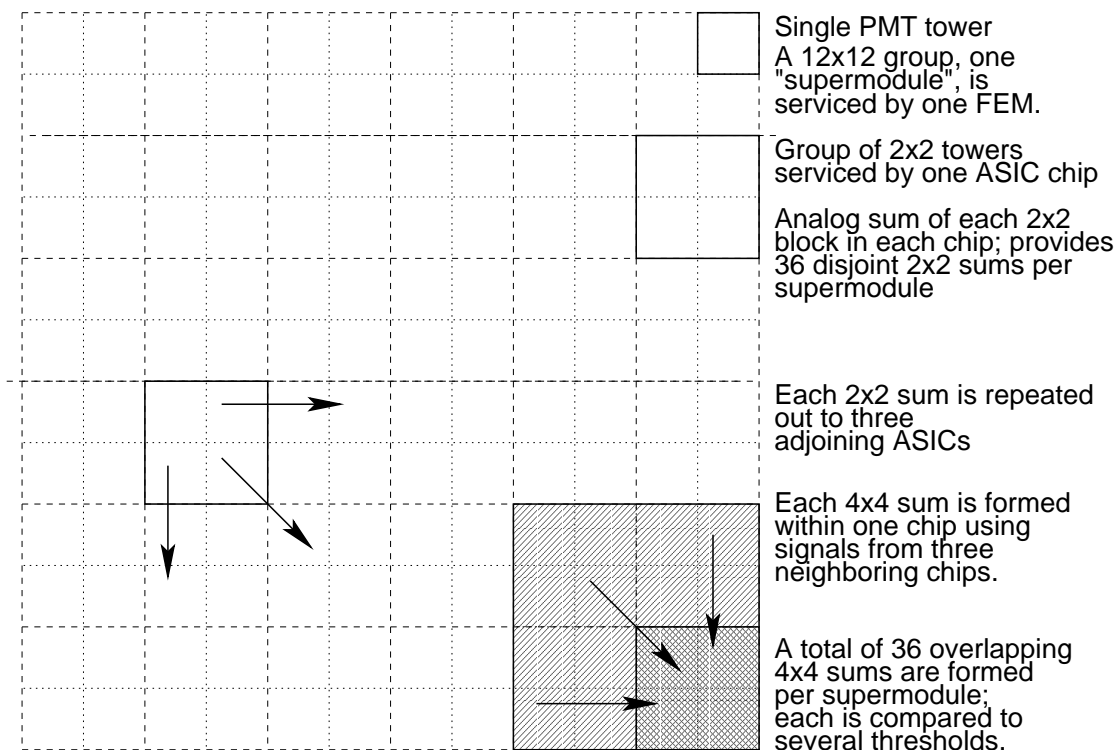


Figure 2.34: The Tower Summing Algorithm in the EmCal

# Chapter 3

## Data Analysis

The measurement of the differential yield  $\frac{1}{N_{trig}} \frac{dN^{assoc}}{d\Delta\phi}$  with the PHENIX detector, which might seem simple at first, is in reality a complicated analysis that requires careful consideration. Besides efficiency corrections, photon and hadron identification issues, there is a further complication from the need for acceptance corrections due to the limited size of the PHENIX detector, which is roughly the same size as the jets. In addition, there were significant run-to-run variations in acceptance and efficiency. In this chapter the techniques for producing fully acceptance corrected yields  $\frac{1}{N_{trig}} \frac{dN^{assoc}}{d\Delta\phi}$  from RHIC Runs 02 and 03 are detailed, and the final correlated yields  $\frac{1}{N_{trig}} \frac{dN^{assoc}}{d\Delta\phi}$  are shown.

### 3.1 Measuring Angular Correlations To Deduce Jet Properties

As mentioned previously, the high multiplicities in the environment of an heavy-ion collision make it difficult to reconstruct jets directly with any of the common techniques used in  $p+p$  or  $e^+ + e^-$ , such as the cone method or  $k_T$  algorithms. The main problem comes from trying to separate background particles from the fragmentation products of a jet.

However, in  $p+p$  collisions it is well known that at higher  $p_T$ , above  $\sim 2$  GeV/c, the contamination from soft processes should be significantly reduced compared

to particles from a hard perturbative QCD process. This was demonstrated in measurements of inclusive  $\pi^0$ -production made in PHENIX [9], where the invariant cross-section of  $\pi^0$  was found to be in extremely good agreement with next-to-leading order (NLO) calculations in pQCD. Given this, one could then perhaps use a high- $p_T$  particle as a jet tag, and look for the “jet-like” peak from the other fragments of that same jet. We will call the high- $p_T$  tag particle the “trigger” particle, and the other particles in the event the “associated” particles. Those “associated” particles that are fragments of the same underlying jet are called “jet associated” particles.

The trigger particle will (hopefully) serve as a proxy for the underlying jet, and one can then deduce information on jet properties by looking at the yield and shape of the associated particles. We say hopefully, because of course in heavy-ion collisions it may be that the trigger particles do not come from jets. But even in that case, the behavior of any correlations will tell us something about the production mechanisms for the particles at high- $p_T$ .

To be more precise, one can look for jet-like angular correlations by looking at the angular distribution of the associated particles in an event relative to the high- $p_T$  trigger particle. That is, one can plot the per-trigger differential yield in  $\Delta\phi$

$$\frac{1}{N_{trig}} \frac{dN^{assoc}}{d\Delta\phi} = \int \frac{1}{N_{trig}} \frac{d^3N^{ch}}{dp^3} dp_T d\eta \quad (3.1)$$

where  $\Delta\phi = \phi_{trig} - \phi_{assoc}$ , and this distribution is for triggered events.

There are many choices for the trigger and associated particles. We use photons as our trigger particles, and charged hadrons as our associated particles. The choice of photons is well-motivated, since they are easy to trigger on. Additionally, at moderate  $p_T$  ( $\sim 2\text{-}4$  GeV/c), they are dominantly from  $\pi^0$  decays, so that one can study meson/baryon differences by comparing these correlations with those from non-identified charged trigger correlations.

Moreover, at  $p_T$ ’s above  $\sim 5$  GeV there have been observations of a large excess of direct photons over decay photons [34], so that these correlations can provide information on  $\gamma - jet$  events. These events are considered to be the cleanest measure for jet-quenching, primarily because the photons are not thought to lose

much energy in the dense medium. This has two primary benefits. Since the direct photon leaves the collision region largely undisturbed, the photon  $p_T$  will be equal to the total jet  $p_T$  on the away side, except for effects from  $k_T$ . Additionally, quark or gluon jets have a strong bias since the jet needs to escape in order for it to be detected; direct photons do not suffer from this bias.

By looking at the structure of the associated production with a trigger particle, one can get a more detailed study of the production mechanisms at high- $p_T$  than what is available from measurements of inclusive spectra. One should be able to give much greater confidence that the particle production at high- $p_T$  is dominated by hard  $2 \rightarrow 2$  scattering. Also, one can look at the detailed modifications of jets and see how the medium affects the jet, and thereby gain information on the medium itself.

## 3.2 Run Selection

In two runs dating from winter 2001 to Spring 2003, RHIC collided beams of Au+Au, d+Au, and p+p. The first run, Run02, consisted of a long Au+Au run followed by a short p+p run. The second run, Run03, was a d+Au run followed by a p+p run. These three colliding systems are very important for systematically separating cold and hot nuclear effects. The run sets used in this analysis consisted of the Run02 Au+Au and the Run03 d+Au and p+p. While it is possible to use the Run02 p+p data set, the Run03 data set was better quality in terms of integrated luminosity and detector stability.

The main decisions driving run selection are good quality assurance, detector stability, and run length. These are decided since we need to eventually mix events, so that one has to mix between events that are from runs with the same geometric acceptance.

We look at the angular distributions of the charged tracks, and the photons, to look for any effects of differences in acceptance. Looking at figures 3.1- 3.3, one can see a large degree of variability during Run02 for the charged track acceptance, which

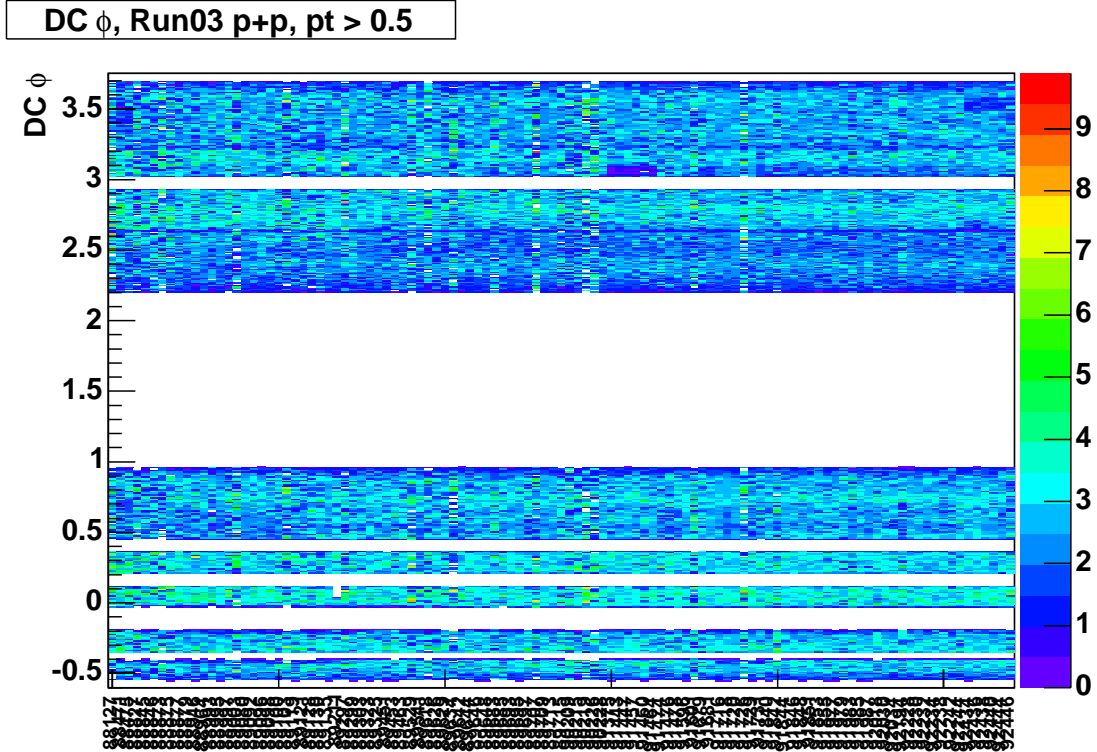


Figure 3.1: DC  $\phi$  vs. run, Run03 p+p

were primarily caused by high-voltage trips in the tracking and pixel chambers, and loose wires in the Drift Chambers. Despite this, due to our need for statistics in order to measure the differential yield,  $\frac{1}{N_{trig}} \frac{dN_{assoc}}{d\Delta\phi}$ , we kept all runs that were long enough and had enough acceptance to use event mixing techniques to estimate the acceptance. Of course, there is generally improvement from year to year so that during Run03 one can see that the detector stability was much better (figures 3.1 and 3.2).

### 3.3 Event Selection

Events are selected based on various Level-1 triggers. For the Run02 Au+Au run, we chose the minimum bias trigger, which is a coincidence between the BBC-LL1 and ZDC blue-logic triggers. For Run03 d+Au and p+p, the events selected were triggered by a coincidence with the ERT-Gamma triggers and BBC-LL1.

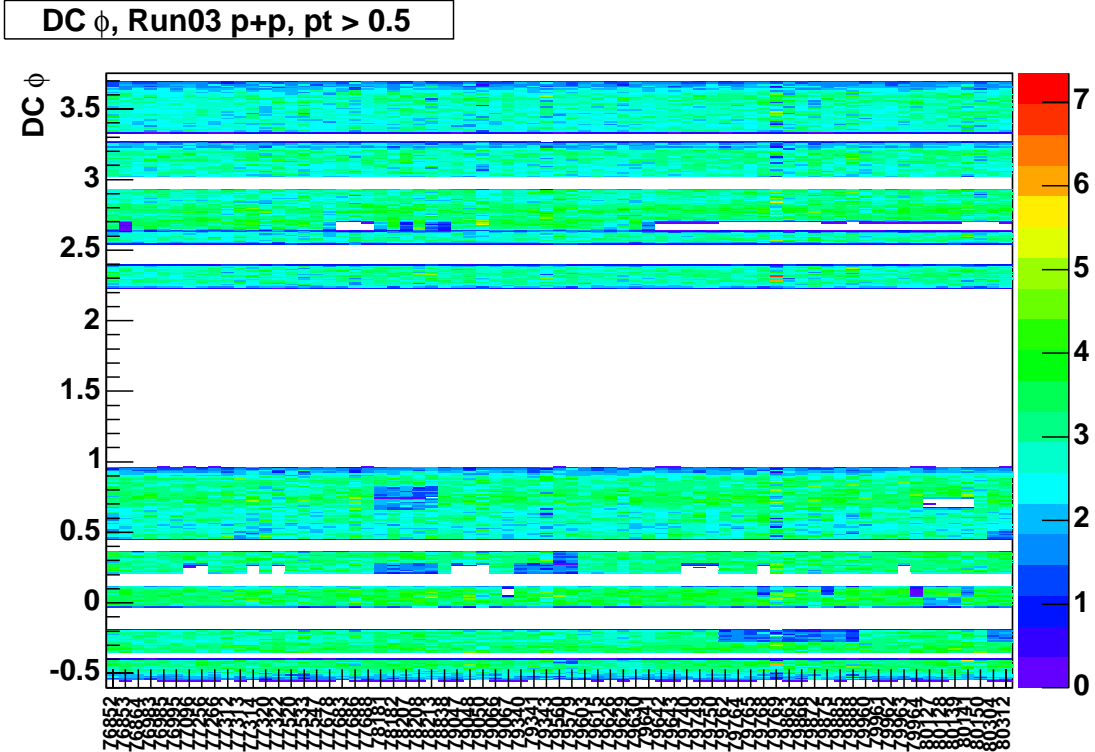


Figure 3.2: DC  $\phi$  vs. run, Run03 d+Au

In addition, a cut on the event vertex was made to reduce backgrounds from the magnet pole-tips. Only events with  $|z - vertex| < 30cm$  were selected.

### 3.4 Centrality Determination

Generally, determining centrality in heavy-ion collisions requires finding some observable which is monotonically related to the number of participants in the collision, which is then itself related to the impact parameter:

$$\text{experimental observable } C \leftrightarrow \text{num. participants} \leftrightarrow \text{impact parameter} \quad (3.2)$$

Hence, one can take an experimental observable, and determine the distribution of  $N_{part}$  which can produce this observable. From the distribution of  $N_{part}$  one can determine the distribution of impact parameters, usually via a Glauber calculation or Monte Carlo. So in this way, one can relate an experimental quantity to fundamental

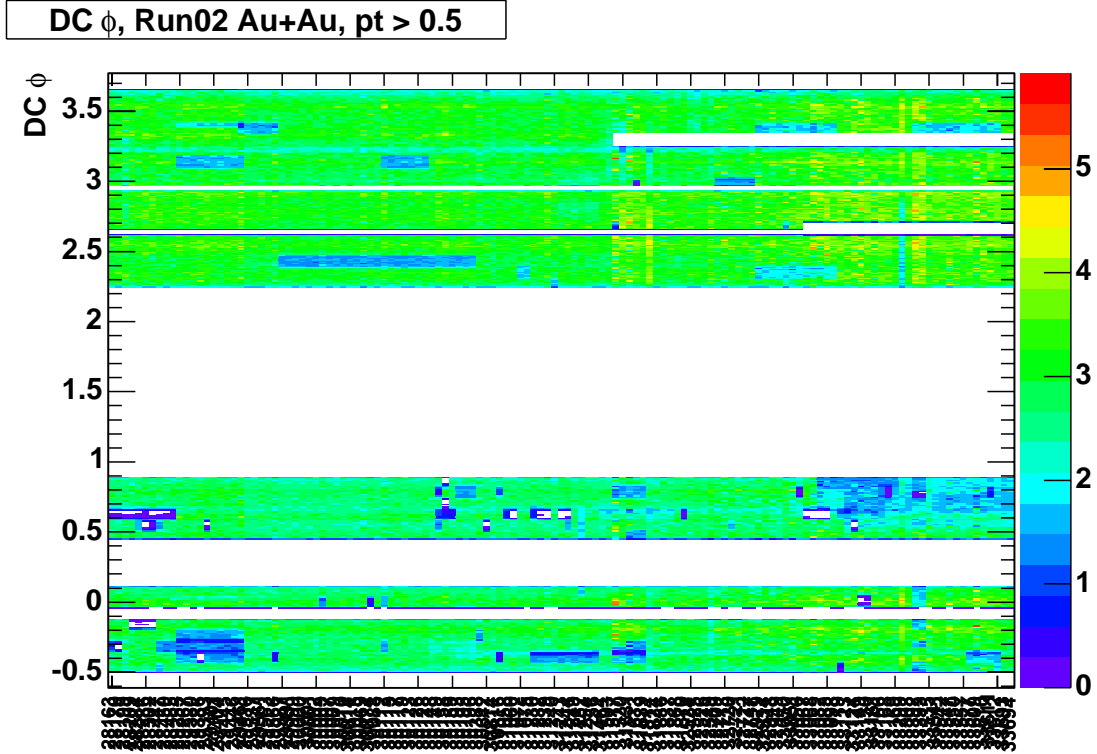


Figure 3.3: DC  $\phi$  vs. run, Run02 Au+Au

knowledge about the centrality of the collision, up to fluctuations in the distributions that connect the observable  $C$  to the number of participants and thence to the impact parameter.

An example of this is given by the number of particles measured in the BBC South (BBCS) during a  $d$ +Au collision. The number of particle hits in BBC South can be assumed to be proportional to the number of participants in the collision (since every participant produces an average number of particles at the BBCS rapidity). If one then assumes that the distribution of hits in BBCS follows a negative binomial, one can calculate the distribution of  $N_{part}$  that will produce a given number of hits in BBCS.

In figure 3.5, we show the charge distribution in BBCS for  $d$ +Au runs. The red slice corresponds to the top 20% most central events in  $d$ +Au, which is determined by taking the top  $20/88 = 22.7\%$  of the BBC triggered  $d$ +Au events. 88% is the

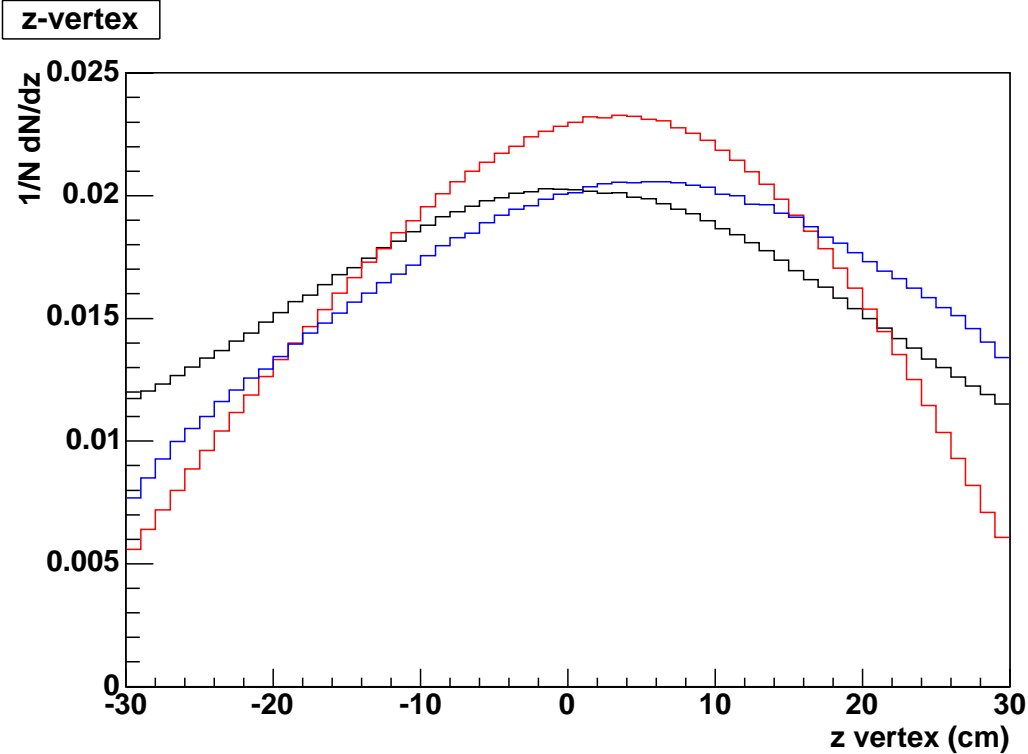


Figure 3.4: The Z-Vertex Distributions for  $p+p$  (blue),  $d+Au$  (red), and  $Au+Au$  (black), from the triggered events used in this analysis

efficiency of the BBC for  $d+Au$  events.

In  $Au+Au$  collisions PHENIX uses a “clock” slice of the two dimensional BBC energy vs. ZDC energy distribution. The main advantage of using the ZDC is that it can more sensitively measure  $N_{part}$  in the most peripheral collisions, allowing fine studies of turn-on effects with  $N_{part}$ . The experimental observable used to measure centrality is

$$cent\_clock = \arctan \frac{ZDC}{BBC - BBC_0} \quad (3.3)$$

The above plot has a “banana” shape because the ZDC energy deposition increases with decreasing centrality (due to lower loss of neutrons from collisions in central events), but then starts to decrease again when more and more of those forward free neutrons are coalesced into charged fragments that are then swept out by the DX Magnet just in front of the ZDC. Meanwhile, the BBC monotonically increases with

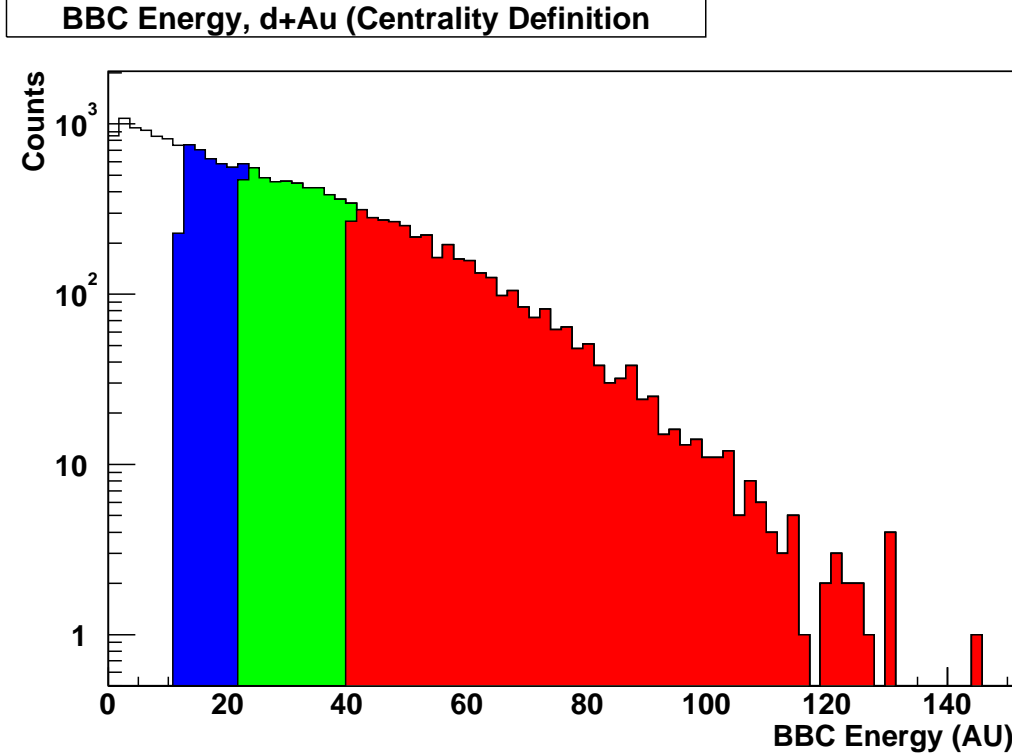


Figure 3.5: Centrality in  $d+Au$  as defined by BBC Energy deposition. The four slices in the distribution correspond to the four centralities in this thesis.

increasing centrality.

The overall efficiency of the minimum-bias triggers in each run (51.6% in  $p+p$ , 88% in  $d+Au$ , and 92.2% in  $Au+Au$ ) is evaluated via PYTHIA simulations in  $p+p$  (and checked with a vernier scan), a Glauber based Monte Carlo using the simple assumptions mentioned above for  $d+Au$ , and the Hijing [58] and JAM [51] event generators in  $Au+Au$ .

### 3.5 Trigger Particle Selection (Photon Identification)

In this analysis we concern ourselves with photons at high- $p_T$ . At these relatively high  $p_T$ 's (above 2.0 GeV) the background contribution can come from these sources:

- Charged Hadrons which shower ( $p$ ,  $p\bar{p}$ ,  $\pi^\pm$ , etc.)

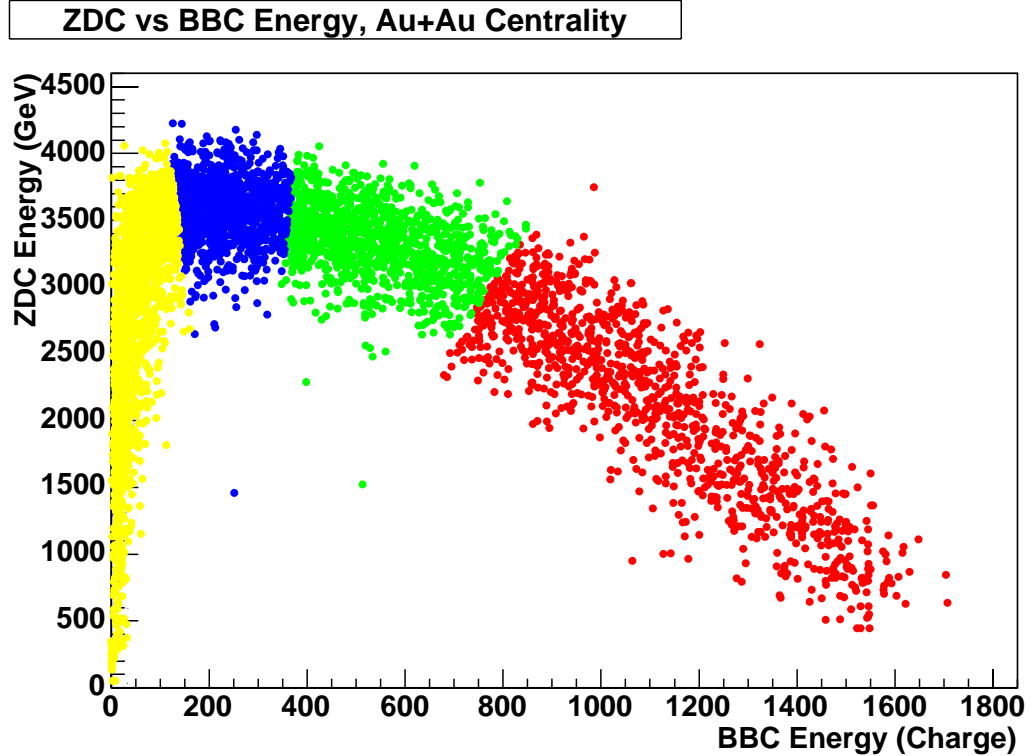


Figure 3.6: Centrality in Au+Au as defined by the BBC-ZDC Energy Correlation. The correlation variable is defined in eq. 3.3, and is called cent\_clock.

- High-Pt electrons/positrons
- Neutral Hadrons (n, nbar,  $K_L^0$ )
- Hot Towers
- Albedo

We believe that contributions from albedo are negligible. For photon identification we make the following cuts:

- $dispy$  and  $dispz < 0.25$
- $|tof| < 1.5$  (PbSc),  $|tof| < 1.8$  (PbGl)
- $pc3d < 20$

These cuts are explained in the following sub-sections. The pc3d charged particle veto cut removes  $> 90\%$  of the charged background. At the relatively high  $p_T$  for the trigger clusters, the tof cut doesn't seem to give very much photon/hadron discrimination. We believe this is partly because the timing resolution isn't quite that good, but more importantly, any hadrons which would deposit such high energy in a cluster would necessarily be at high  $p_T$  and thus come at near light speed times. The major remaining background comes from neutrons, anti-neutrons, and (to a much lower extent)  $K_L^0$ . We discuss the behavior of EmCal clusters on the cuts in the following sub-sections.

### 3.5.1 PC3 Charged Particle Veto

The charged particle veto variable pc3d is defined as the distance between the PC3 hit closest to the cluster and the projection of that cluster onto the PC3 plane. The distribution of pc3d is plotted in figure 3.7, where the foreground pc3d distribution is plotted in black. The red distribution is the “flip-and-slide” pc3d distribution; it is the accidental association of a cluster with a track and represents the distribution of neutral clusters (with some small contamination from charged clusters due to missing PC3 areas). The difference between the black and red histograms comes from charged clusters, and thus is a direct measure of the number of charged tracks in the sample of clusters. One thus has a way to quantitatively count the amount of charged contamination using the pc3d variable, as shown in figure 3.8.

The PC3 Veto Efficiency is generally very good, 95% or better. This is evaluated by calculating the ratio of vetoed clusters over non-vetoed clusters for half-sectors with no dead areas in PC3. This can be considered the maximal PC3 Veto Efficiency, and we normalize the other efficiencies to this value. The PC3 efficiency by itself is 99.5% [3]. The inefficiencies are dominated by dead areas in PC3 from HV or FEM problems.

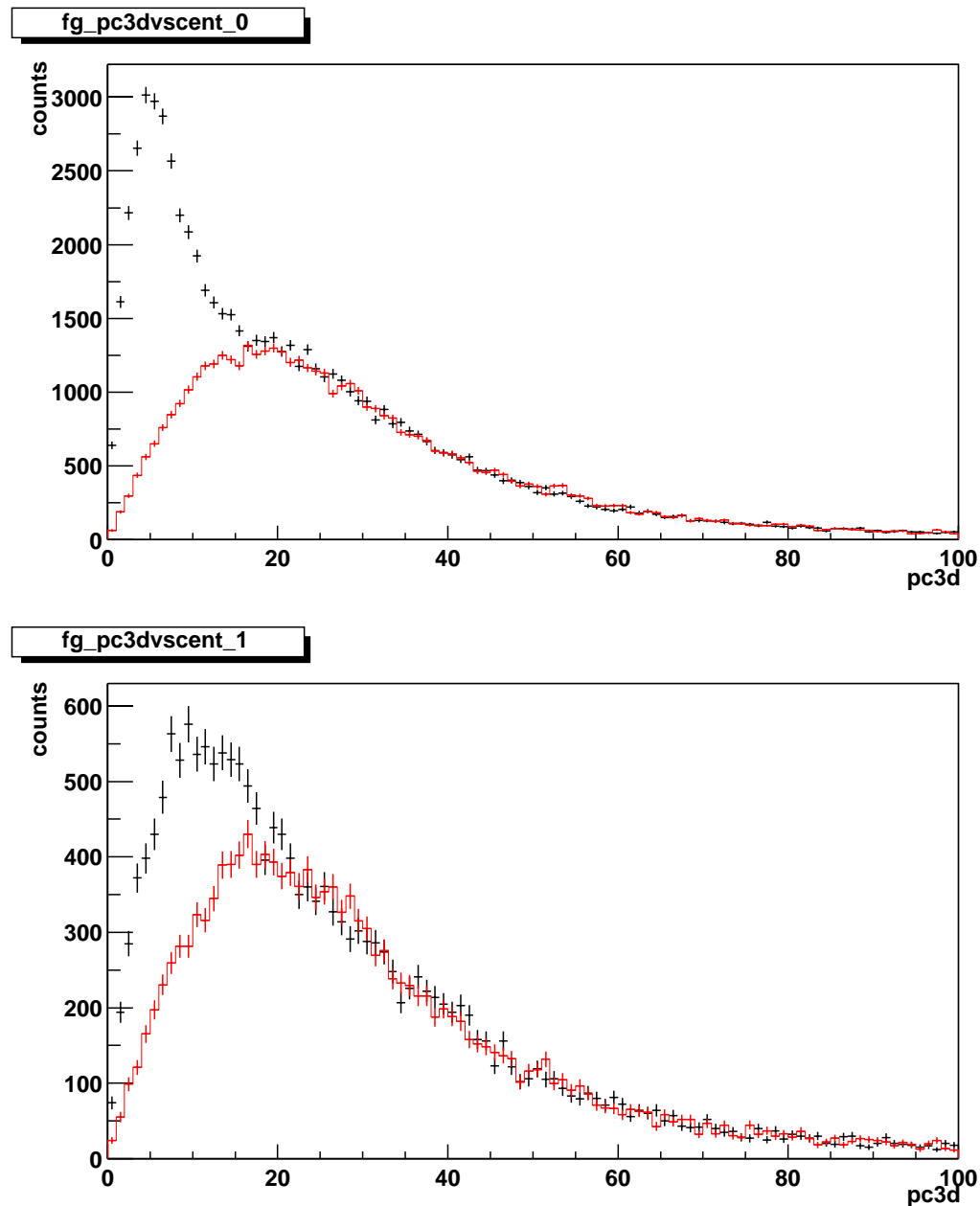
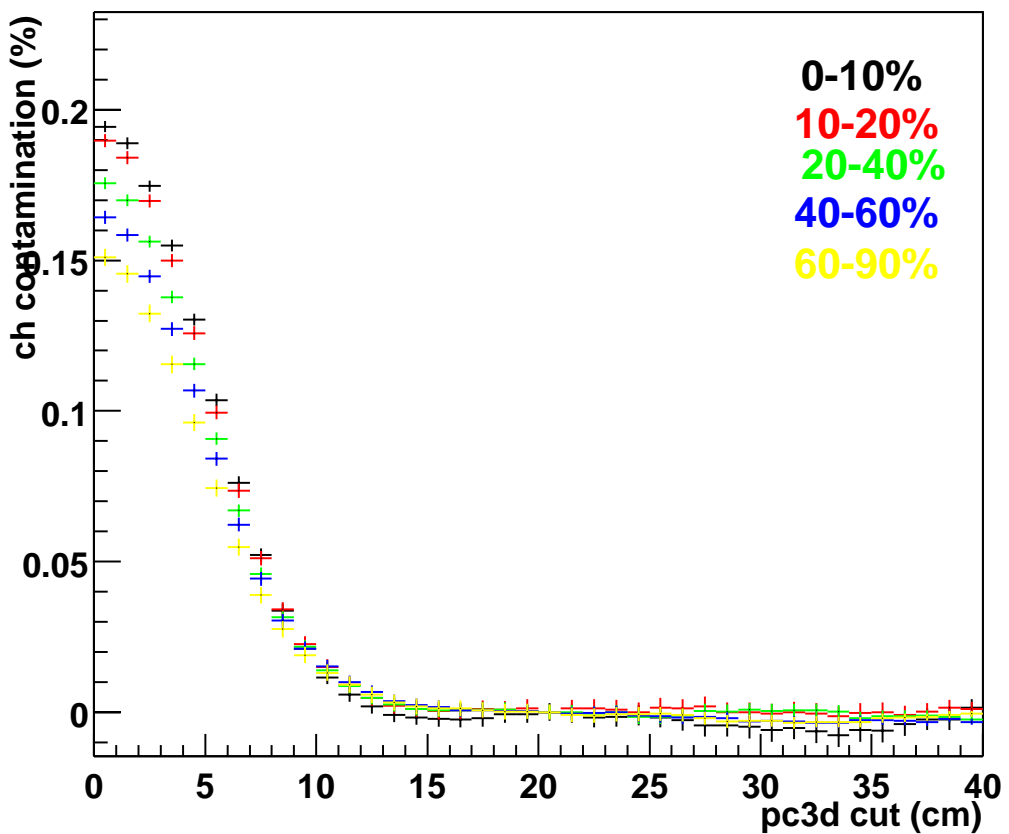
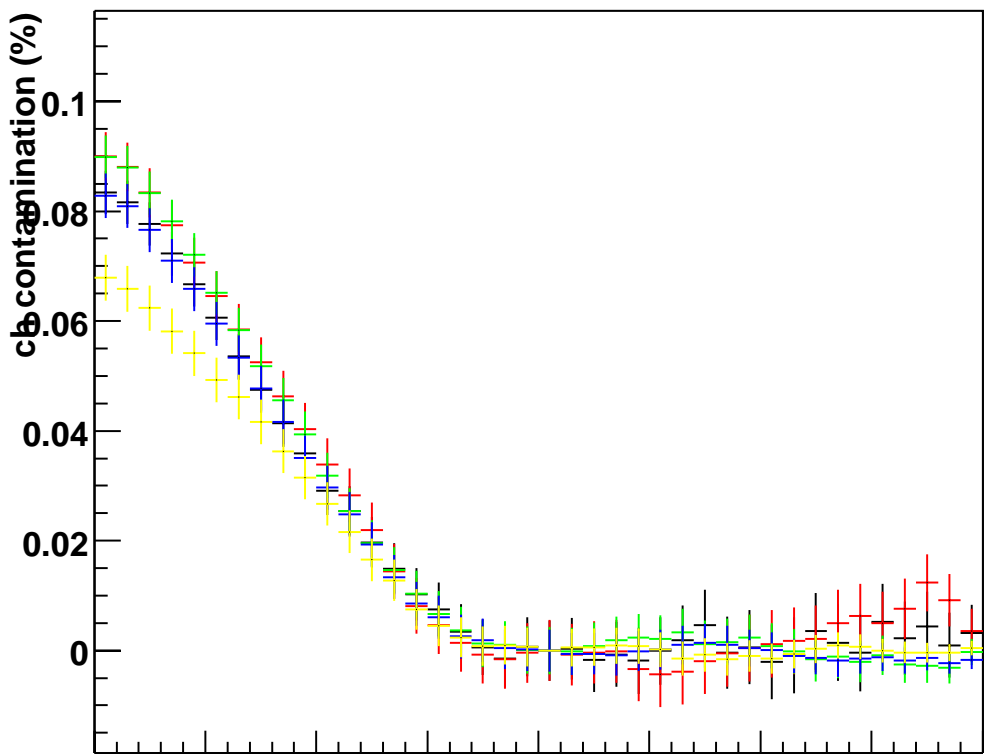


Figure 3.7: pc3d from the same event (black) and from mixed events (red) for PbSc (top) and Pbgl (bottom)

**fg\_pc3dvscent\_0****fg\_pc3dvscent\_1**

### 3.5.2 Time of Flight Cut

One unique feature of the PHENIX EmCal is the ability to measure the time of arrival for photons and hadrons. Since the likely backgrounds come from high- $p_T$  hadrons, the time-of-flight cannot give very good discrimination against hadrons, since the hadrons arrive at the EMC at nearly the speed of light, and also because the hadrons can penetrate partly through the EMC before it showers. Since the particle flight speed is faster than the shower can progress through the EMC, hadrons have a tendency to measure at an earlier time than photons or electrons.

### 3.5.3 Shape Cut using Shower Dispersion

There is a remaining background from fast neutral hadrons and from charged hadrons in regions where the PC3 veto is ineffective. This happens sometimes because of some HV or FEM problem, but also, there are areas of the PC3 which have no acceptance, and therefore can provide only limited veto coverage. These areas are where the PC modules join together, which are at the sector edges, and also down the middle of the central arms at  $\theta = 90^{\circ}$ .

To remove this remaining background, we use a cut on the cluster dispersion, which is the second moment of the energy, and is a way to separate electromagnetic showers from hadronic showers by the shape of the shower. The dispersion in the direction x along the towers is defined as

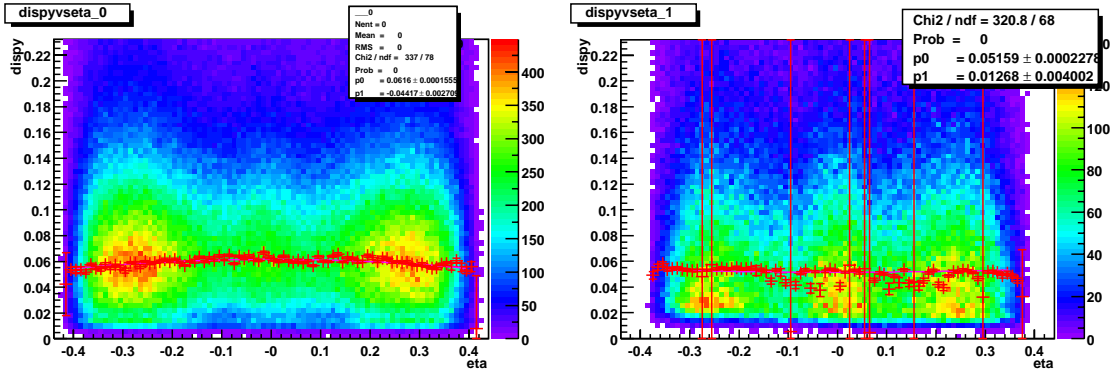
$$D_x = \frac{\sum_i E_i (x_i - \langle x \rangle)^2}{\sum_i E_i} = \frac{\sum_i E_i (x_i^2)}{\sum_i E_i} - x_{cm}^2 \quad (3.4)$$

where  $i$  runs over the towers in the cluster,  $x_i$  and  $E_i$  are the center position and energy of the  $i$ th tower, and  $x_{cm} = \sum_i E_i x_i / \sum_i E_i$  is the first moment of the energy of the cluster in the x-direction, and is analogous to the center of mass. The direction x is either along the horizontal direction (the z-axis) or the vertical direction (y-axis).

Since these are not continuous sums but rather are discrete sums over towers, there is a minimum dispersion of a cluster with two or more modules in the x-

Table 3.1: Correction parameters to the dispersion in the z direction.

type	[0]	[1]	[2]	[3]	[4]
PbSc	0.0575	0.00429	0.176	-0.148	3.92
PbGl	0.0454	-0.0111	0.451	0.545	22.7

Figure 3.9: Dispersion in y as a function of  $\eta$  for PbSc (left) and PbGl (right).

direction, which is

$$D_x^{min} = -(E_{cm} - E_R)(E_{cm} - E_L) \quad (3.5)$$

where  $E_R$  and  $E_L$  are the x-coordinates of the center of the two towers closest to the center of energy in the cluster. This  $D_x^{min}$  is the dispersion calculated from a cluster with just two towers in the x-direction (which one can show trivially after a little algebra). The dispersion used in our cuts is corrected for this “trivial” offset from 0. We use  $D_x^{corr} = D_x - D_x^{min}$  for our cuts.

There is also a correction due to the differences in showers at different angles of incidence. Due to the roughly cylindrical symmetry of PHENIX, the dispersion in the  $\phi$  direction has only a small dependence on  $\eta$ , while the dispersion in z has a strong dependence on  $\eta$ . In figures 3.9 and 3.10, we plot the dispersion as a function of  $\eta$  for the  $\phi$  and  $z$  direction, respectively. The dependence in the z dispersion is corrected out with a 4th order polynomial  $dispz' = \frac{[0]}{pol4(\eta)} dispz$ . The parameters of this fit are given in table 3.1.

Since the relative fluctuations in an high energy electromagnetic shower are small, the shower shape can be well described statistically. In studies of the dispersion cut

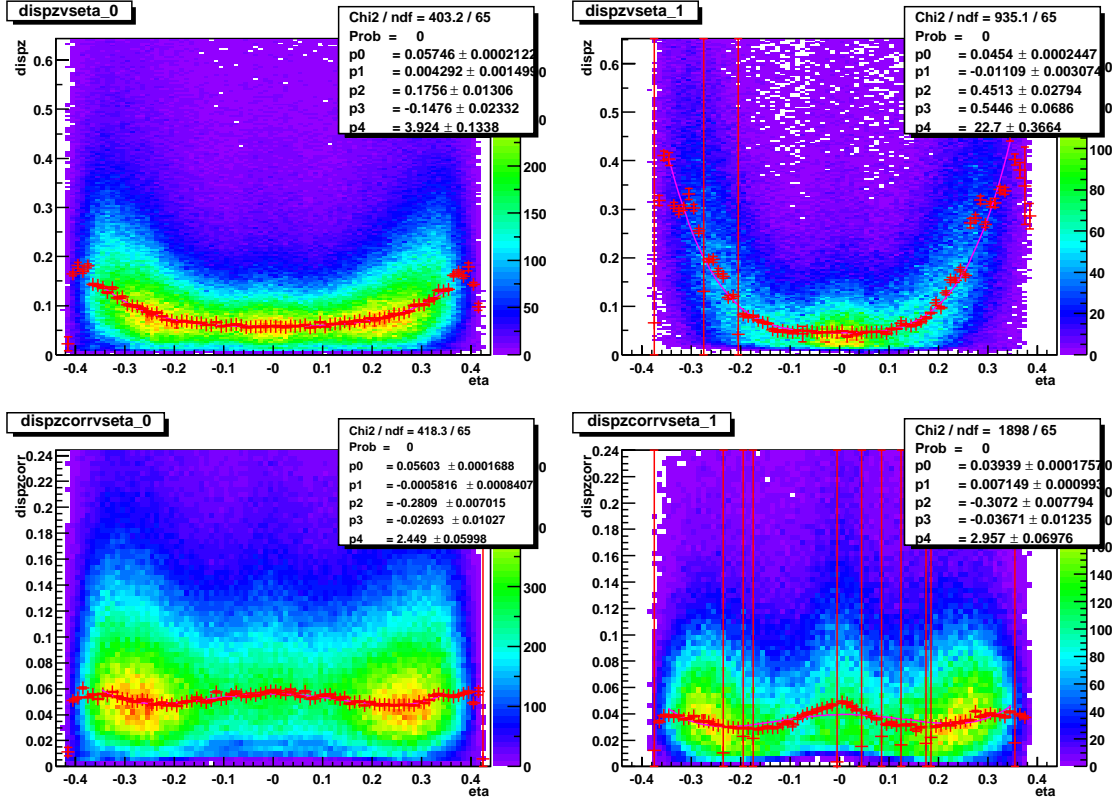


Figure 3.10: Dispersion in z as a function of  $\eta$  for PbSc (left) and PbGl (right). The top plots are uncorrected while the bottom has the  $\eta$  dependence corrected out.

with isolated photons in GEANT, we see that  $> 95\%$  of the photons are kept while cutting  $\sim 50\%$  of the hadrons, where the large uncertainty comes from the difficulties of simulating hadronic showers in Monte Carlo. In the data, overlaps of background particles with the primary shower will decrease this efficiency, so that the efficiency will drop with the multiplicity. However, the rejection of hadronic showers can only increase.

We can study the difference in the effect of the dispersion cut on photons and hadrons by looking at dispersion cut as a function of pc3d cut. (In fact, this is a nice way to study any cluster cut since one can estimate the charged contamination in the clusters as a function of the pc3d variable). In figure 3.11, we plot the maximum disp as a function of pc3d (where maximum is the maximum of either dispy or dispzcorr). At high pc3d we see a constant mean from a Landau fit to the

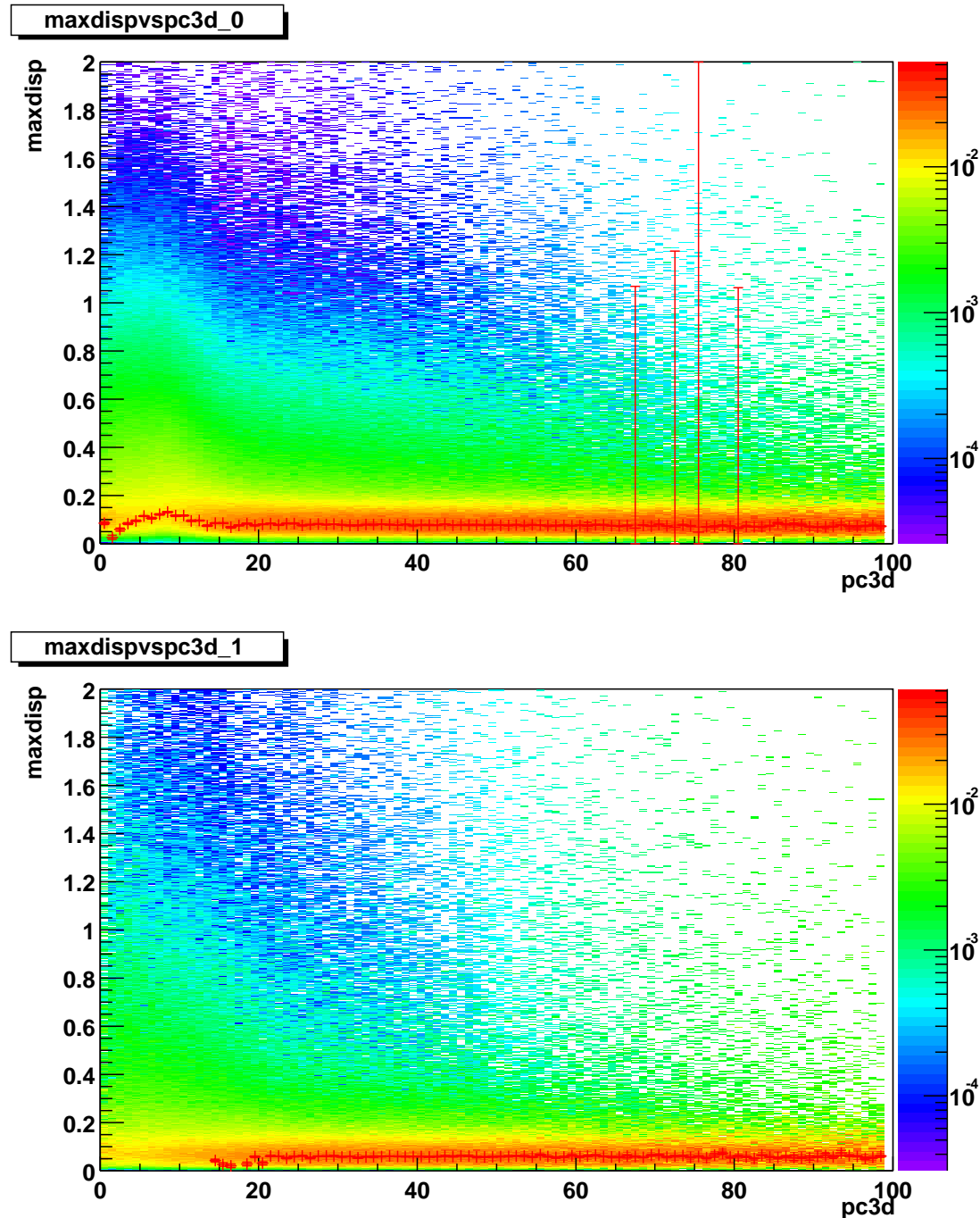


Figure 3.11: Maximum dispersion for photons as a function of pc3d for the PbSc (top) and PbGl (bottom).

### Graph

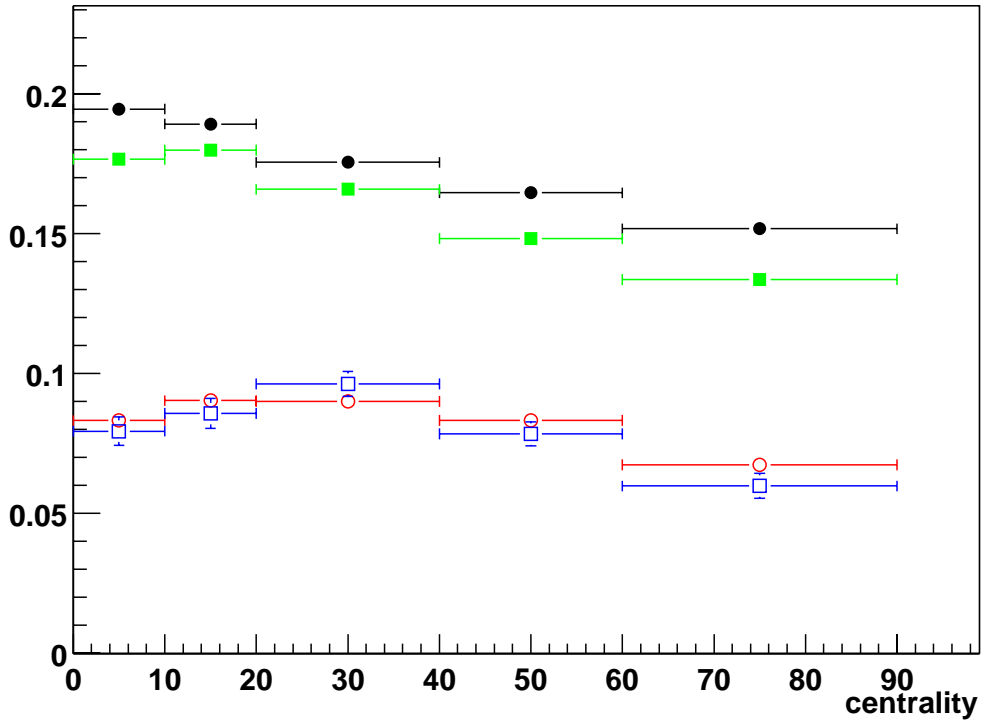


Figure 3.12: Fraction of charged contamination vs. pc3d cut for  $2.0 < p_T < 2.5$  GeV/c (circles) and  $p_T > 2.5$  GeV/c (squares) photons. The filled symbols are for PbSc, and the open circles are for the PbGl.

distribution pc3d distribution, which is the behavior expected if the distributions are dominated by photons. At low pc3d we see that the dispersion develops a large tail to high dispersion from contamination of charged hadrons that shower in the EmCal. This large tail changes the pc3d distribution and causes the Landau fit to fail at  $pc3d \lesssim 20$  cm.

The effectiveness of the dispersion cut on reducing hadron background is shown in figure 3.12, where we have plotted the fractional charged contamination after making all cuts except the pc3d cut.

Table 3.2: Maximum Estimated Neutron/Anti-Neutron Contamination to Photon Triggers

cent (%)	$\bar{p}/p$	$\frac{p+p}{h^+ + h^-}$	PbSc $n + \bar{n}$ (%)	PbGl $n + \bar{n}$ (%)
0-10	0.715676	0.307185	6	2
10-20	0.714281	0.288986	5	2
20-40	0.683842	0.265558	4	3
40-60	0.690543	0.22606	3	2
60-90	0.677838	0.174317	2	1

### 3.5.4 Neutron/Anti-Neutron Contamination

Since the neutron/anti-neutron yields are not measured, we make the assumption that they are the same as the proton/anti-proton yields (which are obtained from the PHENIX measured proton/anti-proton spectra). We then calculate the contamination of  $n/n\bar{n}$  in the photon trigger by taking the measured charge contamination from fig 3.12 and the proton/anti-proton ratios in table 3.2:

The  $p+p$  and  $d+Au$  contamination is very similar to the most peripheral  $Au+Au$  bin.

### 3.5.5 Warm/Hot Towers

One problem that can occur in the EmCal is sparking in the PMT or electronics noise that causes a particular tower or group of towers to fire even when there is little or no energy deposited in the tower. Another problem occurs when the timing electronics are bad, so that no reasonable TOF is measured. These are called warm or hot towers; the subtle difference between the two is that a hot tower is almost always gives a very bad reading, while a warm tower may sometimes give a bad reading, but may also sometimes give a good reading. These noisy towers can influence the correlation result by introducing fake photons. Since these noisy towers are not going to be correlated with a jet, it has no associated hadron production nearby, and hence will lower the measured jet associated yield.

Hot towers are identified by scanning for towers that fire more often than one

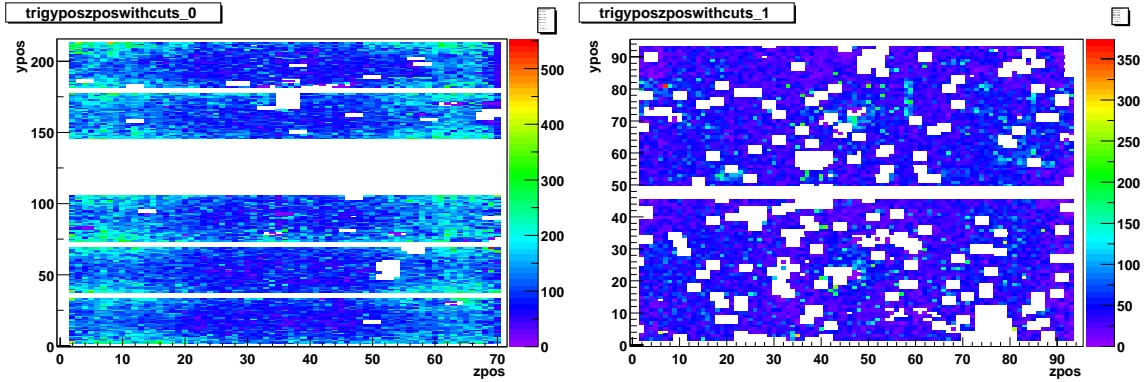


Figure 3.13: Central Tower Positions of Trigger Photons, Au+Au Run02

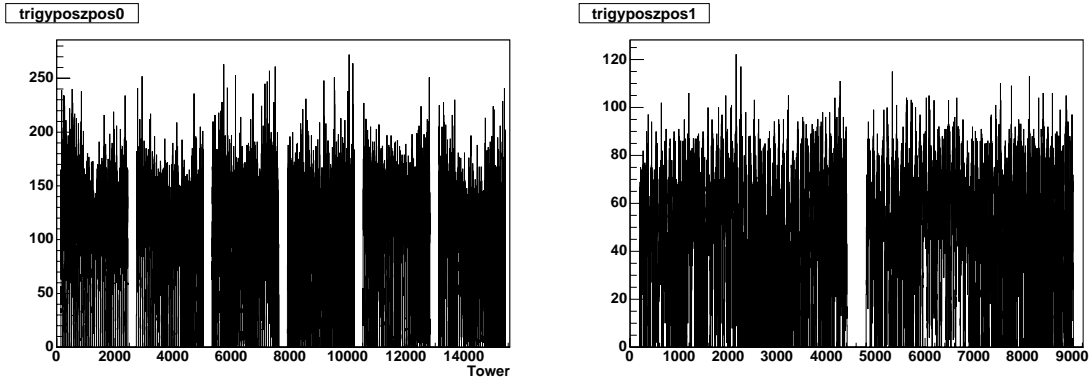


Figure 3.14: Central Tower Positions of Trigger Photons, Run03 p+p. Left, PbSc, Right, PbGl

would predict probabilistically. For each tower, we plot the number of times that tower registers an energy reading within some range, and then look for towers which have a number of hits larger than what one would expect given the fluctuations. The distribution followed by the hit distribution is estimated to be a poisson or negative binomial distribution.

We exclude all clusters which have a bad tower within a  $3 \times 3$  grid. The size of this grid is set by the Moliere radius of an electromagnetic shower in our calorimeter. After all these cuts, we find the percentage of minimum-bias events with a trigger photon greater than  $p_T = 2.0$  GeV is 1.7%.

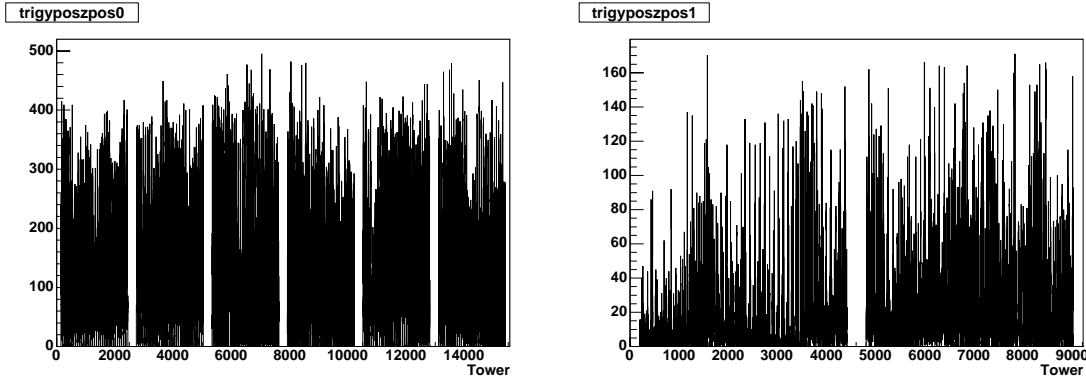


Figure 3.15: Central Tower Positions of Trigger Photons, Run03 d+Au, Left, PbSc, Right, PbGl

### 3.6 Associated Particles Selection (Charged Hadrons Selection)

The charged hadron sample consists of

- Charged hadrons from the vertex
- Products from the weak decays of hyperons and strange mesons
- Conversion electrons (and a few prompt electrons)
- Combinatorial Background from matching cuts

We are interested in the charged hadrons from the vertex, and the other contributions are background which we need to remove. The products from the weak decays can cause the momentum to be mis-measured, but these effects only begin to be significant above  $p_T \sim 4$  GeV/c.

The cuts to select clean charged tracks from the vertex consist of taking tracks measured in the Drift Chamber, and choosing only those that match well to hits in PC1 and PC3. Additionally,

- good quality match of DC track to PC1
- matching cuts of 2.5 sigma in PC3

- RICH  $n0 \leq 0$ , where  $n0$  is the estimated no. of PMT's fired in the RICH by the track.
- DC  $|zed| < 75$ , where  $zed$  is the z position of the track at the DC.

The RICH  $n0$  cut is used to remove some conversion and most of the real electrons, while the DC  $zed$  cut is used as a fiducial cut to ensure good tracking efficiency and reduction of background. The matching cuts of tracks in the DC with hits in PC1 and PC3 removes most of the ghost tracks.

### 3.7 Estimating the Acceptance Function

The acceptance function  $Acc(\Delta\phi)$  is the probability for having two particles separated by an azimuthal angle  $\Delta\phi$  both fall in the detector acceptance. We use event mixing to estimate the acceptance function using deep buffers of trigger and associated particles for the mixing. In order to remove any phi bias in the acceptance from our acceptance estimate we select the charged tracks from minimum bias events in both p+p and d+Au, since the BBC-LL1 trigger is approximately phi-symmetric.

Since we are interested in going to as low in associated  $p_T$  as possible, we studied the effect of  $p_T$  on the acceptance. In figure 3.17 we show the PHENIX  $\phi$  acceptance as a function of  $1/p_T$ . As one goes to lower  $p_T$  particles are bent more, and hence the acceptance changes. For photons the acceptance does not change since they are not bent by the magnetic field. So at lower  $p_T$ , the particles near the photons are swept out, reducing the acceptance near the photon, and increasing the acceptance at  $90^\circ$  to the trigger photon. We can see the effect of this in figure 3.16, where on the left we have plotted the acceptance function for different  $p_T$ . On the right, we plot the acceptance as function of  $p_T$  for three  $\Delta\phi$  bins. We see that at around 1 GeV the acceptance function becomes independent of  $p_T$ .

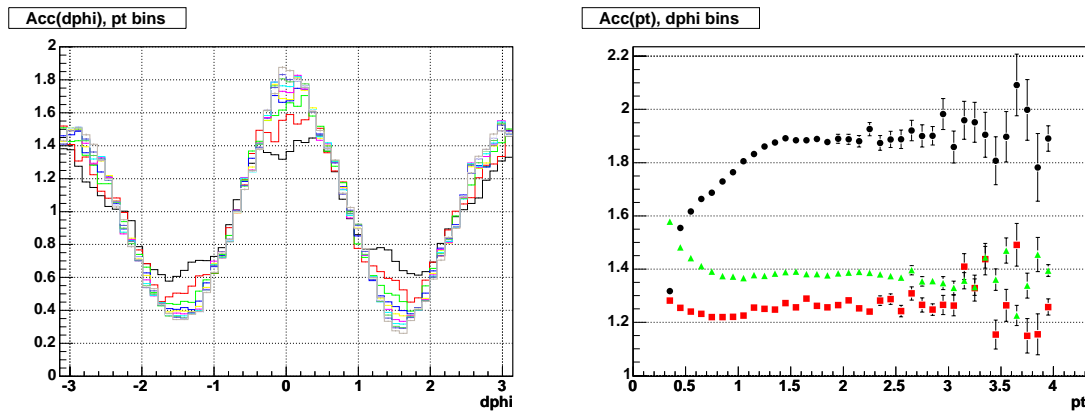


Figure 3.16: Left: The acceptance function for various  $p_T$  bins, from 0.3-0.4 (black), 0.4-0.5 (red), and so on. Right: The acceptance function for three  $\Delta\phi$  bins vs  $p_T$  } for Run03 p+p (left) and d+Au (right). Red is for the bin centered at  $90^\circ$  and is 3 times the actual acceptance value, green is the bin centered at  $180^\circ$ , and black is for the bin centered at  $0^\circ$ .

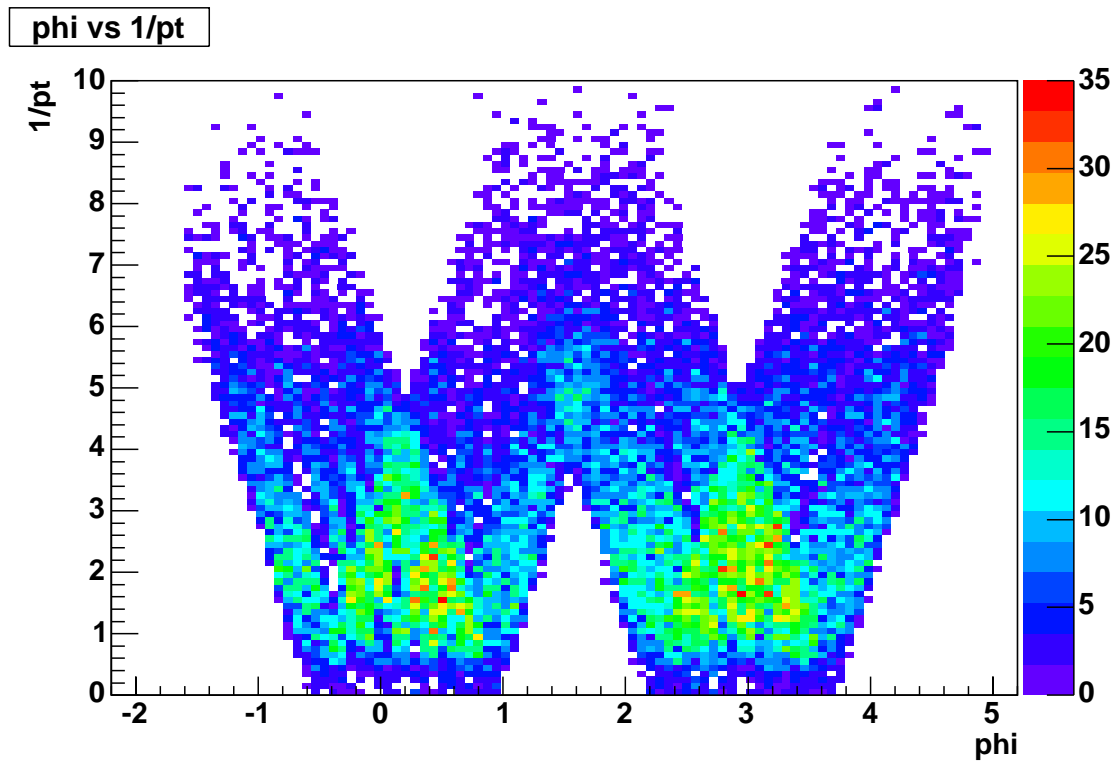


Figure 3.17: The acceptance in phi vs.  $1/p_T$

## 3.8 Charged Track Efficiency Calculations

The efficiency corrections for the finite geometrical acceptance, detector response, and tracking inefficiencies are done using single particle Monte Carlo. As input, a known number of single pions, kaons, and protons are thrown into the detector acceptance, and run through PISA, which is the PHENIX Monte Carlo code. The Monte Carlo code has been tuned so that the performance matches that of the detector, by specifying that the Monte Carlo and the real data have the same dead wires or channels in the DC and PC, checking that the locations of the detectors are similar, and checking that the projected DC track matching to PC1 and PC3 is the same. We then perform our analysis on the simulated data using the same track identification cuts as on the real data analysis.

Since we know the input distributions, we can take the ratio between the particles that survive our cuts to that from the input distribution to determine the efficiency as a function of  $p_T$  (see figure 3.18). Due to the different effect on the efficiency for the different particle types from decays, the input particle particle spectrum is weighted by particle id, so that distributions will reflect the spectrum measured at RHIC.

There were significant run to run variations in the detector response. Thus, this Monte Carlo matching was done for a fiducial run, and then the efficiency for each run was estimated by measuring the average charged track multiplicity, and corrected to the efficiency of the fiducial run. That is, we use a Monte Carlo to determine the efficiency of our fiducial run in Au+Au, and then used the averaged charged multiplicity in the other Au+Au runs to correct run by run for efficiency changes in the tracking detectors (see figure 3.19).

Since one cannot match the charged multiplicity across different run types (eg, between Au+Au and  $p+p$ ), we used measurements of the DC  $\phi$  vs. DC zed (see fig. 3.20), where DC  $\phi$  and DC zed are the  $\phi$  angle and z location of a track at the DC reference radius. We then look for regions of high efficiency in the DC  $\phi$  vs. DC zed plot, and which were high for a given fiducial run. We then scale

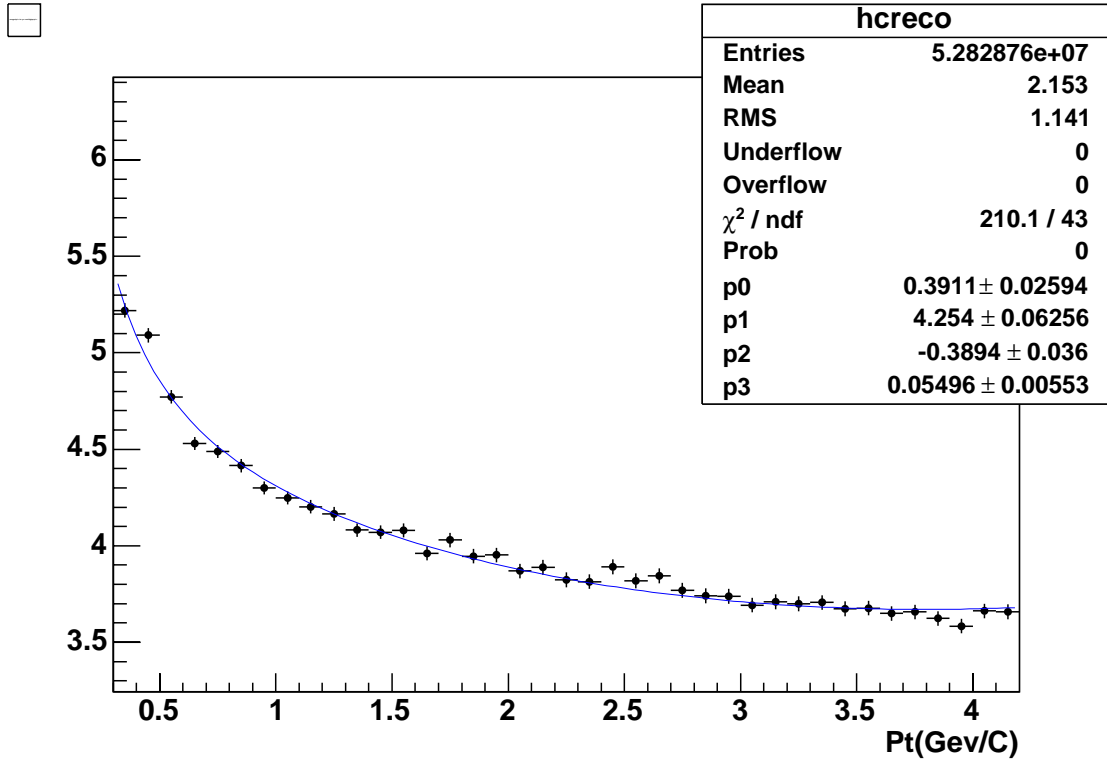


Figure 3.18: The efficiency correction function  $1/\epsilon$ , for a detector with full  $2\pi$  coverage and  $|\text{eta}| < 0.3$ .

the track distributions to match this given DC  $\phi$ , DC zed region between  $p+p$  and  $d+\text{Au}$ , and use the averaged efficiency from the distributions to determine the loss due to differences in dead and inefficient areas across  $p+p$  and  $d+\text{Au}$  runs. We also use this matching technique to connect to our fiducial  $\text{Au}+\text{Au}$  run. From this, we can estimate the efficiency for all runs in our sample. An illustration of the DC  $\phi$  matching between runs is plotted in figure 3.21. The estimated uncertainty in relative efficiencies from this procedure is  $\pm 5\%$ .

### 3.8.1 Efficiency Losses in High Multiplicity Events

The previous efficiency correction function takes care of losses in the detector from dead and missing areas, as well as the tracking efficiency of live areas. However, those simulations of a single particle traversing the detector don't account for the efficiency losses that can occur at high multiplicities, when interference from other

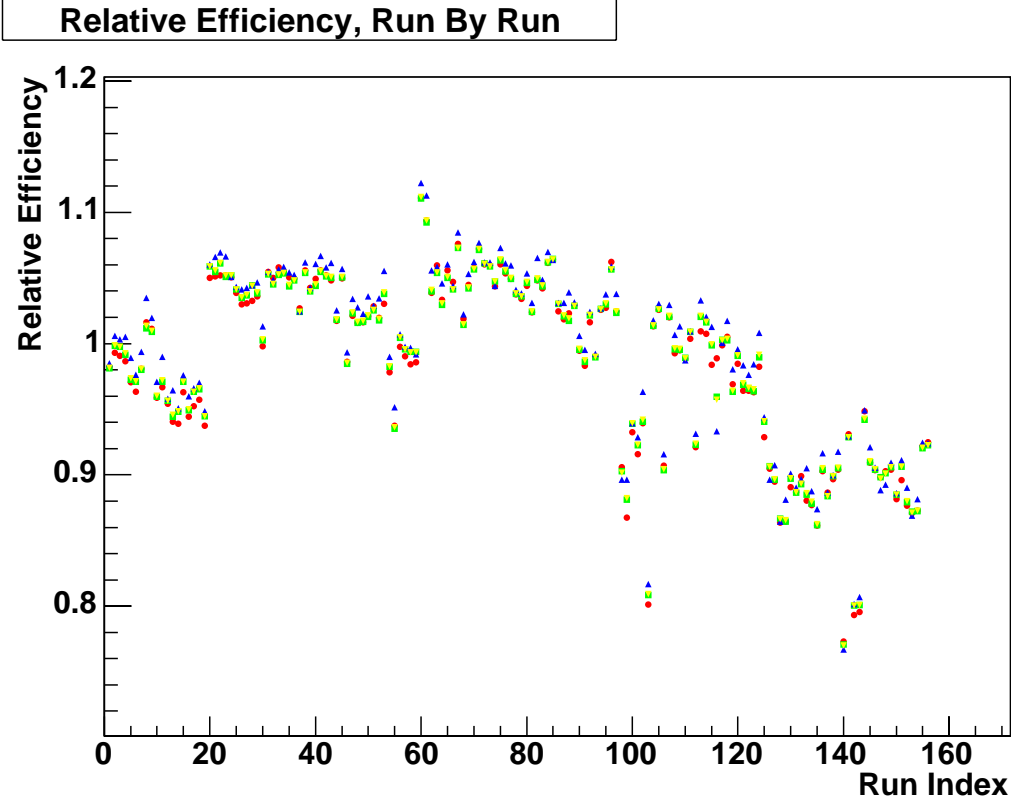


Figure 3.19: Run by Run Charged Track Efficiency Differences, as determined from  $\langle N_{ch} \rangle$  for different  $p_T$  bins, during Run02 Au+Au.

particles can reduce the effectiveness of a detector. There are many possible causes of these inefficiencies. As an example, in a high multiplicity event, there are many particles and many of the wires in the drift chamber will fire. Since there are so many wires hit, the probability that the wrong hits are incorrectly associated to a certain track rises. It is even possible in some cases that a group of hits will accidentally look like they come from a track, and are then associated to a track that never existed (these are hence called ghost tracks).

In these cases, the tracking algorithm will search for the best fit to the correctly associated and also mis-associated hits, and thus reconstruct incorrectly the particle track. This could, for instance, lead to a wrong projection to the outer detectors, and thus not match any clusters in PC3. We would then not reconstruct this track when looking for a match to a PC3 hit.

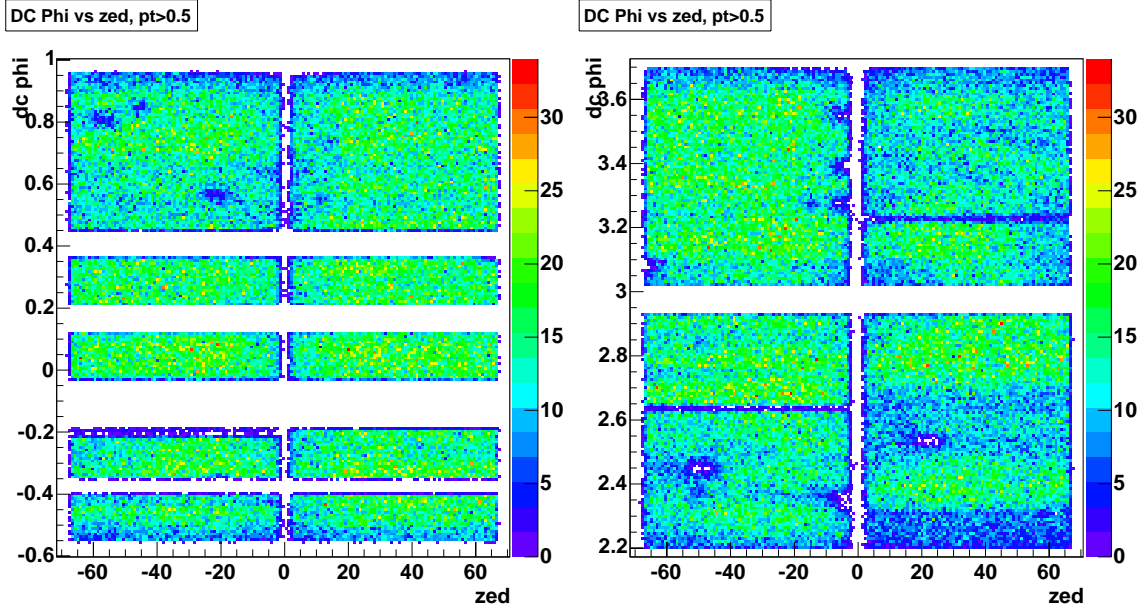


Figure 3.20: The DC  $\phi$  vs DC  $zed$  distribution for accepted tracks. On the left is the East Arm, and on the right is the West Arm. The gaps in  $\phi$  are due to missing HV or broken wires. The gap at  $zed = 0$  comes from a combination of the titanium support bar in the DC, and from the gap in between two PC half-sectors.

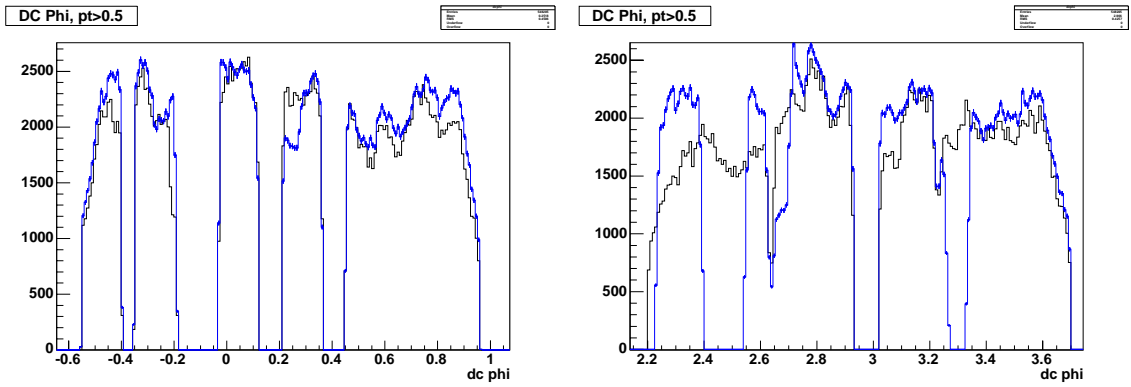


Figure 3.21: The DC  $\phi$  distribution for accepted tracks, for the West (left) and East (right) Arms. Once a region of high efficiency in  $\phi$  is matched, the ratio of the integral of the above distributions gives a measure of the relative efficiency between the two runs. Note that the vertical scale is in arbitrary units.

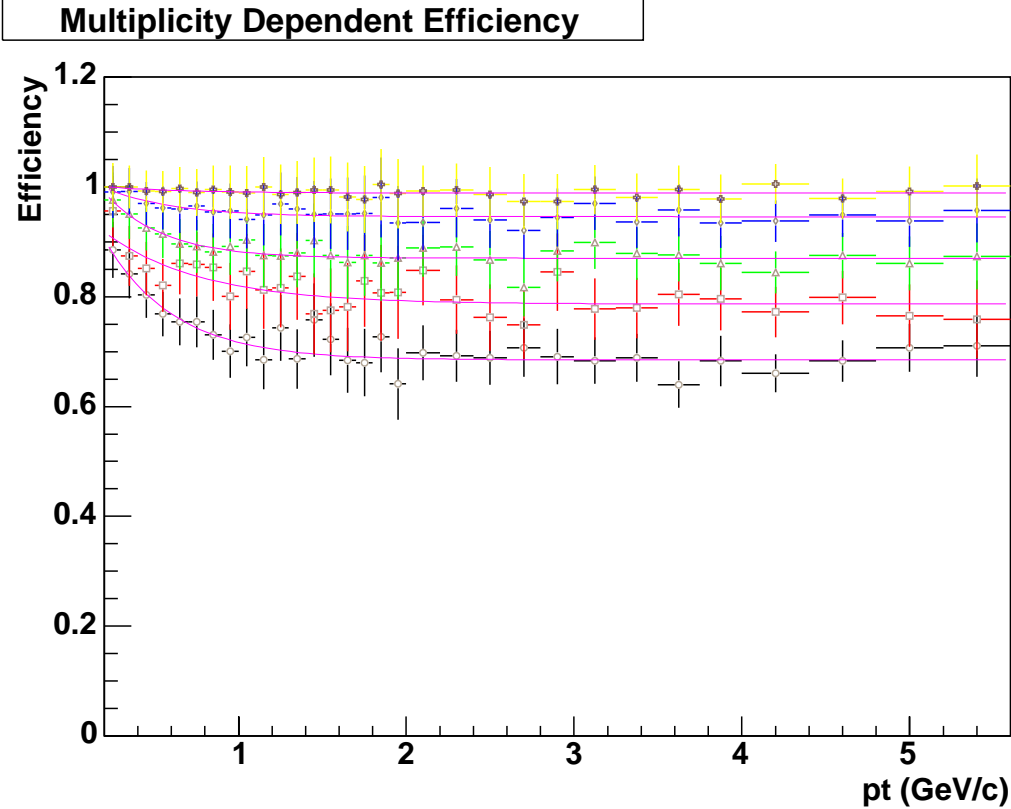


Figure 3.22: The multiplicity dependent efficiency as a function of  $p_T$  for different centralities in Au+Au. There is about a 70% efficiency loss in the most central Au+Au events.

As another example, one might have a track that follows nearly the same path as another track. The Combinatorial Hough Transform will be unable to separate two tracks closer together than the grid spacing in  $(\phi, \alpha)$ , so only one of the two tracks will be reconstructed.

There are many other possibilities that might result in efficiency losses, depending on the detectors used, cuts made, and how well the reconstruction software performs. In any event, a general procedure to estimate these efficiency losses with multiplicity is to embed single particle tracks from Monte Carlo into real events, and evaluate how many of these single known tracks are properly reconstructed. One can even study how the tracks are modified. In figure 3.22, the efficiency as a function of  $p_T$  for the five centrality bins used in this thesis are given.

### 3.9 Corrections for Particles that Fall out of Eta Acceptance

Our analysis corrects the yield to that measured by a perfect detector with an acceptance of  $|\eta| < 0.30$  and full  $2\pi$  coverage in  $\phi$ , or  $\Delta\phi$ . In general, jets have a wide range of rapidities, but due to our trigger requirement, we select those near-side jets that fall into our acceptance, while the away side jet has a nearly flat rapidity distribution, since in general the hard-scattering selects a range in  $x_1$  and  $x_2$ . For a detector with perfect  $\Delta\phi$  and  $\Delta\eta$  acceptance, one would see in the  $\Delta\phi - \Delta\eta$  plane a cone of fragments around the trigger particle and a broad flat distribution in  $\Delta\eta$  centered along the line  $\Delta\phi \sim \pi$ .

Our detector sits at a fixed  $\eta$ , so that in the  $\Delta\phi - \eta$  plane, one sees the distribution for all the jets that fall inside our given  $\eta$  window. This is illustrated in figure 3.23, which shows the fragmentation distribution in  $\eta$  for a near side jet triggered by a photon at  $\eta_{trig}$ . In this case the particles with  $\eta < x_L$  and  $\eta > x_R$  will fall out of our  $\eta$  acceptance. One can then calculate the yield that falls out of the eta acceptance, since it is simply the convolution of the  $\eta_{trig}$  distribution with the parts of the jet distribution that fall out of the acceptance. The  $\frac{dN}{d\eta_{trig}}$  distribution has been measured to be flat, and we assume that the jet distribution factorizes in  $\Delta\phi$  and  $\Delta\eta$ , so that  $J(\Delta\phi, \Delta\eta) = \Phi(\Delta\phi)H(\Delta\eta)$ . Under these assumptions, one can calculate the correction as

$$\text{fraction lost } f = \int_{-\eta_{max}}^{\eta_{max}} \frac{dN}{d\eta_{trig}} \frac{1}{2} \{ \text{erfc}(x_R) + \text{erfc}(x_L) \} d\eta_{trig} \quad (3.6)$$

where  $x_R = (\eta_{max} - \eta_{trig})/\sqrt{2\sigma}$ ,  $x_L = (\eta_{max} + \eta_{trig})/\sqrt{2\sigma}$ , and  $\text{erfc} = 1 - \text{erf}$ . The correction is plotted in figure 3.24.

The effect of the particles falling out our  $\eta$  acceptance is almost the same as what is measured by the acceptance function  $\text{Acc}(\Delta\eta)$ , ie, the acceptance function is proportional to the probability that a particle at a  $\Delta\eta$  will be accepted. The one discrepancy comes from the particles that fall out of the limits of the acceptance function, where  $\text{Acc}(\Delta\eta)$  is zero, ie, it has no information.

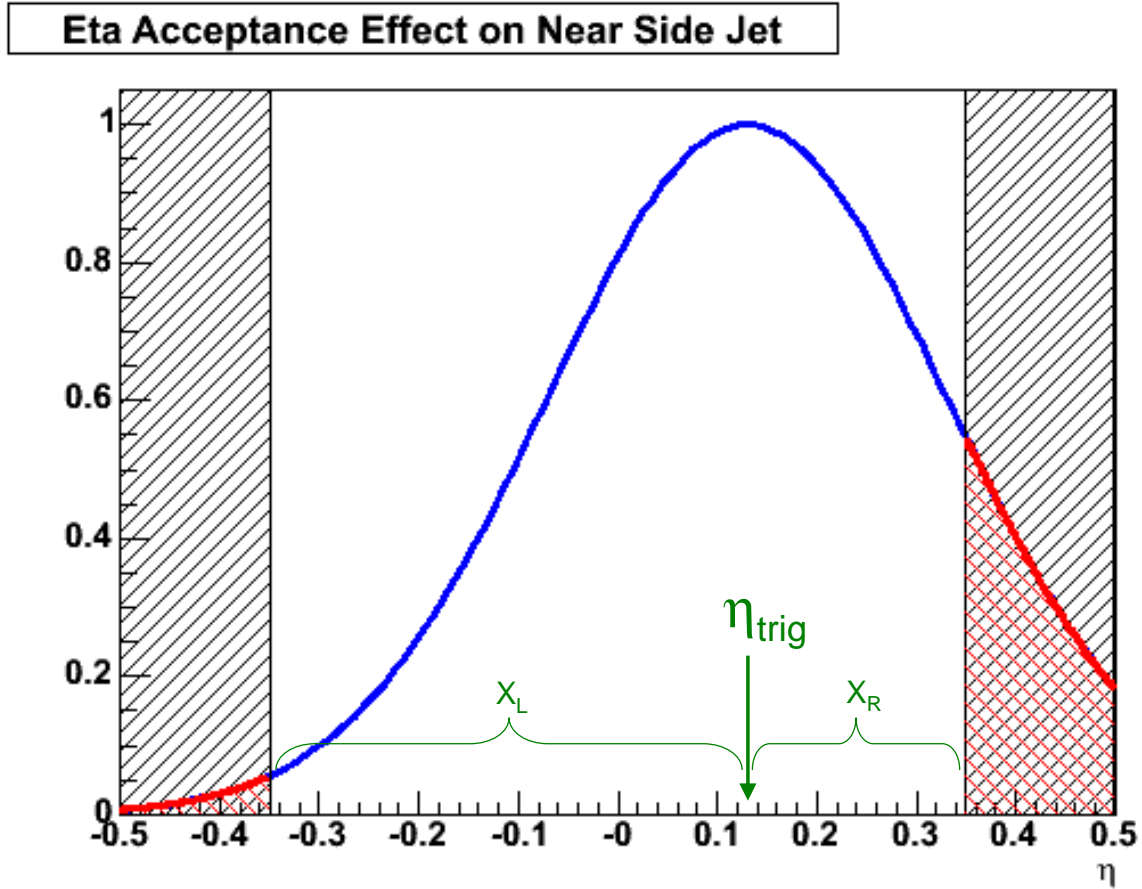


Figure 3.23: The PHENIX acceptance in  $\eta$  for a jet with a gaussian profile.

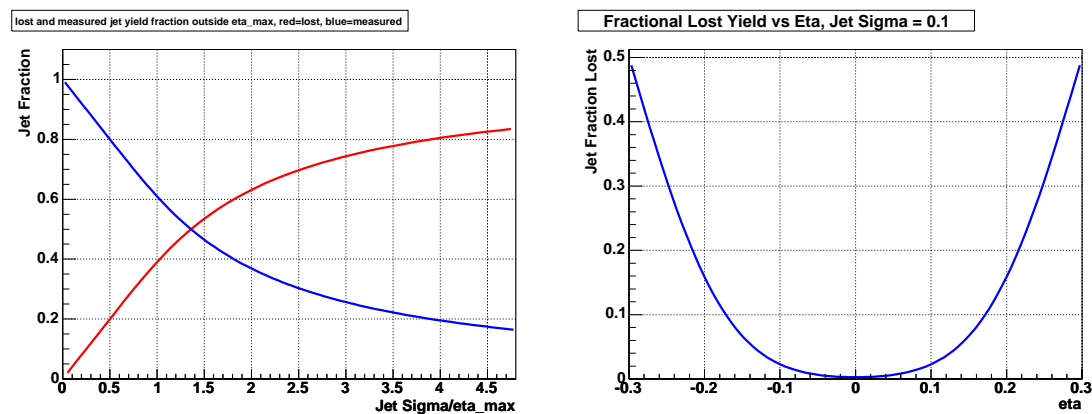


Figure 3.24: The p+p and d+Au near and far jet widths as a function of centrality

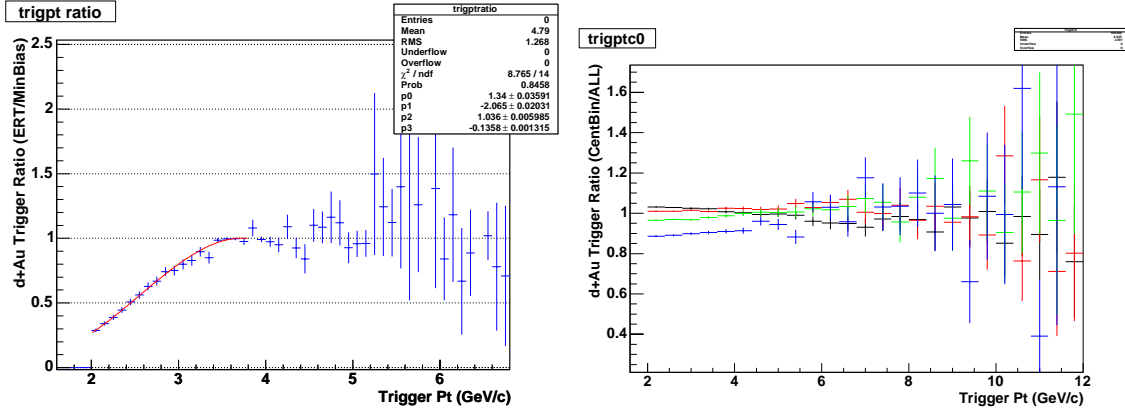


Figure 3.25: The ratio of the trigger photon spectrum in ERT over MinBias triggers (left). The ratio of the photon spectrum for different centralities in ERT events (right).

### 3.9.1 Threshold Bias of the ERT Trigger

Since we used ERT triggered events, there is a threshold turn-on to the photons that we use in our analysis. In figure 3.25, we plot the ratio of the photon spectra for ERT triggered over min-bias triggered events in d+Au. One finds an efficiency of 30% for 2 GeV photons, rising to maximal efficiency for 3.5 GeV photons. We also plot the ratio of the photon spectra for various centralities over the total sample in ERT triggered events. In conclusion, there is a strong threshold bias to ERT triggered events in d+Au, but this bias has only a very weak centrality dependence. This threshold bias affects the measured jet yields because in the turn-on region the triggered spectrum is harder, and therefore selects harder jets, which in turn tends to raise the associated jet yields. This effect can be seen in fig. 3.26, where we compare the correlations between minbias and ERT triggered samples, first for photons with  $p_T > 2.5$  GeV/c, and then for photons with  $p_T > 3.5$  GeV/c, in the region where the turn-on effects disappear. The correlations for ERT 2.0 GeV photons have a higher associated yield than that of min-bias, while for the ERT 3.5 GeV photons the associated yields are consistent with min-bias.

The correction for this can be evaluated if one knows the dependence on the jet yields as a function of the trigger  $p_T$ . The yield is a convolution of the trigger

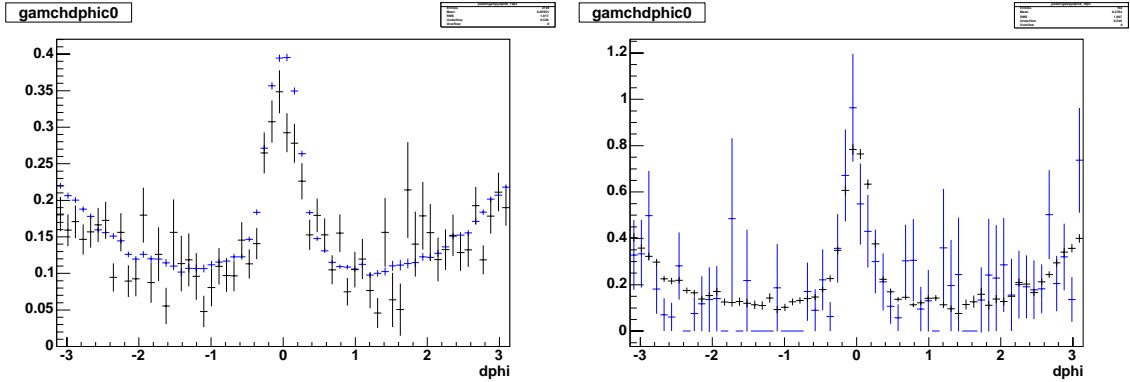


Figure 3.26: A comparison of conditional yields in  $d+Au$  for ERT vs. MinBias events. On the left is the conditional yield for trigger  $p_T > 2.0$  GeV/c, where a clear trigger bias can be seen, while on the right the bias disappears for trigger  $p_T > 3.5$  GeV/c.

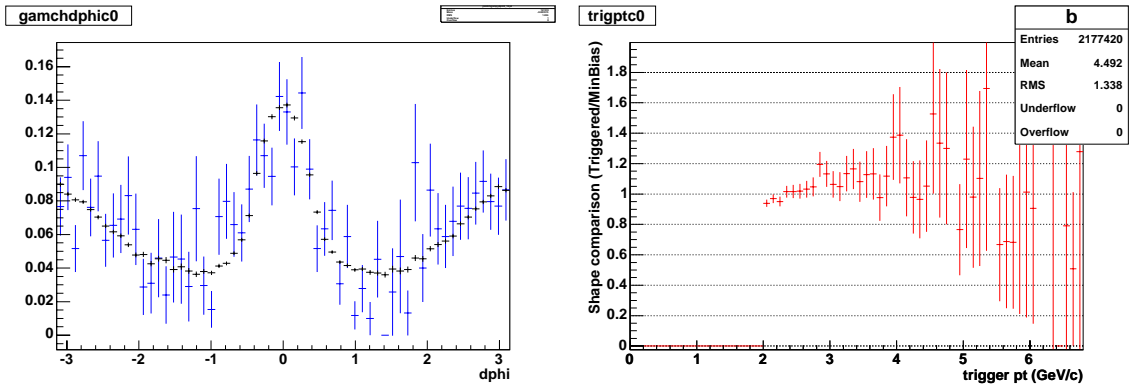


Figure 3.27: The effect of the trigger bias on the  $p+p$  yields. On the left is the comparison between the yield in ERT events compared to min-bias, while on the right is the ratio between the trigger photon spectrum and the min-bias photon spectrum.

spectrum with the associated yield:

$$n_{jet}^{corr} = \frac{\int \frac{1}{\epsilon_{trig}} \frac{dN^{trig}}{dp_T} n_{jet}(p_T) dp_T}{\int \frac{1}{\epsilon_{trig}} \frac{dN^{trig}}{dp_T} dp_T} \quad (3.7)$$

where  $n_{jet} = b + m p_T$  is the dependence of the associated yield with trigger  $p_T$ , and is shown in figure 4.13. We can check this by comparing to results where we take much smaller trigger bins, which will reduce the effect of the threshold bias.

In the case of Run03  $p+p$ , there is a much smaller effect from the threshold turn-

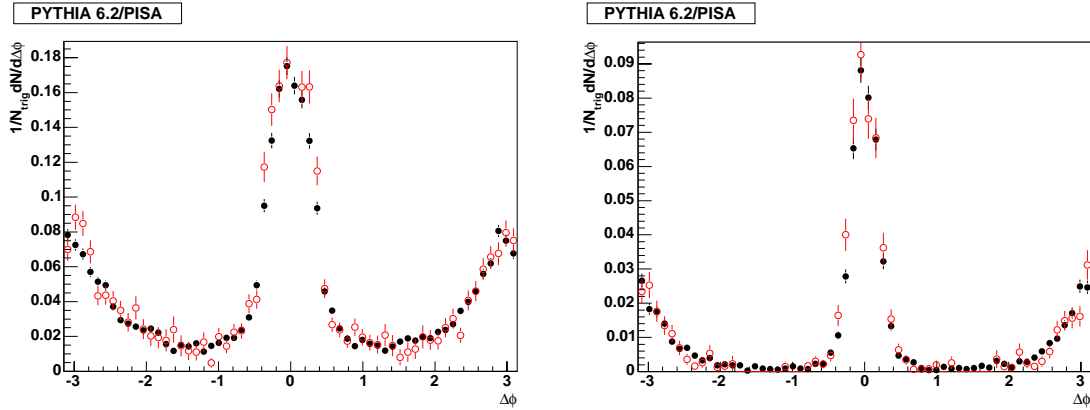


Figure 3.28: Comparison between reconstructed correlations in PHENIX simulation (red) and original PYTHIA input (black), for trigger photons with  $p_T > 2.5$  GeV/c, and associated charged hadrons with  $1.0 < p_T < 2.0$  (left) and  $2.0 < p_T < 4.0$  (right).

on (fig. 3.27). The trigger was tuned during the  $d$ +Au run, so that during the p+p run the primary trigger threshold was set at 1.8 GeV, and reached full efficiency by 2.0 GeV (except for masked out areas).

### 3.10 Verification of Method using Monte Carlo

To verify the above analysis, we tested the ability to reconstruct and identify photon-charged correlations by generating PYTHIA 6.2 [56] events, which gives us a known input. We then run these PYTHIA events through the PHENIX detector simulation (PISA), and check whether we can reconstruct the original PYTHIA input using our analysis code. In this way, we can test in detail the exact same cuts and correction techniques used in our analysis, and verify its behavior. We generated 60000 events in PYTHIA 6.2, keeping all events with a 2.5 GeV photon in the PHENIX acceptance. In figure 3.28 we plot a comparison between the known PYTHIA input and the result after running through our detector Monte Carlo, PHENIX reconstruction code, and analysis modules. There is quite good agreement, showing that our reconstruction and analysis software can correct back to the original input using the techniques described above.

### 3.11 Measuring Elliptic Flow

PHENIX reconstructs the reaction plane in an heavy-ion collision by measurement of the distribution of energies in the BBCs. Since the BBCs are not azimuthally symmetric<sup>1</sup>, one needs to compute the weighting as a function of  $\phi$  that is needed for the BBC to perform as a perfectly azimuthally symmetric detector. The weighting is done by taking the measuring the average distribution in  $\phi$  over many events, and fitting this functional form by a Fourier Series. The inverse of this function gives the weighting necessary to “flatten” out the  $\phi$  distribution measured by the BBCs, that is, to correct out the azimuthal asymmetries of the BBC detector. This weighting has to be done for every run, since changes in the transverse location of the beam can change the correction needed.

The reaction plane resolution generally degrades with lower multiplicities and lower values of ellipticity. Hence, the reaction plane resolution is poor in both the most central events (where the ellipticity is lowest) and in the most peripheral bins (where the multiplicity is lowest). The reaction plane is experimentally defined as

$$\tan n\Psi_{BBC} = \frac{\sum_i ADC_i \sin n\phi_i}{\sum_i ADC_i \cos n\phi_i} \quad (3.8)$$

where  $i$  sums over each BBC PMT.

The flattening procedure to correct the BBC asymmetries is broken down into three steps:

1. Ring Gain Correction. This corrects for any phi-dependent asymmetries that occur when the beam axis is not perfectly along the z-axis. The procedure consists of equalizing the mean ADC value for any PMTs at a common distance  $r$  from the z-axis, using the correction factor  $C_{ring}$ :

$$C_{ring} = \frac{ADC_{ring}}{ADC_{PMT}} \quad (3.9)$$

2. Average Shift Correction. This correction is equivalent to taking out the 4 pmts that break hexagonal symmetry in the BBC's, and is done by calculating the average

---

<sup>1</sup>Rather, they have (almost) hexagonal symmetry

overall shift in the x and y directions for all PMT's.

$$C_x^{shift} = \langle \sum ADC_i \cos n\phi_i \rangle \quad (3.10)$$

$$C_y^{shift} = \langle \sum ADC_i \sin n\phi_i \rangle \quad (3.11)$$

$$\tan n\Psi_{BBC} = \frac{\sum_i ADC_i \sin n\phi_i - C_y^{shift}}{\sum_i ADC_i \cos n\phi_i - C_x^{shift}} \quad (3.12)$$

3. Flattening correction. The final flattening correction is then calculated using a fit of the BBC  $\phi$ -distribution to a fourier series:

$$\Delta\Psi = \sum_k A_k \cos kn\Psi_{obs} + B_k \sin kn\Psi_{obs} \quad (3.13)$$

$$n\Psi_{corrected} = n\Psi_{obs} + \Delta\Psi \quad (3.14)$$

These corrections are done on a run by run basis.

The reaction plane resolution is given by

$$\sigma = \langle \cos n(\Psi_{measured} - \Psi_{true}) \rangle \quad (3.15)$$

To evaluate the resolution, one can take the north BBC and compare it to the south BBC, since

$$\langle \cos n(\Psi_N - \Psi_S) \rangle = \langle \cos n((\Psi_N - \Psi_{true}) - (\Psi_S - \Psi_{true})) \rangle \quad (3.16)$$

$$= \langle \cos n(\Psi_N - \Psi_{true}) \rangle \langle \cos n(\Psi_S - \Psi_{true}) \rangle \quad (3.17)$$

$$+ \langle \sin n(\Psi_N - \Psi_{true}) \rangle \langle \sin n(\Psi_S - \Psi_{true}) \rangle \quad (3.18)$$

$$= \langle \cos n(\Psi_N - \Psi_{true}) \rangle \langle \cos n(\Psi_S - \Psi_{true}) \rangle \quad (3.19)$$

Since the north and south BBC are symmetric, they should have the same resolution, and therefore

$$\langle \cos n(\Psi_{measured} - \Psi_{true}) \rangle = \sqrt{\langle \cos n(\Psi_N - \Psi_S) \rangle} \quad (3.20)$$

## 3.12 Systematic Errors

The various systematic errors on the final results, which have been mentioned in the thesis, are collected in this section for easier presentation.

The possible systematic errors in the correlated yields are

- Event Mixing
- Charged Particle Efficiency
- Hot Towers in the trigger - reduced to 0
- neutron/anti-neutron,  $K_L^0$  - effects depend on the associated particles with each trigger type

Assuming that the contributions to the trigger photons come from only the above sources, then the following equation is satisfied:

$$P^\gamma + P^{n/\bar{n}} + P^{K_L^0} + P^{hot} = 1 \quad (3.21)$$

The per-event yield of associated charged particles is the weighted average of the various contributions:

$$N_{assoc} = P^\gamma N_{assoc}^\gamma + P^{n/\bar{n}} N_{assoc}^{n/\bar{n}} + P^{K_L^0} N_{assoc}^{K_L^0} + P^{hot} N_{assoc}^{hot} \quad (3.22)$$

The  $P^{hot}$  term is included only to show it's effect - we believe that hot towers have been eliminated in this analysis. If there were hot towers, they would reduce the associated yield in direct relation to the percentage of hot towers in the trigger sample, since  $N_{assoc}^{hot} \approx 0$ .

The possible systematic errors in the background are

- $v_2$  of  $\approx 10\%$
- background level of  $\approx 0.5\%$

There are two  $v_2$  values, one for the trigger and one for the associated particles. The  $v_2$  values have a completely correlated systematic uncertainty of  $\approx 10\%$ , in addition to the statistical error.

# Chapter 4

## Results

### 4.1 Per-Trigger Differential Yields in $\Delta\phi$

After selecting a trigger photon, we can then plot the distribution of charged hadrons relative to this high- $p_T$  leading photon,  $\frac{1}{N_{trig}} \frac{dN^{assoc}}{d\Delta\phi}$ . The photons are dominantly from decays of high- $p_T$   $\pi^0$ 's that are fragments from a jet. Thus, this analysis uses the photon as an estimator for the underlying parton. This is necessary because of the impossibility of reconstructing jets fully in heavy-ion collisions.

Since the decay of the  $\pi^0$  and the fragmentation of the jet is well known, this is generally not a problem. Also, by using the same cuts, one can directly compare results between  $p+p$  and  $\text{Au+Au}$ , to look for jet modifications. That is, by selecting the same trigger photons in a  $p+p$  and a  $\text{Au+Au}$  analysis, if there are no modifications to the jet then the two results should be identical.

In figure 4.1. the correlated yield is plotted for minimum-bias  $p+p$ ,  $d+\text{Au}$ , and  $\text{Au+Au}$ , selected using trigger photons with  $p_T^{trig} > 2.25 \text{ GeV}/c$ , and charged hadrons with  $2.0 < p_T^{assoc} < 4.0 \text{ GeV}/c$ . One can see the vast increase in the background when going from  $p+p$  and  $d+\text{Au}$  to  $\text{Au+Au}$ , which gets worse as one lowers the associated  $p_T$  bin. This shows the primary difficulty in jet analyses in heavy-ion collisions. The background in  $p+p$  and  $d+\text{Au}$  is expected to be flat, but in  $\text{Au+Au}$  there is an expected correlation due to coupling of jet  $v_2$  with elliptic flow  $v_2$ . The “jet” signal are the two peaks, the “near” jet that contains the trigger

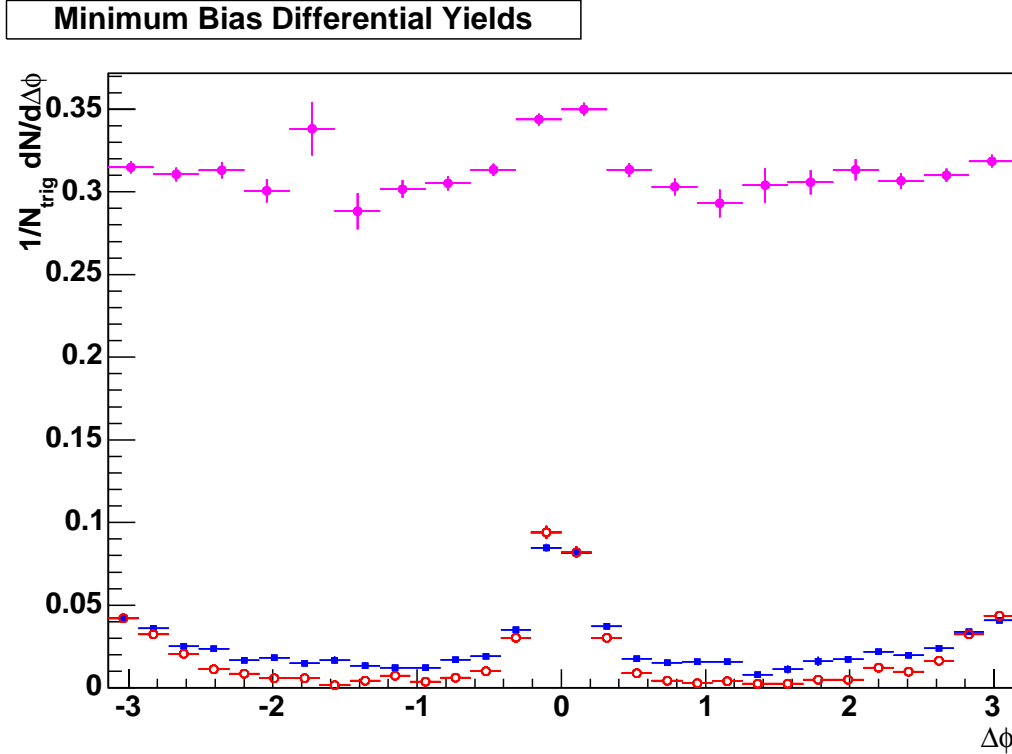


Figure 4.1:  $p+p$ ,  $d+Au$ ,  $Au+Au$ ,  $p_T^{trig} > 3.5 GeV/c$

photon (and is centered at 0), and the “away” jet centered at  $\pm\pi$ .

To keep the terminology straight, we will call all charged hadrons “associated particles”, and call those hadrons that are left after subtracting out the background “jet associated particles”. That is, the particles left after background subtraction are believed to have fragmented from the same jet.

#### 4.1.1 Behavior of the Underlying Event (Pedestal)

We begin by looking at the underlying event (also variously called the background or the pedestal), since that must be subtracted before one can consider the jet associated yields. In  $p+p$  and  $d+Au$  we assume that the underlying event is flat in  $\Delta\phi$ . In figure 4.2 we show the integrated yield of the background particles, as a function of the mean number of participants  $\langle N_{part} \rangle$ .

We see that the background per participant in  $p+p$  is higher, and seems to drop

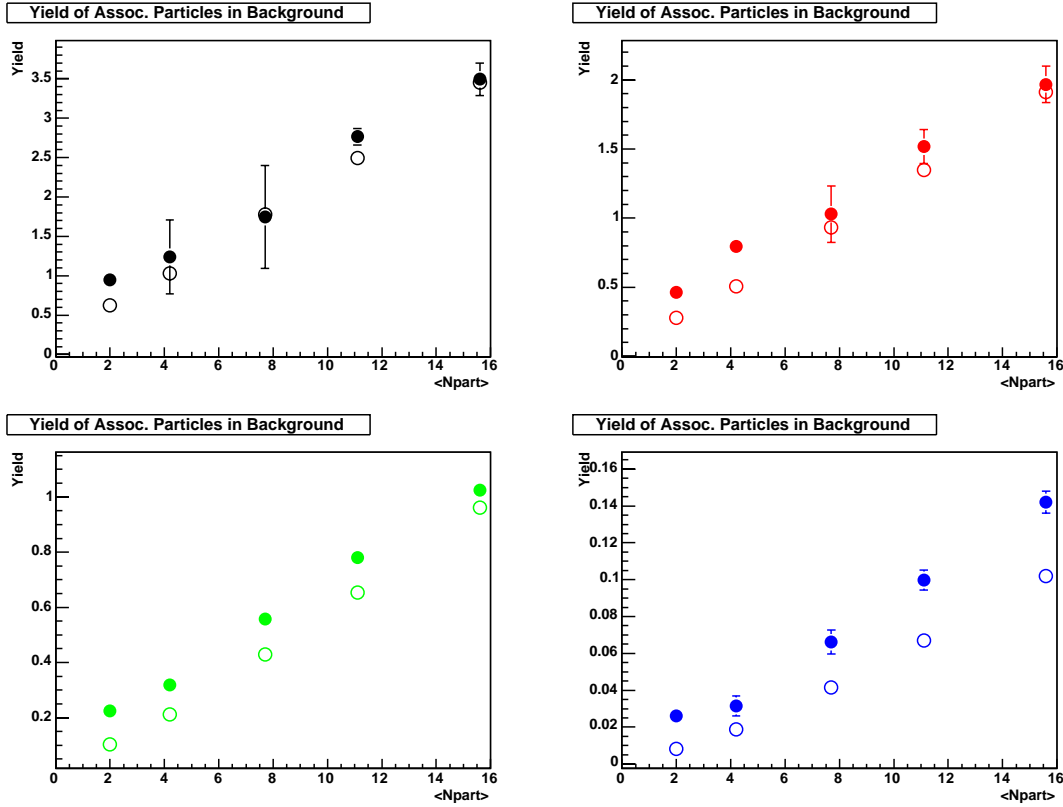


Figure 4.2: The level of the background under the jet peaks, for  $p+p$  ( $N_{part} = 2$ ) and  $d+Au$ . The solid circles are determined via a fit and the open circles are determined absolutely by weighting minimum bias multiplicities (see text).

as a function of npart. This can be described by

$$Bkg\ Yield = A \times \langle N_{part} \rangle + B \quad (4.1)$$

where A is the number of background particles produced per participant in an untriggered  $d+Au$  event, and B is the number of additional background particles in the pedestal produced by a hard collision. So we can understand the  $d+Au$  collision as a superposition of a hard collision with a more or less regular soft collision that one might find with a minimum bias trigger.

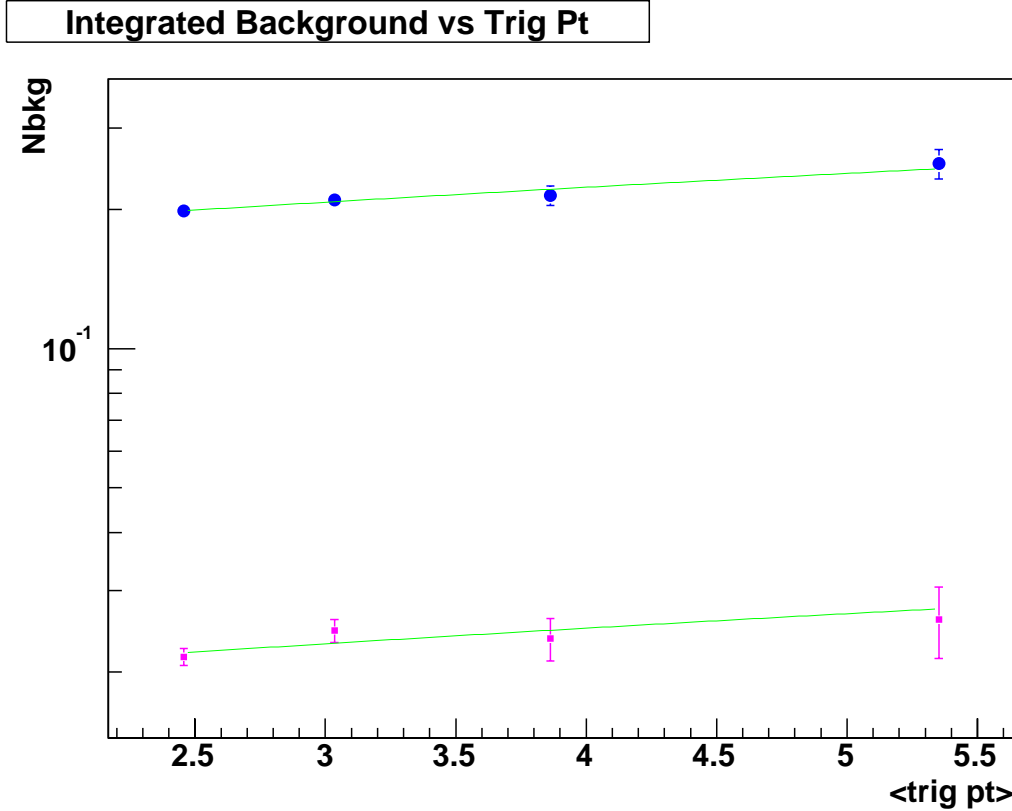


Figure 4.3: The yield of particles in the underlying event for  $p+p$ , as a function of the trigger  $p_T$ , for associated particles with  $1 < p_T < 2$  (blue) and  $2 < p_T < 4$  (magenta)

#### 4.1.2 Dependence of Underlying Event on Trigger

As a function of the trigger  $p_T$ , previous experiments have shown an increase in the yield of particles in the underlying event. We confirm this for  $p+p$  collisions at  $\sqrt{s} = 200$  GeV, as shown in figure 4.3. There is no wide agreement on the explanation for this, but some possible reasons cited are the possibility of 3-jet events, radiative effects, intrinsic  $k_T$ , or the possibility that more central  $p+p$  events have both higher backgrounds and higher probability for harder scattering. In any case, for our current purposes, we note that the increase is fairly small - a fit to the 1-2 GeV bin results in a slope of  $0.021 \pm 0.005$ , and seems to be independent of the associated  $p_T$ . This is useful since the effect is small enough that we can ignore it

when considering backgrounds in Au+Au events. Additionally, we can use higher  $p_T$  trigger bins to constrain the uncertainty in decoupling the wide, overlapping gaussians found at the lower associated bins. At higher trigger  $p_T$ , the jet shapes are narrower and thus leave less ambiguity in the  $90^\circ$  region.

The importance of studying the underlying event is highlighted by the QCD working group at Snowmass 2001. In this thesis we do not proceed to study this further since we are only interested in subtracting off this background to get our jet physics signal.

### 4.1.3 Jet Widths

One can measure the width of the jet using the angular correlations measured. While the widths are not in principle gaussian, they can be parametrized that way. We fit the  $p+p$  and  $d+\text{Au}$  data to

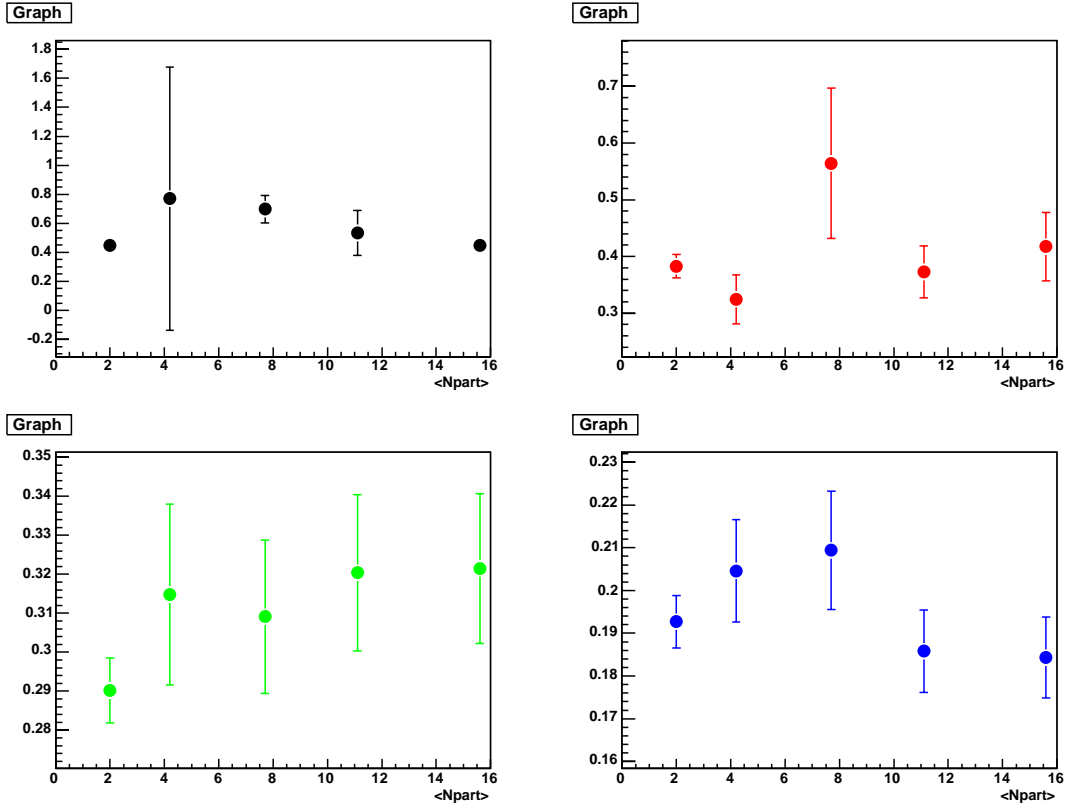
$$\frac{1}{N_{trig}} \frac{dN^{assoc}}{d\Delta\phi} = n_{bkg} + \frac{n_{jet}}{\sqrt{2\pi}\sigma_n} e^{-\frac{\Delta\phi^2}{2\sigma_n^2}} + \frac{f_{jet}}{\sqrt{2\pi}\sigma_f} e^{-\frac{(\Delta\phi-\pi)^2}{2\sigma_f^2}} \quad (4.2)$$

Changes in the jet shape between  $p+p$  and  $d+\text{Au}$  point towards nuclear effects. In particular, the away jet is thought to show some broadening due to an increased intrinsic  $k_T$  from parton multiple scattering in the cold nucleus.

#### 4.1.3.1 Widths in $\Delta\phi$

The widths for the near side and far side associated particles are plotted in figure 4.4.

In these plots, the  $p+p$  data are plotted at  $N_{part} = 2$ . The widths on the near side for  $d+\text{Au}$  are consistent with that of  $p+p$ . The widths on the far side, within errors, are also consistent, though there is potentially some small increase in  $d+\text{Au}$ . However, the increase in width is much smaller than that expected from the increase in  $k_T$ .

Figure 4.4: The  $p+p$  and  $d+Au$  near jet widths as a function of centrality

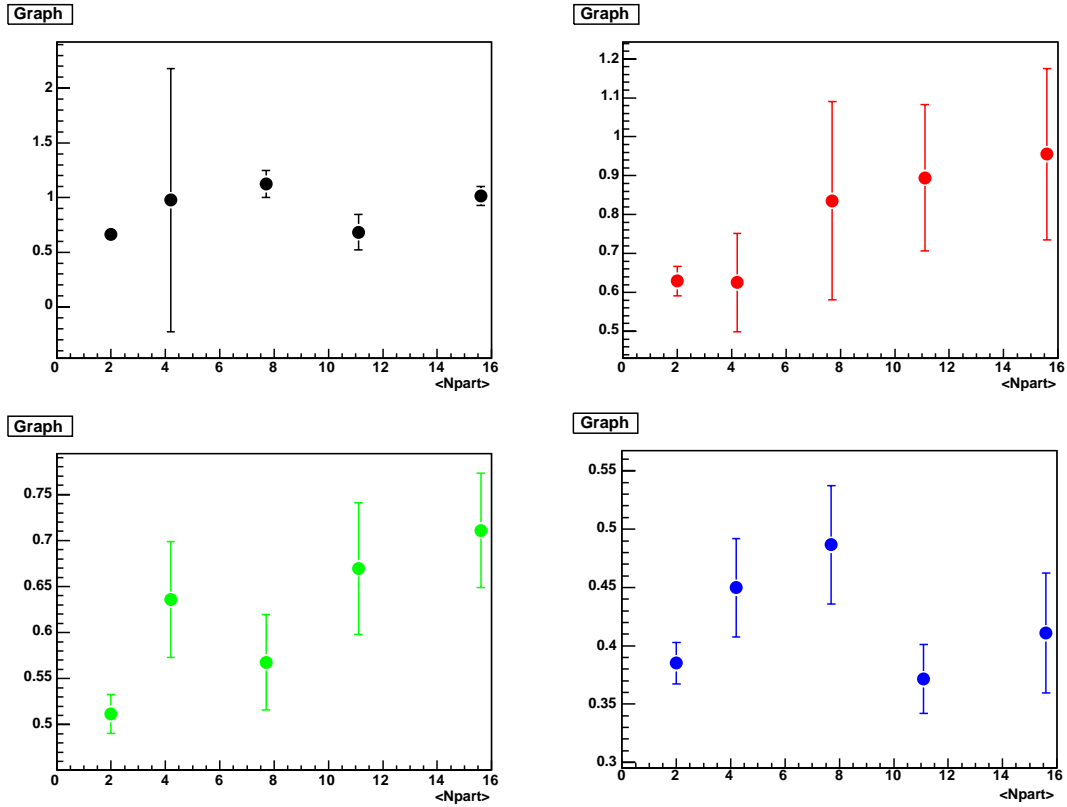
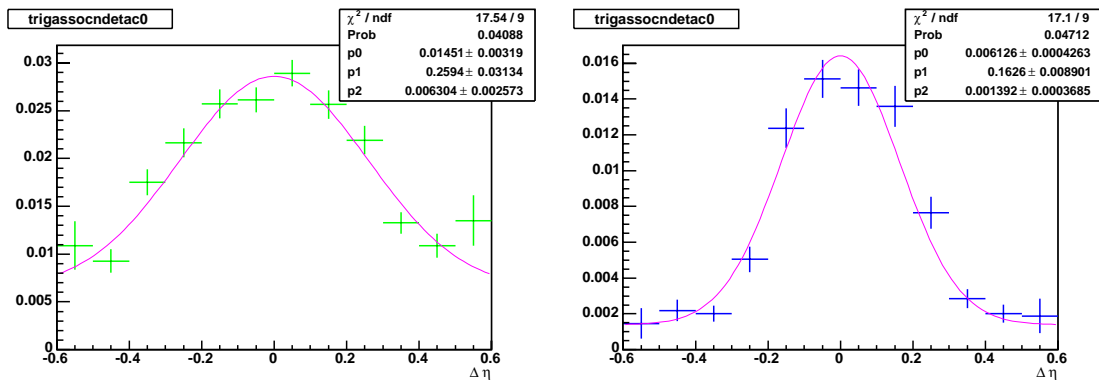
#### 4.1.3.2 Widths in $\Delta\eta$

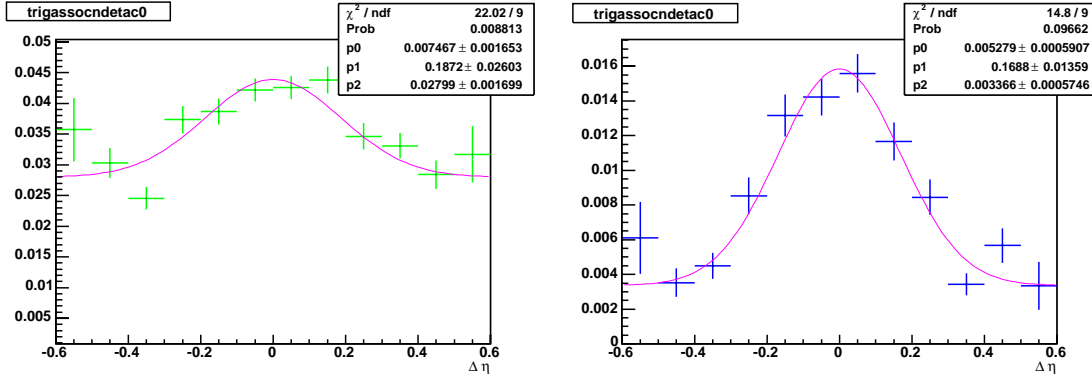
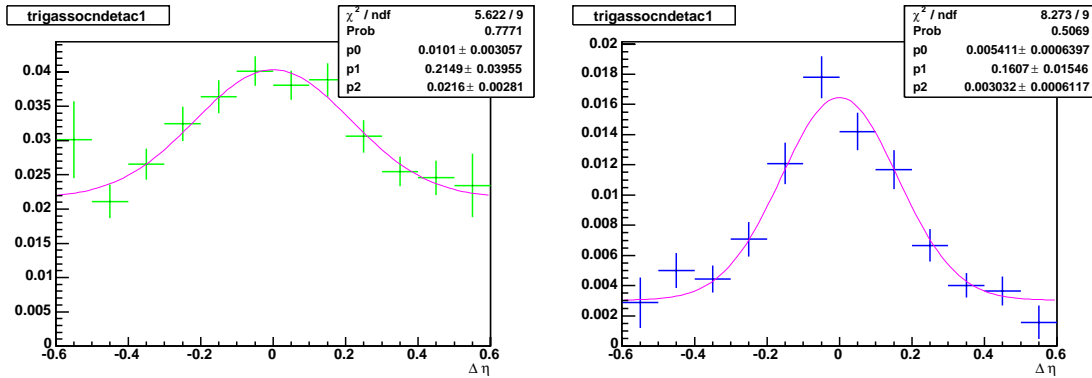
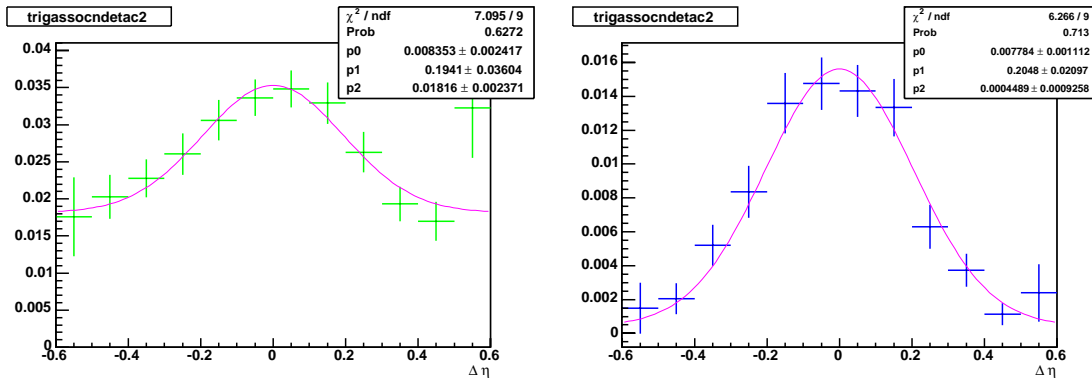
The widths in  $\Delta\eta$  require more care than in  $\Delta\phi$ , due to the limited acceptance of PHENIX in  $\eta$ . In figure 4.6, we show the plot for  $\Delta\eta$  of the near side jet, which is for those particles that satisfy  $|\Delta\phi| < \frac{2\pi}{20}$ . There doesn't seem to be much centrality dependence in  $d+Au$  versus that seen in  $p+p$ .

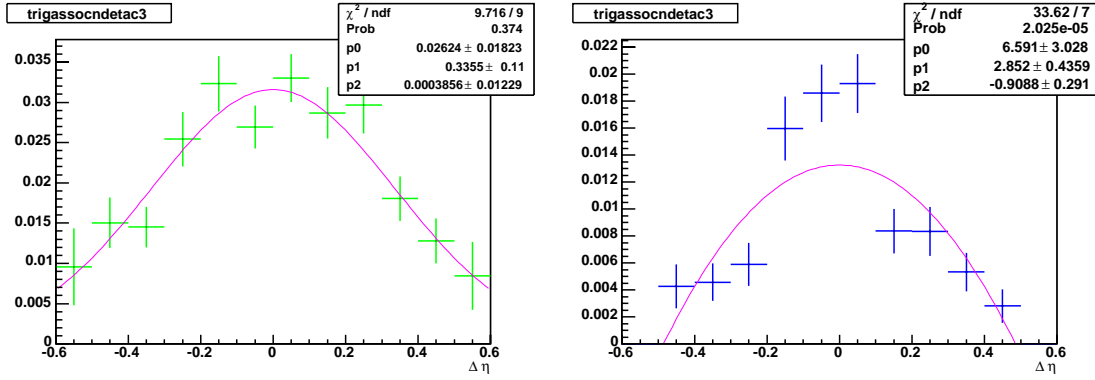
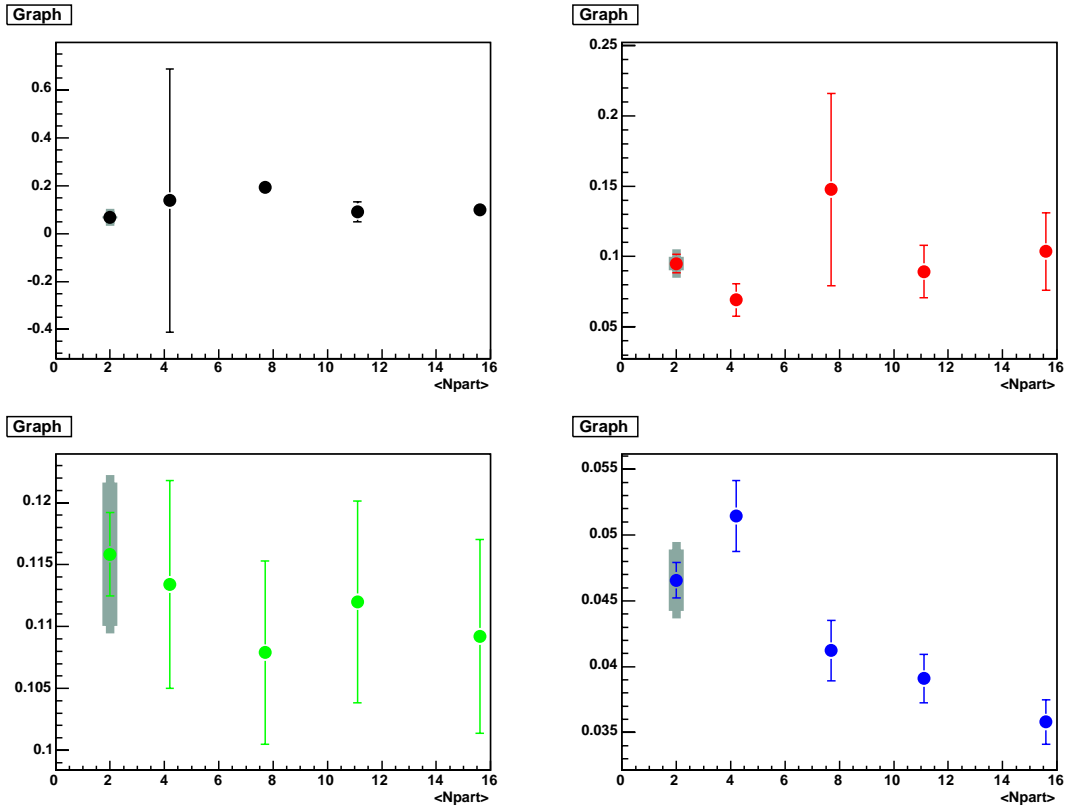
#### 4.1.4 Jet Yields in $p+p$ and $d+Au$

On the other hand, we find that there is a centrality dependence to the associated yields, which we have plotted in figure 4.11. The drop is clearest in the 2-4 GeV/c associated bin (blue), where we see a drop of 20% in both the near and far side. For the other bins, the signal is more or less consistent with being flat.

The yields as a function of the trigger pt for  $p+p$  events are shown in figure 4.13,

Figure 4.5: The  $p+p$  and  $d+Au$  far jet widths as a function of centralityFigure 4.6:  $p+p$ ,  $3.5 < p_T^{trig} < 20.0 GeV/c$ ,  $\Delta\eta$  distribution

Figure 4.7:  $d+Au$ ,  $3.5 < p_T^{trig} < 20.0 GeV/c$ ,  $\Delta\eta$  distribution, 0-20% CentralFigure 4.8:  $d+Au$ ,  $3.5 < p_T^{trig} < 20.0 GeV/c$ ,  $\Delta\eta$  distribution, 20-40% CentralFigure 4.9:  $d+Au$ ,  $3.5 < p_T^{trig} < 20.0 GeV/c$ ,  $\Delta\eta$  distribution, 40-60% Central

Figure 4.10:  $d+Au$ ,  $3.5 < p_T^{trig} < 20.0 GeV/c$ ,  $\Delta\eta$  distribution, 60-88% CentralFigure 4.11: The  $p+p$  and  $d+Au$  near jet associated yields after pedestal subtraction. The color codes represent the  $p_T$  bin of the associated particles, with black =  $0.3-0.6$  GeV, red =  $0.6-1.0$  GeV, green =  $1.0-2.0$  GeV, and blue =  $2.0-4.0$  GeV

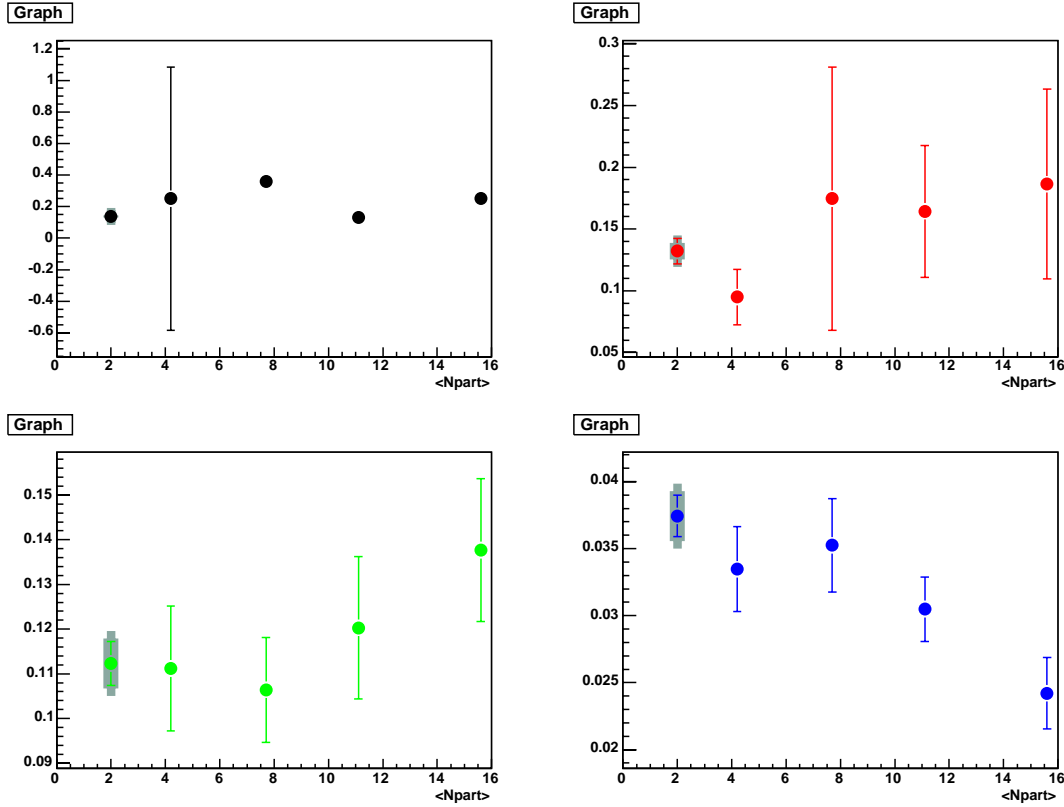


Figure 4.12: The p+p and d+Au away jet associated yields after pedestal subtraction. The color codes represent the  $p_T$  bin of the associated particles, with black = 0.3-0.6 GeV, red = 0.6-1.0 GeV, green = 1.0-2.0 GeV, and blue = 2.0-4.0 GeV

assoc pt	$b_{nbkg}$	$m_{nbkg}$	$b_{njet}$	$m_{njet}$	$b_{fjet}$	$m_{fjet}$
1.0-2.0	0.17774	0.0210673	-0.000442246	0.034669	-0.00215448	0.0342384
2.0-4.0	0.0137673	0.00618437	-0.0261763	0.0216498	-0.0217847	0.0169293

and one can see that the associated yields scale linearly with the trigger  $p_T$ . The fit parameters are given in table 4.1.4. The jet associated yields rise much faster than the additional background, and the near equality between the near and far jet slopes implies that the photons are linearly associated with the underlying jet energy.

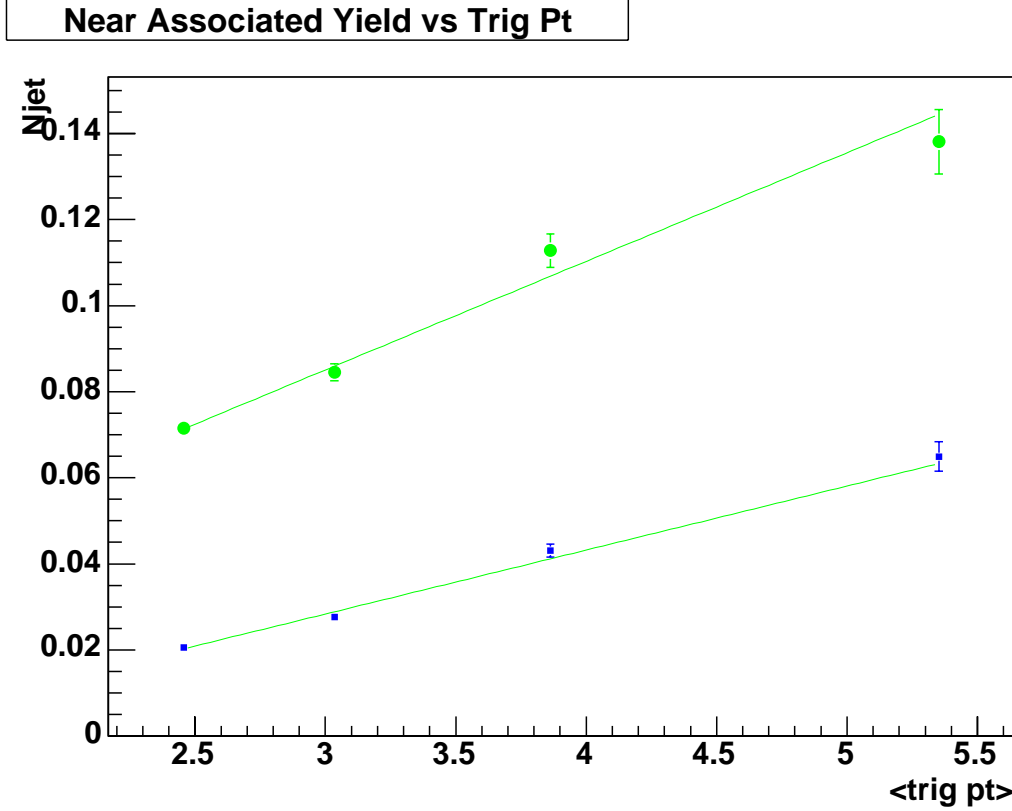


Figure 4.13: The  $p+p$  integrated near and far side jet yields, after pedestal subtraction, as a function of the trigger  $p_T$

## 4.2 Jet Yields in Au+Au

The “jet” yields in Au+Au require far more care than in  $d$ +Au or  $p+p$ , not only because the magnitude of the background is far higher, but also because there might be additional effects that create another source of correlation in  $\Delta\phi$  besides just that due to fragmentation. An example of this comes from elliptic flow, which modulates the flat background into a  $\cos(2\phi)$ ,

One must assume some model for the background. For the Au+Au case, we make the simplest ansatz possible to model what the background should be. We assume that the triggered events with jets consist of a simple superposition of the jet plus an underlying event which is the same as an untriggered heavy ion event, but which has a centrality distribution that is weighted toward more central events due

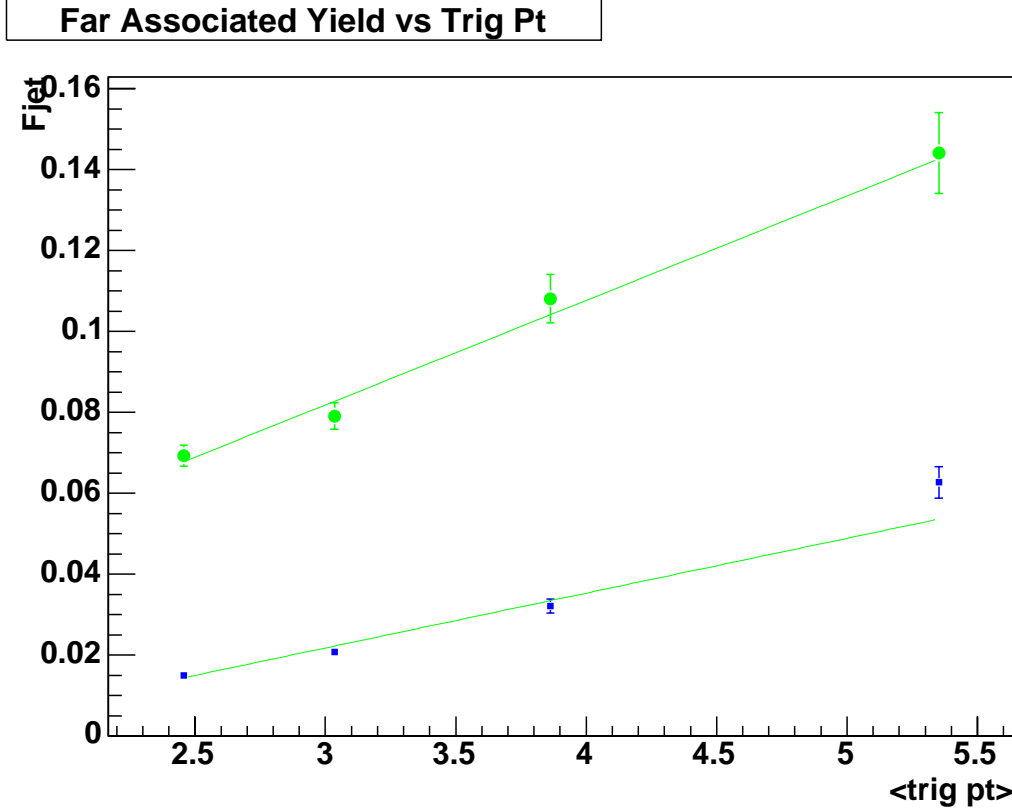


Figure 4.14: The p+p integrated near and far side jet yields, after pedestal subtraction, as a function of the trigger  $p_T$

to the centrality bias of the trigger. We further assume there are only two sources of correlations in  $\Delta\phi$ , one coming from the jet fragmentation, and the other coming from coupling of jet  $v_2$  with the underlying event  $v_2$ . In the following section, we work out the formula for the background.

#### 4.2.1 Preliminaries, Assumptions

In doing pair correlations where the contributions are either from jets or from elliptic flow, there exists an inherent ambiguity since there are two possible references for the phi origin. One can choose either the jet axis ( $\Psi_J$ ) or the reaction plane ( $\Psi_R$ ):

$$\phi_J = \phi - \Psi_J \quad (4.3)$$

$$\phi_R = \phi - \Psi_R \quad (4.4)$$

In addition, while each event has one reaction plane, in principle there could be more than one jet axis per event, especially at lower  $p_T$  where multiple mini-jets may be a sizable component of particle production.

The single particle jet distribution w.r.t. the underlying jet axis for that particle is

$$\frac{dN^{jet}}{d\phi_J} \equiv N^{jet} Jet(\phi_J) = N^{jet} \left( \frac{N^{near}}{N^{jet}} \frac{e^{-\frac{(\phi_J)^2}{2\sigma^2}}}{(2\pi\sigma^2)^{\frac{1}{2}}} + \frac{N^{far}}{N^{jet}} \frac{e^{-\frac{(\phi_J)^2}{2\sigma_{far}^2}}}{(2\pi\sigma_{far}^2)^{\frac{1}{2}}} \right) \quad (4.5)$$

(Unless otherwise stated, in this and in all other distributions, we always mean the per event distribution.)

We also assume that the single particle jet distribution w.r.t. to the reaction plane is

$$\frac{dN^{jet}}{d\phi_R} = \frac{N^{jet}}{2\pi} (1 + 2v_2^{jet} \cos(2\phi_R)) \quad (4.6)$$

One gets the distribution w.r.t. to the reaction plane from the jet axis by convoluting the single particle jet shape with the jet axis distribution w.r.t. the reaction plane. If the reports of a non-zero  $v_2$  in the fragmentation dominated  $pt > 6$  GeV/c region turn out to be true, it implies that the jet axis has a  $v_2$  w.r.t. the reaction plane, and that would justify eq. 4.6. As  $v_2^{jet} \rightarrow 0$  we recover the case that the jet axis is completely uncorrelated w.r.t. the reaction plane.

Note that we have normalized the gaussian and  $\cos(2\phi)$  distribution so that  $N_{jet}$  represents the actual number of jet particles per event. We will gloss over the complication that the gaussian should be periodic over  $2\pi$ , which one can analytically do by introducing the Dirac Comb. We state that these complications go away since in our calculations integration over  $2\pi$  of the periodic gaussian is equivalent to integration over  $(-\infty, +\infty)$  of a single gaussian, and so in the rest of the calculations we will just use one gaussian. The interested reader can find the details in Appendix A.

The distribution of the particles from elliptic flow in the event have the distribution

$$\frac{dN^{flow}}{d\phi_R} = \frac{N^{flow}}{2\pi} (1 + 2v_2^{flow} \cos(2\phi_R)) \quad (4.7)$$

by definition. Of course, when one measures  $dN/d\phi_R$ , the flow and jet v2 components cannot be distinguished and one instead measures their weighted average

$$v_2^{tot} = \frac{N^{jets}v_2^{jet} + N^{flow}v_2^{flow}}{N^{jets} + N^{flow}} \quad (4.8)$$

$$N^{tot} = N^{jets} + N^{flow} \quad (4.9)$$

$$\frac{dN^{tot}}{d\phi_R} = \frac{N^{tot}}{2\pi}(1 + 2v_2^{tot} \cos(2\phi_R)) \quad (4.10)$$

We explicitly note the difference between  $v_2^{flow}$ , caused by hydrodynamic elliptic flow,  $v_2^{jet}$ , caused by a phi dependence to the jet energy loss induced by the collision geometry, and  $v_2^{tot}$ , the weighted  $v_2$  sum of the inclusive particles, which is what one actually measures w.r.t. the reaction plane since one can't a priori separate the jet particles from the flow particles. Of course that  $v_2^{tot}$  is possibly different for different classes of events. There would be a different fraction of jet-like particles for high- $p_T$  triggered events and thus triggered events would place greater weight to the jet-like  $v_2$ , for example.

In the same manner, we would also like to note that "total" is only well defined once one specifies an event sample. This may seem like a trivial statement but in the following sections we would like the reader to keep that in mind. So for example, if one selected high- $p_T$  triggered events and those events were all triggered due to a jet, one would have a total number of particles

$$N^{tot} = N^{jet} + N^{bg} \quad (4.11)$$

$$= N^{jet} + (N^{jets} + N^{flow}) \quad (4.12)$$

where  $N^{jet}$  is the number of particles from the triggered jet, and  $N^{jets}$  counts the number of particles from jets in the underlying heavy ion event. In other words, the total number of particles in the triggered sample is greater than the non-triggered sample, and the difference is the number of particles in the jet that triggered the events.

### 4.3 Yield Analysis

In the case when one measures the yield  $dN^{ch}/d\Delta\phi$ , there is one trigger particle (leading  $p_T$  particle) per event, and that trigger particle defines the axis for that event. The trigger particle may either come from a jet, from elliptic flow, or from noise (such as mis-identified photons, hot towers, etc.). We will ignore the noise component for this analysis since that is an experimental issue and can be reduced via appropriate cuts. So for trigger particles, we have

$$P_{jet} + P_{flow} = 1 \quad (4.13)$$

There are two bins of particles, the trigger bin (labeled with a 1), and the second bin (labeled 2). The particles in bin 2 (assuming one has a trigger jet in that event) has the distribution

$$\frac{dN^{tot2}}{d\phi_R} = N^{jet2} Jet(\phi_R - \psi_J) + N^{bg2} \frac{1 + 2v_2^{bg2} \cos(2\phi_R)}{2\pi} \quad (4.14)$$

where  $\psi_J$  is not specified and is free to range from 0 to  $2\pi$  (after averaging over all possible  $\psi_J$  the first term above would have the same form as eq. 4.6). Here  $N^{tot2} = N^{jet2} + N^{bg2}$  is the total number of particles in our second bin, and bg is the label for all the particles in the underlying heavy-ion event (ie, not coming from a triggered jet). Since the event comes from a triggered sample, the second bin contains  $N^{jet2}$  particles from the triggered jet, plus  $N^{bg2}$  particles from the underlying heavy-ion event, which is composed of particles from jets (which are almost always lower  $p_T$  jets) and elliptic flow. In fact, there is some experimental data supporting the assertion that underlying heavy-ion event to be the same as that of an untriggered, minimum bias sample. Of course, in events that are triggered by a high- $p_T$  flow particle, there is no jet and the first term in eq. 4.14 goes away.

In the case when we have a trigger flow particle the pair distribution is

$$\begin{aligned}
\left( \frac{dN}{d\Delta\phi} \right)_{Flow} &= \int_0^{2\pi} \int_0^{2\pi} \frac{dN^1}{d\phi_1} \frac{dN^2}{d\phi_2} \delta(\phi_2 - (\phi_1 - \Delta\phi)) d\phi_1 d\phi_2 \\
&= \int_0^{2\pi} \frac{dN^1}{d\phi_1} \frac{dN^2}{d(\phi_1 - \Delta\phi)} d\phi_1 \\
&= \frac{N^{bg2}}{(2\pi)^2} \int_0^{2\pi} (1 + 2v_2^{flow1} \cos(2\phi_R))(1 + 2v_2^{bg2} \cos(2(\phi_R - \Delta\phi))) d\phi_R \\
&= \frac{N^{bg2}}{(2\pi)^2} \int_0^{2\pi} [1 + 2v_2^{flow1} \cos(2\phi_R) + 2v_2^{bg2} \cos(2(\phi_R - \Delta\phi)) \\
&\quad + 4v_2^{flow1} v_2^{bg2} \cos(2\phi_R)(\cos(2\phi_R) \cos(2\Delta\phi) + \sin(2\phi_R) \sin(2\Delta\phi))] d\phi_R \\
&= N^{bg2} \frac{1 + 2v_2^{flow1} v_2^{bg2} \cos(2\Delta\phi)}{2\pi} \tag{4.15}
\end{aligned}$$

which is identical to the flow-flow form that has been used at lower energies when jets were not a large contributor to particle production [44].

When the trigger particle comes from a jet the pair distribution is

$$\begin{aligned}
\left( \frac{dN}{d\Delta\phi} \right)_{Jet} &= \int_0^{2\pi} \frac{dN^1}{d\phi} \frac{dN^2}{d(\phi - \Delta\phi)} d\phi \\
&= \int_0^{2\pi} Jet(\phi_J) N^{jet2} Jet(\phi_J - \Delta\phi) d\phi_J \\
&\quad + \int_0^{2\pi} Jet(\phi_R) N^{bg2} \frac{1 + 2v_2^{bg2} \cos(2(\phi_R - \Delta\phi))}{2\pi} d\phi_R \\
&= N^{jet2} Jet Jet(\Delta\phi) + N^{bg2} \frac{1 + 2v_2^{bg2} v_2^{jet1} \cos(2\Delta\phi)}{2\pi} \tag{4.16}
\end{aligned}$$

$Jet Jet(\Delta\phi)$  is the pair correlation of the trigger particle with the fragmented particles from the jet:

$$Jet Jet(\Delta\phi) = f^{near} \frac{e^{-\frac{(\Delta\phi)^2}{2\sigma_n^2}}}{(2\pi\sigma_n^2)^{\frac{1}{2}}} + f^{far} \frac{e^{-\frac{(\Delta\phi - \pi)^2}{2\sigma_f^2}}}{(2\pi\sigma_f^2)^{\frac{1}{2}}} \tag{4.17}$$

where  $\sigma_n^2 = \sigma_{n1}^2 + \sigma_{n2}^2$  and  $\sigma_f^2 = \sigma_{f1}^2 + \sigma_{f2}^2$ . Eq. 4.16 simply states that the near and far side jet shape is smeared by the trigger particle's resolution of  $\sigma_{n1}$  relative to the underlying jet axis, that any second fourier correlation of the trigger jet particles with the reaction plane gets convoluted with the second fourier correlation of the particles from the underlying heavy ion event. Note that the jet-jet pairs only add

an inter-jet correlation and do not create a second order correlation due to the correlations to the reaction plane, since they are both perfectly correlated in exactly the same way to the reaction plane.

Note carefully the nomenclature we have used; jet refers to particles that come explicitly from the jet which serves as the trigger particle, flow refers to a particle from elliptic flow, and bg refers to particles in the underlying event, where an assumption has been made that this underlying event is the same between jet triggered and flow triggered events. Terms labeled with a 1 refer to the trigger bin, and 2 refers to the second bin.

The final distribution one measures is the weighted average of the above two distributions:

$$\begin{aligned} \frac{dN}{d\Delta\phi} &= P^{jet} \left( \frac{dN}{d\Delta\phi} \right)_{Jet} + (1 - P^{jet}) \left( \frac{dN}{d\Delta\phi} \right)_{Flow} \\ &= P^{jet} N^{jet2} JetJet(\Delta\phi) + P^{jet} N^{bg2}/2\pi + (1 - P^{jet}) N^{bg2}/2\pi + \\ &\quad 2N^{bg2} v_2^{bg2} (P^{jet} v_2^{jet1} + (1 - P^{jet}) v_2^{flow1}) \cos(2\Delta\phi)/2\pi \end{aligned}$$

which, after combining factors and recognizing that  $v_2^{trig} = P^{jet} v_2^{jet1} + (1 - P^{jet}) v_2^{flow1}$ , becomes

$$\frac{dN}{d\Delta\phi} = P^{jet} N^{jet2} JetJet(\Delta\phi) + N^{bg2} (1 + 2v_2^{bg2} v_2^{trig} \cos(2\Delta\phi)) \quad (4.18)$$

Note that the jet-flow crossterms fold into the  $v_2$  background term, and that  $v_2^{trig}$  is the  $v_2$  one actually measures for inclusive particles in the trigger bin. The integral of eq. 4.18 is  $P^{jet} N^{jet2} + N^{bg2}$ , which is exactly what one expects since triggering on a jet particle contributes  $N^{jet2} + N^{bg2}$  to the average, while triggering on flow particles contributes simply  $N^{bg2}$

## 4.4 Au+Au Results

The correlation functions for two associated  $p_T$  bins in Au+Au are shown in figures 4.15 and 4.16. They have been fully efficiency corrected, and are for trigger photons

Table 4.1:  $v_2$  values

cent (%)	0.3-0.6	0.6-1.0	1.0-2.0	2.0-4.0	$\gamma, 2.25+$
0-10	0.02110117	0.02861627	0.0468459	0.0728357	0.068142
10-20	0.0491291	0.0789173	0.112505	0.155085	0.136506
20-40	0.0560148	0.0927227	0.140352	0.195884	0.172937
40-60	0.0717563	0.121421	0.176455	0.230657	0.20
60-90	0.0358781	0.0607105	0.0882275	0.115329	0.10

above 2.25 GeV/c and associated bins of  $1.0 < p_T^{assoc} < 2.0$  and  $2.0 < p_T^{assoc} < 4.0$ .

#### 4.4.1 Au+Au Background

The background is estimated by using minimum bias events, and weighting the  $p_T$  distribution by the centrality distribution of our trigger selection. This is done after run by run efficiency corrections to the  $p_T$  spectrum. The pedestal value, as determined from  $p+p$ , is added. This is based our assumption that a triggered heavy-ion event consists of a jet superposed on a centrality weighted, minimum bias incoherent heavy ion event. That is, we assume that the jet perturbs the underlying heavy ion event only minimally.

$$N_{bkg} = \sum_{i=cent} f_i \left( \frac{1}{N_i} \int \frac{dn^{assoc}}{dp_T} dp_T \right) + (\text{pp pedestal}) \quad (4.19)$$

The systematic error on this procedure, as estimated from looking at different run groups, is about 0.5%.

We then modulate the above background using the formula in equation 4.18. The  $v_2$  values are given in table 4.1. For the most peripheral bin, where the resolution was too poor to determine  $v_2$  adequately, we assumed half the  $v_2$  value of the 40-60% bin, and allowed for a systematic error of the full range of the 40-60% value. We assumed a systematic error of 15% on each  $v_2$  value, or 21% in quadrature for the error of the product of the  $v_2$ 's.

The fully subtracted distributions are shown in figure 4.17. They show the jet associated yield in heavy-ions, as a function of centrality, for two associated  $p_T$  bins.

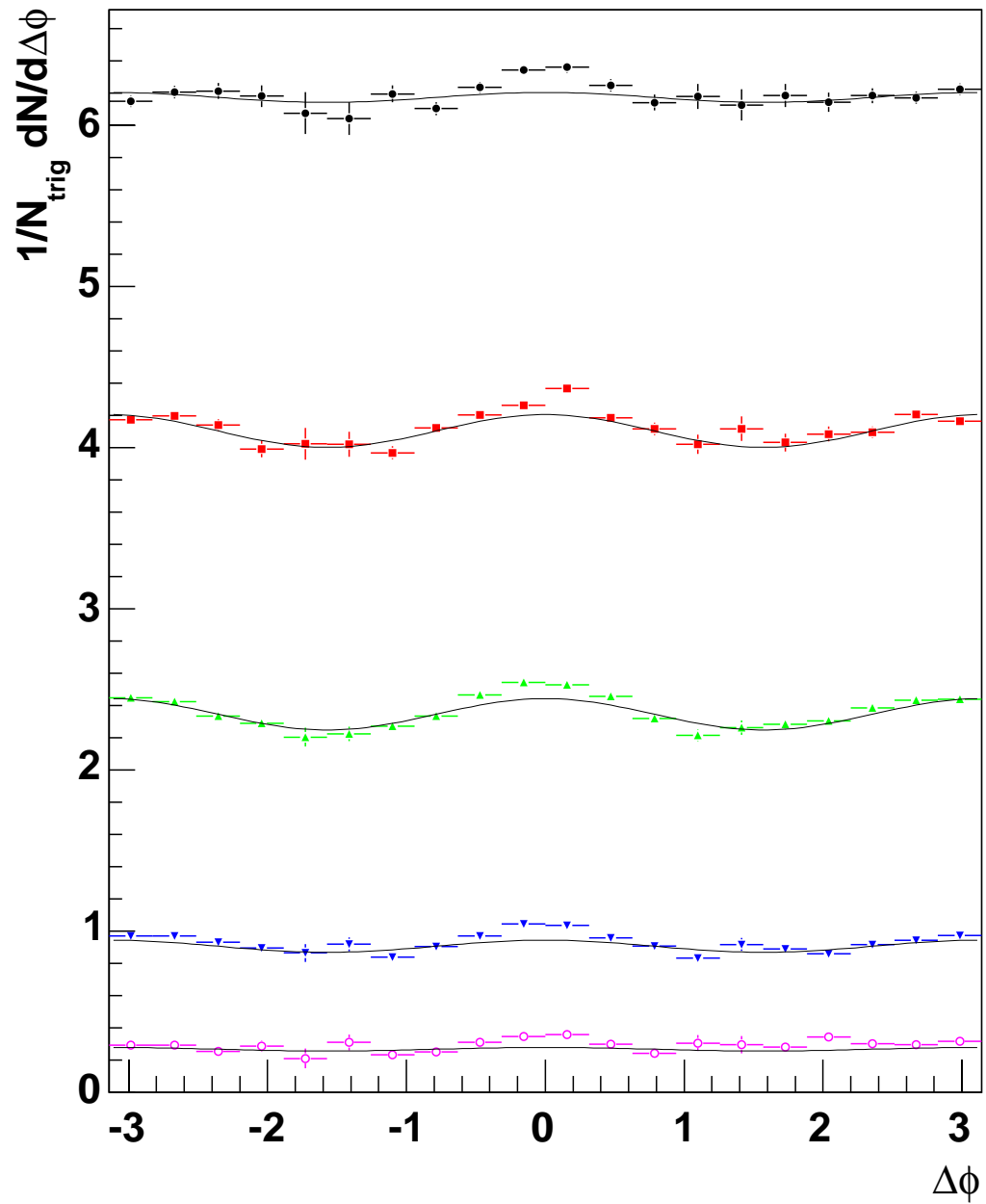


Figure 4.15: Au+Au,  $2.25 < p_T^{trig} < 20.0 GeV/c$ ,  $1.0 < p_T^{assoc} < 2.0 GeV/c$

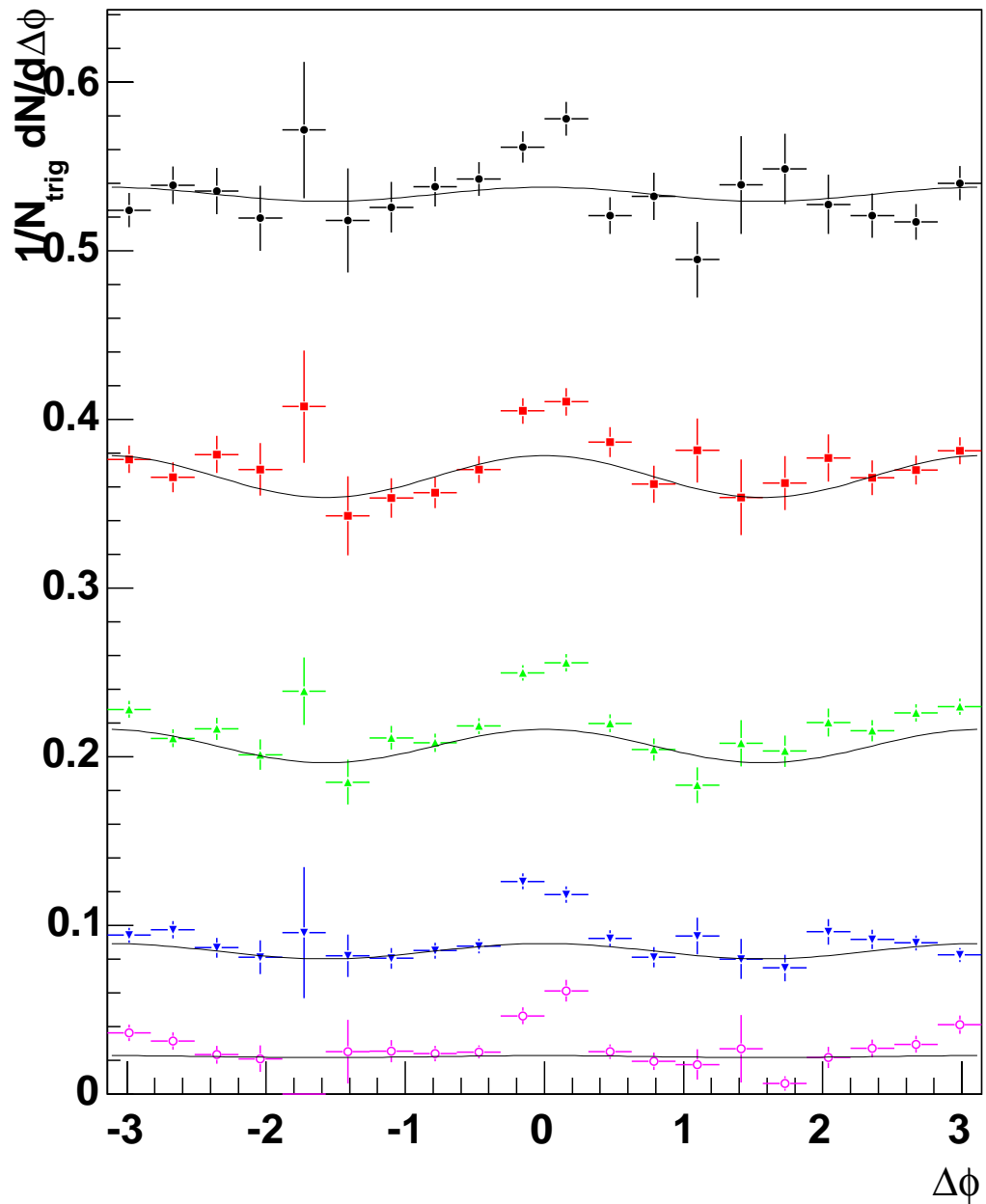


Figure 4.16: Au+Au,  $2.25 < p_T^{trig} < 20.0 \text{GeV}/c$ ,  $2.0 < p_T^{assoc} < 4.0 \text{GeV}/c$

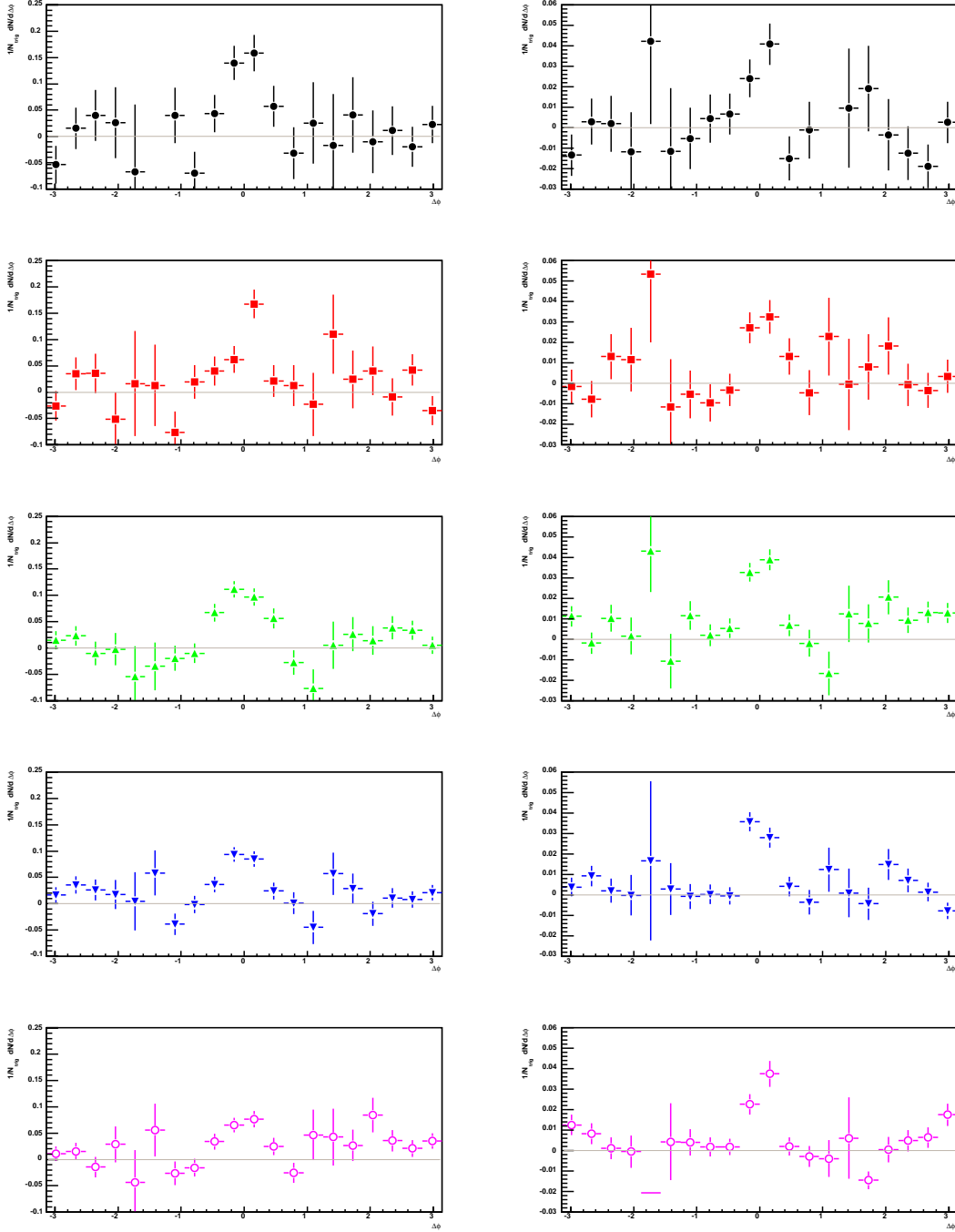


Figure 4.17: Run02 Au+Au,  $2.25\text{GeV}/c < p_T^{\text{trig}}$ , Background subtracted  $\frac{1}{N_{\text{trig}}} \frac{dN^{ch}}{d\phi}$  distributions, for associated bins of  $1.0 < p_T^{\text{assoc}} < 2.0$  (left) and  $2.0 < p_T^{\text{assoc}} < 4.0$  (right). From top to bottom are centralities 0-10, 10-20, 20-40, 40-60, 60-90%.

**Near Side Jet Widths**

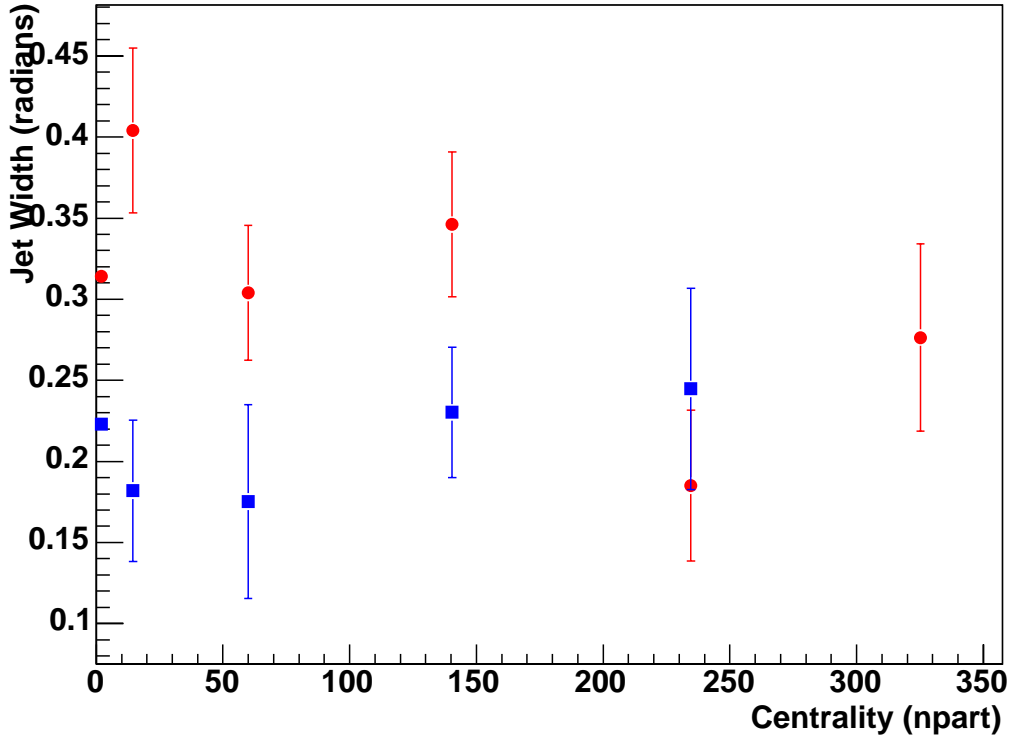


Figure 4.18: Run02 Au+Au,  $2.25GeV/c < p_T^{trig}$ , jet widths

In figure 4.18, we show the near side width as a function of centrality. There does not seem to be a significant difference between the  $p+p$  and Au+Au near widths.

In figures 4.19 and 4.20, we show the integrated near and far side jet associated yields as a function of centrality, and the comparison to  $p+p$ . The near yields are integrated over  $|\Delta\phi| < 36^\circ$  and the away side yields are integrated over  $|\Delta\phi| < 72^\circ$ . The systematic error bands were calculated assuming maximal  $1\sigma$  deviations of the systematic errors in  $v_2$  and  $N_{bkg}$ . That is, we assumed that the  $v_2$  and  $N_{bkg}$  were fully correlated in estimating the systematic error. The near side seems relatively flat with centrality, while the far side shows a steady loss of yield with centrality, for both associated bins. In figure 4.21, we overlay the jet associated yield plots for the most central 10% and the 60-90% centrality bins.

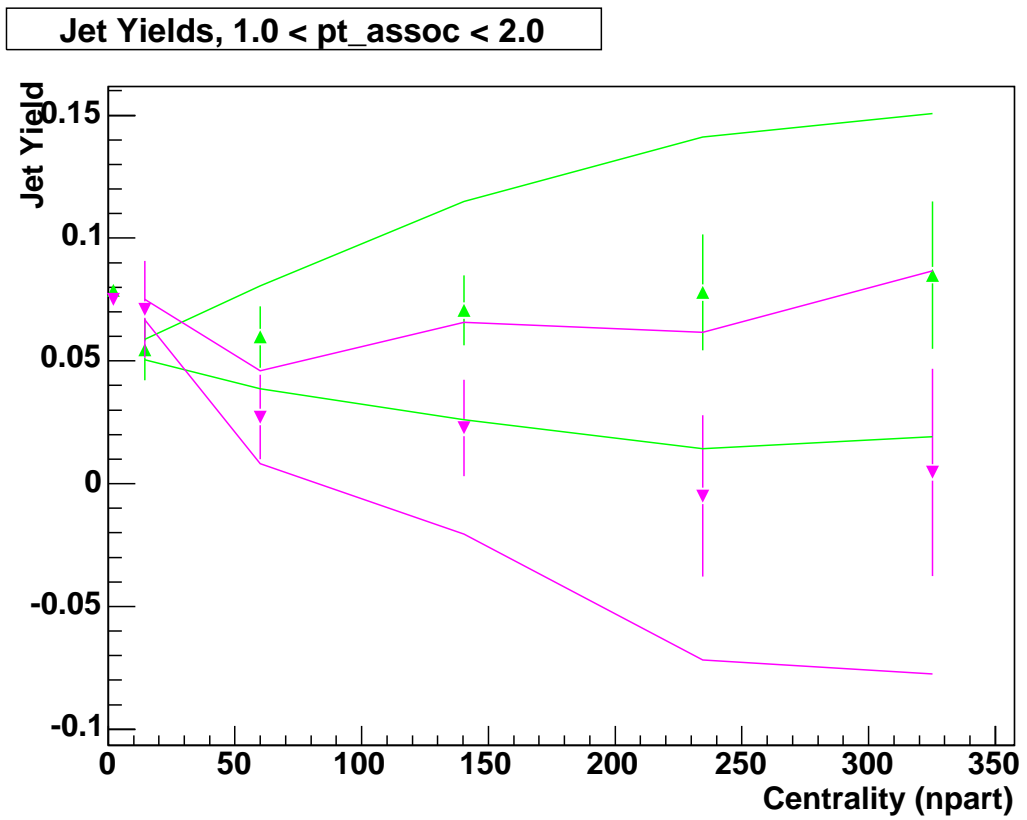


Figure 4.19: Run02 Au+Au,  $2.25\text{GeV}/c < p_T^{\text{trig}}, 1.0 < p_T^{\text{assoc}} < 2.0$ , Associated Jet Yields

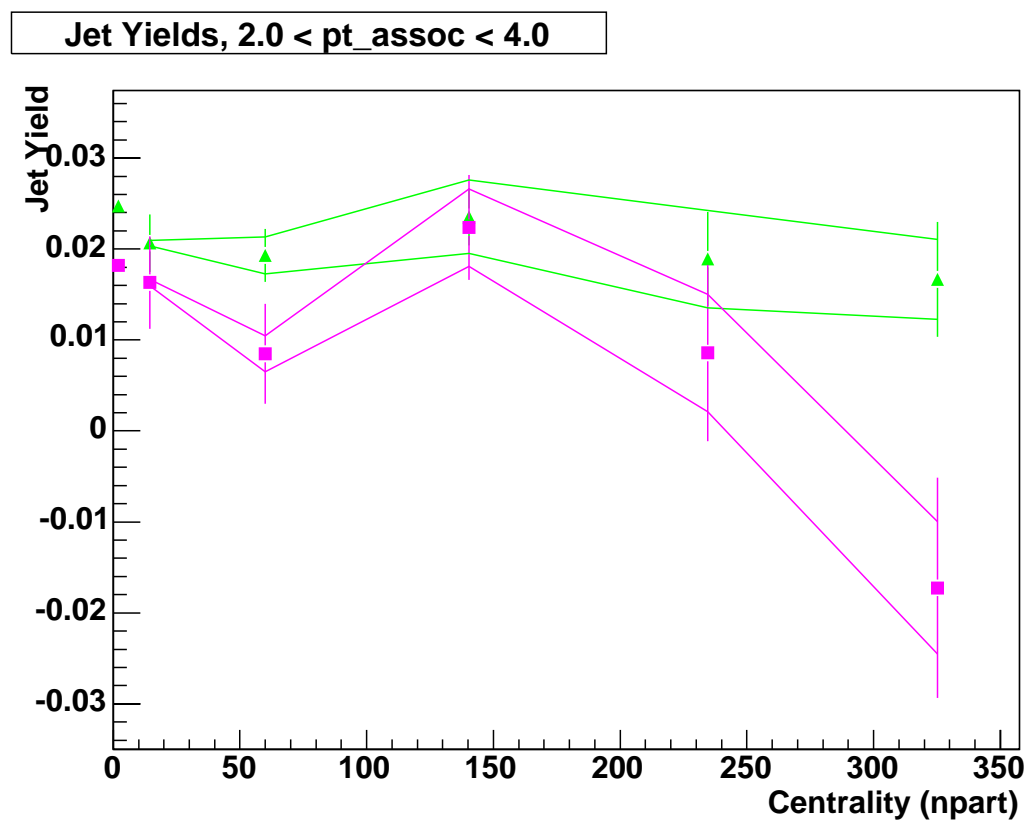


Figure 4.20: Run02 Au+Au,  $2.25 GeV/c < p_T^{\text{trig}} < 2.5 GeV/c$ ,  $2.0 < p_T^{\text{assoc}} < 4.0$ , Associated Jet Yields

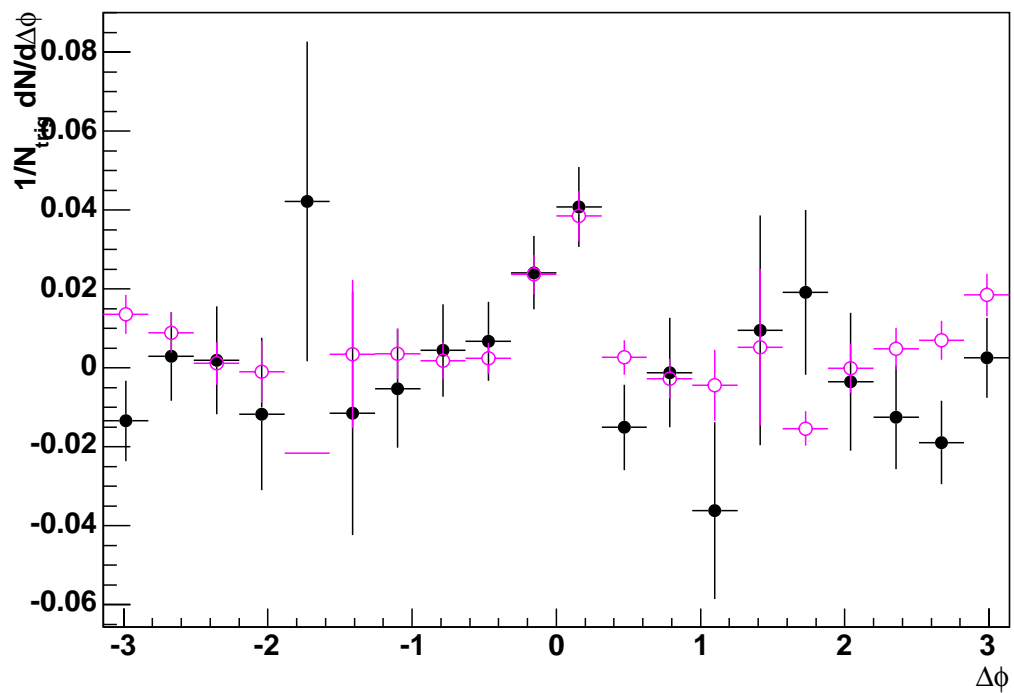


Figure 4.21: Run02 Au+Au,  $2.25GeV/c < p_T^{trig}$ , Background subtracted  $\frac{1}{N_{trig}} \frac{dN^{ch}}{d\phi}$  distributions, for associated bins of  $2.0 < p_T^{assoc} < 4.0$ , centralities 0-10 and 60-90%.

# Chapter 5

## Discussion

While the suppression of high- $p_T$  particles as seen in the inclusive  $p_T$  distributions already indicates strong modifications to behavior at high  $p_T$ , the inclusive distributions cannot probe the properties of this loss directly, and specifically, cannot tell whether jet energy loss in a dense colored medium is the correct paradigm for describing effects at RHIC.

$\gamma$ -hadron correlations provides evidence for jet-like structures at high- $p_T$ , allowing for a jet-suppression interpretation of the behavior at high- $p_T$ . In addition, and perhaps more importantly, correlations allow one to study the modifications to jet structure due to propagation of the jet in the dense medium created in the aftermath of a heavy ion collision, or probe cold nuclear effects on jets in  $d$ +Au collisions.

### 5.1 Sources of Trigger Photons

The sources of  $\gamma$ 's are dominated by decays from mesons, with the majority of these decays coming from  $\pi^0$ 's. The next biggest contributor are  $\eta$ 's, at about 15%. At the energy of the trigger photons in this analysis, the QCD direct photon contribution is thought to be very small. In addition to these physics sources, there is also a neutron/anti-neutron background contribution to the trigger photons, since these cannot be removed by a charge veto. While a shower-shape cut helps to remove many of these contributions, fluctuations in the hadron shower make some neutron interactions look very much like a photon. We have estimated these background

particle	$\frac{dN_x/dm_T}{dN_\pi^0/dm_T}$	decay branch	branching ratio
$\pi^0$	1.0	$\pi^0 \rightarrow \gamma\gamma$	98.798%
		$\pi^0 \rightarrow e^+e^-\gamma$	1.198%
$\eta$	0.55	$\eta \rightarrow \gamma\gamma$	32.21%
		$\eta \rightarrow \pi^+\pi^-\gamma$	4.77%
		$\eta \rightarrow e^+e^-\gamma$	$4.9 \times 10^{-3}$
		$\eta \rightarrow \pi^0\gamma\gamma$	$7.1 \times 10^{-4}$
		$\eta \rightarrow \mu^+\mu^-\gamma$	$3.1 \times 10^{-4}$
$\omega$	0.8	$\omega \rightarrow \pi^0\gamma$	8.5%
		$\omega \rightarrow \eta\gamma$	$6.5 \times 10^{-4}$
$\eta'$	0.8	$\eta' \rightarrow \rho\gamma$	30.2%
		$\eta' \rightarrow \omega\gamma$	3.01%
		$\eta' \rightarrow \gamma\gamma$	2.11%

Table 5.1: Hadron Decay Parameters Used in Calculating Contributions to Photons contributions in section 3.5.4, and find them to range from 2-8% of the total yield of trigger photons, with a higher percentage of background in the more central events. The growth in the neutron contamination background is consistent with the relative increase of baryons seen at RHIC.

To determine the contributions to the trigger  $\gamma$ 's from the various meson sources, various decay simulations were run. To start with, the PHENIX measured  $\pi^0$  spectrum was fit to a Hagedron-modified power-law: 5.1 we lis

$$\frac{dN_\pi^0}{dp_T} = A(1 + \frac{p_T}{p_0})^{-n} \quad (5.1)$$

Then we generated many  $\pi^0$ 's assuming a flat rapidity distribution and with a  $p_T$  distribution as given by the fit above. These  $\pi^0$ 's are then decayed to the channels given in table 5.1, with the given branching ratios: The other meson contributions are estimated assuming  $m_T$ -scaling, that is, assuming that the shapes of the  $m_T$ -spectrum are the same, but with the ratios given in table 5.1. The contributing channels for the other mesons are also given in the table above. In figure 5.1 we plot the ratio of  $\gamma/\pi^0$ , as a function of  $p_T$ , for the various decay contributions. The main contribution comes from  $\pi^0$ (85%), with most of the rest coming decays of the  $\eta$ . The contributions from direct photons in the  $p_T$  ranges of this study are negligible.

The trigger photons are highly correlated in angle and energy to the decayed

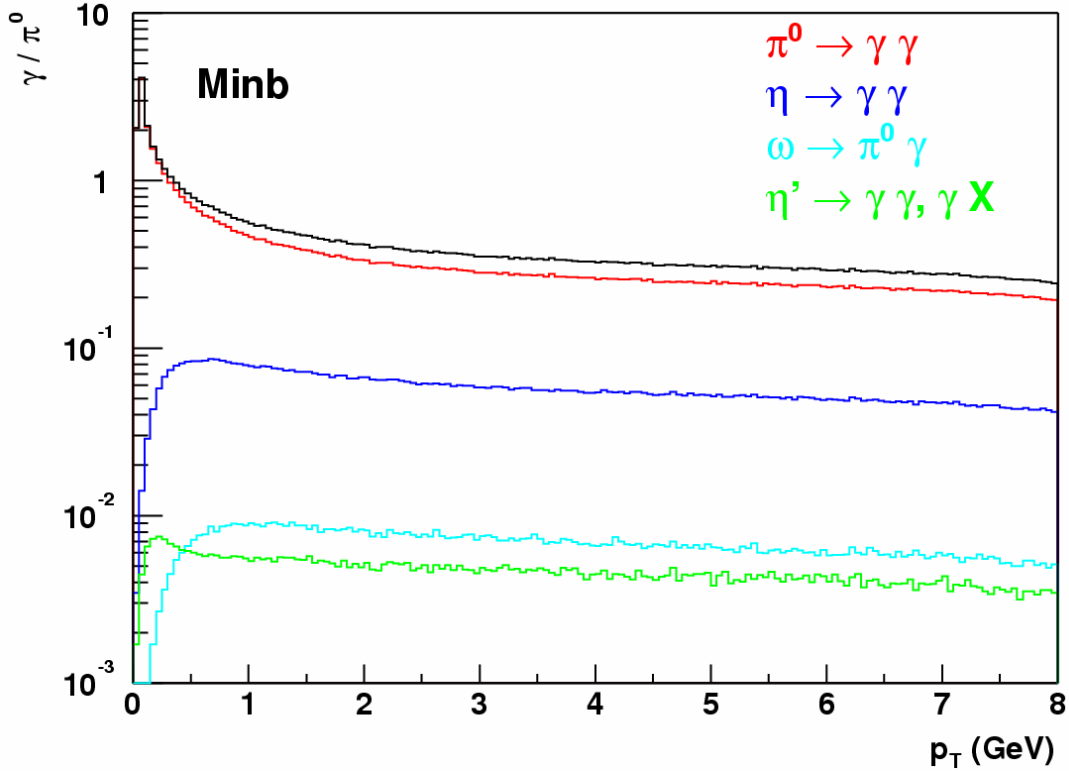


Figure 5.1:  $\gamma/\pi^0$  ratio for Decays from the Main Meson Contributors in Minimum Bias Au+Au events. At  $\sim 2.25$  GeV/c, the main contributions come from  $\pi^0$  and  $\eta$ 's.

meson, which are themselves primarily from the fragmentation of a jet, so they serve as a good proxy for the jet. This kind of leading particle analysis is necessary because of the high backgrounds in Au+Au. However, because the analysis is based on leading particles, there is a large bias towards higher  $z$  in the fragmentation. That is, the jets that are triggered upon are primarily those that fragment with higher  $z$ .

This is not much of a problem because in principle, we use the  $p+p$  data as a baseline, using the exact same analysis techniques. That is, the null hypothesis is that if there are no differences in the correlations between  $d$ +Au and Au+Au with  $p+p$ , then there are no extra effects of jet production in the cold or hot nuclear medium. So similarities or differences in the angular shape and jet associated yield in nuclear systems compared to  $p+p$  collisions will tell us what happens to jets in a

nuclear medium. This is the beginning of the “jet tomography” of .

One important aspect of  $\gamma$ -hadron correlation studies is that, at higher  $p_T$ , direct photons from gluon Compton processes will begin to dominate. Since photons interact only electromagnetically, they are only weakly affected by the hot nuclear medium, and thus will reach the detector largely unscathed. Since these photons do not fragment, they give a direct measure of the energy in the hard scattering. That is, they are very similar to a fully reconstructed jet, but they have the feature that they can be experimentally accessed in heavy-ion collisions. Since the away side jet should be balanced in energy, they allow for direct and well controlled measurements of modifications to the away side jet. Additionally, unlike quark or gluon jets, direct photons will probe the entire spatial volume of the heavy-ion collision, and not suffer from surface effects, as we will explain below. Unfortunately, this requires an order or magnitude more statistics than are available from the current data set.

## 5.2 Cold Nuclear Effects in d+Au

Since there is little produced material for outgoing jets to propagate through,  $d+Au$  collisions provide a control system that is only sensitive to modifications of jet behavior in cold nuclear systems, by either initial state or final state effects. In figure 5.2, a picture of a jet propagating through the nucleus is shown, showing possible multiple scattering before and after a hard collision.

This initial-state multiple scattering is widely believed to be the cause of the Cronin-Effect [16]. One can potentially address this multiple scattering by looking for increases in  $k_T$ , which is the transverse momentum component of partons relative to the beam axis. Increases in  $k_T$  should manifest themselves as a broadening of the width of the away side jet.

The near side and far side widths are plotted in 4.4 and 4.5, respectively. The near width reflects the  $j_T$  from the fragmentation of the jet (along with some smearing due to the meson decay). The far side jet, however, will not be exactly collinear

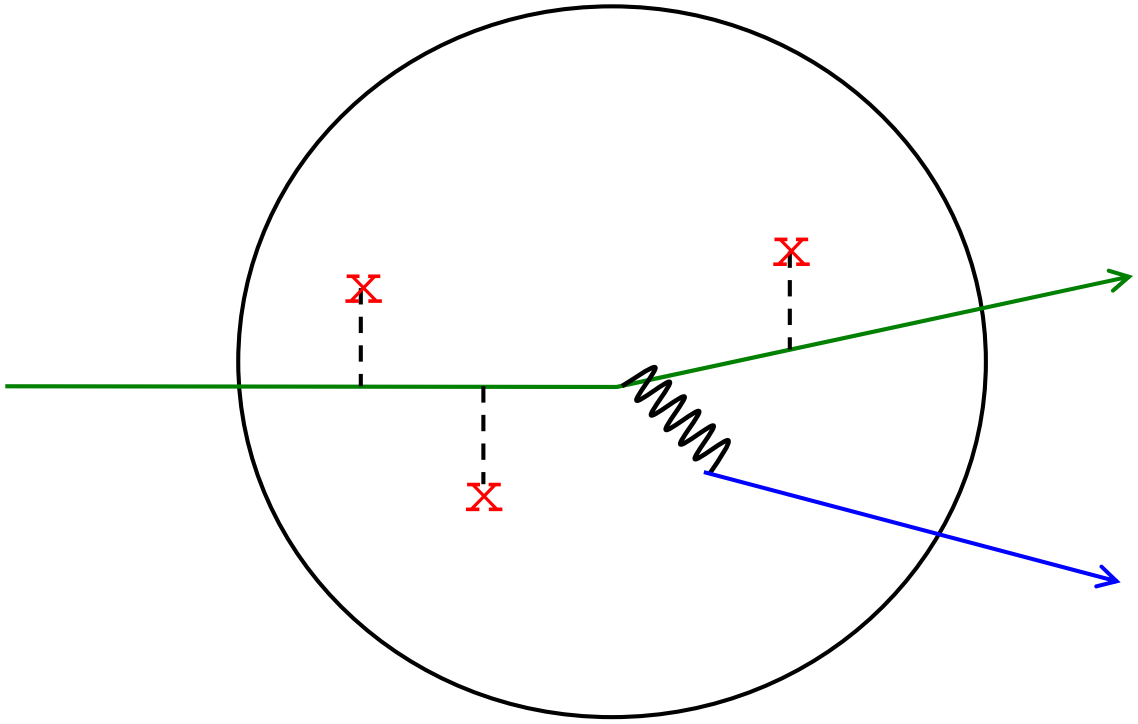


Figure 5.2: An incoming parton scatters multiple times before the hard scattering event, and the outgoing parton can also scatter multiple times before leaving the nucleus, as seen from the frame where the nucleus is at rest. The jet propagates only through the nucleus, and therefore suffers only from cold nuclear effects.

with the near side jet, due to effects from  $k_T$ . The results from this thesis show a comparable width on the near side between  $p+p$  and  $d+\text{Au}$ , consistent with jet fragmentation in vacuum for both cases. This is also true on the far side; there seems to be only a small increase in the away side width, and therefore only a small increase in  $k_T$  in  $d+\text{Au}$  collisions compared to  $p+p$  collisions.

The more interesting effect seen in  $d+\text{Au}$  collisions comes from the drop in the jet associated yields for moderately higher  $p_T$ , in the  $\sim 2\text{-}4$  GeV/c range for trigger photons of 3.5 GeV/c. This drop in the associated yields might point to a deeper understanding of the Cronin effect. From the multiple scattering explanations of the Cronin effect one naively expects no change in the associated yields, since the  $p_T$ -broadening occurs at the parton level. These  $p_T$  broadened jets are expected to fragment normally, so that one should not see a modification to the associated yields

given the same cut on trigger photons. What we see, instead, is a change such that it seems as if the  $\langle z \rangle$  selected by a trigger photon is pushed higher in more central collisions, leaving less energy,  $(1 - z)P_{jet}$ , in the remaining string for producing a 2-4 GeV/c associated particle.

This point is highlighted by the fundamental inability of collinear factorization coupled with higher order effects from multiple scattering to describe the  $\eta$  dependence of particle production at high  $p_T$  [2], and in particular the inability of these models to describe the enhancement in production at backward rapidities (in the direction of the Au-going side). The results for  $R_{CP}$  for different values of  $\eta$  are plotted in figures 5.3 and 5.4, which shows a pattern of suppression at forward (deuteron-going side) pseudo-rapidities, with a continuous trend towards enhancement at backward rapidities.

In a  $2 \rightarrow 2$  hard scattering process, the *eta* of the final-state hadrons reflect approximately the distribution of momentum fractions  $x$ . Thus, different regions in  $\eta$  will sample different regions of  $x$  in the deuteron and Au nucleus. In particular, hadrons produced in the forward regions of  $1.2 < \eta < 2.4$  select  $0.004 < x_{Au} < 0.06$ , and in the backward regions  $-2.2 < \eta < -1.2$  selects  $x_{Au} \sim 0.13$ . Hence, one possible explanation for the pseudo-rapidity dependence is a much stronger shadowing/anti-shadowing of the gluon distribution functions in the regions of  $x_{Au}$  indicated above [36] [45]. In the context of the Color-Glass Condensate model, this shadowing/anti-shadowing is explained by the fusion of gluons at low  $x$  (shadowing), and where these fused gluons then create an enhancement at some higher  $x$  (anti-shadowing).

This is particularly interesting because the centrality dependence of this shadowing has never been measured before. Nuclear DIS experiments sample all centralities of the nucleus, and so their results represent an average over all centralities. Previous fixed target experiments have not been able to do these studies as a function of centrality. Thus, for the first time, RHIC has allowed experimenters to study modifications to the distribution functions, and in particular the gluon distributions, as

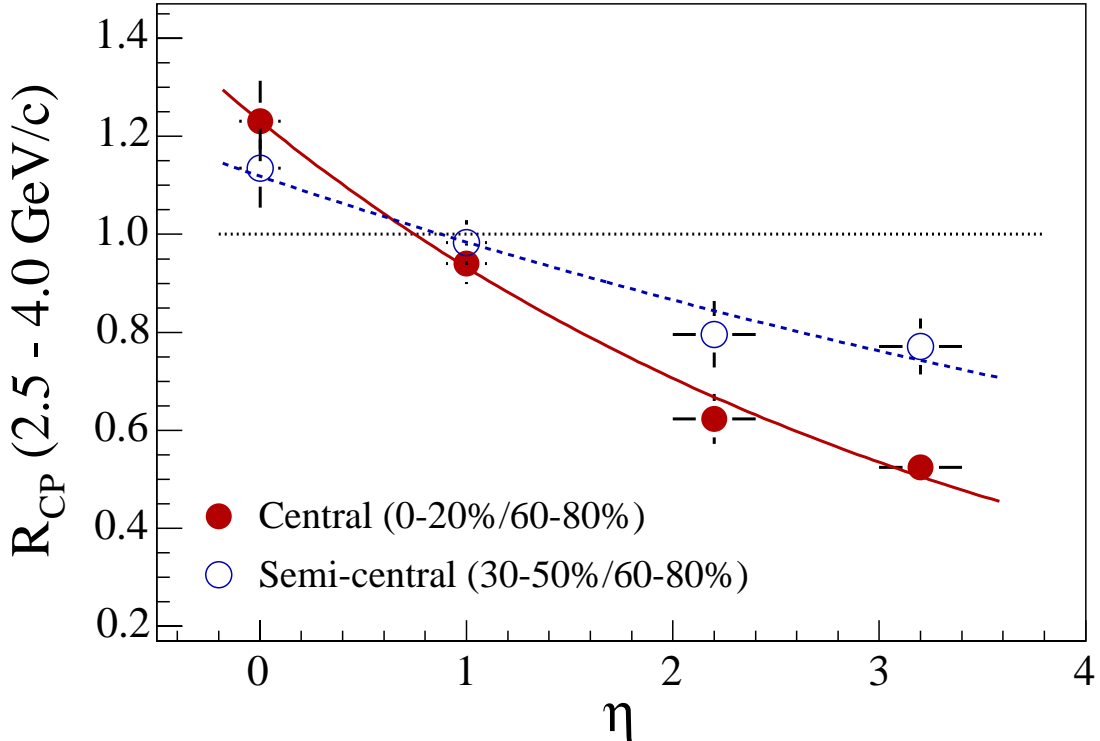


Figure 5.3:  $R_{CP}(\eta)$  for  $2.5 < p_T < 4.0$  GeV/c particles as measured by the Brahms Collaboration [20].

a function of centrality.

Because of these modifications to the gluon distributions, the mix of outgoing gluon jets to quark jets will be modified, with an increase in  $gg \rightarrow gg$  and  $gg \rightarrow q\bar{q}$  over  $gq \rightarrow gq$  processes. Thus, the average outgoing jet in central  $d$ +Au is gluon-enriched, and hence has an averaged fragmentation function which is softer than those jets from peripheral  $d$ +Au. No quantitative study of this kind has been done presently.

There may also be final state effects which have been ignored up to now, which is equivalent to saying that leading twist collinear factorization breaks down for hard scattering in a nucleus, due to the multiple parton correlations that might occur. In figure 5.2, we show what happens to a parton as it crosses the nucleus in the rest

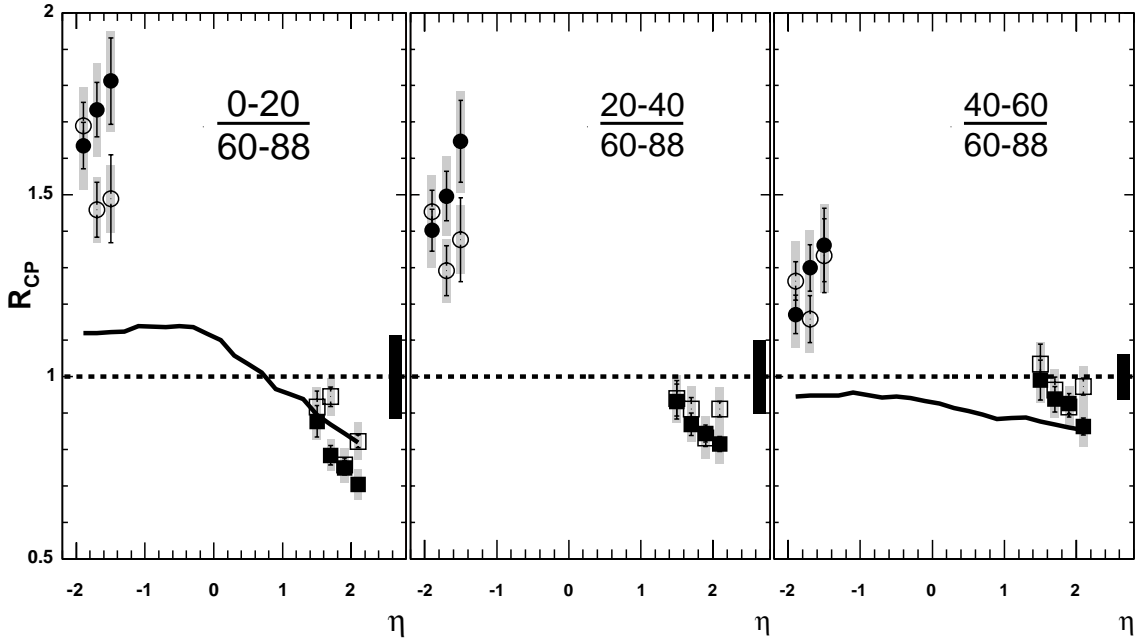


Figure 5.4:  $R_{CP}(\eta)$  for  $1.5 < p_T < 4.0$  GeV/c particles as measured by the PHENIX Collaboration (private communication, Chun Zhang).

frame of the nucleus. The parton from the incoming parton has a few soft initial scatters, then has a hard scatter, and the outgoing parton has a few more multiple scatters. This induces non-negligible power corrections, which have been recently computed, and which may eventually explain the present results [53].

While at present the theoretical situation with jets in nuclear systems is not completely settled, the modification of the associated yields seen in this analysis is an important observation for understanding any cold nuclear effects which may occur. This is important in its own right as a laboratory for understanding QCD, but additionally, these cold nuclear effects need to be understood if one wants to quantitatively understand jet modifications in heavy-ion collisions.

### 5.3 Jets in Au+Au

Outgoing scattered partons in Au+Au collisions, in addition to cold nuclear effects, will experience modifications due to propagation through the produced dense medium left in the wake of the colliding nuclei, and thus can be used as a probe of

this medium, which could potentially be a quark-gluon plasma.

Like the  $d+\text{Au}$  results, there do not seem to be a large change in the near side widths in  $\text{Au}+\text{Au}$  with respect to the values in  $p+p$  (figure 4.18). Also, the near side associated yields at moderate  $p_T$  (1.0-4.0 GeV/c) seem to be comparable to that seen in  $p+p$ . Both these results are indicative of vacuum fragmentation, that is, that the jets seem to propagate out of the medium (losing energy along the way) and fragment very similarly to  $p+p$ .

The situation on the away side is very different, however. As one gets to greater centralities, the away side jet gradually disappears, reducing to nothing in the 10% most central collisions. This shows that there is a large quenching of the away side jet, which is most likely due to the large distance that the away side jet must cross to get out of the medium. In a jet-quenching scenario, only those jets near the surface are triggered upon, since they are the only ones that lose low enough amounts of energy to escape that one can trigger upon the leading decay photon. These jets then fragment normally after escaping. The away side jet must traverse the collision overlap region, and there lose large amounts of energy.

This effect has been simulated in a simple Glauber Monte Carlo, where energy density is assumed to be proportional to the  $N_{part}$  distribution and drops with time as  $1/t$ , in keeping with a longitudinal expansion of the medium. The spatial origins of the jets are proportional to the  $N_{coll}$  distribution. The jets are then propagated in a random direction, and lose energy according to several formulations. It was found that for any scenario where energy loss monotonically increases with the length traversed, there are more jet losses in the center of the overlap region than on the surface (see figure 5.5). Thus, there is always a “surface” effect to jet survival, assuming only that jet energy loss is monotonically increasing with length. The magnitude of this surface survival effect depends on the specific energy loss scenario, and the space-time development of the medium.

Since we have investigated down to associated  $p_T$  of 1 GeV/c, the radiated gluons must either be below this 1 GeV/c cutoff, or they are absorbed in the medium

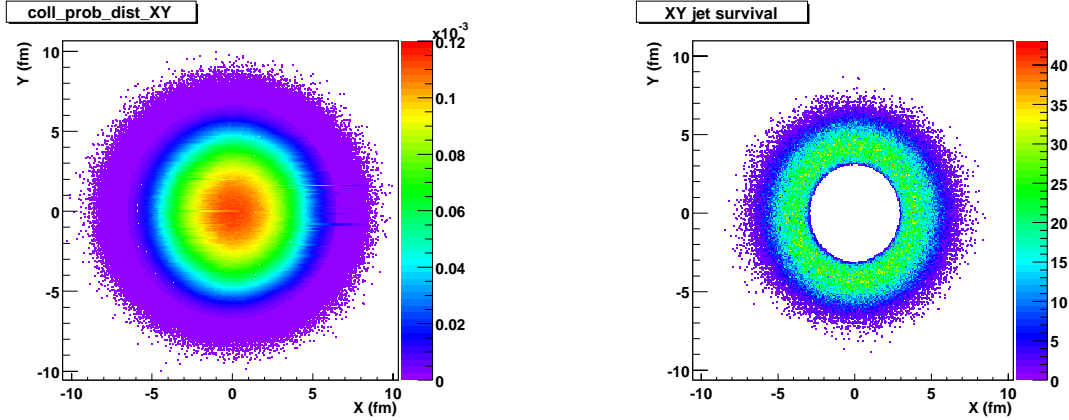


Figure 5.5: The distribution of originating positions  $N_{coll}(x, y)$  in the transverse plane for hard-scattered partons in an Au+Au collision (left). The distribution of positions for surviving jets (right).

as the parton traverses out of the medium. Thus, in this analysis, we have seen unambiguous observation of jet quenching, and constrained the range of possibilities for the expected radiated gluons to show up.

# Bibliography

- [1] Alberto Accardi. Cronin effect in proton nucleus collisions: A survey of theoretical models. 2002.
- [2] Alberto Accardi. Cronin effect from backward to forward rapidity: A tale of two mysteries. 2004.
- [3] K. Adcox et al. Construction and performance of the phenix pad chambers. *Nucl. Instrum. Meth.*, A497:263–293, 2003.
- [4] K. Adcox et al. Phenix central arm tracking detectors. *Nucl. Instrum. Meth.*, A499:489–507, 2003.
- [5] K. Adcox et al. Phenix detector overview. *Nucl. Instrum. Meth.*, A499:469–479, 2003.
- [6] C. Adler et al. The rhic zero-degree calorimeters. *Nucl. Instrum. Meth.*, A499:433–436, 2003.
- [7] S. S. Adler et al. Absence of suppression in particle production at large transverse momentum in  $s(nn)^{**}(1/2) = 200$ -gev d + au collisions. *Phys. Rev. Lett.*, 91:072303, 2003.
- [8] S. S. Adler et al. Elliptic flow of identified hadrons in au + au collisions at  $s(nn)^{**}(1/2) = 200$ -gev. *Phys. Rev. Lett.*, 91:182301, 2003.
- [9] S. S. Adler et al. Mid-rapidity neutral pion production in proton proton collisions at  $s^{**}(1/2) = 200$ -gev. *Phys. Rev. Lett.*, 91:241803, 2003.

- [10] S. S. Adler et al. Phenix on-line systems. *Nucl. Instrum. Meth.*, A499:560–592, 2003.
- [11] S. S. Adler et al. Suppressed pi0 production at large transverse momentum in central au + au collisions at  $s(nn)^{**}(1/2) = 200$ -gev. *Phys. Rev. Lett.*, 91:072301, 2003.
- [12] M. Aizawa et al. Phenix central arm particle id detectors. *Nucl. Instrum. Meth.*, A499:508–520, 2003.
- [13] Y. Akiba et al. The phenix ring imaging cherenkov detector. *Nucl. Instrum. Meth.*, A453:279–283, 2000.
- [14] H. Akikawa et al. Phenix muon arms. *Nucl. Instrum. Meth.*, A499:537–548, 2003.
- [15] M. Allen et al. Phenix inner detectors. *Nucl. Instrum. Meth.*, A499:549–559, 2003.
- [16] D. Antreasyan et al. Production of hadrons at large transverse momentum in 200- gev, 300-gev and 400-gev p p and p n collisions. *Phys. Rev.*, D19:764, 1979.
- [17] L. Aphecetche et al. Phenix calorimeter. *Nucl. Instrum. Meth.*, A499:521–536, 2003.
- [18] Michele Arneodo. Nuclear effects in structure functions. *Phys. Rept.*, 240:301–393, 1994.
- [19] S. H. Aronson et al. Phenix magnet system. *Nucl. Instrum. Meth.*, A499:480–488, 2003.
- [20] I. Arsene et al. On the evolution of the nuclear modification factors with rapidity and centrality in d + au collisions at  $s(nn)^{**}(1/2) = 200$ -gev. 2004.

- [21] R. Baier, Yuri L. Dokshitzer, Alfred H. Mueller, S. Peigne, and D. Schiff. Radiative energy loss and  $p(t)$ -broadening of high energy partons in nuclei. *Nucl. Phys.*, B484:265–282, 1997.
- [22] R. Baier, Yuri L. Dokshitzer, Alfred H. Mueller, S. Peigne, and D. Schiff. Radiative energy loss of high energy quarks and gluons in a finite-volume quark-gluon plasma. *Nucl. Phys.*, B483:291–320, 1997.
- [23] R. Baier, Yuri L. Dokshitzer, Alfred H. Mueller, and D. Schiff. Medium-induced radiative energy loss: Equivalence between the bdmqs and zakharov formalisms. *Nucl. Phys.*, B531:403–425, 1998.
- [24] Gordon Baym. Rhic: From dreams to beams in two decades. *Nucl. Phys.*, A698:XXIII–XXXII, 2002.
- [25] S. Belikov, J. Hill, J. Lajoie, H. Skank, and G. Sleege. Phenix trigger system. *Nucl. Instrum. Meth.*, A494:541–547, 2002.
- [26] J. D. Bjorken. Energy loss of energetic partons in quark - gluon plasma: Possible extinction of high  $p(t)$  jets in hadron - hadron collisions. FERMILAB-PUB-82-059-THY.
- [27] F. Borkowski, P. Peuser, G. G. Simon, V. H. Walther, and R. D. Wendling. Electromagnetic form-factors of the proton at low four - momentum transfer. *Nucl. Phys.*, B93:461, 1975.
- [28] J. W. Cronin et al. Production of hadrons with large transverse momentum at 200-gev, 300-gev, and 400-gev. *Phys. Rev.*, D11:3105, 1975.
- [29] K. Eggert et al. Angular correlations between the charged particles produced in  $p p$  collisions at isr energies. *Nucl. Phys.*, B86:201, 1975.
- [30] K. Eggert et al. Angular correlations in proton proton collisions producing a high transverse momentum pi0. *Nucl. Phys.*, B98:73, 1975.

- [31] K. J. Eskola, V. J. Kolhinen, and P. V. Ruuskanen. Scale evolution of nuclear parton distributions. *Nucl. Phys.*, B535:351–371, 1998.
- [32] K. J. Eskola, V. J. Kolhinen, and C. A. Salgado. The scale dependent nuclear effects in parton distributions for practical applications. *Eur. Phys. J.*, C9:61–68, 1999.
- [33] H. Fessler et al. A tower structured scintillator lead photon calorimeter using a novel fiber optics readout system. *Nucl. Instr. Meth.*, A228:303, 1985.
- [34] Justin Frantz. Phenix direct photons in 200-gev p + p and au + au collisions. *J. Phys.*, G30:S1003–S1006, 2004.
- [35] D. F. Geesaman, K. Saito, and Anthony W. Thomas. The nuclear emc effect. *Ann. Rev. Nucl. Sci.*, 45:337–390, 1995.
- [36] Francois Gelis and Jamal Jalilian-Marian. From dis to proton nucleus collisions in the color glass condensate model. ((t)). *Phys. Rev.*, D67:074019, 2003.
- [37] Miklos Gyulassy and Xin-nian Wang. Multiple collisions and induced gluon bremsstrahlung in qcd. *Nucl. Phys.*, B420:583–614, 1994.
- [38] H. Hahn et al. The rhic design overview. *Nucl. Instrum. Meth.*, A499:245–263, 2003.
- [39] M. Harrison, T. Ludlam, and S. Ozaki. Rhic project overview. *Nucl. Instrum. Meth.*, A499:235–244, 2003.
- [40] M. Hirai, S. Kumano, and M. Miyama. Determination of nuclear parton distributions. *Phys. Rev.*, D64:034003, 2001.
- [41] M. Hirai, S. Kumano, and T. H. Nagai. Nuclear parton distribution functions and their uncertainties. 2004.
- [42] K. Ikematsu et al. A start-timing detector for the collider experiment phenix at rhic-bnl. *Nucl. Instrum. Meth.*, A411:238–248, 1998.

- [43] O. Kaczmarek, F. Karsch, P. Petreczky, and F. Zantow. Heavy quark anti-quark free energy and the renormalized polyakov loop. *Phys. Lett.*, B543:41–47, 2002.
- [44] Frithjof Karsch. Lattice qcd at high temperature and density. *Lect. Notes Phys.*, 583:209–249, 2002.
- [45] Dmitri Kharzeev, Yuri V. Kovchegov, and Kirill Tuchin. Nuclear modification factor in d + au collisions: Onset of suppression in the color glass condensate. 2004.
- [46] L. D. Landau. *The Collected Papers of L. D. Landau*. Pergamon Press, New York, 1st edition, 1965.
- [47] L. D. Landau and I. Pomeranchuk. Electron cascade process at very high-energies. *Dokl. Akad. Nauk Ser. Fiz.*, 92:735–738, 1953.
- [48] L. D. Landau and I. Pomeranchuk. Limits of applicability of the theory of bremsstrahlung electrons and pair production at high-energies. *Dokl. Akad. Nauk Ser. Fiz.*, 92:535–536, 1953.
- [49] A. B. Migdal. Bremsstrahlung and pair production in condensed media at high-energies. *Phys. Rev.*, 103:1811–1820, 1956.
- [50] J. T. Mitchell et al. Event reconstruction in the phenix central arm spectrometers. *Nucl. Instrum. Meth.*, A482:491–512, 2002.
- [51] Y. Nara, N. Otuka, A. Ohnishi, K. Niita, and S. Chiba. Study of relativistic nuclear collisions at ags energies from p + be to au + au with hadronic cascade model. *Phys. Rev.*, C61:024901, 2000.
- [52] M. Peskin and D. V. Schroeder. *An Introduction to Quantum Field Theory*. Addison-Wesley Publishing Co., Reading, Massachusetts, 1st edition, 1995.
- [53] Jian-wei Qiu and Ivan Vitev. Coherent qcd multiple scattering in proton nucleus collisions. 2004.

- [54] Yu. Ryabov. Low-mass drift chambers of the phenix central spectrometers at rhic. *Nucl. Instrum. Meth.*, A494:194–198, 2002.
- [55] T. Sakaguchi et al. Development of front end electronics for phenix rich. *Nucl. Instrum. Meth.*, A453:382–385, 2000.
- [56] Torbjorn Sjostrand et al. High-energy-physics event generation with pythia 6.1. *Comput. Phys. Commun.*, 135:238–259, 2001.
- [57] P. Steinberg et al. The data collection modules and atm-based event builder for the phenix experiment at rhic. *IEEE Trans. Nucl. Sci.*, 47:304–308, 2000.
- [58] Xin-Nian Wang and Miklos Gyulassy. Hijing: A monte carlo model for multiple jet production in p p, p a and a a collisions. *Phys. Rev.*, D44:3501–3516, 1991.
- [59] Xin-Nian Wang, Miklos Gyulassy, and Michael Plumer. The lpm effect in qcd and radiative energy loss in a quark gluon plasma. *Phys. Rev.*, D51:3436–3446, 1995.

# Appendix A

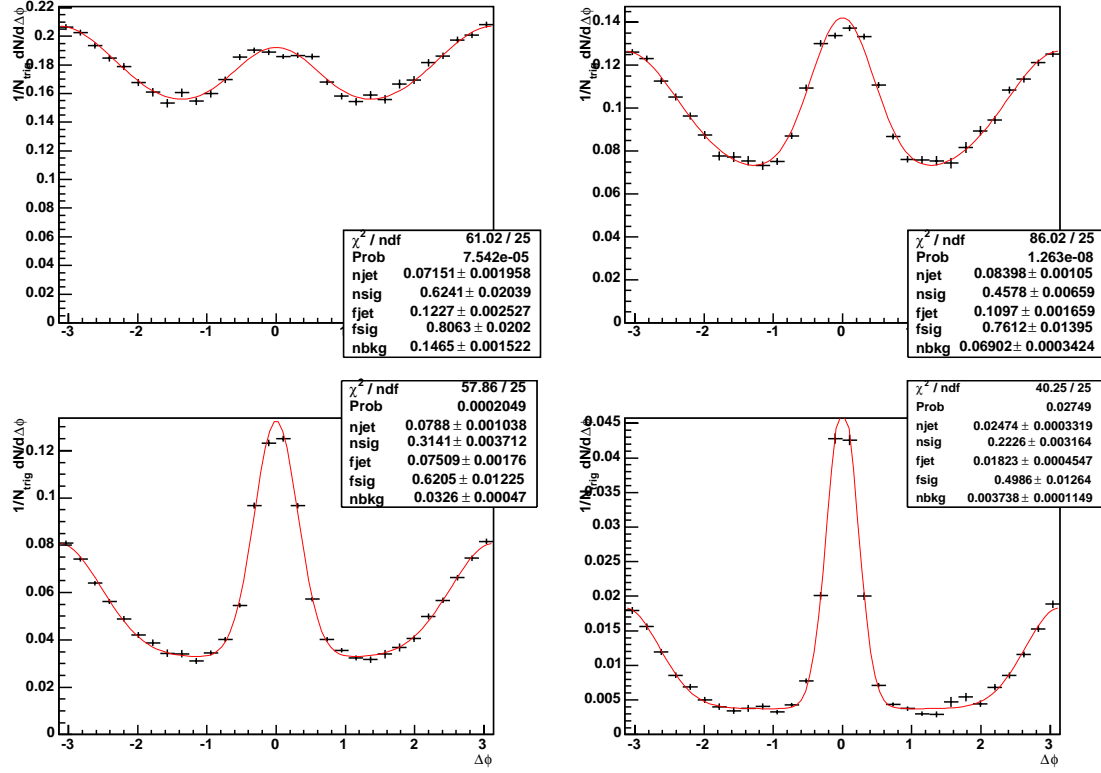
## Associated Yields

The following sections contain the correlated angular yields for  $p+p$ ,  $d+\text{Au}$ , and  $\text{Au}+\text{Au}$ .

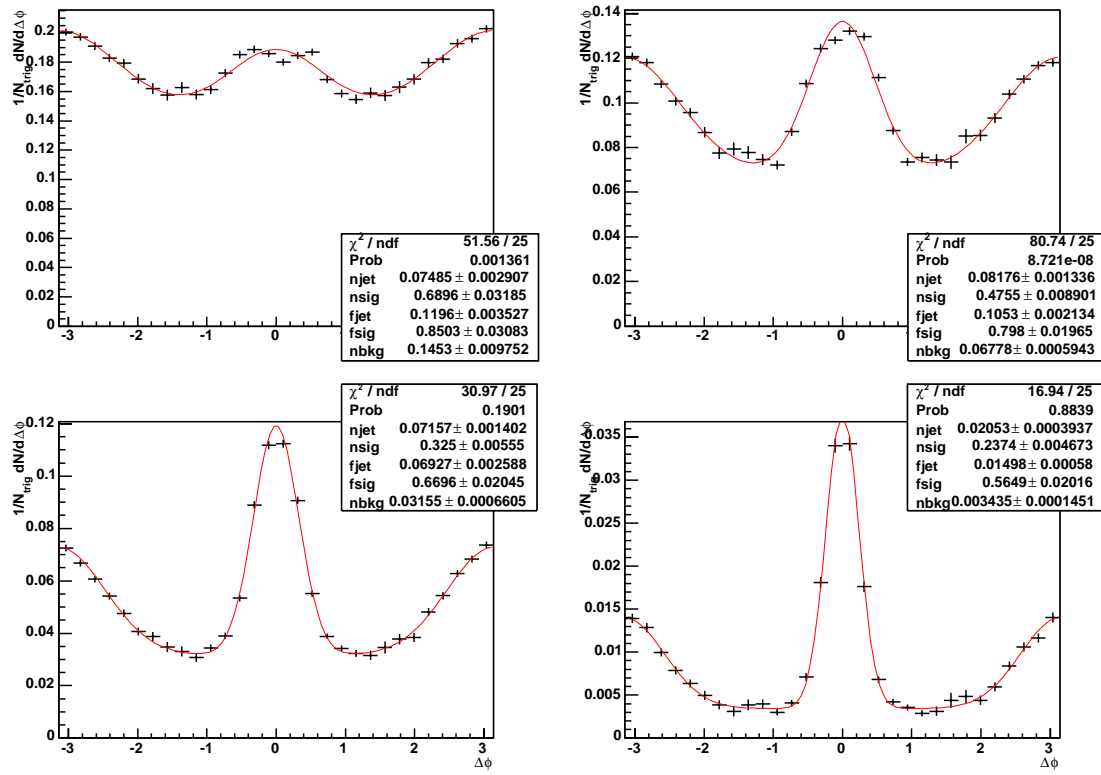
The following associated yields in  $p+p$  and  $d+\text{Au}$  are fit with a near side gaussian, a far side gaussian, and a flat distribution, using a procedure where only the near side gaussian plus flat distribution is fit first, then the far side is fit in a similar manner, so that the parameters from those fits can be used to seed the full fit. The full fit function is

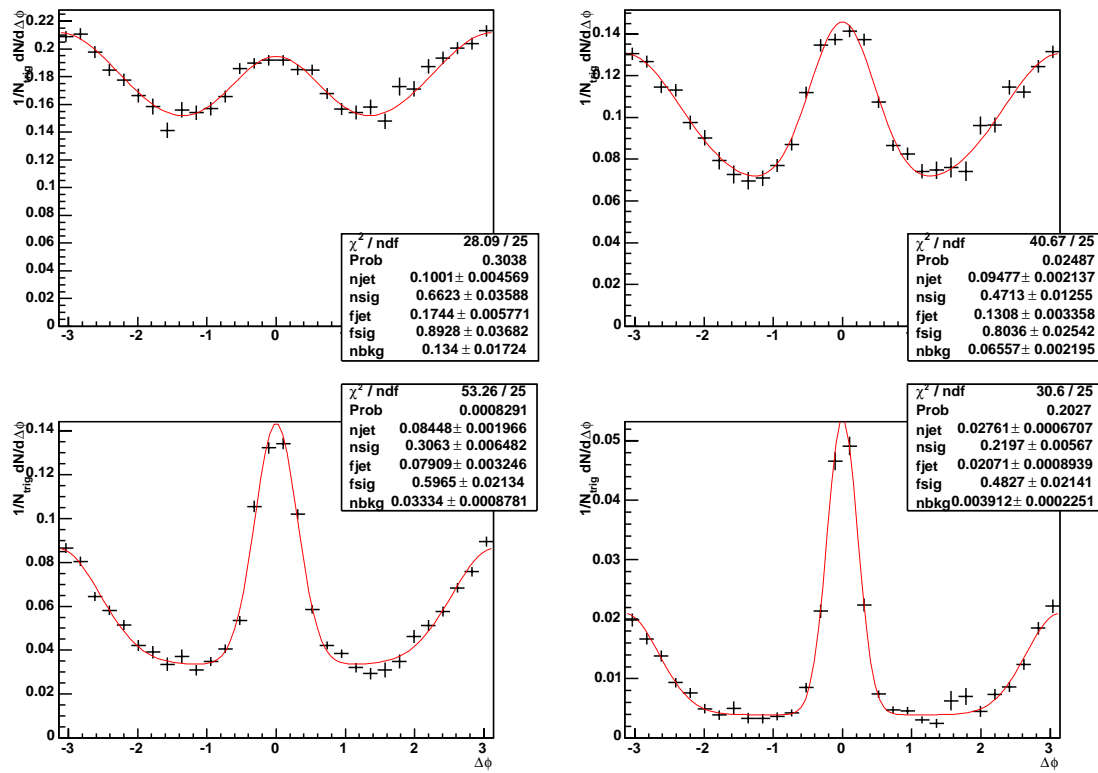
$$\frac{1}{N_{trig}} \frac{dN^{assoc}}{d\Delta\phi} = n_{bkg} + \frac{n_{jet}}{\sqrt{2\pi}\sigma_n} e^{-\frac{\Delta\phi^2}{2\sigma_n^2}} + \frac{f_{jet}}{\sqrt{2\pi}\sigma_f} e^{-\frac{(\Delta\phi-\pi)^2}{2\sigma_f^2}} \quad (\text{A.1})$$

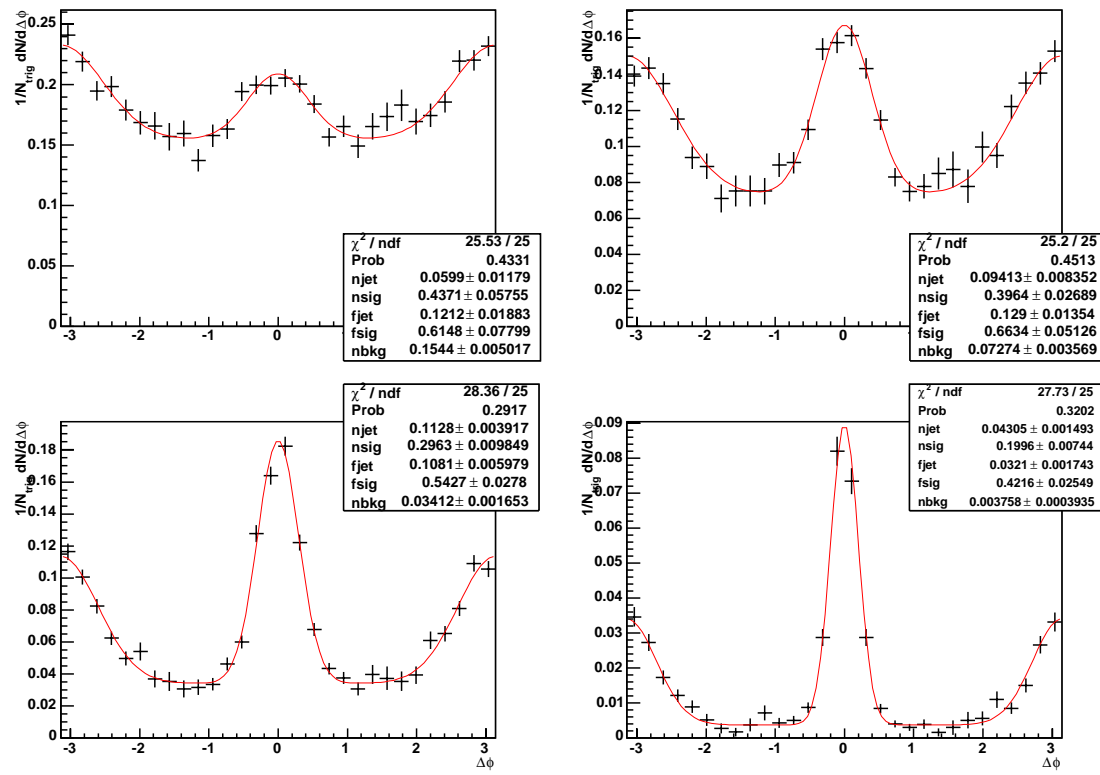
and is defined over a periodic space of period  $2\pi$ , and  $n_{jet}$  is the number of particles in the jet fragment associated with the near side trigger,  $f_{jet}$  is the number of particles in the jet fragment associated with the far side trigger, and  $\sigma_n$  and  $\sigma_f$  are the widths of the near and far side jet, respectively.

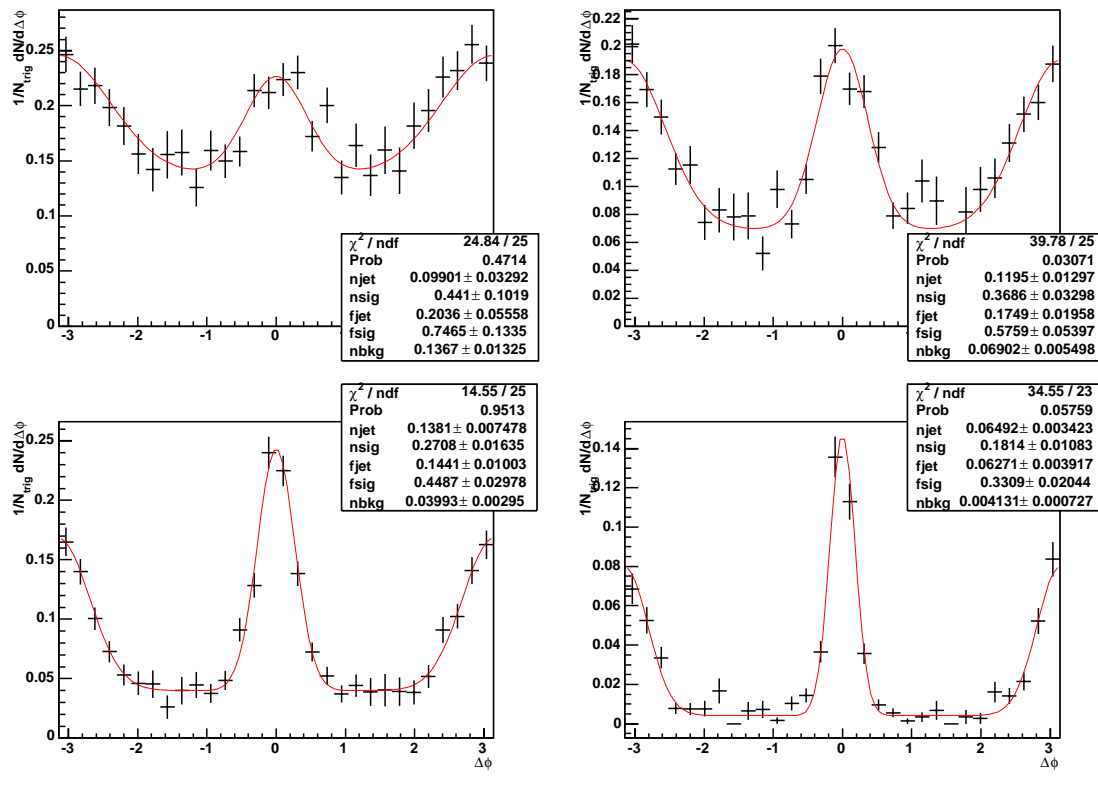
Figure A.1:  $p+p$ ,  $2.25 < p_T^{trig} < 20.0 \text{ GeV}/c$ 

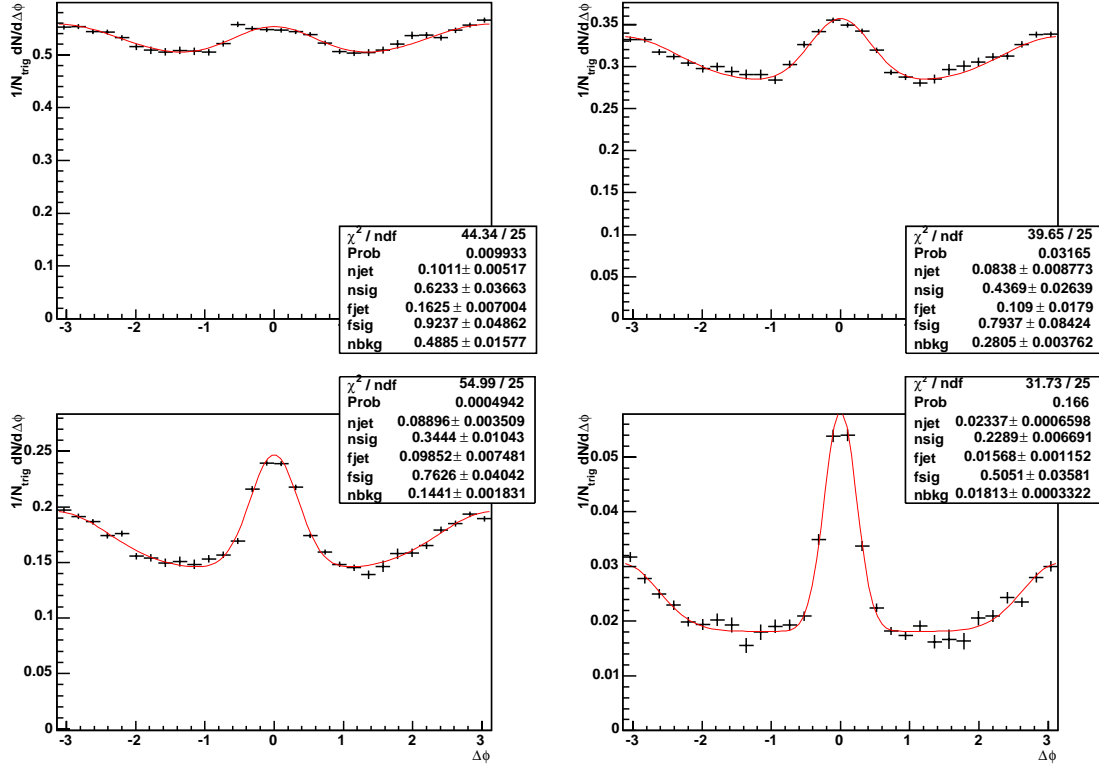
## A.1 Associated Yields in $p+p$

Figure A.2:  $p+p$ ,  $2.25 < p_T^{\text{trig}} < 2.75 \text{ GeV}/c$

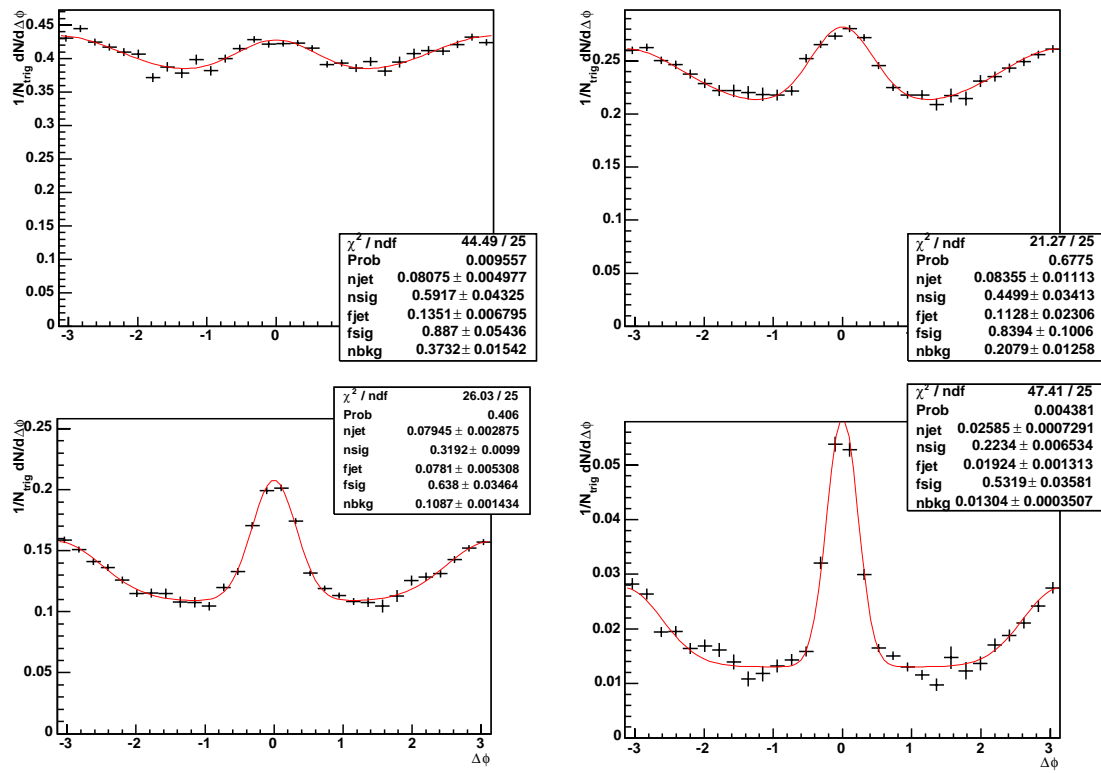
Figure A.3:  $p+p$ ,  $2.75 < p_T^{\text{trig}} < 3.5 \text{ GeV}/c$

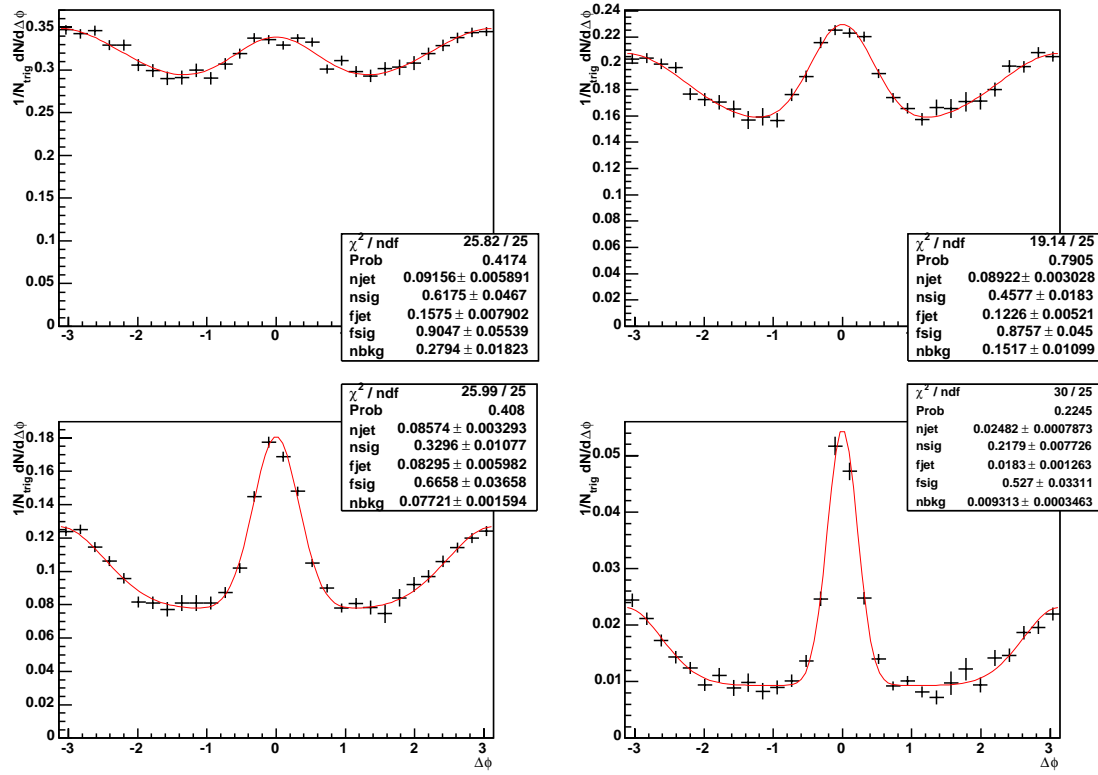
Figure A.4:  $p+p$ ,  $3.5 < p_T^{\text{trig}} < 4.5 \text{GeV}/c$

Figure A.5:  $p+p$ ,  $4.5 < p_T^{trig} < 20.0 \text{ GeV}/c$

Figure A.6:  $d+Au$ ,  $2.25 < p_T^{trig} < 20.0 GeV/c$ , 0-20% central

## A.2 Associated Yields in $d+Au$

Figure A.7:  $d+\text{Au}$ ,  $2.25 < p_T^{\text{trig}} < 20.0 \text{GeV}/c$ , 20-40% central

Figure A.8:  $d+Au$ ,  $2.25 < p_T^{\text{trig}} < 20.0 GeV/c$ , 40-60% central

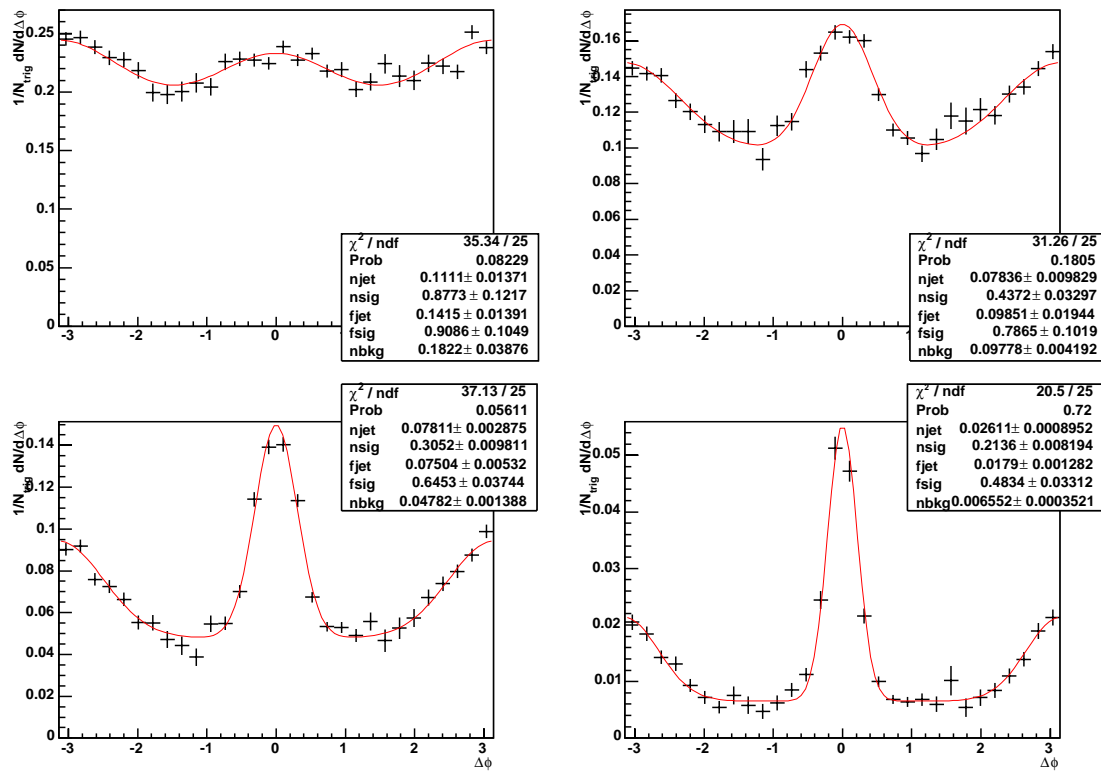
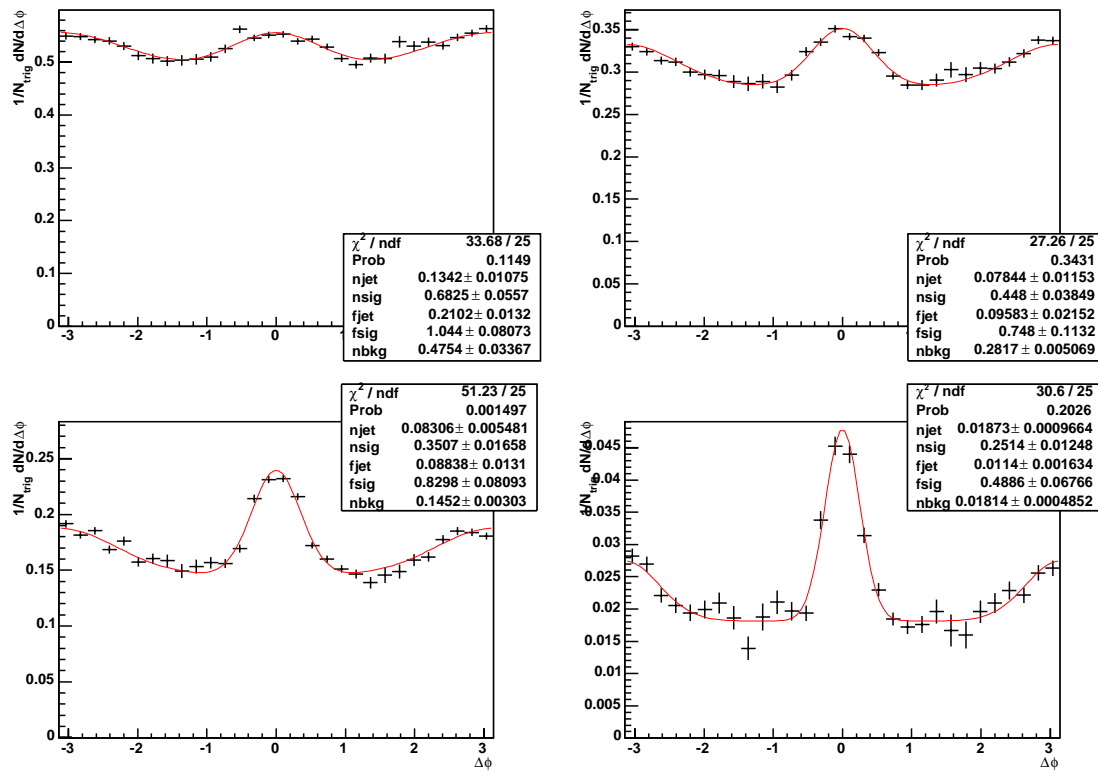
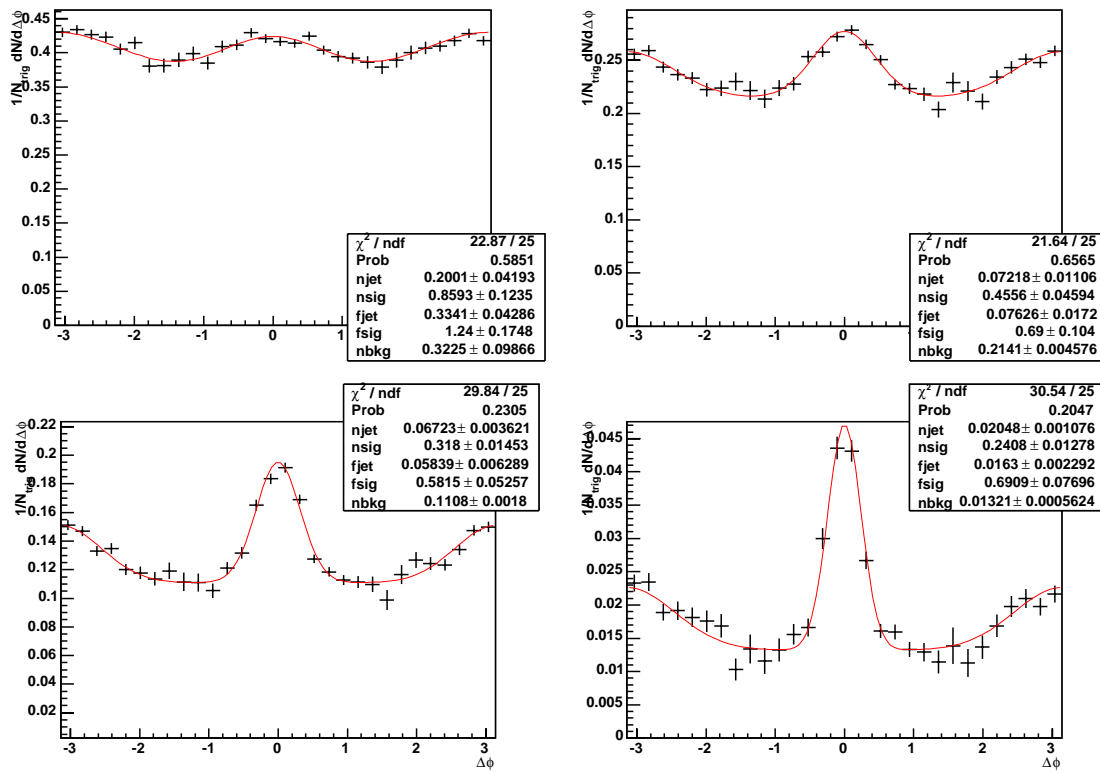
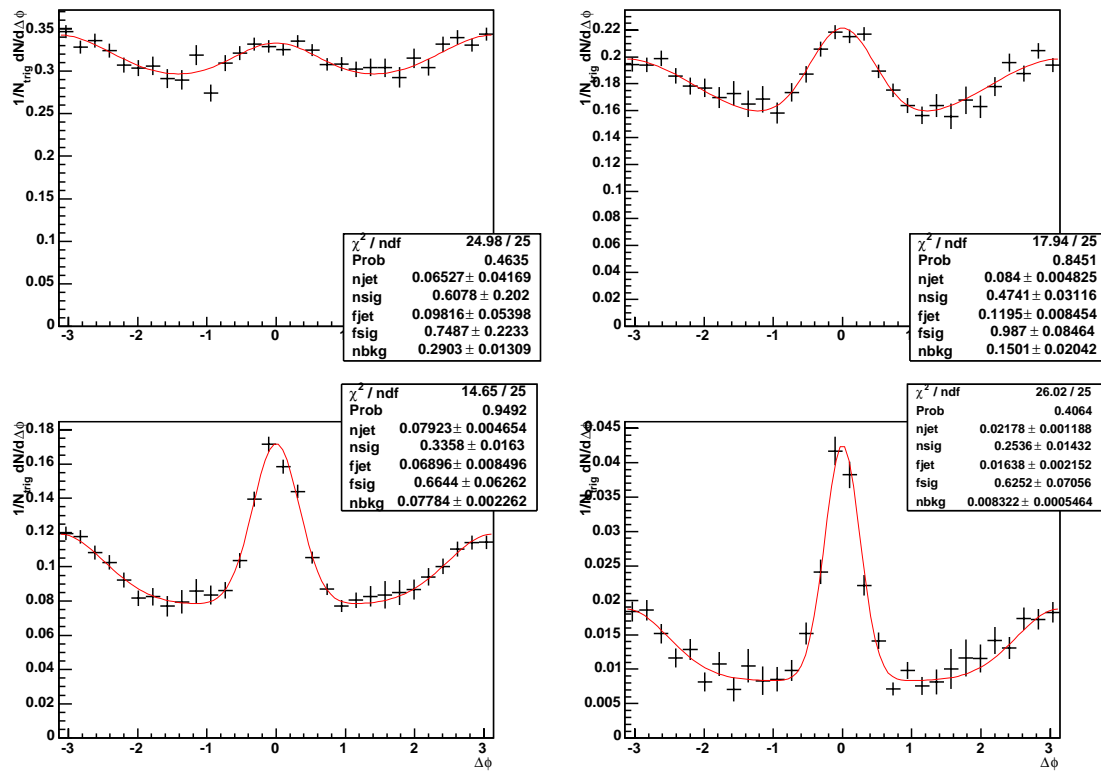
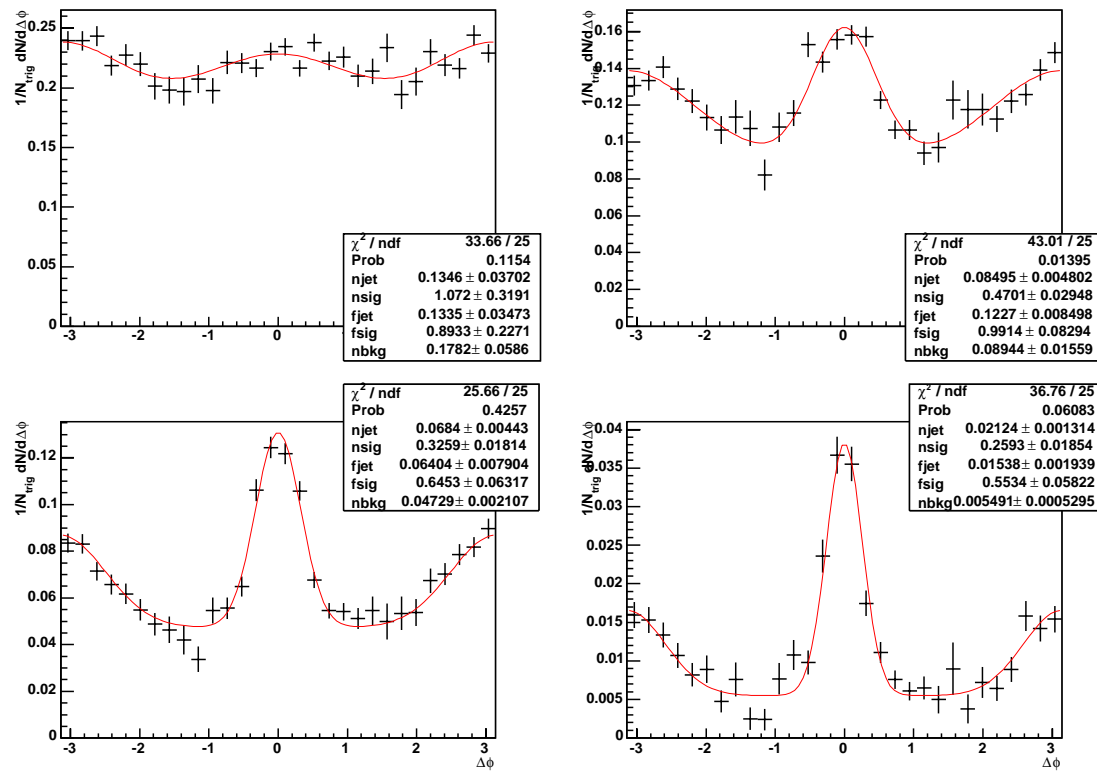


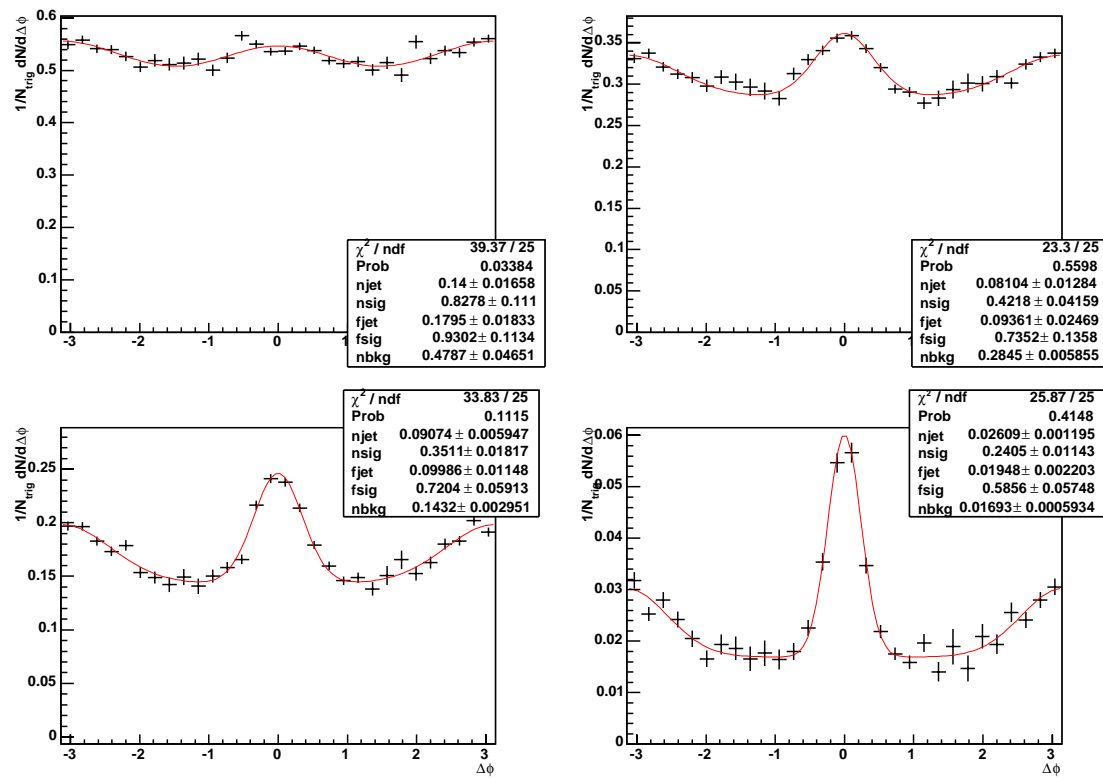
Figure A.9:  $d+\text{Au}$ ,  $2.25 < p_T^{\text{trig}} < 20.0 \text{GeV}/c$ , 60-88% central

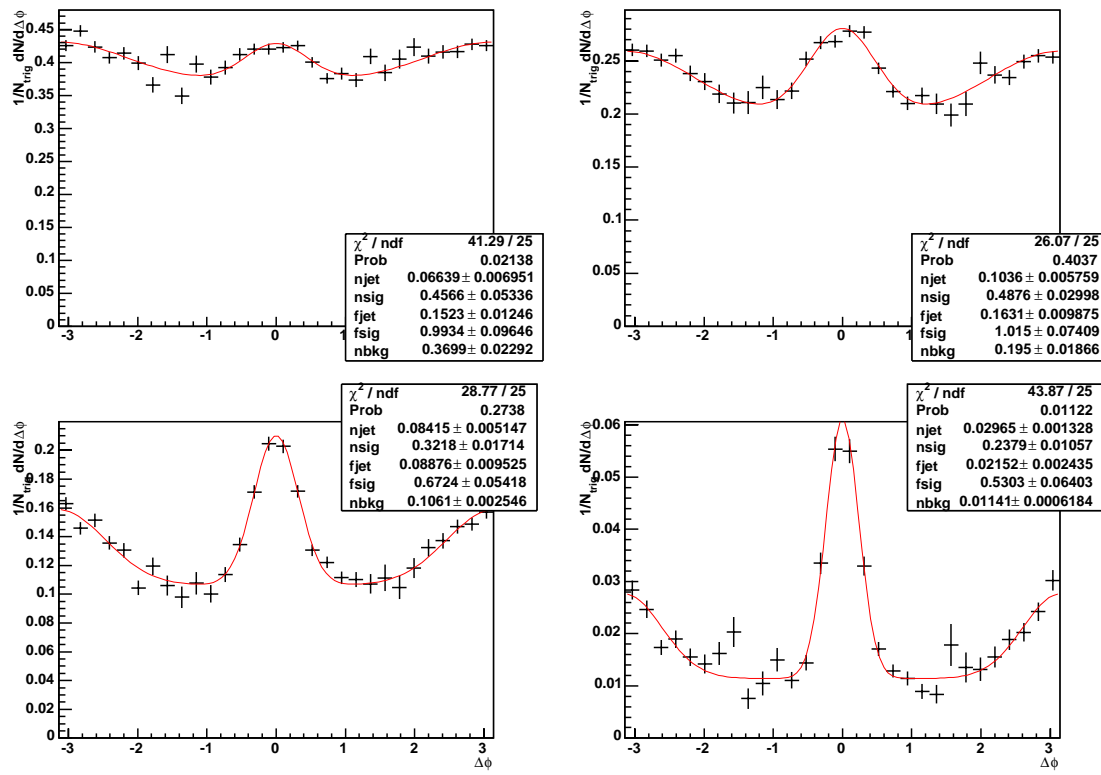
Figure A.10:  $d+Au$ ,  $2.25 < p_T^{trig} < 2.75 GeV/c$ , 0-20% central

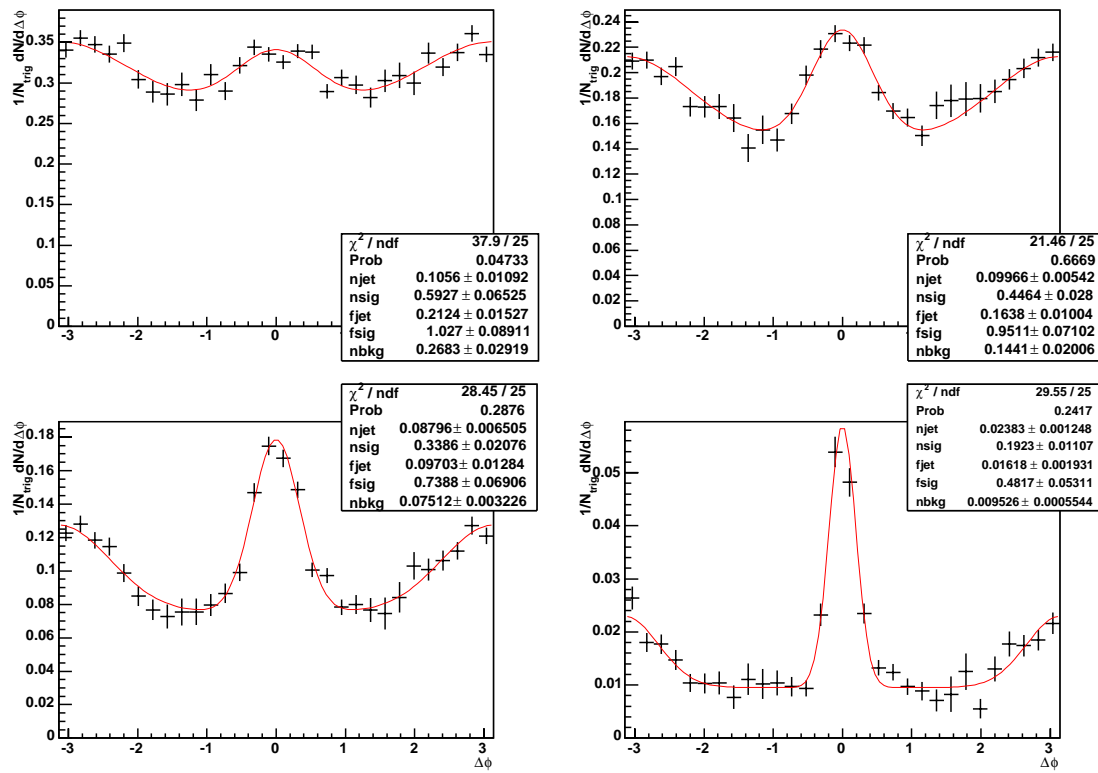
Figure A.11:  $d+\text{Au}$ ,  $2.25 < p_T^{\text{trig}} < 2.75 \text{GeV}/c$ , 20-40% central

Figure A.12:  $d+\text{Au}$ ,  $2.25 < p_T^{trig} < 2.75 \text{GeV}/c$ , 40-60% central

Figure A.13:  $d+Au$ ,  $2.25 < p_T^{trig} < 2.75 GeV/c$ , 60-88% central

Figure A.14:  $d+Au$ ,  $2.75 < p_T^{trig} < 3.5 GeV/c$ , 0-20% central

Figure A.15:  $d+Au$ ,  $2.75 < p_T^{trig} < 3.5 GeV/c$ , 20-40% central

Figure A.16:  $d+Au$ ,  $2.75 < p_T^{trig} < 3.5 GeV/c$ , 40-60% central

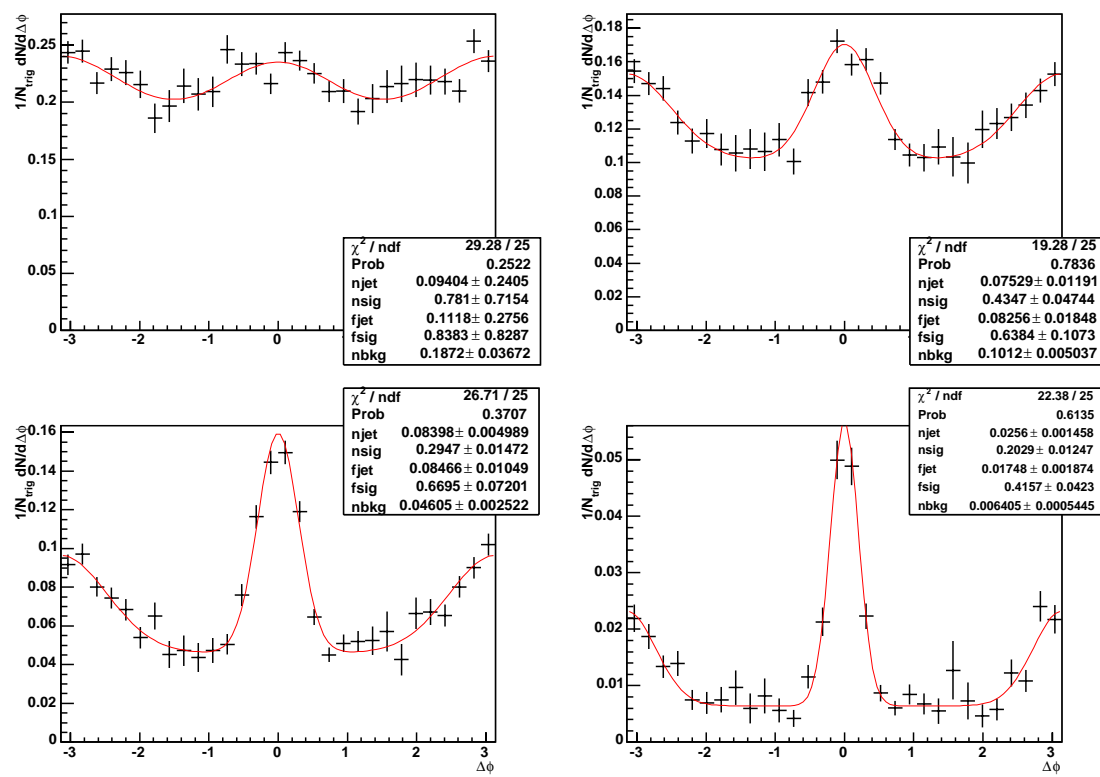
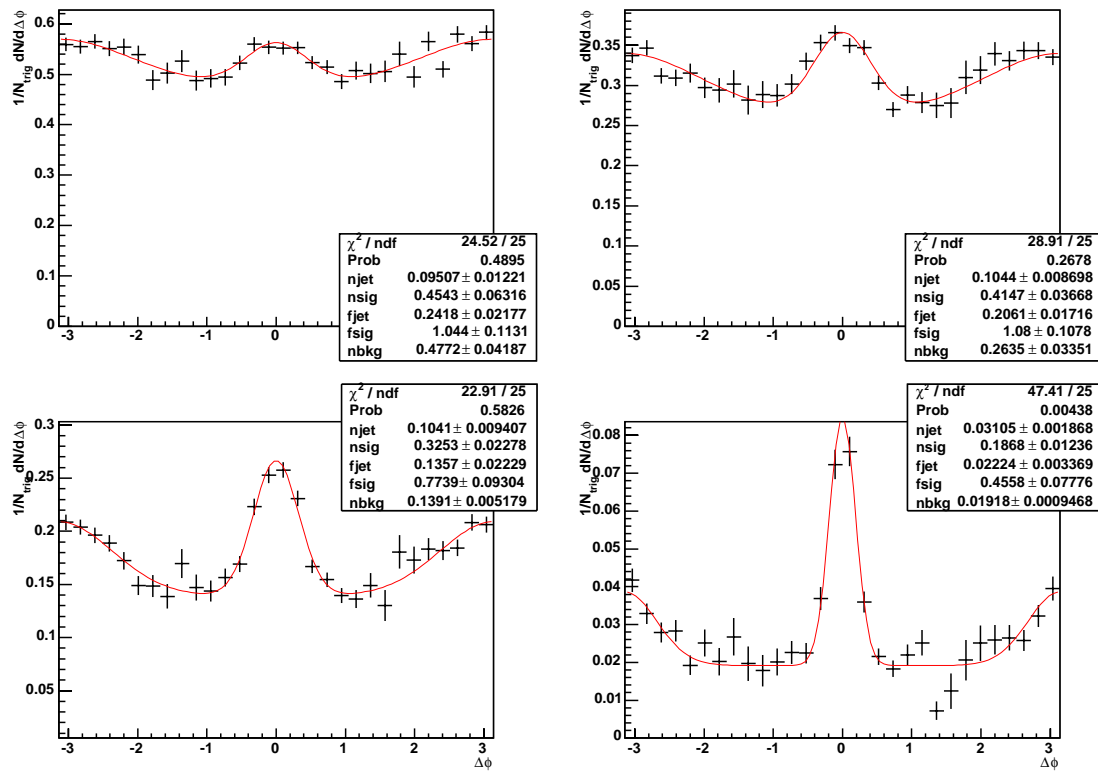


Figure A.17:  $d+Au$ ,  $2.75 < p_T^{trig} < 3.5 GeV/c$ , 60-88% central

Figure A.18:  $d+Au$ ,  $3.5 < p_T^{trig} < 4.5 GeV/c$ , 0-20% central

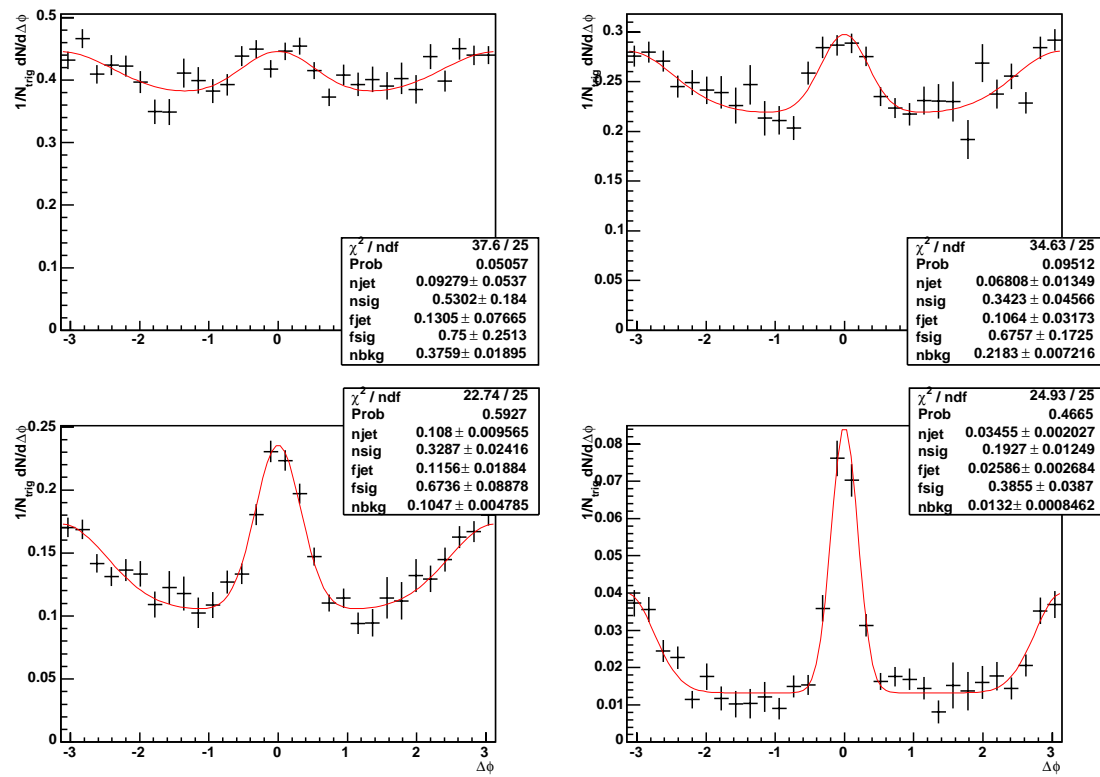
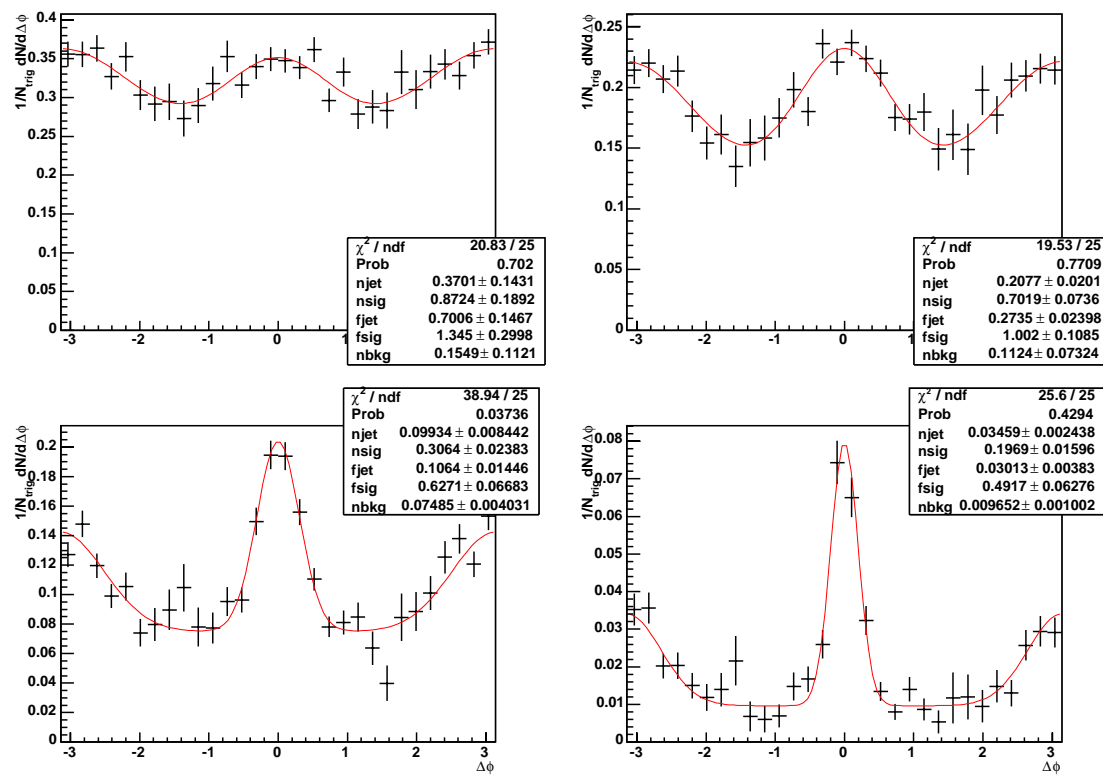
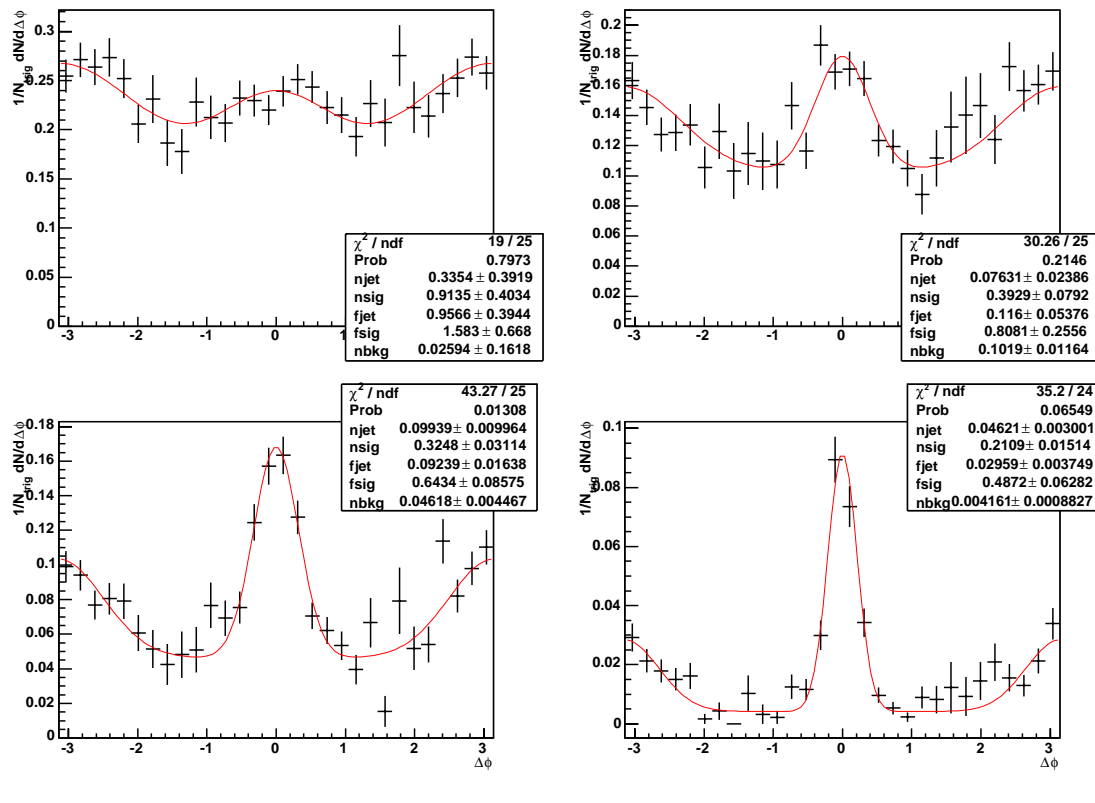
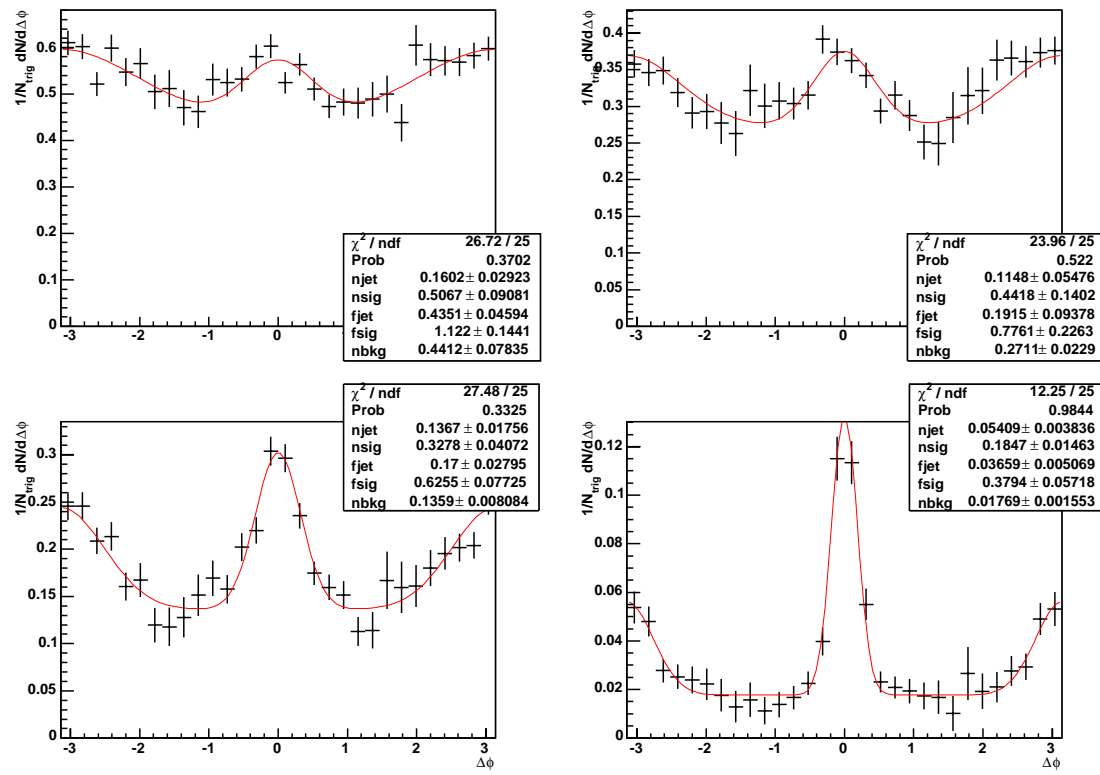


Figure A.19:  $d+Au$ ,  $3.5 < p_T^{trig} < 4.5 GeV/c$ , 20-40% central

Figure A.20:  $d+Au$ ,  $3.5 < p_T^{trig} < 4.5 GeV/c$ , 40-60% central

Figure A.21:  $d+Au$ ,  $3.5 < p_T^{trig} < 4.5 GeV/c$ , 60-88% central

Figure A.22:  $d+\text{Au}$ ,  $4.5 < p_T^{\text{trig}} < 20.0 \text{ GeV}/c$ , 0-20% central

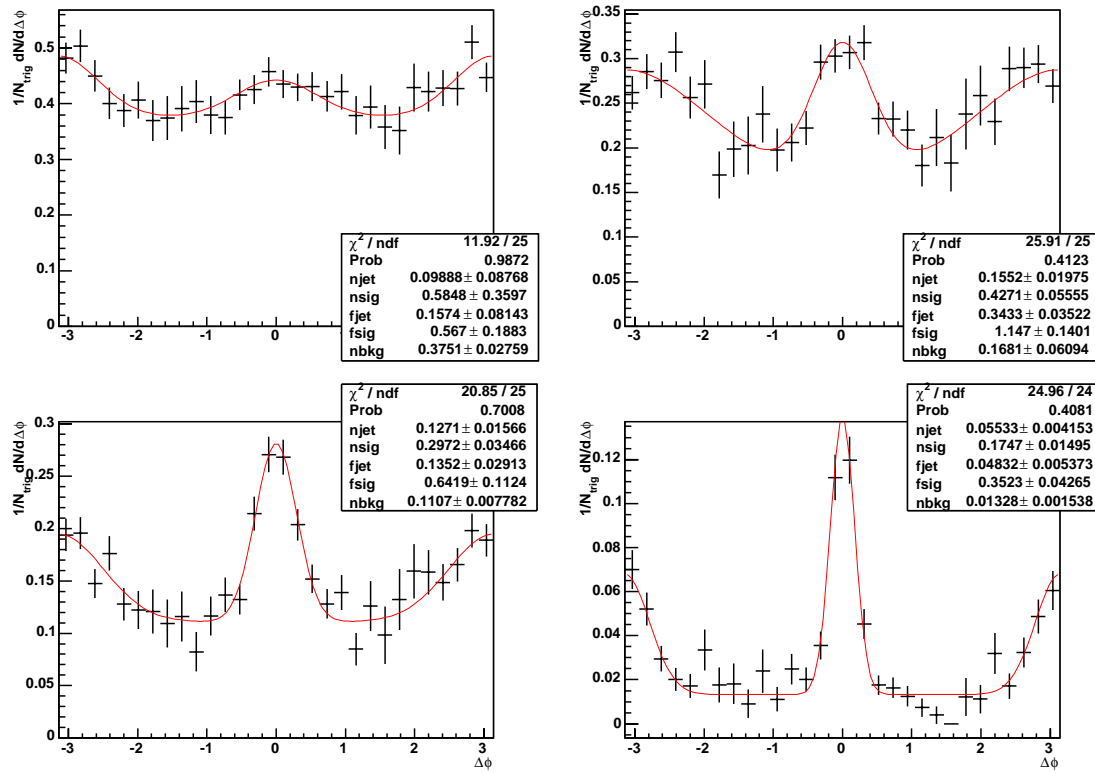
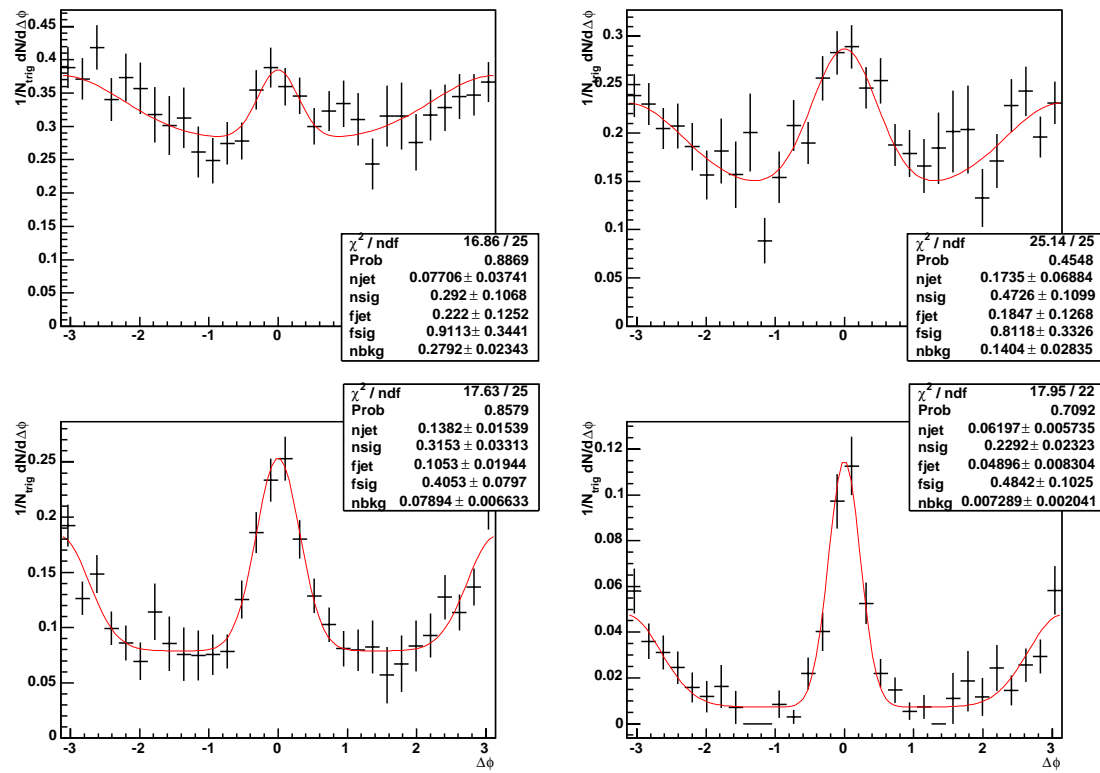


Figure A.23:  $d+\text{Au}$ ,  $4.5 < p_T^{\text{trig}} < 20.0 \text{ GeV}/c$ , 20-40% central

Figure A.24:  $d+\text{Au}$ ,  $4.5 < p_T^{\text{trig}} < 20.0 \text{ GeV}/c$ , 40-60% central

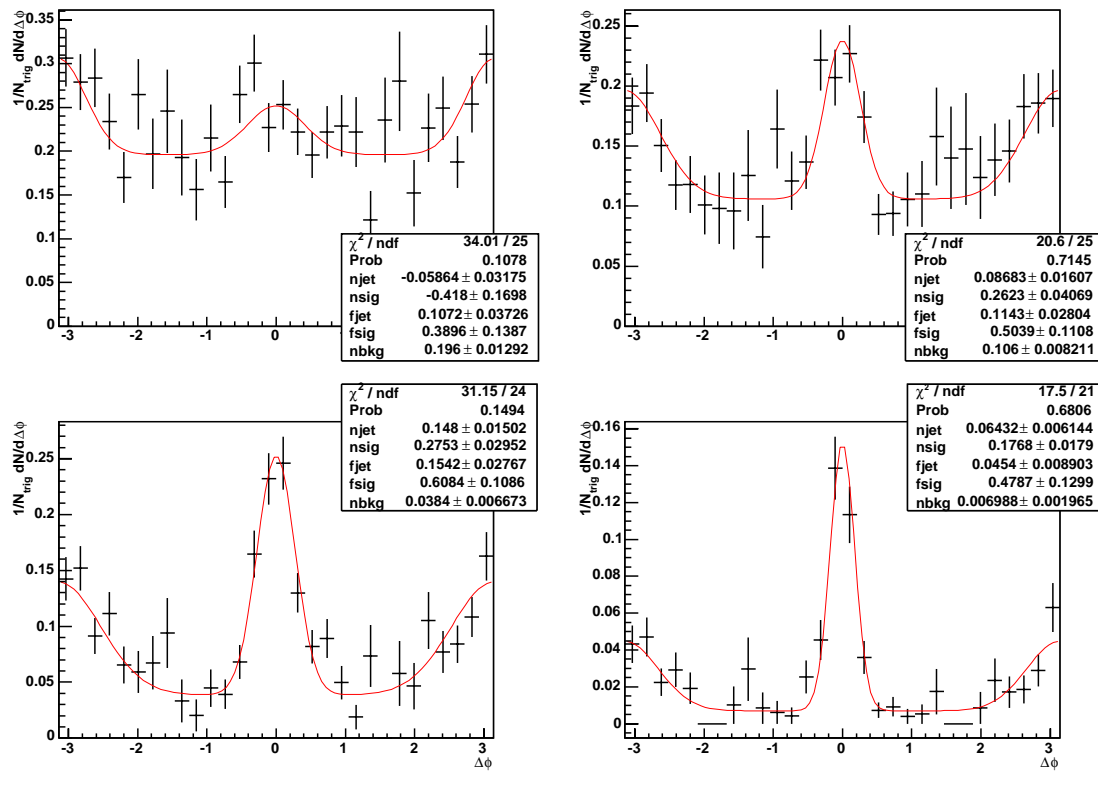


Figure A.25:  $d+\text{Au}$ ,  $4.5 < p_T^{\text{trig}} < 20.0 \text{GeV}/c$ , 60-88% central

### A.3 Associated Yields in Au+Au

The Au+Au yields are not fit, due to the difficulty of convergence on the small signal atop the large background. Additionally, fits assume something about the signal shape, whereas we are searching for possible modifications of jet behavior in heavy-ion collisions. Rather than a fit, the backgrounds are calculated absolutely, as described in this thesis.

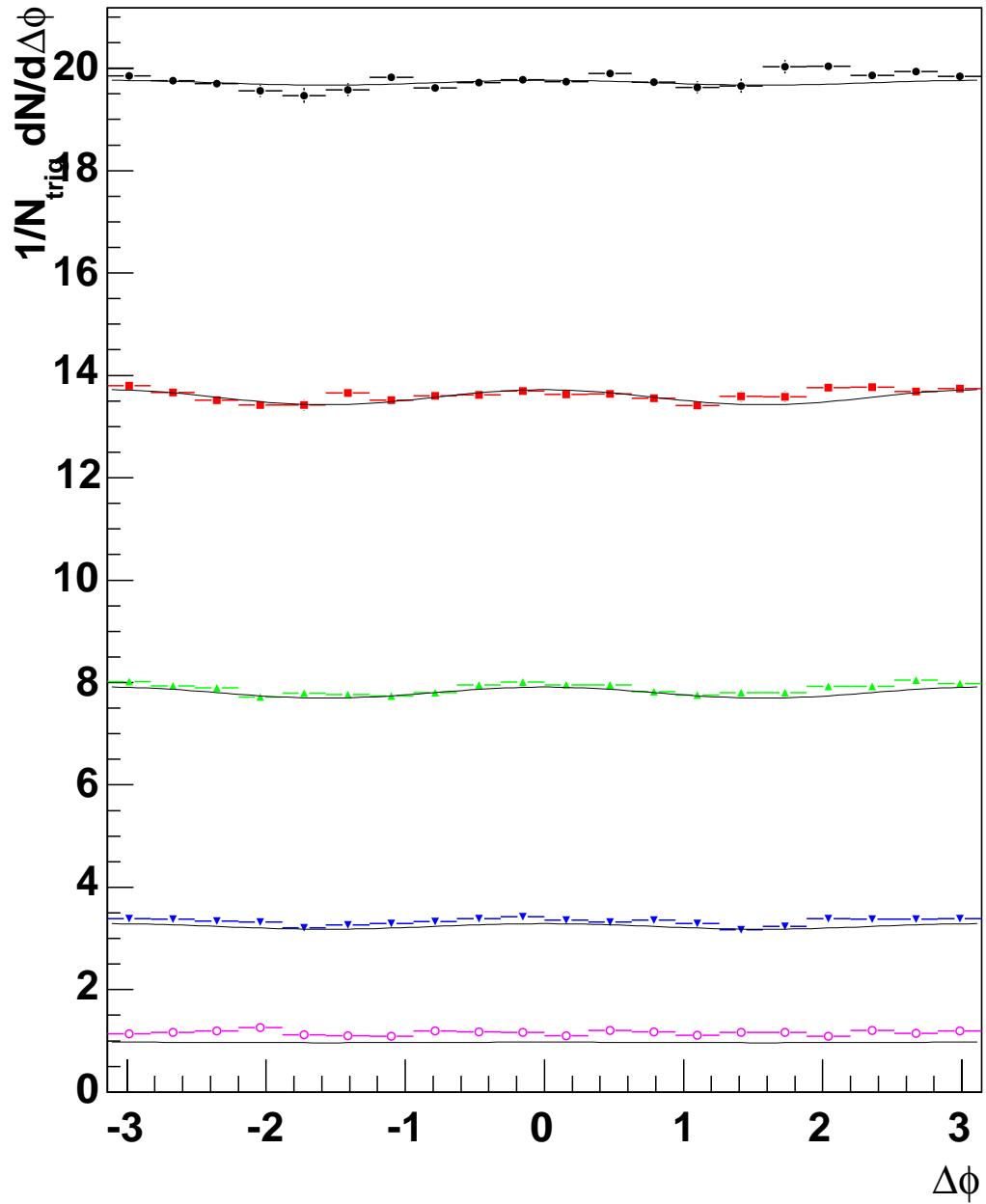


Figure A.26: Au+Au,  $2.25 < p_T^{trig} < 20.0 GeV/c$ ,  $0.3 < p_T^{assoc} < 0.6 GeV/c$

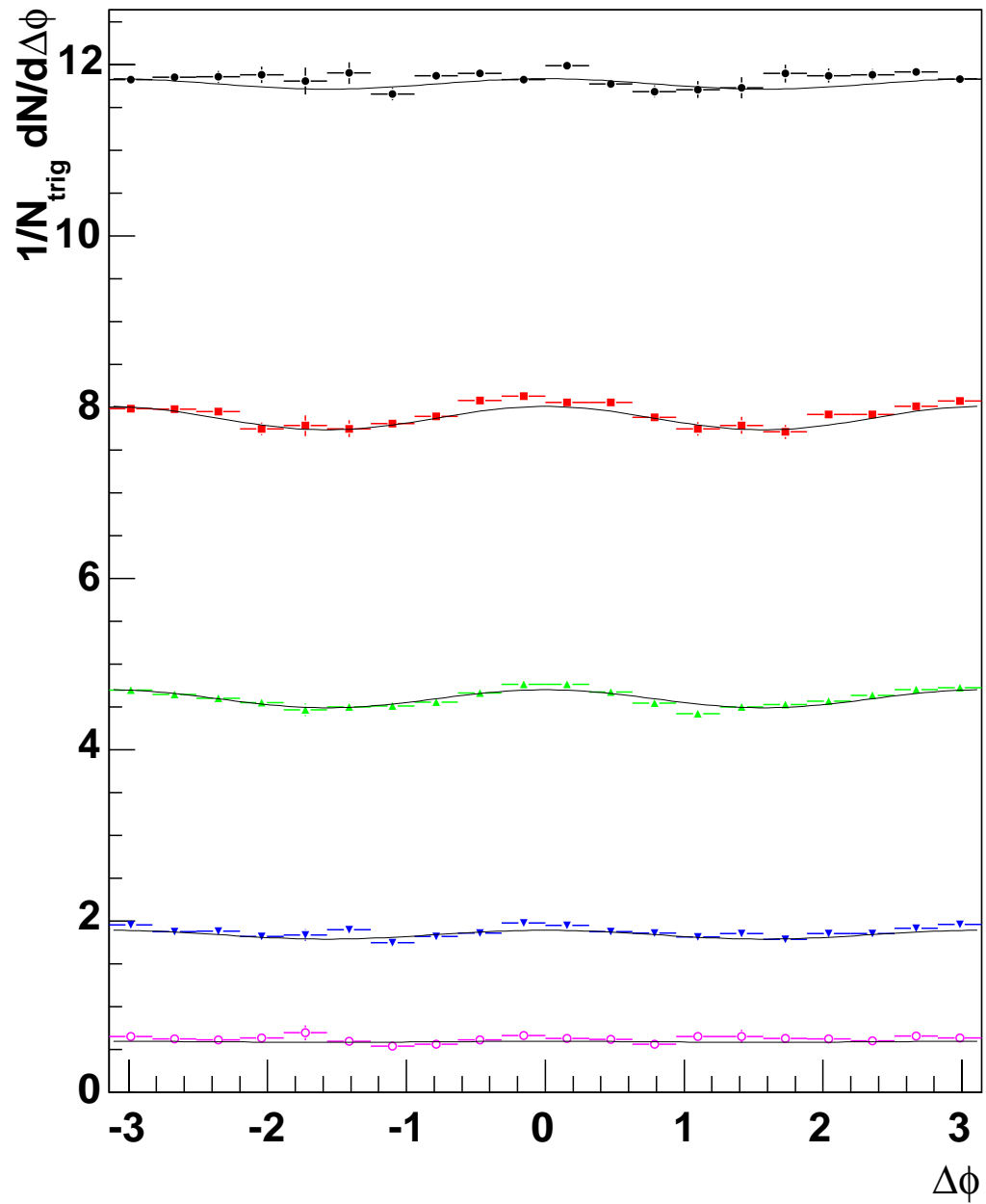


Figure A.27: Au+Au,  $2.25 < p_T^{trig} < 20.0 GeV/c$ ,  $0.6 < p_T^{assoc} < 1.0 GeV/c$

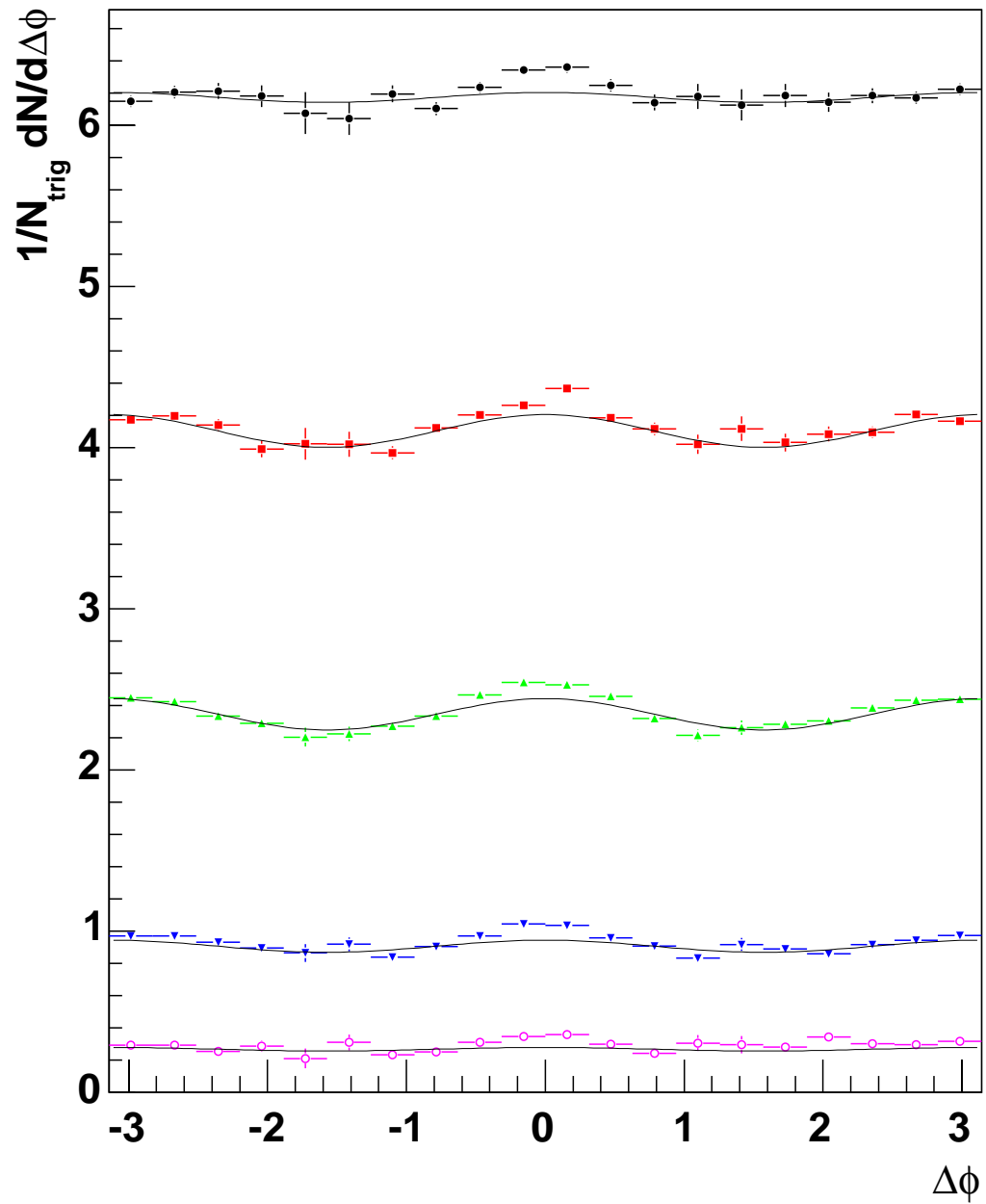


Figure A.28: Au+Au,  $2.25 < p_T^{trig} < 20.0 GeV/c$ ,  $1.0 < p_T^{assoc} < 2.0 GeV/c$

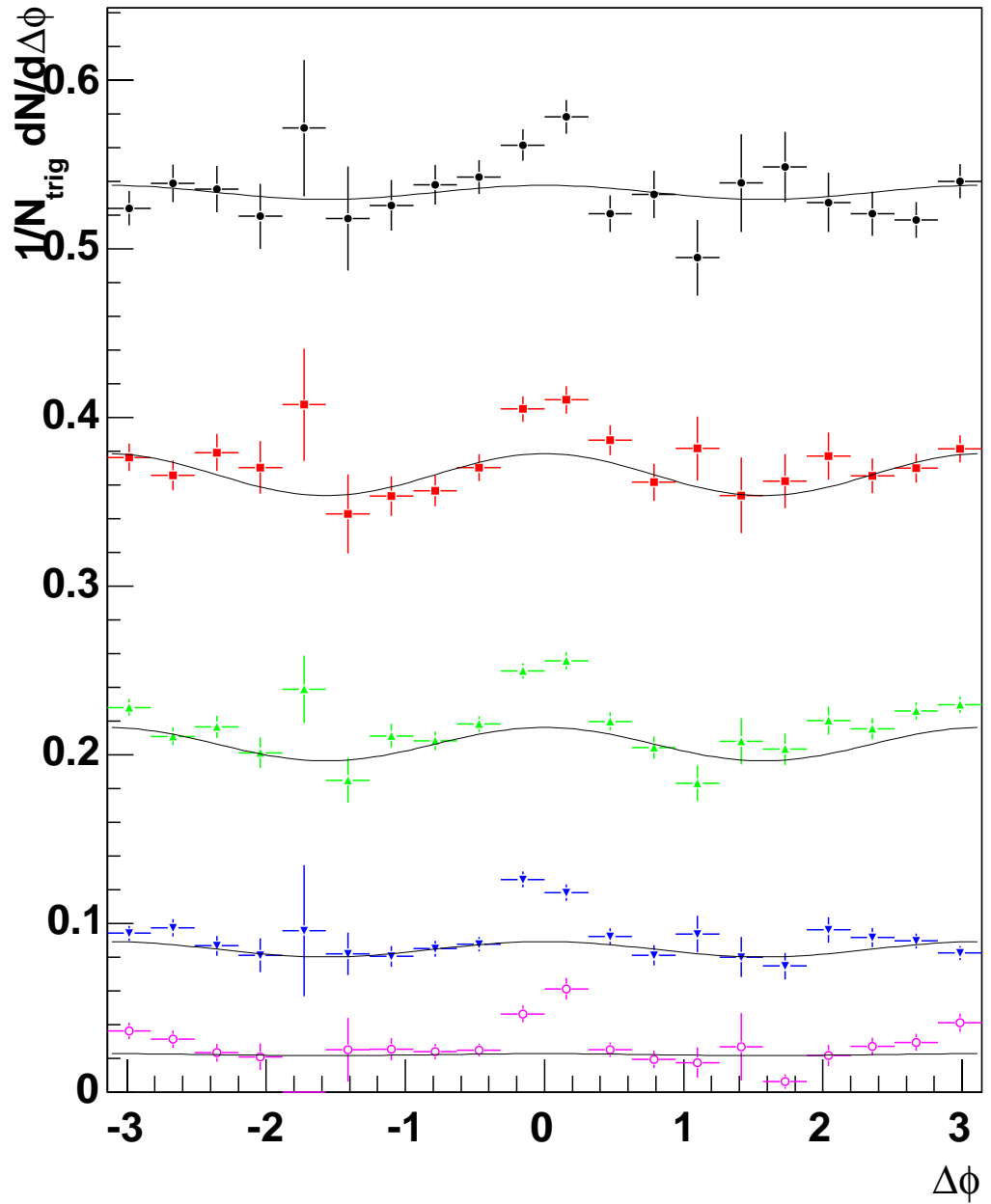


Figure A.29: Au+Au,  $2.25 < p_T^{trig} < 20.0 \text{GeV}/c$ ,  $2.0 < p_T^{assoc} < 4.0 \text{GeV}/c$

## Appendix B

# Phenix Collaboration, Run02 and Run03

S.S. Adler,<sup>5</sup> S. Afanasiev,<sup>17</sup> C. Aidala,<sup>5,9</sup> N.N. Ajitanand,<sup>43</sup> Y. Akiba,<sup>20,38</sup> A. Al-Jamel,<sup>34</sup> J. Alexander,<sup>43</sup> R. Amirikas,<sup>12</sup> K. Aoki,<sup>24</sup> L. Aphecetche,<sup>45</sup> R. Armendariz,<sup>34</sup> S.H. Aronson,<sup>5</sup> R. Averbeck,<sup>44</sup> T.C. Awes,<sup>35</sup> R. Azmoun,<sup>44</sup> V. Babintsev,<sup>15</sup> A. Baldissari,<sup>10</sup> K.N. Barish,<sup>6</sup> P.D. Barnes,<sup>27</sup> B. Bassalleck,<sup>33</sup> S. Bathe,<sup>6,30</sup> S. Batsouli,<sup>9</sup> V. Baublis,<sup>37</sup> F. Bauer,<sup>6</sup> A. Bazilevsky,<sup>5,15,38,br</sup> S. Belikov,<sup>16,15</sup> Y. Berdnikov,<sup>40</sup> S. Bhagavatula,<sup>16</sup> M.T. Bjorndal,<sup>9</sup> J.G. Boissevain,<sup>27</sup> H. Borel,<sup>10</sup> S. Borenstein,<sup>25</sup> M.L. Brooks,<sup>27</sup> D.S. Brown,<sup>34</sup> N. Bruner,<sup>33</sup> D. Bucher,<sup>30</sup> H. Buesching,<sup>5,30</sup> V. Bumazhnov,<sup>15</sup> G. Bunce,<sup>5,38,br</sup> J.M. Burward-Hoy,<sup>26,27,44</sup> S. Butsyk,<sup>44</sup> X. Camard,<sup>45</sup> J.-S. Chai,<sup>18</sup> P. Chand,<sup>4</sup> W.C. Chang,<sup>2</sup> S. Chernichenko,<sup>15</sup> C.Y. Chi,<sup>9</sup> J. Chiba,<sup>20</sup> M. Chiu,<sup>9</sup> I.J. Choi,<sup>52</sup> J. Choi,<sup>19</sup> R.K. Choudhury,<sup>4</sup> T. Chujo,<sup>5</sup> V. Cianciolo,<sup>35</sup> Y. Cobigo,<sup>10</sup> B.A. Cole,<sup>9</sup> M.P. Comets,<sup>36</sup> P. Constantin,<sup>16</sup> M. Csanad,<sup>elite</sup> T. Csorgo,<sup>21</sup> J.P. Cussonneau,<sup>45</sup> D. d'Enterria,<sup>9</sup> D.G. d'Enterria,<sup>45</sup> K. Das,<sup>12</sup> G. David,<sup>5</sup> F. Deak,<sup>elite</sup> H. Delagrange,<sup>45</sup> A. Denisov,<sup>15</sup> A. Deshpande,<sup>38,br</sup> E.J. Desmond,<sup>5</sup> A. Devismes,<sup>44</sup> O. Dietzsch,<sup>41</sup> J.L. Drachenberg,<sup>1</sup> O. Drapier,<sup>25</sup> A. Drees,<sup>44</sup> K.A. Drees,<sup>5</sup> R. du Rietz,<sup>29</sup> A. Durum,<sup>15</sup> D. Dutta,<sup>4</sup> V. Dzhordzhadze,<sup>46</sup> Y.V. Efremenko,<sup>35</sup> K. El Chenawi,<sup>49</sup> A. Enokizono,<sup>14</sup> H. En'yo,<sup>38,riken,br</sup> B. Espagnon,<sup>36</sup> S. Esumi,<sup>48</sup> L. Ewell,<sup>5</sup> D.E. Fields,<sup>33,38,br</sup> C. Finck,<sup>45</sup> F. Fleuret,<sup>25</sup> S.L. Fokin,<sup>23</sup> B.D. Fox,<sup>38,br</sup> Z. Fraenkel,<sup>51</sup> J.E. Frantz,<sup>9</sup> A. Franz,<sup>5</sup> A.D. Frawley,<sup>12</sup> Y. Fukao,<sup>24,38,riken,br</sup> S.-Y. Fung,<sup>6</sup> S. Gadrat,<sup>28</sup> S. Garpman,<sup>29,†</sup> M. Germain,<sup>45</sup> T.K. Ghosh,<sup>49</sup> A. Glenn,<sup>46</sup> G. Gogiberidze,<sup>46</sup> M. Gonin,<sup>25</sup> J. Gosset,<sup>10</sup> Y. Goto,<sup>38,riken,br</sup> R. Granier de Cassagnac,<sup>25</sup> R. Granier de Cassagnac,<sup>25</sup> N. Grau,<sup>16</sup> S.V. Greene,<sup>49</sup> M. Grosse Perdekamp,<sup>ill,uiuc,38,br</sup> W. Guryn,<sup>5</sup> H.-A.-A. Gustafsson,<sup>29</sup> T. Hachiya,<sup>14</sup> J.S. Haggerty,<sup>5</sup> H. Hamagaki,<sup>8</sup> A.G. Hansen,<sup>27</sup> E.P. Hartouni,<sup>26</sup> M. Harvey,<sup>5</sup> K. Hasuko,<sup>38</sup> R. Hayano,<sup>8</sup> N. Hayashi,<sup>38</sup> X. He,<sup>13</sup> M. Heffner,<sup>26</sup> T.K. Hemmick,<sup>44</sup> J.M. Heuser,<sup>38,44</sup> M. Hibino,<sup>50</sup> P. Hidas,<sup>21</sup> H. Hiejima,<sup>ill,uiuc</sup> J.C. Hill,<sup>16</sup> R. Hobbs,<sup>33</sup> W. Holzmann,<sup>43</sup> K. Homma,<sup>14</sup> B. Hong,<sup>22</sup> A. Hoover,<sup>34</sup> T. Horaguchi,<sup>38,riken,br</sup> T. Ichihara,<sup>38,riken,br</sup> V.V. Ikonnikov,<sup>23</sup> K. Imai,<sup>24,38</sup> M. Inaba,<sup>48</sup> M. Inuzuka,<sup>8</sup> D. Isenhower,<sup>1</sup> L. Isenhower,<sup>1</sup> M. Ishihara,<sup>38</sup> M. Issah,<sup>43</sup> A. Isupov,<sup>17</sup> B.V. Jacak,<sup>44</sup>

- W.Y. Jang,<sup>22</sup> Y. Jeong,<sup>19</sup> J. Jia,<sup>44</sup> O. Jinnouchi,<sup>38,riken,brc</sup> B.M. Johnson,<sup>5</sup>  
 S.C. Johnson,<sup>26</sup> K.S. Joo,<sup>31</sup> D. Jouan,<sup>36</sup> F. Kajihara,<sup>8</sup> S. Kametani,<sup>8,50</sup>  
 N. Kamihara,<sup>38,47</sup> M. Kaneta,<sup>38,riken,brc</sup> J.H. Kang,<sup>52</sup> S.S. Kapoor,<sup>4</sup> K. Katou,<sup>50</sup>  
 T. Kawabata,<sup>8</sup> A. Kazantsev,<sup>23</sup> S. Kelly,<sup>colorado,9</sup> B. Khachaturov,<sup>51</sup>  
 A. Khanzadeev,<sup>37</sup> J. Kikuchi,<sup>50</sup> D.H. Kim,<sup>31</sup> D.J. Kim,<sup>52</sup> D.W. Kim,<sup>19</sup> E. Kim,<sup>42</sup>  
 G.-B. Kim,<sup>25</sup> H.J. Kim,<sup>52</sup> E. Kinney,<sup>colorado</sup> W.W. Kinnison,<sup>27</sup> A. Kiss,<sup>elite</sup>  
 E. Kistenev,<sup>5</sup> A. Kiyomichi,<sup>38,48</sup> K. Kiyoyama,<sup>32</sup> C. Klein-Boesing,<sup>30</sup>  
 H. Kobayashi,<sup>38,riken,brc</sup> L. Kochenda,<sup>37</sup> V. Kochetkov,<sup>15</sup> D. Koehler,<sup>33</sup>  
 T. Kohama,<sup>14</sup> R. Kohara,<sup>14</sup> B. Komkov,<sup>37</sup> M. Konno,<sup>48</sup> M. Kopytine,<sup>44</sup>  
 D. Kotchetkov,<sup>6</sup> A. Kozlov,<sup>51</sup> P.J. Kroon,<sup>5</sup> C.H. Kuberg,<sup>1,27</sup> G.J. Kunde,<sup>27</sup>  
 K. Kurita,<sup>38,riken,brc</sup> Y. Kuroki,<sup>48</sup> M.J. Kweon,<sup>22</sup> Y. Kwon,<sup>52</sup> G.S. Kyle,<sup>34</sup>  
 R. Lacey,<sup>43</sup> V. Ladygin,<sup>17</sup> J.G. Lajoie,<sup>16</sup> Y. Le Bornec,<sup>36</sup> A. Lebedev,<sup>16,23</sup>  
 S. Leckey,<sup>44</sup> D.M. Lee,<sup>27</sup> S. Lee,<sup>19</sup> M.J. Leitch,<sup>27</sup> M.A.L. Leite,<sup>41</sup> X.H. Li,<sup>6</sup>  
 H. Lim,<sup>42</sup> A. Litvinenko,<sup>17</sup> M.X. Liu,<sup>27</sup> Y. Liu,<sup>36</sup> C.F. Maguire,<sup>49</sup> Y.I. Makdisi,<sup>5</sup>  
 A. Malakhov,<sup>17</sup> V.I. Manko,<sup>23</sup> Y. Mao,<sup>7,peking,38</sup> G. Martinez,<sup>45</sup> M.D. Marx,<sup>44</sup>  
 H. Masui,<sup>48</sup> F. Matathias,<sup>44</sup> T. Matsumoto,<sup>8,50</sup> M.C. McCain,<sup>1</sup> P.L. McGaughey,<sup>27</sup>  
 E. Melnikov,<sup>15</sup> F. Messer,<sup>44</sup> Y. Miake,<sup>48</sup> J. Milan,<sup>43</sup> T.E. Miller,<sup>49</sup> A. Milov,<sup>44,51</sup>  
 S. Mioduszewski,<sup>5</sup> R.E. Mischke,<sup>27</sup> G.C. Mishra,<sup>13</sup> J.T. Mitchell,<sup>5</sup> A.K. Mohanty,<sup>4</sup>  
 D.P. Morrison,<sup>5</sup> J.M. Moss,<sup>27</sup> F. Mühlbacher,<sup>44</sup> D. Mukhopadhyay,<sup>51</sup>  
 M. Muniruzzaman,<sup>6</sup> J. Murata,<sup>38,riken,brc</sup> S. Nagamiya,<sup>20</sup> J.L. Nagle,<sup>colorado,9</sup>  
 T. Nakamura,<sup>14</sup> B.K. Nandi,<sup>6</sup> M. Nara,<sup>48</sup> J. Newby,<sup>46</sup> P. Nilsson,<sup>29</sup> A.S. Nyanin,<sup>23</sup>  
 J. Nystrand,<sup>29</sup> E. O'Brien,<sup>5</sup> C.A. Ogilvie,<sup>16</sup> H. Ohnishi,<sup>5,38</sup> I.D. Ojha,<sup>3,49</sup>  
 H. Okada,<sup>24,38</sup> K. Okada,<sup>38,riken,brc</sup> M. Ono,<sup>48</sup> V. Onuchin,<sup>15</sup> A. Oskarsson,<sup>29</sup>  
 I. Otterlund,<sup>29</sup> K. Oyama,<sup>8</sup> K. Ozawa,<sup>8</sup> D. Pal,<sup>51</sup> A.P.T. Palounek,<sup>27</sup> V. Pantuev,<sup>44</sup>  
 V.S. Pantuev,<sup>44</sup> V. Papavassiliou,<sup>34</sup> J. Park,<sup>42</sup> W.J. Park,<sup>22</sup> A. Parmar,<sup>33</sup>  
 S.F. Pate,<sup>34</sup> H. Pei,<sup>16</sup> T. Peitzmann,<sup>30</sup> V. Penev,<sup>17</sup> J.-C. Peng,<sup>illu,iuc,27</sup> H. Pereira,<sup>10</sup>  
 V. Peresedov,<sup>17</sup> A. Pierson,<sup>33</sup> C. Pinkenburg,<sup>5</sup> R.P. Pisani,<sup>5</sup> F. Plasil,<sup>35</sup>  
 M.L. Purschke,<sup>5</sup> A.K. Purwar,<sup>44</sup> J. Qualls,<sup>1</sup> J. Rak,<sup>16</sup> I. Ravinovich,<sup>51</sup>  
 K.F. Read,<sup>35,46</sup> M. Reuter,<sup>44</sup> K. Reygers,<sup>30</sup> V. Riabov,<sup>37,40</sup> Y. Riabov,<sup>37</sup>  
 G. Roche,<sup>28</sup> A. Romana,<sup>25</sup> M. Rosati,<sup>16</sup> S. Rosendahl,<sup>29</sup> P. Rosnet,<sup>28</sup> V.L. Rykov,<sup>38</sup>  
 S.S. Ryu,<sup>52</sup> M.E. Sadler,<sup>1</sup> N. Saito,<sup>24,38,riken,brc</sup> T. Sakaguchi,<sup>8,50</sup> M. Sakai,<sup>32</sup>  
 S. Sakai,<sup>48</sup> V. Samsonov,<sup>37</sup> L. Sanfratello,<sup>33</sup> R. Santo,<sup>30</sup> H.D. Sato,<sup>24,38</sup> S. Sato,<sup>5,48</sup>  
 S. Sawada,<sup>20</sup> Y. Schutz,<sup>45</sup> V. Semenov,<sup>15</sup> R. Seto,<sup>6</sup> M.R. Shaw,<sup>1,27</sup> T.K. Shea,<sup>5</sup>  
 I. Shein,<sup>15</sup> T.-A. Shibata,<sup>38,47</sup> K. Shigaki,<sup>14,20</sup> T. Shiina,<sup>27</sup> M. Shimomura,<sup>48</sup>  
 A. Sickles,<sup>44</sup> C.L. Silva,<sup>41</sup> D. Silvermyr,<sup>27,29</sup> K.S. Sim,<sup>22</sup> J. Simon-Gillo,<sup>27</sup>  
 C.P. Singh,<sup>3</sup> V. Singh,<sup>3</sup> M. Sivertz,<sup>5</sup> A. Soldatov,<sup>15</sup> R.A. Soltz,<sup>26</sup> W.E. Sondheim,<sup>27</sup>  
 S. Sorensen,<sup>46</sup> S.P. Sorensen,<sup>46</sup> I.V. Sourikova,<sup>5</sup> F. Staley,<sup>10</sup> P.W. Stankus,<sup>35</sup>  
 E. Stenlund,<sup>29</sup> M. Stepanov,<sup>34</sup> A. Ster,<sup>21</sup> S.P. Stoll,<sup>5</sup> T. Sugitate,<sup>14</sup> J.P. Sullivan,<sup>27</sup>  
 S. Takagi,<sup>48</sup> E.M. Takagui,<sup>41</sup> A. Taketani,<sup>38,riken,brc</sup> M. Tamai,<sup>50</sup> K.H. Tanaka,<sup>20</sup>  
 Y. Tanaka,<sup>32</sup> K. Tanida,<sup>38</sup> M.J. Tannenbaum,<sup>5</sup> A. Taranenko,<sup>43</sup> P. Tarján,<sup>11</sup>  
 J.D. Tepe,<sup>1,27</sup> T.L. Thomas,<sup>33</sup> M. Togawa,<sup>24,38</sup> J. Tojo,<sup>24,38</sup> H. Torii,<sup>24,38,riken,brc</sup>  
 R.S. Towell,<sup>1</sup> V-N. Tram,<sup>25</sup> I. Tserruya,<sup>51</sup> Y. Tsuchimoto,<sup>14</sup> H. Tsuruoka,<sup>48</sup>  
 S.K. Tuli,<sup>3</sup> H. Tydesjö,<sup>29</sup> N. Tyurin,<sup>15</sup> T.J. Uam,<sup>31</sup> H.W. van Hecke,<sup>27</sup>  
 J. Velkovska,<sup>5,44</sup> M. Velkovsky,<sup>44</sup> V. Veszprémi,<sup>11</sup> L. Villatte,<sup>46</sup> A.A. Vinogradov,<sup>23</sup>  
 M.A. Volkov,<sup>23</sup> E. Vznuzdaev,<sup>37</sup> X.R. Wang,<sup>13</sup> Y. Watanabe,<sup>38,riken,brc</sup>  
 S.N. White,<sup>5</sup> N. Willis,<sup>36</sup> F.K. Wohn,<sup>16</sup> C.L. Woody,<sup>5</sup> W. Xie,<sup>6</sup> Y. Yang,<sup>7</sup>

A. Yanovich,<sup>15</sup> S. Yokkaichi,<sup>38,riken\_rbrc</sup> G.R. Young,<sup>35</sup> I.E. Yushmanov,<sup>23</sup>  
 W.A. Zajc,<sup>9</sup> C. Zhang,<sup>9</sup> S. Zhou,<sup>7</sup> S.J. Zhou,<sup>51</sup> J. Zimányi,<sup>21</sup> L. Zolin,<sup>17</sup> X. Zong,<sup>16</sup>  
 (PHENIX Collaboration)

<sup>1</sup>Abilene Christian University, Abilene, TX 79699, USA

<sup>2</sup>Institute of Physics, Academia Sinica, Taipei 11529, Taiwan

<sup>3</sup>Department of Physics, Banaras Hindu University, Varanasi 221005, India

<sup>4</sup>Bhabha Atomic Research Centre, Bombay 400 085, India

<sup>5</sup>Brookhaven National Laboratory, Upton, NY 11973-5000, USA

<sup>6</sup>University of California - Riverside, Riverside, CA 92521, USA

<sup>7</sup>China Institute of Atomic Energy (CIAE), Beijing, People's Republic of China

<sup>8</sup>Center for Nuclear Study, Graduate School of Science, University of Tokyo, 7-3-1  
 Hongo, Bunkyo, Tokyo 113-0033, Japan

<sup>9</sup>Columbia University, New York, NY 10027 and Nevis Laboratories, Irvington,  
 NY 10533, USA

<sup>10</sup>Dapnia, CEA Saclay, F-91191, Gif-sur-Yvette, France

<sup>11</sup>Debrecen University, H-4010 Debrecen, Egyetem tér 1, Hungary

<sup>12</sup>Florida State University, Tallahassee, FL 32306, USA

<sup>13</sup>Georgia State University, Atlanta, GA 30303, USA

<sup>14</sup>Hiroshima University, Kagamiyama, Higashi-Hiroshima 739-8526, Japan

<sup>15</sup>Institute for High Energy Physics (IHEP), Protvino, Russia

<sup>16</sup>Iowa State University, Ames, IA 50011, USA

<sup>17</sup>Joint Institute for Nuclear Research, 141980 Dubna, Moscow Region, Russia

<sup>18</sup>KAERI, Cyclotron Application Laboratory, Seoul, South Korea

<sup>19</sup>Kangnung National University, Kangnung 210-702, South Korea

<sup>20</sup>KEK, High Energy Accelerator Research Organization, Tsukuba-shi, Ibaraki-ken  
 305-0801, Japan

<sup>21</sup>KFKI Research Institute for Particle and Nuclear Physics (RMKI), H-1525  
 Budapest 114, POBox 49, Hungary

<sup>22</sup>Korea University, Seoul, 136-701, Korea

<sup>23</sup>Russian Research Center "Kurchatov Institute", Moscow, Russia

<sup>24</sup>Kyoto University, Kyoto 606, Japan

<sup>25</sup>Laboratoire Leprince-Ringuet, Ecole Polytechnique, CNRS-IN2P3, Route de  
 Saclay, F-91128, Palaiseau, France

<sup>26</sup>Lawrence Livermore National Laboratory, Livermore, CA 94550, USA

<sup>27</sup>Los Alamos National Laboratory, Los Alamos, NM 87545, USA

<sup>28</sup>LPC, Université Blaise Pascal, CNRS-IN2P3, Clermont-Fd, 63177 Aubiere  
 Cedex, France

<sup>29</sup>Department of Physics, Lund University, Box 118, SE-221 00 Lund, Sweden

<sup>30</sup>Institut fuer Kernphysik, University of Muenster, D-48149 Muenster, Germany

<sup>31</sup>Myongji University, Yongin, Kyonggido 449-728, Korea

<sup>32</sup>Nagasaki Institute of Applied Science, Nagasaki-shi, Nagasaki 851-0193, Japan

<sup>33</sup>University of New Mexico, Albuquerque, NM, USA

<sup>34</sup>New Mexico State University, Las Cruces, NM 88003, USA

<sup>35</sup>Oak Ridge National Laboratory, Oak Ridge, TN 37831, USA

<sup>36</sup>IPN-Orsay, Universite Paris Sud, CNRS-IN2P3, BP1, F-91406, Orsay, France

<sup>37</sup>PNPI, Petersburg Nuclear Physics Institute, Gatchina, Russia

<sup>38</sup>RIKEN (The Institute of Physical and Chemical Research), Wako, Saitama  
351-0198, JAPAN

<sup>39</sup>RIKEN BNL Research Center, Brookhaven National Laboratory, Upton, NY  
11973-5000, USA

<sup>40</sup>St. Petersburg State Technical University, St. Petersburg, Russia

<sup>41</sup>Universidade de São Paulo, Instituto de Física, Caixa Postal 66318, São Paulo  
CEP05315-970, Brazil

<sup>42</sup>System Electronics Laboratory, Seoul National University, Seoul, South Korea

<sup>43</sup>Chemistry Department, Stony Brook University, SUNY, Stony Brook, NY  
11794-3400, USA

<sup>44</sup>Department of Physics and Astronomy, Stony Brook University, SUNY, Stony  
Brook, NY 11794, USA

<sup>45</sup>SUBATECH (Ecole des Mines de Nantes, CNRS-IN2P3, Université de Nantes)  
BP 20722 - 44307, Nantes, France

<sup>46</sup>University of Tennessee, Knoxville, TN 37996, USA

<sup>47</sup>Department of Physics, Tokyo Institute of Technology, Tokyo, 152-8551, Japan

<sup>48</sup>Institute of Physics, University of Tsukuba, Tsukuba, Ibaraki 305, Japan

<sup>49</sup>Vanderbilt University, Nashville, TN 37235, USA

<sup>50</sup>Waseda University, Advanced Research Institute for Science and Engineering, 17  
Kikui-cho, Shinjuku-ku, Tokyo 162-0044, Japan

<sup>51</sup>Weizmann Institute, Rehovot 76100, Israel

<sup>52</sup>Yonsei University, IPAP, Seoul 120-749, Korea